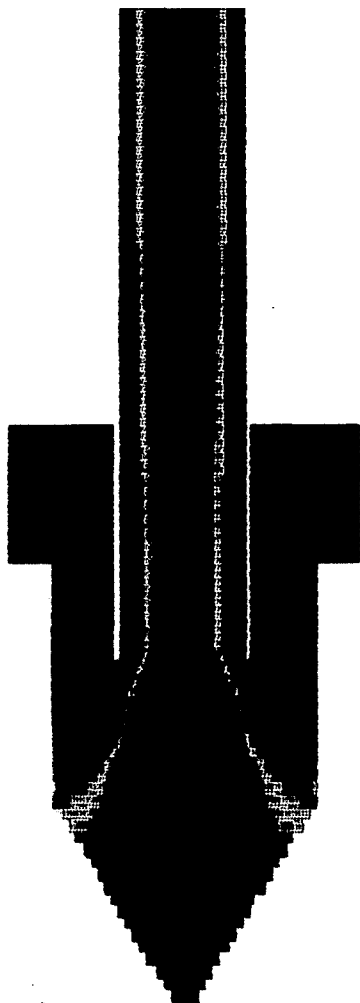
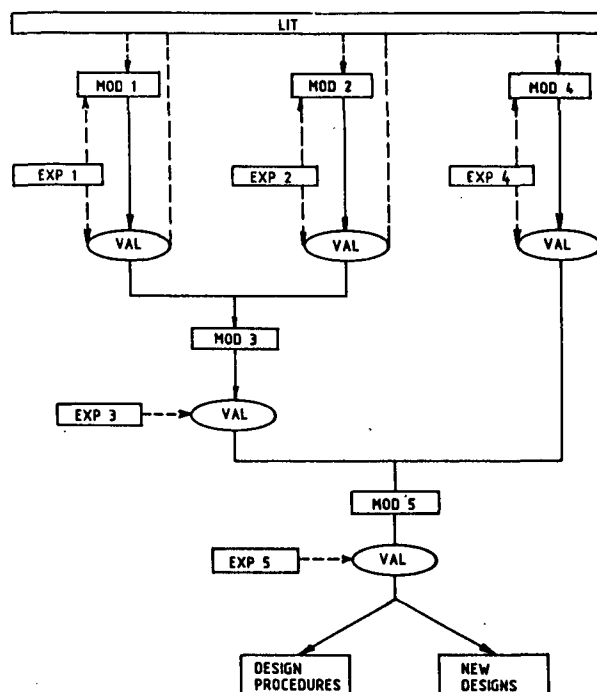


A new approach to the design of gas-liquid separators for the oil industry



R.A. Swanborn

TR diss
1672



- MOD1 reproduces the gas flow field inside a basic separation unit;
- MOD2 describes the behaviour of the liquid phase (particle trajectories, reentrainment and creep phenomena);
- MOD3 describes the behaviour of a basic separation unit;
- MOD4 quantifies the measure of maldistribution across a full size separator; no need to model this with the earlier mentioned fluid dynamic codes;
- MOD5 combines the predictive powers of MOD3 and MOD4 and should therefore be able to describe the behaviour of an actual scaled separator over a broad range of operating conditions;
- EXP1 a. provides the fluid dynamic code with necessary physical information to start with (starting conditions) and
b. provides the experimental data to validate MOD1 with (gas flow field measurements)
- EXP2 identifies and quantifies phenomena related to the liquid phase (reentrainment, creep, particle trajectories);
- EXP3 provides the experimental data to validate MOD3 with (operating characteristics of a basic separation unit over a broad range of operating conditions);
- EXP4 a. provides physical information (starting conditions) for MOD4;
b. provides the experimental data to validate MOD4 with;
- EXP5 provides the experimental data to validate MOD5 with (operating characteristics of an actual scaled separator over a broad range of operating conditions);
- LIT represents the information acquired through literature investigation used for validating and supplementing models.
- VAL validation

452238
317 888 >
GA diss 16 72

A NEW APPROACH TO THE DESIGN OF GAS-LIQUID
SEPARATORS FOR THE OIL INDUSTRY

Front cover: An unrealistic simulation of the gas flow field inside a reverse flow cyclone (see section 7.5).

Innerside of front cover: Project structure and nomenclature (see chapter 4).

A NEW APPROACH TO THE DESIGN OF GAS-LIQUID
SEPARATORS FOR THE OIL INDUSTRY

PROEFSCHRIFT



ter verkrijging van de graad van doctor aan de
Technische Universiteit Delft, op gezag van de
Rector Magnificus, Prof.drs. P.A. Schenck,
in het openbaar te verdedigen ten overstaan van een
commissie door het College van Dekanen daartoe aangewezen,
op dinsdag 25 oktober 1988 te 14.00 uur

door

ROMBOUT ADRIAAN SWANBORN

geboren te Point Fortin, Trinidad
mijnningenieur

TR diss
1672

Dit proefschrift is goedgekeurd door de promotoren
Prof.ir. E.J. de Jong en Prof.dr.ir. J. de Graauw

ADDENDUM TO: "A NEW APPROACH TO THE DESIGN OF GAS-LIQUID
SEPARATORS FOR THE OIL INDUSTRY",

by R.A. Swanborn

It has not been stated clearly in chapter 6, section 6.3.2., block RFC-EXP3 and RFC-EXP4 that the determined characteristics of (single)cyclone type E and of (multi)cyclones type B and C, all of which have been designed by Paladon Engineering Ltd., should not be considered as representative for the characteristics of the equipment that is presently designed by this company for commercial purposes.

The cyclone separator-designs that have been tested in this study have been put at our disposal by Paladon, but concern preliminary development versions that are different from the commercial equipment of this firm both with respect to geometry and principle of operation. The cyclones tested were a design specifically being considered to overcome erosion problems in high sand loading applications only.

Some of the most important negative characteristics with respect to other designs as tested in this study, can be explained directly by the presence of extra features, not accommodated in the conventional commercial designs, but obviously not yet of the optimal geometrical form in the tested versions.

*"To some, science is an exalted goddess,
to others a cow which provides them
with butter"*

B. Russell, 1928

Aan mijn ouders en Ella

CONTENTS

SUMMARY AND CONCLUSIONS

SAMENVATTING EN CONCLUSIES

| | |
|---|----|
| 1. INTRODUCTION | 1 |
| 2. CLASSIFICATION OF PRESENT GAS/LIQUID SEPARATION APPLICATIONS | 5 |
| 2.1 Introduction | 5 |
| 2.2 Basic description of a gas production system | 5 |
| 2.3 Inventory of separator locations | 8 |
| 2.3.1 Introductory remarks | 8 |
| 2.3.2 Wellhead separation | 8 |
| 2.3.3 Scrubbing | 9 |
| 2.3.4 Offshore gas winning | 14 |
| 2.3.5 Onshore gas winning | 14 |
| 2.4 Evaluation of separator inlet conditions and requirements | 15 |
| 3. PRESENT TECHNOLOGY | 17 |
| 3.1 Introduction | 17 |
| 3.2 Basic gas/liquid separation mechanisms | 20 |
| 3.3 Sedimentation | 23 |
| 3.3.1 General aspects | 23 |
| 3.3.2 Knock-out vessels | 23 |
| 3.4 Inertial separation | 26 |
| 3.4.1 Introductory remarks | 26 |
| 3.4.2 Inertial separation by mesh type separators | 26 |
| 3.4.3 Inertial separation with vane-type separators | 28 |
| 3.4.4 Cyclone type separators | 32 |
| 3.4.4.1 Preliminary remarks | 32 |
| 3.4.4.2 (Reverse flow) Dust cyclones | 34 |
| 3.4.4.3 Mist cyclones | 35 |
| 3.4.4.4 Multicyclones | 39 |
| 3.4.4.5 Straight through cyclones | 40 |
| 3.4.4.6 Characteristics of cyclone type separators | 44 |

| | | |
|---------|---|----|
| 3.5 | Diffusional separation | 46 |
| 3.6 | Existing separator types | 48 |
| 3.6.1 | Horizontal or vertical position | 49 |
| 3.6.2 | Number of separation stages | 50 |
| 3.7 | Evaluation of present technology | 52 |
| 4. | DESCRIPTION OF THE CURRENT RESEARCH PROJECT | 55 |
| 4.1 | Structure of chapter | 55 |
| 4.2 | Formulation of research objectives | 55 |
| 4.3 | Project strategy and tools | 57 |
| 4.3.1 | Introductory remarks | 57 |
| 4.3.2 | Project strategy and tools | 58 |
| 4.4 | Scope of present report | 61 |
| 5. | RESULTS: LITERATURE SEARCH | 63 |
| 5.1 | Introduction | 63 |
| 5.2 | Determination of the inlet conditions | 63 |
| 5.3 | Friction factors at gas/liquid interface | 67 |
| 5.3.1 | Form of gas/liquid interface | 67 |
| 5.3.2 | Friction factors of liquid film/gas systems | 69 |
| 5.3.2.1 | Introductory remarks | 69 |
| 5.3.2.2 | Wall friction factors of liquid films | 69 |
| 5.3.2.3 | Interfacial friction factor of liquid films | 70 |
| 5.3.3 | Friction factors of rotating liquid film/gas systems | 72 |
| 5.4 | Reentrainment and related effects | 73 |
| 5.4.1 | Film break-up mechanisms | 73 |
| 5.4.2 | Initiation criteria of reentrainment | 74 |
| 5.4.3 | The rate of reentrainment | 79 |
| 5.4.4 | Droplet size distribution of reentrainment | 80 |
| 5.4.5 | Direction of and initial velocity of reentrained droplets | 81 |
| 5.5 | Characterization of swirl elements and swirling flows | 82 |
| 5.5.1 | Introductory remarks | 82 |
| 5.5.2 | Examples of rotating flow fields | 82 |
| 5.5.3 | Characterization of swirl elements and swirling flows | 82 |

| | |
|---|-----|
| 6. TEST FACILITIES AND EXPERIMENTAL RESULTS | 91 |
| 6.1 Structure of chapter | 91 |
| 6.2 Test facilities | 91 |
| 6.2.1 Introduction | 91 |
| 6.2.2 Test-rig 1 (block EXP1, EXP2) | 92 |
| 6.2.3 Test-rig 2 (block EXP2, EXP3, EXP5) | 94 |
| 6.2.4 Test-rig 3 (block EXP2, EXP4, EXP5) | 98 |
| 6.3 Experimental results | 102 |
| 6.3.1 Axial cyclones | 102 |
| 6.3.2 Reverse flow cyclones | 108 |
| 6.3.3 Vanes | 118 |
| 7. MODELLING RESULTS | 129 |
| 7.1 Introduction | 129 |
| 7.1.1 Structure of chapter | 129 |
| 7.1.2 Modelling techniques | 129 |
| 7.2 Numerical modelling of gas flow fields | 130 |
| 7.2.1 Physical background | 130 |
| 7.2.2 Mathematical background | 135 |
| 7.2.3 Fluid dynamic codes used | 136 |
| 7.3 Physical modelling of gas/liquid interactions | 136 |
| 7.3.1 Introductory remarks | 136 |
| 7.3.2 Behaviour of droplet phase | 137 |
| 7.3.3 Behaviour of the liquid film | 139 |
| 7.4 Axial cyclone models | 147 |
| 7.4.1 Block AC-MOD1 | 148 |
| 7.4.2 Block AC-MOD2 | 157 |
| 7.4.3 Block AC-MOD3 | 160 |
| 7.4.3.1 Structure of model | 160 |
| 7.4.3.2 Primary separation efficiency | 160 |
| 7.4.3.3 Maximal capacity | 162 |
| 7.4.4 Blocks AC-MOD4/MOD5 | 164 |
| 7.5 Reverse flow cyclones | 165 |
| 7.5.1 Block RFC-MOD1 | 165 |
| 7.5.2 Block RFC-MOD2 | 166 |

| | |
|--|------|
| 7.5.3 Block RFC-MOD3 | 167 |
| 7.5.3.1 Primary separation efficiency of a reverse flow cyclone | 167 |
| 7.5.3.2 Maximal capacity of a reverse flow cyclone | 168 |
| 7.5.3.3 Pressure drop of a reverse flow cyclone | 169 |
| 7.5.4 Block RFC-MOD4 | 169 |
| 7.5.5 Block RFC-MOD5 | 171 |
| 7.6 Vanes | 172 |
| 7.6.1 Block V-MOD1 | 172 |
| 7.6.2 Block V-MOD2 | 173 |
| 7.6.3 Block V-MOD3 | 175 |
| 7.6.4 Block V-MOD4 | 177 |
| 7.6.5 Block V-MOD5 | 179 |
| 8. CONCLUSIONS: IMPROVED DESIGNS AND DESIGN PROCEDURES | 181 |
| 8.1 Introduction | 181 |
| 8.2 Improved designs | 181 |
| 8.2.1 Axial cyclones | 181 |
| 8.2.2 Reverse flow cyclones | 187 |
| 8.2.3 Vanes | 188 |
| 8.3 Improved design equations | 192 |
| 8.3.1 Introductory remarks | 192 |
| 8.3.2 Traditional axial cyclones | 192 |
| 8.3.3 Reverse flow cyclones | 196 |
| 8.3.4 Vanes | 198 |
| LIST OF SYMBOLS | 203 |
| REFERENCES | 205 |
| APPENDICES | |
| A 3.3.2 Knock-out vessels | A. 1 |
| 3.4.2 Mesh type separators | A. 5 |
| 3.4.3 Vane type separators | A.12 |
| 3.4.4.2 Reverse flow cyclones | A.19 |
| 3.4.4.3 Mist cyclones | A.37 |

| | | |
|---------|--|------|
| 3.4.4.4 | Multicyclones | A.39 |
| 3.4.4.5 | Straight-through cyclones | A.40 |
| 3.5. | Diffusional separation | A.44 |
| B | Representative examples of swirling flow characterizations | B.1 |
| B.1 | Swirling flow in a smooth pipe | B.1 |
| B.2 | Swirling flow in axial cyclones | B.2 |
| B.3 | Swirling flow in reverse flow cyclones | B.3 |
| C | Experimental results | C.1 |
| D | Turbulence models | D.1 |
| D.1 | Turbulence models based on the concept of Boussinesq | D.1 |
| D.1.1 | Background of Boussinesq models | D.1 |
| D.1.2 | Zero PDE models | D.2 |
| D.1.3 | One PDE models | D.3 |
| D.1.4 | Two PDE models | D.3 |
| D.2 | Direct modelling of turbulent shear stresses | D.4 |

CURRICULUM VITAE

ACKNOWLEDGEMENTS

SUMMARY AND CONCLUSIONS

The most important gas/liquid separations that take place in oil field operation have been investigated.

An inventory has been made of the conditions under which the separations have to take place and which requirements have to be fulfilled.

The presently available separator types have been evaluated with respect to the suitability to fulfil the requirements listed above.

It appeared that many separator types were not specifically designed for high pressure gas/liquid separation (rather for either atmospheric gas/liquid or high pressure gas/dust separation).

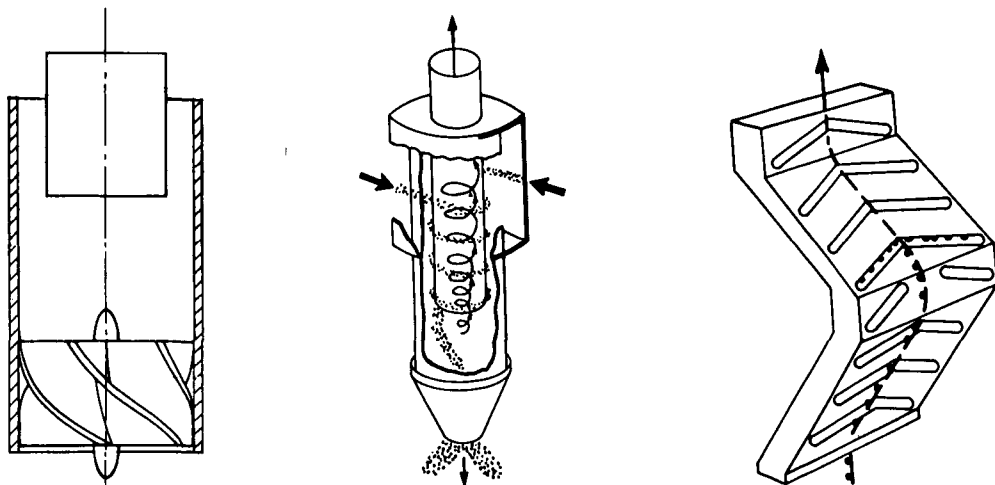
It also appeared that in many cases the behaviour of the separator could not be reliably predicted under the conditions of the practical application.

For this reason efforts were concentrated on developing improved designs and generally valid design rules for improved and existing separator types.

The separator types under investigation were mainly axial, reverse flow and vane type separators.

Each of these separator types makes use of the inertia of the mist particles to effect their separation.

The principles of operation are schematically depicted below.



To develop improved designs and improved design equations, physical and mathematical models were set up that describe the phenomena inside the separator over a wide range of operating conditions.

These models are on one hand based on numerical solution schemes that describe the behaviour of a fluid in motion, and on the other hand on rules that describe the gas/liquid interactions specific to these separators.

An extensive experimental program accompanied the development of these models to ensure their validity.

With these models two new separator designs were developed, that both show considerably improved operating characteristics with respect to the traditional high pressure gas/liquid separators.

A new axial cyclone design was developed and tested of which the throughput is not longer confined by the traditional mechanism of limitation. This resulted in a drastically improved size/throughput ratio.

Also a new vane design was developed and tested, which shows the same improved size/throughput ratio.

An important conclusion that was drawn from the design equations that were derived from the models was the fact that traditionally the influence of operating pressure is nearly always misjudged. It is underestimated in case of one type of axial cyclone separator and overestimated in case of most other cyclone and vane type separators. This was also demonstrated by experimental results.

In nearly all cases this misconception has lead to separators of which the size is not optimal for application, an important requirement for offshore operations. Therefore, practical rules were given how to account for operating pressure in the design of the separator types under investigation.

SAMENVATTING EN CONCLUSIES

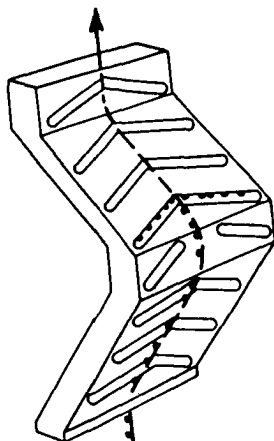
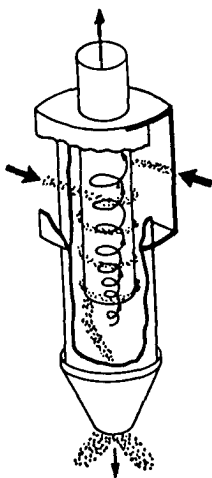
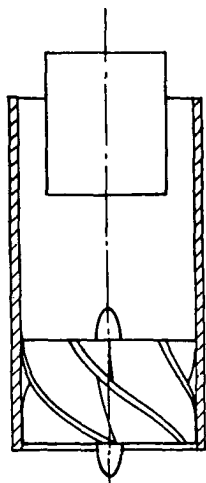
Dit proefschrift begint met een opsomming van de belangrijkste plaatsen in olie/gas produktiesystemen waar gas/vloeistofscheiding plaatsvindt.

De bedrijfsomstandigheden waaronder de diverse scheidingsoperaties plaatsvinden, worden geanalyseerd en de eisen aan de scheidingsoperaties worden geïnventariseerd. Hierna worden de beschikbare separatoren geëvalueerd zodat een overzicht kan worden gegeven van de tekortkomingen die de huidige stand der techniek met zich meebrengt.

Het blijkt dat de meeste in gebruik zijnde separator typen niet specifiek voor hogedruk gas/vloeistof scheiding ontworpen zijn, doch eerder voor hoge druk stofscheiding of atmosferische gas/vloeistof scheiding. Tevens blijkt dat in veel gevallen het gedrag van de separator onder bedrijfsomstandigheden niet nauwkeurig voorspeld kan worden.

Daarom richt het verdere onderzoek zich voornamelijk op de ontwikkeling van nieuwe separator ontwerpen en algemeen geldende ontwerpregels voor de nieuwe en traditionele separator typen.

De drie separator typen die onderzocht worden, zijn de axiaal cycloon, de reverse flow cycloon en de vaneplaat afscheider. Het werkingsprincipe van elk van de drie berust op traagheidsafscheiding en is onderstaand schematisch afgebeeld.



Om verbeterde separator ontwerpen en ontwerpregels te ontwikkelen worden fysische en mathematische modellen geformuleerd die de verschijnselen in een separator beschrijven voor een ruim bereik van bedrijfsomstandigheden. Enerzijds bestaan deze modellen uit mathematische oplosmethoden die gasstromingsvelden voorspellen, anderzijds uit toegespitste fysische modellen die de gas/vloeistof interacties in een scheider beschrijven. De modelontwikkeling gaat gepaard met een experimenteel programma om de betrouwbaarheid van de modelvoorspellingen te allen tijde te kunnen verifiëren.

Vanuit deze modellen worden twee nieuwe separator typen ontwikkeld die aanzienlijk verbeterde karakteristieken vertonen in vergelijking met traditionele hoge druk gas/vloeistofseparatoren.

Een nieuwe axiaal cycloon wordt ontwikkeld en getest waarvan de capaciteit niet langer door het traditionele mechanisme wordt begrensd. Dit resulteert in een aanzienlijk verbeterde capaciteit/grootte verhouding.

Er wordt ook een verbeterde vane ontwikkeld die dezelfde verbeterde capaciteit/grootte verhouding vertoont.

Een belangrijke conclusie die getrokken wordt uit de nieuw ontwikkelde ontwerpregels is dat de invloed van de werkingsdruk bijna altijd fout beoordeeld wordt. Deze invloed wordt onderschat in geval van één type axiaal cycloon en overschat in geval van de meeste andere soorten cyclonen en vanes. Dit wordt ook aangetoond met experimentele resultaten. In bijna alle gevallen leidt dit misverstand tot separatoren die niet de optimale grootte voor de toepassing hebben, een belangrijke vereiste voor offshore operaties. Daarom worden voor de drie onderzochte separator typen praktische regels gegeven hoe de opschaling naar hogere werkdrukken uitgevoerd dient te worden.

1. INTRODUCTION

The offshore activities in the oil- and gas-industry have grown strongly in the last fifteen years. As a consequence the demand for equipment suited for application on the spatially restricted drilling and production platforms has increased.

Somewhat comparable with the influence the space programmes of the sixties had on the electronic industry, the offshore activities have given an impulse to the development of an assortment of products and techniques which are characterized by efficiency, reliability and little maintenance.

As an example of the diversity within this assortment, one can see on the one hand the specially developed concrete construction techniques that were applied during the erection of the platforms in the Gullfaks field and on the other hand the very compact and robust rotating process equipment (especially turbines and compressors). Many research and development efforts have preceded these novelties.

This study for optimization of gas/liquid separators was also born under the signs described above.

Together with oil/water separation, gas/liquid separation is an important process operation that is essential on an offshore production platform.

The well fluids are purified of liquid and contaminations that have been produced from the reservoir.

To prevent erosion, plugging and corrosion of valuable process equipment it is of great importance that sand and water are separated in the earliest possible stage of the production.

The process equipment that is used for these operations is of considerable size and weight and has for a long time been subject to optimization attempts. One of the problems encountered in this field is the fact that the behaviour of the multiphase flow under the prevailing circumstances is complex and very difficult to predict, even in the mechanical separators under discussion in this report which are usually quite simple in their geometry.

Where quantitative descriptions of the properties of this type of process equipment are deficient, empirical designs flourish. The value of these empirics is high, as it is based on decennia of oil field experience.

However, these relations are much less suited for design optimization when they are stretched beyond their original range of application.

A complication that occurs when attempting to quantify the behaviour of these multiphase flows is that under high pressure the properties of the mixture may differ considerably from those of the same mixture under atmospheric conditions. This effect requires expensive experimental equipment to conduct experiments under actual circumstances and equally expensive computing equipment and software to carry out numerical flow simulations.

As, up to now, only relatively small companies have been involved in the design and fabrication of a large part of this particular separation equipment, much of the necessary, expensive, research in this field has been neglected. Many examples are found of incorrectly sized separators. This has induced some better financed oil related industries to tackle these problems. Presently, some large research institutes (particularly in Norway and the United States) are conducting very thoroughly structured research programmes to investigate the multiphase flow behaviour under the mentioned conditions.

The research project described here has been set up more modestly.

Shell Internationale Petroleum Maatschappij B.V., the Ministry of Economic Affairs of The Netherlands, Sombroek Zaandam B.V. and Stork Ketels B.V. were willing to finance a research project that aimed at gaining more insight into the phenomena that restrict the capacity and efficiency of gas/liquid separation in natural gas production.

It is expected that recommendations can be formulated for a more significant and uniform design procedure and, moreover, that completely new separator designs, specifically suited for application offshore can be suggested.

The sponsors of the project have the commercial rights of new designs.

In figure 1.1 the logical structure of this report is presented. It comprises the results and conclusions reached in the first four years of this study. A continuation of the project for three years has been started.

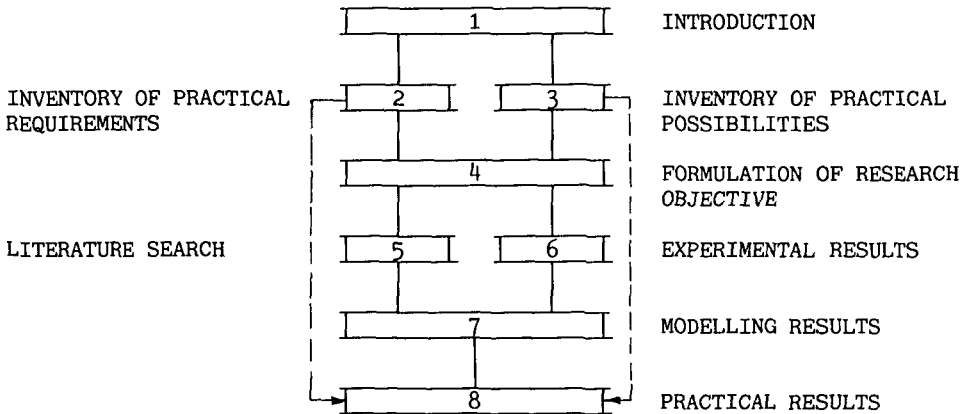


Figure 1.1 Structure of this report

In chapter 2 attention will be paid to the different conditions practical separators have to operate under. This will help to specify the tasks of a separator.

Chapter 3 will give an overview of present technology with its possibilities and limitations. The discrepancy between the requirements of chapter 2 and the possibilities of chapter 3 will form the basis of chapter 4, in which the objectives and strategy of the present research project will be formulated and elaborated.

Chapters 5, 6 and 7 will mainly deal with the different types of investigation that have been carried out in order to gather the information necessary to reach the formulated objectives. Chapter 5 will give the results of a literature search, chapter 6 the results of experimental investigations and chapter 7 the results of modelling efforts.

In chapter 8 this information will be translated to practical terms. Design procedures that are better suited for application under the prevailing conditions will be proposed. Three novel separator internals will be introduced, of which two will be tested. They will combine the advantages of several existing separator designs.

2. CLASSIFICATION OF PRESENT GAS/LIQUID SEPARATION APPLICATIONS

2.1 Introduction

This chapter gives an overview of frequently encountered applications of gas/liquid separators. The overview comprises separators in offshore and onshore production systems. Onshore separator locations are included because off- and onshore production systems are integrated. This way it will be possible to highlight some specific differences between both types of separators. A basic general production flowsheet is described in section 2.2, so that in section 2.3 the typical gas/liquid separation operations that take place in the different variations of this basic flowsheet can be catalogued according to operating conditions and required properties.

2.2 Basic description of a gas production system

As already mentioned, produced gas contains liquid and solid constituents. The removal of these forms the most important process step before delivery can take place. The liquids almost invariably consist of water and hydrocarbons that are gaseous under reservoir conditions but condense during production due to the decrease in gas pressure and temperature. However, oil may be coproduced from the reservoir.

Solid particles have to be removed because of erosion problems. The removal of water is necessary because:

- a. in presence of CO_2 and H_2S (two other possible constituents of natural gas) water forms a highly corrosive mixture;
- b. under certain conditions water together with hydrocarbon components can form "hydrates", flaky solids, which could cause plugging.

The extent to which the natural gas should be free of water is usually expressed in terms of the water dew point of the gas. This is the temperature at which water starts to condense from the gas.

For obvious reasons hydrocarbon condensates are not allowed in sales gas.

They form, however, less hazards during preliminary production and processing than water, so that in many production systems natural gas and its hydrocarbon condensates are allowed to coexist much longer. For sales gas the specifications of liquid hydrocarbon contents are also often expressed in terms of dew points. The specified dew points usually relate to the minimum occurring temperature of the sales gas (approximately between -3°C and -8°C).

Normally the removal of the liquids from produced gas is carried out in two steps.

The first step, the so-called wellhead separation, takes place under high pressure. With this operation the solids should be removed from the gas to prevent erosion of the equipment further downstream. Together with the solids the bulk of the already condensed liquids will be removed from the gas. Behind this separator often some flow or pressure control valve will regulate the gas flow to its desired value.

This results in a decrease in pressure and temperature, which will in most cases cause condensation of more liquids, both water and hydrocarbons (the latter because of retrograde condensation). This explains why the liquid separation efficiency of the wellhead separator is not considered critical. In this stage the gas is often cooled to effect the condensation of even more liquids, after which the second separation step will take place. With this step the gas will be brought to the specifications required for delivery to the sales gas network. This applies to both the water (of which the removal is called "dehydration") and the liquid hydrocarbon content (which will be referred to as "condensates scrubbing").

This second separation step usually consists of several interdependent individual separation and treating steps. It is in some cases difficult to compare with the straight forward wellhead separation, for instance because of the addition of chemicals, like glycol, to the gas flow to assist in the process.

There are several basic dehydration/scrubbing processes. The most popular are described in section 2.3.3.

When describing the "basic" gas production system in relation to possible applications of gas/liquid separators one important distinction must be made: whether gas is produced on- or offshore.

Obviously, offshore operations will impose extra demands on the design procedure as to size and weight of a separator, which results in extra constraints. An other important aspect is that the form of the basic flowsheet for offshore production/processing may differ fundamentally from the simple onshore flowsheet. Because the water content can be very harmful to the gas pipe line it should be removed as soon as possible. This means that the dehydration of the gas on a production platform has to be sufficient to prevent water condensation during pipeline transportation to onshore facilities.

As extra undersea pipelines are very expensive, the liquid hydrocarbons condensed sofar will be transported with the gas in one pipeline to be separated again onshore. This implies that the second separation step, which separates simultaneously the water and the condensates, must be split up into an offshore and an onshore part.

A schematic explanation of the above is given in figures 2.1A and 2.1B.

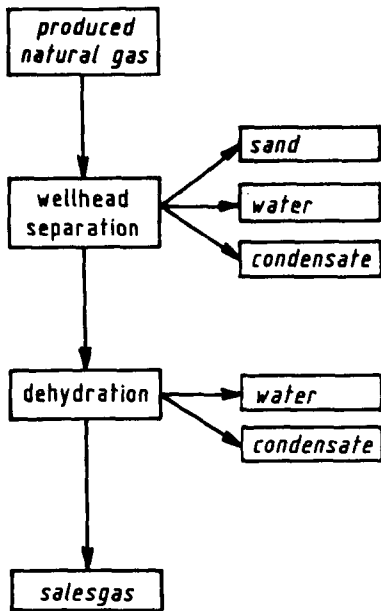


Fig. 2.1A Simplified onshore production flowsheet

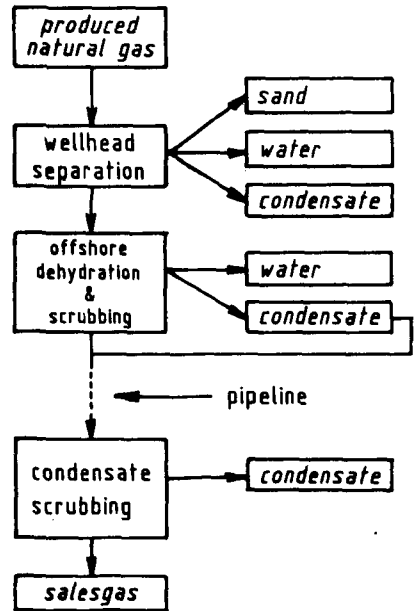


Fig. 2.1B Simplified offshore production flowsheet

2.3 Inventory of separator locations

2.3.1 Introductory remarks

As described in the previous section, two different criteria characterize the location of a separator:

- whether the separation step takes place up- or downstream in the process flowsheet (wellhead separation or scrubbing/dehydration);
- whether the gas is produced on- or offshore.

The characterization of each location takes place by defining the inlet conditions and the requirements of the separation operation.

The inlet conditions are determined according to the following properties:

1. Physical properties of gas phase; especially gas density that is mainly determined by operating pressure and gas composition.
2. Physical properties of liquid phase; especially surface tension, viscosity and density.
3. Drop size distribution of liquid phase;
4. Gas to liquid ratio;
5. Occurrence of possible fouling agents (sand, wax) in gas.

The requirements according to:

1. Separation efficiency (with respect to mists, slugs and solids);
2. Turn down ratio;
3. Allowable pressure drop;
4. Possible size constraints.

After characterization of all the individual locations tables 2.I and 2.II in section 2.4 give a summary of all inventories.

2.3.2 Wellhead separation

The conditions under which wellhead separation must take place are often extreme. Gas pressures may range up to 600 bar and erosive solid particles may shorten the lifetime of the internals considerably. The liquid in the gas consists of water and hydrocarbons, of which the droplet size depends to

a great extent on restrictions upstream in the piping (choke, sharp bends etc.). Under certain conditions formation of slugs may occur, for instance where the production line runs across the sea bottom. The amount of liquid in the gas flow depends greatly on the composition of the gas and difference in conditions in reservoir and separator. The liquid separation efficiency is not of critical importance when directly downstream of the wellhead separator equipment is situated that causes condensation of more liquids, either deliberately (heat exchangers) or not (choke valves). An extra separator section is usually installed after the wellhead separator to prevent liquid overloading of the next process operations.

The most important operating conditions are:

- The form of the liquid loading may vary from mist to slug;
- Both solid (sand) and liquid (water and hydrocarbon) particles may have to be separated;
- Pressures may range up to 600 bar, depending on the gasfield; temperatures up to 80-100°C;

and the most important separator requirements:

- Ability to separate particulates from high density gasses;
- Well able to separate slugs;
- Good separation of solid material.

2.3.3 Scrubbing

For good order it is repeated that the word "scrubbing" will be used as the general term for thorough separation of liquids from the gas flow.

"Dehydration" refers specifically to the removal of water from the gas.

From the following it will be clear that some dehydration processes can not resort under gas/liquid separation as they rather achieve a gas/gas separation. They are described in this chapter because these dehydration processes are nearly always accompanied by one or more gas/liquid separation steps, necessary for successful operation.

The two basic forms of scrubbing/dehydration are:

1. Cooling the gas beneath the specified dew point and separating the condensed liquids from the gas (gas/liquid separation);
2. Drying the gas with desiccants.

ad 1. Scrubbing/dehydration by gascooling

This dehydration method is better known as Low Temperature Separation (LTS). The gas is cooled down to such a temperature that after separation of the condensed liquids the gas will remain dry even at lower pressures above the specified dew point. The advantage of this method is that in one separation step both water and hydrocarbon condensates are recovered.

There are two common ways of lowering the gas temperature:

- 1) By using the cooling that occurs when the gas is expanded adiabatically;
- 2) By refrigerating the gas mechanically, a method which is used when the well pressure is already too low for the above cooling method. This method has become popular in onshore operations in The Netherlands.

In both cases large heat exchangers are necessary to make efficient use of the refrigeration. In the second case large quantities of energy are consumed by the mechanical refrigeration. Depending on the thermodynamics of a given gas, separation temperatures down to approximately -25°C may be necessary to fulfil the requirements for sales gas. These low temperatures are necessary, as the separation takes place at considerably higher pressures than at which the gas will be transported in the distribution network (see for instance figure 2.2).

When too low temperatures are reached before the separation step hydrate formation can occur in the gas. Therefore, an (hydrate-)inhibitor (in most cases diethyleneglycol, DEG) is injected at, or upstream of, the heat exchanger. A possible configuration is shown in figure 2.3.

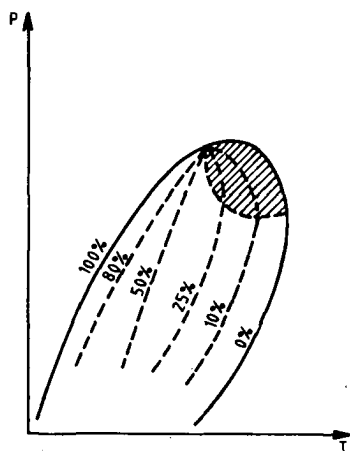


Fig. 2.2 Example of a phase loop

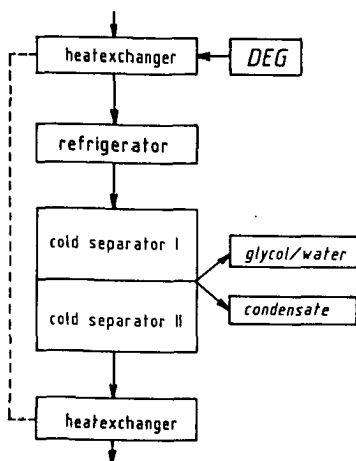


Fig. 2.3 Simplified set-up of LTS process

In most cases a second, tandem (filter) separator is situated directly downstream of the "cold" separator as a measure against possible malfunctioning of the latter. The separation efficiency of this filter separator must be as high as possible, because the gas is supplied to the sales gas network directly after this separation step.

Summary of the operating conditions and required properties:

Main separator

Operating conditions: 1. Form of liquid loading: ranging from mist to slug, depending on upstream flowsheet and piping;
2. Liquid loading: consisting of glycol/water and hydrocarbons;
3. Pressures: ranging from approximately 70-90 bar; temperatures: down to approximately -25°C.

Required properties: 1. High/Very high efficiency on mists;
2. Very high efficiency on slugs;
3. Low pressure drop.

Tandem separator

Operating conditions: 1. As the liquid offered to this separator is carried over from the cold separator, it will generally be low in concentration and very fine;
2. See above;
3. See above.

Required properties: 1. Very high efficiency on mists;
2. Low pressure drop.

In both cases a low pressure drop is required because the gas delivered to the sales gas network has to meet a certain minimum pressure. The inlet pressure of the separator has to be chosen as close as possible to this minimum pressure, because the condensation of hydrocarbons increases with decreasing pressure (retrograde condensation).

ad 2. Dehydration by making use of desiccants

Two types of desiccants may be applied: liquid or solid. Solid desiccants (calcium chloride, silicagel) are used when extremely low water dew points have to be reached, and/or when only small amounts of gas have to be processed. Generally, solid desiccants have lower drying capacities than

liquid desiccants. This is the reason why initial and operating costs of a dehydration system based on a liquid desiccant are lower. As the role of the gas/liquid separation step is only modest in a solid desiccant dehydration process, the following section is focussed on liquid desiccant processes. The by far most popular dehydration process (especially offshore), glycol absorption, is described next.

Dehydration by glycol absorption (liquid desiccant)

The popularity of this process is due to its compactness, robustness and easy operation. Gas is brought in contact with glycol (in most cases triethyleneglycol, TEG) in a contacting tower. The glycol absorbs only water vapour from the gas and is regenerated.

A simplified flowsheet is depicted in figure 2.4. For the size and energy consumption of the glycol regeneration section it is very important that the gas is free of condensed liquids when it enters the contacting tower. Free hydrocarbons will hinder water vapour absorption.

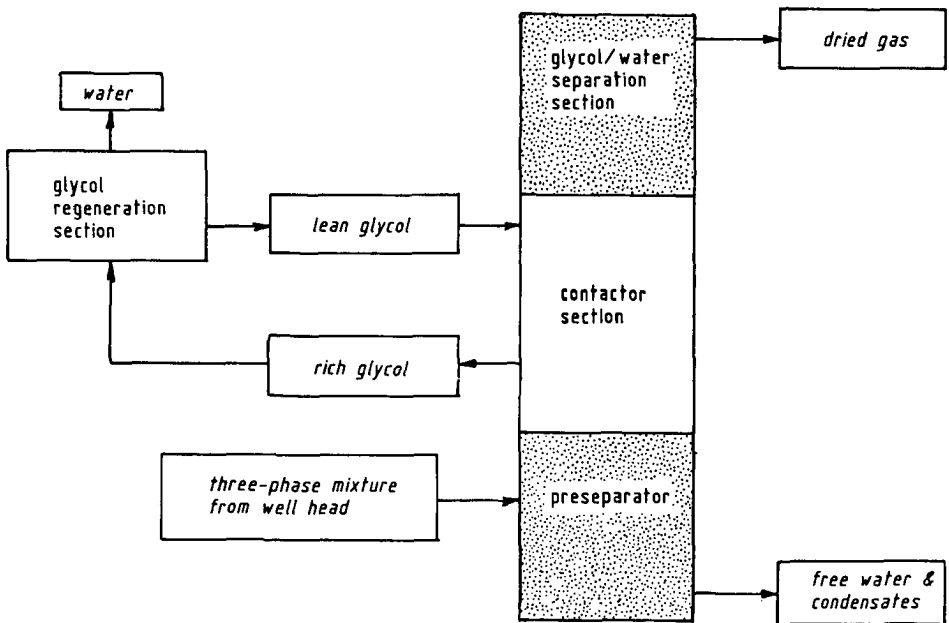


Figure 2.4 Flowsheet of glycol dehydration unit

Water and condensate will strongly increase the energy consumption of this regeneration section. An inlet separation section is situated directly upstream of the contacting tower to eliminate these liquids. The specific design of this inlet separator depends on the amount and form of the free liquids in the gas and thus on the upstream flowsheet and gas properties. Downstream of the contacting section (in the top section of the contacting tower itself or in a separate vessel) a second separation section is situated to catch entrained glycol/water solution. Glycol loss is one of the parameters that influences the economics of this process. The inlet separator will be referred to as absorption separator I, the entrainment separator as absorption separator II.

For both separators a summary of the operating conditions and the required properties is listed below.

Absorption separator I

Operating conditions:

1. Form of liquid loading: ranging from mist to slug;
2. Liquid loading: consisting of water, hydrocarbons and glycol or methanol as hydrate inhibitors (depending on process, see next section) may be present;
3. Pressures: ranging from 70-100 bar; temperatures: approximately from 25-40°C.

Required properties:

1. Very high efficiency on mists;
2. Very high efficiency on slugs;
3. Low pressure drop (except for offshore applications, see next section).

Absorption separator II

Operating conditions:

1. As this liquid is carried-over from the contacting section, it will generally be a mist;
2. Liquid loading consists of glycol/water;
3. See above.

Required properties:

1. High efficiency on glycol mists;
2. As for pressure drop: see above.

In the previous section the operating conditions in up- or downstream positions have been described. In the next section the influence of on- or offshore operation is elaborated.

2.3.4 Offshore gas winning

The usual North-Sea gas treatment consists of wellhead separation followed by glycol dehydration. The hydrocarbon condensates separated so far are brought back in the gas flow and separated again onshore. There, the first separation is carried out by massive slug catchers to accommodate the accumulated slugs, often followed by a second coarse separation step before the gas is brought to specifications by, in many cases, LTS. Two common alternatives exist: glycol dehydration takes place on the platform on which the wellhead separator is situated (situation I, table 2.II), or dehydration takes place on a central processing platform to which more production units are connected (situation II). In the latter case hydrate formation is possible, as sea water temperatures range down to 3°C. Therefore, to prevent hydrate formation methanol might be injected in the gas flow seasonally, or DEG permanently. In this way free liquids in the pipeline may build up to slugs. In case of a combined production/processing platform (situation II), the inlet conditions of the dehydration section will be much more favourable, because no glycol will be present as hydrate inhibitor and probably no slugs will have built up upstream.

For the wellhead separator only constraints with respect to size and weight are added to the requirements for an onshore separator. This could influence requirements concerning turndown ratio as well: when the reservoir pressure declines, volumetric gas flow increases and causes the need for a larger capacity. This problem is usually solved much easier onshore by placing a second separator in parallel.

The inlet conditions of the two alternative situations described above are summarized in table 2.I.

2.3.5 Onshore gas winning

Onshore the situation is much like figure 2.1A, in which in one single scrubbing step both the water- and the hydrocarbon dew point are brought to specification (situation III). It is possible to inject a hydrate inhibitor between wellhead- and dehydration-section when low temperatures are expected. When longer stretches of pipeline run between these sections slug formation may occur.

2.4 Evaluation of separator inlet conditions and requirements

In this section the information presented in 2.2 and 2.3 is summarized.

| Separator location Inlet conditions | Well head separator | Pre-separator TEG | | Post-separator TEG | | LTS (onshore) (or separator of similar function) | |
|--|---------------------|-------------------|----------|--------------------|----------|---|---------|
| | | onshore | offshore | onshore | offshore | | |
| | | | sit. I | | sit. II | | |
| Operating pressure (bar) | 100 - 600 | ~ 70 | ~ 100 | ~ 70 | ~ 100 | ~ 70 | |
| Liquid sorts | hc,w | hc,w,g | hc,w | hc,w,g | w,g | w,g | hc,w,g |
| Liquid to gas kg/10 ⁶ Nm ³ | 1000 - 6000 | 500 - 1000 | | 100-500 | 100-500 | 100-1000 | |
| DSD | m,sl | m,sl(?) | m | m,sl(?) | m | m | m,sl(?) |
| Fouling agents present | poss. | poss. | poss. | poss. | - | - | - |

g = glycol hc = hydrocarbon m = mist sl = slug w = water

Table 2.I Inventory of the inlet conditions of the separator locations

| Separator location Inlet conditions | Well head separator | | Pre-separator TEG | | | Post-separator TEG | | LTS (onshore) (or separator of similar function) |
|--|---------------------|----------|-------------------|------------------------------|----|--------------------|----------|---|
| | onshore | offshore | onshore | offshore sit. I sit. II | | onshore | offshore | |
| High sep. eff. on: | | | | | | | | |
| mist | d | | c * | c | c | c ** | c* | c** |
| slug | c | | c | c | c | NA | NA | c |
| sand/wax | c | | c | c | c | NA | NA | c |
| High turndown ratio | d | c | d | c | c | d | c | d |
| Low allowable press.drop | nc | nc | nc/d | nc | nc | nc/d | nc | c |
| Small size | d | c | d | c | c | d | c | d |

nc = not critical NA = not applicable d = desirable c = critical * d₅₀ ~ 10μ
** d₅₀ ~ 1μ

Table 2.II Inventory of the corresponding requirements

With the information presented in this chapter it will be possible to roughly characterize the inlet conditions of a certain type of separator and the requirements it should fulfil. Not all possible flowsheet configurations with respect to gas/liquid separators have been described, but the majority of applications is covered.

It appears that in practice it is very difficult to quantify the form of the liquid phase in the pipelines more precisely. Often the size and arrival frequency of slugs are difficult to predict. Moreover, the exact droplet size distribution of a mist is an unknown factor. As most separator performances depend to a large extent on the form of the liquid phase, this lack of knowledge can introduce a considerable uncertainty in the design procedures of separators.

3. PRESENT TECHNOLOGY

3.1 Introduction

This chapter gives an overview of present industrial separation techniques. Attention is paid to principles of operation, operating characteristics and presently available design procedures. As there are many different separation devices (which can, alone or in combination, form a practical separator) most of the literature searches that form the basis of this chapter are described in separate appendices to keep this overview readable.

The general structure of chapter 3 is given in figure 3.1. This figure also gives an overview of the different separation devices that will be discussed.

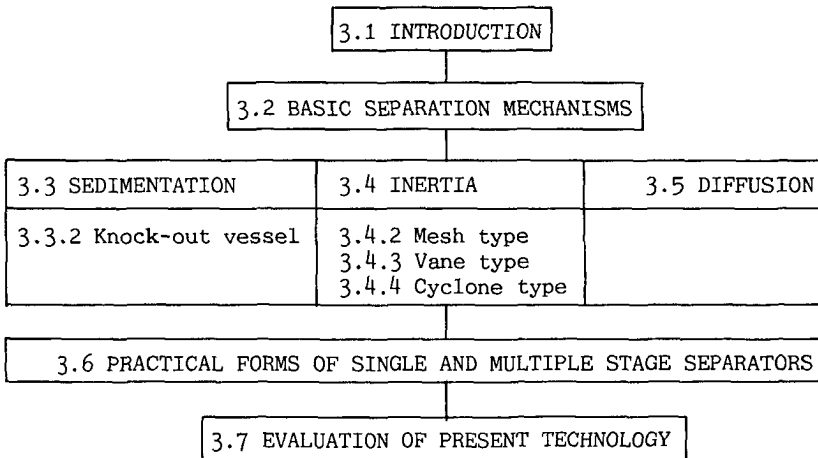


Figure 3.1 General structure of chapter 3

The three basic physical separation methods are described briefly in section 3.2. The practical applications of each separation method are characterized extensively in sections 3.3-3.5. Figure 3.2 gives the form of the characterization of each separation device mentioned in figure 3.1.

| PRINCIPLE OF OPERATION | |
|---|---|
| Literature search THEORETICAL BACKGROUND (appendix) | Literature search DESIGN PROCEDURES (appendix) |
| 1. Separation efficiency 2. Maximum capacity 3. Pressure drop | 1. Separation efficiency 2. Maximum capacity 3. Pressure drop |

| CHARACTERISTICS OF SEPARATION DEVICE | |
|---|---|
| OPERATING CHARACTERISTICS | AVAILABLE DESIGN PROCEDURES AND EXPECTED RELIABILITY |
| a. Separation efficiency b. Throughput per unit volume (size) c. Pressure drop d. Ability to separate non-liquid constituents e. Turndown ratio f. Capital and operational costs g. Other | Influence of 1. Operating pressure 2. Liquid loading 3. Physical properties of liquid on a. Separation efficiency b. Maximum capacity c. Turn down ratio d. Pressure drop |

Figure 3.2 Form of the characterization of the separation devices described in 3.3, 3.4 and 3.5

First, the general operating principles and possible practical variations of the design are described. Subsequently, the operating and design characteristics are summarized according to the enumeration given in figure 3.2. The two literature searches on which the above characterizations are based are given in appendix A under corresponding section numbers. One literature study is made of the theoretical background of the principle of operation of each separation device, the other of the available corresponding practical design procedures. The expected reliability of these design procedures is indicated in the tables that summarize this information further in this chapter. The validity of most of the design procedures is established in section 7.4.

After characterization of all listed separation devices, section 3.6 will describe the most important practical separators which are composed or consist of the earlier described elements. Finally, section 3.7 will give a summary of the characteristics of the nowadays most popular separator designs.

This section will be concluded with the definitions of some of the operating characteristics that will be used to judge the capabilities of separator devices on:

Separation efficiency

The definition of efficiency of a gas/liquid separator is simple and unambiguous. If a gas/liquid mixture (characterized by ϕ_g , ϕ_{v1} , droplet size distribution (dsd) and physical properties) is separated, the separation efficiency is defined as $\eta_s = \phi_{v2}/\phi_{v1}$, in which ϕ_{v2} is the flow of separated liquid (figure 3.3). η_s depends on ϕ_g , ϕ_{v1} , dsd, physical properties of original mixture and separator geometry. A good physical model of the behaviour of the separator (or design procedure) should quantify the influence of each variable on η_s . Design equations, however, usually apply only under certain circumstances and are specific for a certain geometry.

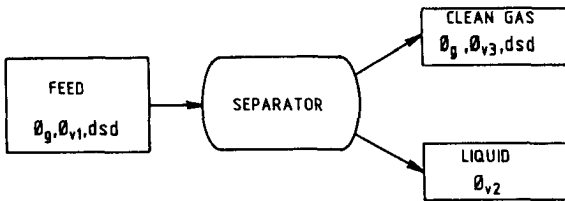


Figure 3.3 Nomenclature of separator operation

Through-put per unit volume (size)

Some separator geometries can handle larger gas flows at a certain size than others. Especially for offshore applications this plays an important role.

Turndown ratio

The turndown ratio, defined as the ratio between minimum and maximum gas flow at a certain minimum separation efficiency, is important when variations in gas flow are expected.

Pressure drop

The pressure drop depends on the same variables as separation efficiency. In cases in which the pressure drop across the separator is critical, it is necessary to be able to predict it. In most cases empirical correlations exist that are specific for a certain geometry.

Ability to separate non-liquid constituents

In chapter 2 it appeared that sometimes non-liquid particles (sand, wax) are offered to separators. Some separators possess a geometry that is not suited for the collection or drainage of these constituents. Apart from direct consequences with respect to the separation efficiency of these components, exposing the separator to these substances can lead to plugging of internal parts. This leads to deterioration of the separation characteristics with respect to liquids as well.

Capital and operational costs

This characteristic evidently has a strong influence on the determination which solution will be chosen for a certain application. However, the financial context of this technology strongly depends on factors which lie outside the scope of this report. Therefore, in the next sections only general recommendations are given if a choice has to be made between technically equivalent alternatives.

3.2 Basic gas/liquid separation mechanisms

In general, a droplet is considered to be separated from the carrier gas when it comes in touch with obstacles in the gas flow or when it reaches one of the walls (or other limitations) of the space in which the mixture flows. The captured droplet coalesces in a liquid film on either obstacle or wall, and is then drained. The different separation mechanisms that will be described hereafter aim at creating a relative velocity of the droplets in respect to the gas. This way droplets are concentrated at specific locations of the separator, where they are captured and drained as described before.

The different separation mechanisms are based on:

- a. sedimentation (gravity settling);
- b. inertial forces;
- c. diffusion;
- d. electrostatic forces;
- e. ultrasonic agglomeration.

Although all five mentioned principles have been applied successfully and although ultrasonic agglomeration could offer some very distinct advantages in designing very compact separators, only the first three are of importance in the present gas/liquid separation technology of the oil and gas industry. For this reason only these mechanisms will be paid attention to in the rest of this report. Before the different practical applications of these three separation mechanisms will be described, some general theoretical background of each is given below.

ad a. Sedimentation (gravity settling)

When lowering the velocity of a gas/liquid mixture sufficiently, droplets can experience considerable influence of gravity and will settle down. If it is assumed that the gravity force is only opposed by the drag force and that for $Re < 1$ Stokes' Law will apply, the relative settling velocity can be quantified according to equation 3.1.

$$v_p = \frac{(\rho_l - \rho_g) g d^2}{18 \mu} \quad (3.1)$$

ad b. Inertial forces

The velocity vector of a droplet in a non-rectilinearly moving gas flow will generally not be identical to the velocity vector of the gas flow at that location (at least when $\rho_g \neq \rho_l$). The stronger the variations in velocity and direction of the gas and the larger the mass of the droplet, the larger the relative movement of the droplet in respect to the gas flow (see fig. 3.4). When only drag forces are taken into account the following derivations will illustrate the qualitative statements above.

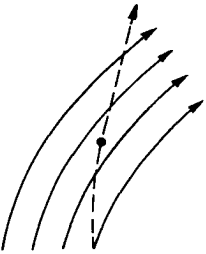


Figure 3.4
Inertia of particle

The drag force on the particle:

$$\vec{F}_D(t) = \frac{1}{4} \pi d_D^2 C_D \cdot \frac{1}{2} \rho_g (\vec{v}_g(t) - \vec{v}_p(t))^2 \quad (3.2)$$

The acceleration of the particle under influence of this drag force:

$$\frac{dv_p}{dt} = \frac{3}{4} \cdot \frac{\rho_g}{d_D(\rho_l - \rho_g)} \cdot C_D \cdot (\vec{v}_g(t) - \vec{v}_p(t))^2 \quad (3.3)$$

When $\vec{v}_g(t)$ is known the trajectory of a particle can be determined. It can then be predicted under which circumstances a droplet will be captured.

ad c. Diffusion

Under influence of the impacts of the surrounding gas molecules, very small particles ($d_p < 1 \mu m$) will show random movement variations (better known as Brownian movement). The relative trajectory that the droplets travel under influence of this effect is usually very small. It is quantified as follows:

$$X_m = \sqrt{\frac{4 RT K_m t}{3 \pi^2 \mu N D_p}} \quad \text{Einstein and Smoluchowski} \quad (3.4)$$

in which K_m = Stokes Cunningham Correction path; varies between 1 (particles of $10 \mu m$) to 3-5, depending on temperature (particles of $0.1 \mu m$)

N = Avogadro's number

R = gas constant

X_m = length of path

t = time

These three separation mechanisms serve distinctly different purposes.

Sedimentation is mainly applied in situations in which it is necessary to (pre-)separate large volumes of coarse liquid elements. This method is hardly useful for mist separation. Inertial separation on the other hand is mainly applied in situations in which fairly low volumes of mist have to be separated and is not suited to handle high liquid loadings. Diffusional separation is applied when it is necessary to collect even the finest droplets to achieve a very high separation efficiency. Only very low liquid loadings can be offered to a separator based on this principle.

The following sections describe practical applications of these three separation principles. Each description is structured according to figure 3.2. One should bear in mind that for many separations in practice requirements have to be fulfilled that can not be offered by only one of these three mechanisms. Therefore, the designs described in the following sections should rather be regarded as modules which can form a complete separator, sometimes alone but most often with other modules.

3.3 Sedimentation

3.3.1 General aspects

Sedimentation (gravity settling) is the simplest and oldest form of gas/liquid separation. It is mainly used as a means to separate coarse liquid elements (slugs and large droplets) from the gas flow.

In section 3.3.2 attention will be paid to the following two applications:

1. When mist particles in the gas are not considered detrimental to further gas handling processes (for instance in feed lines to flare-stacks) a separator might be based only on gravity separation.
2. Gravity settling is also often used for preseparating the bulk of the liquid in a gas, so that hereafter the gas flow is suited for mist separation. This concept leads to compound separators in which the first stage relies on gravity separation.

3.3.2 Knock-out vessels

1. Principle of operation

Two basic separator types exist that make use of gravity settling:

- Simple separators for coarse separation purposes;
- Compound separators, in which the gas must be prepared for the mist extraction stage.

As the most important geometrical variables have to be determined in an analogous way for both types, no further differentiation will be made in this section. In later sections attention will be paid to separators that accommodate more stages.

Usually a separator making use of this principle, called "knock-out vessel", is a large empty horizontal or vertical vessel (figures 3.5 and 3.6) in which upon entrance a large reduction in gas velocity will take place.

In a vertical vessel the droplets, that have a terminal settling velocity larger than the upward gas velocity, will be separated.

In a horizontal vessel the droplets that reach the gas/liquid interface inside the vessel in the time the gas passes through the vessel will be separated.

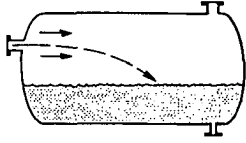


Figure 3.5 Horizontal separator

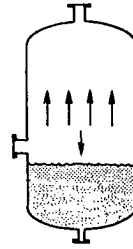


Figure 3.6 Vertical separator

In both cases the separated liquid is collected in the lower part of the vessel. The liquid drainage velocity is chosen so that entrained gas bubbles are permitted to escape to the surface. In the design of a knock-out vessel it is very important that the two-phase flow is evenly distributed across the cross section of the separator. For this purpose a large variety of mostly proprietary inlet device designs exists (fig. 3.7).

A second purpose of the inlet devices is to separate liquids by inertial effects that are created by the turnings imposed on the gas flow. One issue not to be overlooked in this respect is the fact that sharp turnings of the gas flow, especially those caused by baffle plates or inversed cones and as such meant to invoke large inertial forces, may adversely affect the functioning of the separator. Droplets may be shattered and redispersed in the gas flow at droplet sizes possibly smaller than those offered to the separator.

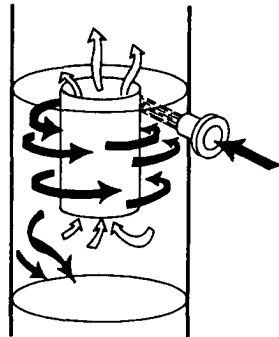
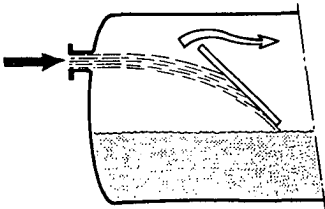


Figure 3.7A Inlet devices 1 and 2

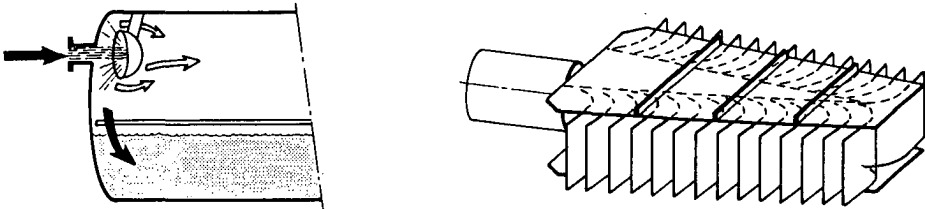


Figure 3.7B Inlet devices 3 and 4

2. Characteristics of knock-out vessels (see appendix A 3.3.2)

2.A Operating characteristics

- separation efficiency : low for mists; $d_{s,0} \sim 150 \mu\text{m}$ for water/air under atmospheric conditions
- flow per unit volume : low; for vertical separators the load factor λ amounts to 0.07; for horizontal separators to 0.15

$$(\lambda = v_{g\text{max}} \cdot \sqrt{\frac{\rho_g}{\rho_l - \rho_g}})$$
- turn down ratio : no theoretical lower limit to gas velocity
- pressure drop : low; determined mainly by size and shape of in- and outlet nozzles
- ability to separate non-liquid constituents : reasonable
- installation and operational costs : as required surface area increases strongly with increasing pressure ($v_{g\text{max}} \sim \rho_g^{-1/2}$), costs will show same tendency (for a given constant volume rate)

2.B Availability and reliability of design procedures

In table 3.I the availability and expected reliability of different design correlations are summarized.

For these separator types or -modules the determination of the turn down ratio and pressure drop is either trivial or not of interest.

| | as a function of geometry | as a function of oper. press | as a function of liq. loading | as a function of liq. property |
|---|------------------------------|---------------------------------|----------------------------------|-----------------------------------|
| separation eff. availability exp. reliability | + +/- | + +/- | - - | only density +/- |
| max. capacity availability exp. reliability | + + | + + | - - | only density - |

Table 3.I

3.4 Inertial separation

3.4.1 Introductory remarks

To clean the gas stream from smaller particles than can be achieved economically by gravity separation, the mist is subjected to inertial forces. At present three practical separator types used for mist collection are based on this separation mechanism. They are described in the next three sections. The structure depicted in figure 3.2 and described in section 3.1 will be used.

3.4.2 Inertial separation by mesh type separators

1. Principle of operation

The most common way to induce variations in the gas flow direction is to place wire mesh in the gas flow. The wire mesh consists of multiple layers of blankets consisting of asymmetrical interlocking loops of wire. As the gas containing entrained droplets passes through a wire mesh, the gas easily finds its way round the wires, while the droplets, which are heavier, can not take the turns and impinge on the wires (fig. 3.8).

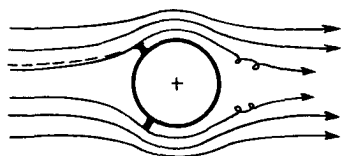


Figure 3.8 Principle of wire mesh separation

The separated droplets form films around the wires that run down through the mesh pad. At the underside of the pad the films break up into large droplets that fall back against the gas flow. The most common metal mesh type used is approximately 0.3 mm in diameter, the average porosity is approximately 97% while the total height of the pad usually has a value of 100 mm.

The two most popular possibilities of application of a mesh pad are depicted in figures 3.9 and 3.10.

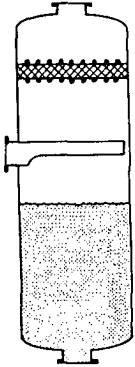


Figure 3.9 Vertical mesh pad

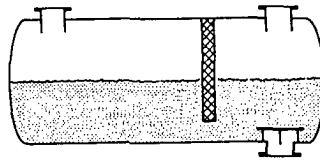


Figure 3.10 Horizontal mesh pad

The following descriptions and conclusions will all relate to the vertically flowed through meshpad (figure 3.9). They are also indicative for the horizontally flowed through version.

2. Characteristics of meshtype separators

2.A Operating characteristics

- separation efficiency : high; $d_{50} \sim 5 \mu\text{m}$
- flow per unit volume : low; if $v_{\text{gmax}} = \lambda \sqrt{\frac{\rho_l - \rho_g}{\rho_g}}$ then
 $\lambda \approx 0,11$ for most applications
- turn down ratio : 1/3 (1 bar, droplet sizes $> 10 \mu\text{m}$)
- pressure drop : low, $\Delta P \sim 5 \text{ mbar}$ (water/air, 1 bar)
- ability to separate non-liquid constituents : very poor
- installation and operational costs : relatively high because of large required plan area

2.B Availability and reliability of design procedures

In table 3.II the availability and expected reliability of different design correlations are summarized.

| | as a function of geometry | as a function of oper. press | as a function of liq. loading | as a function of liq. property |
|------------------------|------------------------------|---------------------------------|----------------------------------|-----------------------------------|
| separation eff. | | | | |
| availability | + | + | - | - |
| exp. reliability | + | + | - | - |
| max. capacity | | | | |
| availability | + | + | + | + |
| exp. reliability | +/- | + | ? * | ? * |
| turndown ratio | | | | |
| availability | + | + | + | + |
| exp. reliability | + | + | ? * | ? * |
| pressure drop | | | | |
| availability | + | + | + | + |
| exp. reliability | ? | + | ? | ? |

* crucial design information

Table 3.II

3.4.3 Inertial separation with vane-type separators

1. Principle of operation

Vane-type separators generally consist of a series of narrowly spaced uniformly tortuous plates positioned in parallel to the direction of the gas flow. The gas flow has to make more or less sharp turns through the free spacings between the plates (fig. 3.11). The entrained droplets will not be able to follow these changes of direction and will impinge on the plates. The liquid film which is formed this way is drained from the separation chamber.

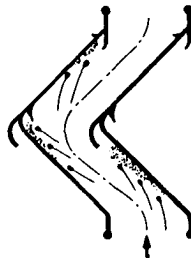


Figure 3.11 Principle of vane type separation

Designs for vertically flowed through vane-type separators

For vane-type separators that flow through vertically, designs exist in which the liquid is drained through shielded slots (fig. 3.12). Also simpler vane-type designs exist in which the liquid is drained countercurrently in direct contact with the gas flow (fig. 3.13).

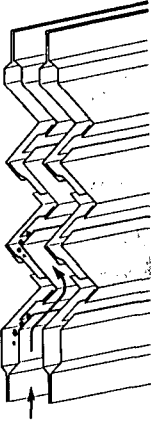


Figure 3.12 Shielded liquid drainage

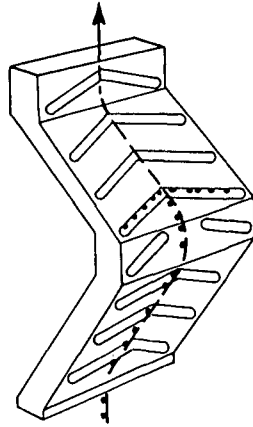


Figure 3.13 Counter-current drainage

Designs for horizontally flowed through vane-type separators

Horizontally flowed through vane-type separators (figure 3.14) nearly all feature shielded liquid drainage. There is little quantitative information on the influences of vane-blade geometry. Although not always acknowledged, the design of the flow path and the positioning of the drainage scoops or -slits is crucial for high through-put operation. Gardner [1977] mentions the occurrence of ribbons of draining liquid in front of the actual drainage slits which probably means that eddies are generated at detrimental locations, thus preventing the liquid from draining in the slits. In appendix A 3.4.3 some, to a large extent useless, attempts to quantify the influences of some design parameters are reported. The possibilities to optimize vane profiles and geometries for specific applications are fully not exploited.

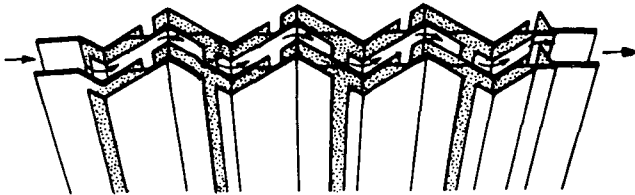
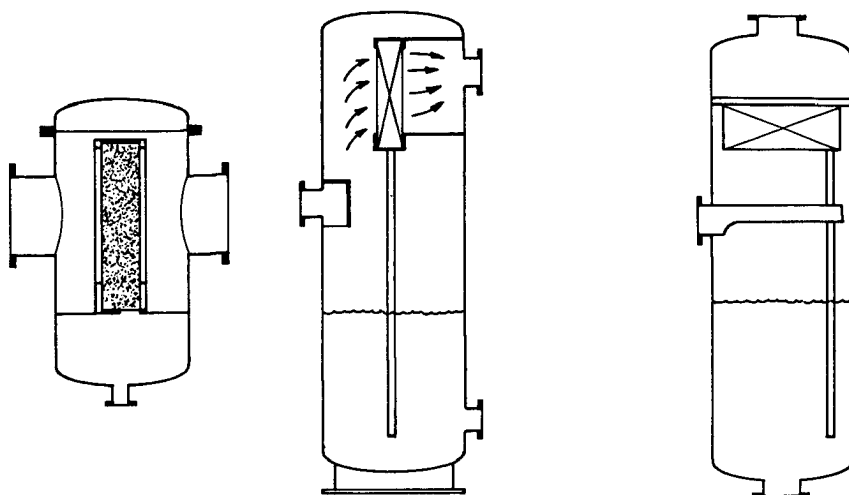


Figure 3.14 Horizontal vane design

Figures 3.15A and B show two separator designs based on horizontally flowed through vane packs and figure 3.15C one based on a vertically flowed through vane pack (with internal drainage).



Figures 3.15A and B Horizontally flowed through vane packs

Figure 3.15C Vertically flowed through vane packs

2. Characteristics of vane type separators

2.A Operating characteristics

- separation efficiency : good; $d_{s,0} = 7-20 \mu\text{m}$, depending on design
- flow per unit volume : in case of shielded liquid drainage (reentrainment-limited): high ($v_{g\text{max}} \sim 8-9 \text{ m/s}$, corresponding $\lambda \sim 0.3$ (the use of the load factor is quite inappropriate in this case; see appendix A, page A.11), water/air, 1 bar); in case of flooding limited operation: medium ($v_{g\text{max}} \sim 5-6 \text{ m/s}$, water/air, 1 bar)
- turn down ratio : approximately $1/4$, (water/air, 1 bar, $d_{s,0} > 15 \mu\text{m}$; in case of flooding limited operation approximately $1/3$ (water/air, 1 bar, $d_{s,0} > 15 \mu\text{m}$), but also depending on liquid loading

- pressure drop : low; $\Delta P \sim 5-10$ mbar (water/air 1 bar)
- ability to separate non-liquid constituents : poor, although danger of plugging is less immediate than in case of wire mesh operation
- installation and operational costs : relatively low, because of high specific capacities
- other : operation possible up to higher operating pressures than in case of mesh-pads *)

*) Vane-type separators can be used up to pressures of 75-100 bars. The maximum allowable velocity inside the vane decreases with increasing pressure (see appendix A 3.4.3). Because the minimum allowable velocity increases with increasing gas density (inertial forces become smaller), the turn-down ratio decreases considerably. At the operating pressures mentioned it is still just large enough for practical operation.

2.B Availability and reliability of design procedures

In table 3.III the availability and expected reliability of different design correlations are summarized.

| | as a function of geometry | as a function of oper. press | as a function of liq. loading | as a function of liq. property |
|------------------------|------------------------------|---------------------------------|----------------------------------|-----------------------------------|
| separation eff. | | | | |
| availability | + | + | - | - |
| exp. reliability | - - | - - * | ? | ? |
| max. capacity | | | | |
| availability | + | + | - | - |
| exp. reliability | - - | - - * | * | * |
| turndown ratio | | | | |
| availability | + | + | - | - |
| exp. reliability | - | - * | NI | NI |
| pressure drop | | | | |
| availability | +/- | + | - | - |
| exp. reliability | - | + | NI? | NI? |

* crucial design information NI not of interest

Table 3.III

3.4.4 Cyclone type separators

3.4.4.1. Preliminary remarks

In a cyclone the gas/liquid mixture performs a spiral movement inside a cylindrical body, by which the droplets are flung out and collected on the inner wall of the cyclone. This separation device has found wide-spread application. Not only in the mist, but especially in the dust separation industry it has proved to be a very valuable tool.

As most theoretical investigations have been performed on dust cyclones, a substantial part of the information given in this section will relate to these types of cyclones. However, most of the theories that are developed for these cyclones are directly applicable to mist cyclones.

Several designs make use of the separation principle described above.

Principle differences in geometries can be found in respect to the way:

1. the liquid film is extracted from the cyclone body;
2. the swirl is induced;
3. upscaling can take place.

ad 1.

- a) most often the cleaned gas flow is reversed so that it can flow back through the vortex finder which is placed concentrically within the incoming gas flow. The liquid can then be collected underneath without the danger of remixing (fig. 3.16). In the following this type of cyclone will be referred to as "reverse flow" cyclone.
- b) the second method is simpler in concept but more critical in design: the cleaned gas and separated liquid keep moving in the same direction to a point where the liquid is removed sideways through longitudinal or concentric slits in the cylinder wall while the gas is forced through a central exit tube. At this location there is danger of reentrainment (fig. 3.17). This cyclone will be referred to as "straight through".

ad 2.

Two groups of popular swirl inducing devices exist: the gas is either introduced tangentially through guide vanes or axially through a swirl element into the cylindric body.

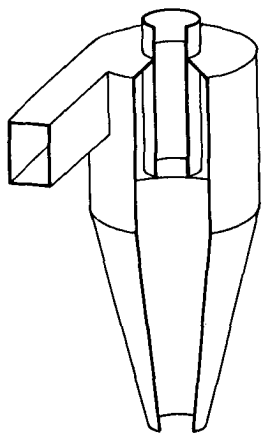


Fig. 3.16 Reverse flow
cyclone

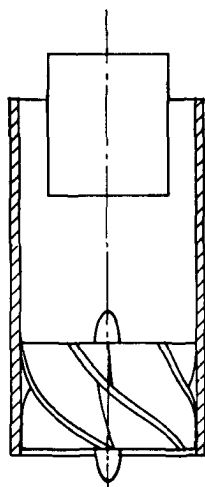


Fig. 3.17 Straight through
cyclone

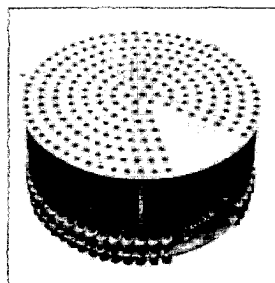


Fig. 3.18 Multi-
cyclone

ad 3.

It is clear that the smaller the radius of rotation the larger the separating effect will be. However, the radius for a single cyclone can not be chosen as small as one would like for a given gas flow. In the first place the spinning gas flow could gain so much velocity that the wall film would be reentrained. In the second place the pressure drop, which will prove to increase with the square of the gas flow through a cyclone, could become excessive. So, for a certain cyclone size a limit gas flow is set.

In order to be able to process larger gas flows at the same separation efficiency a number of small cyclones is placed in parallel (fig. 3.18). This is a very popular separation device.

The various cyclone geometries are described in the next sections. In 3.4.4.2 the reverse flow dust cyclone is treated. 3.4.4.3 deals with the specific differences with respect to reverse flow mist cyclones. In 3.4.4.4 multicyclones consisting of reverse flow cyclones are described and 3.4.4.5 is devoted to axial cyclones. In each of these sections the structure is the same as depicted in figure 3.1 except that the operating characteristics (item 2, figure 3.1) of all cyclone types are listed together in section 3.4.4.6.

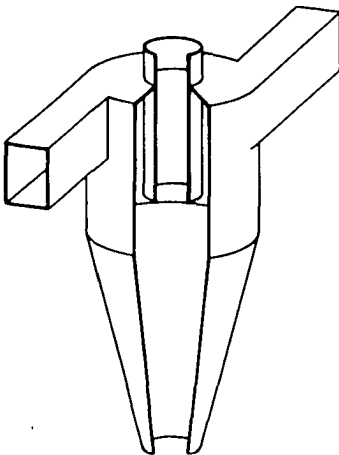
3.4.4.2 (Reverse flow) Dust cyclones

1. Introduction

In appendix A 3.4.4.2 an overview is given of theories and design procedures concerning dust separating cyclones. The prediction of collection efficiency and pressure drop of a certain cyclone can be considered similar in broad ranges for both mist and dust separation. However, the prediction of maximal capacity might very well show distinct differences, because the onset of reentrainment of the liquid film inside a mist cyclone, which determines maximal capacity, is a property quite specific for gas/liquid separation devices. More attention to these specific differences will be paid in section 3.4.4.3.

Generally a reverse flow dust cyclone consists of an inlet section, a separation chamber, a dust discharge and a gas outlet section (figure 3.16). In the corresponding section in appendix A is explained how variations of the geometry of these cyclone parts influence the operating characteristics of the cyclone. Usually the inlet to a cyclone is of the single tangential type (figure 3.16), but also designs exist that make use of a multiple tangential (figure 3.19) or an axial inlet (figure 3.20).

Most theoretical work has been performed for the former inlet type, although the latter types have some advantageous features as well. Special attention is paid to these effects at the end of subsection 2.A of appendix A 3.4.4.2.



inlet

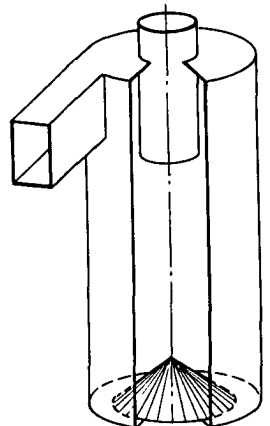
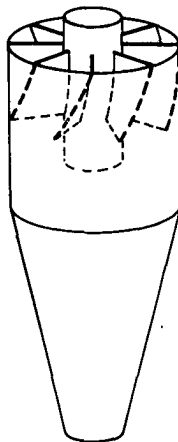


Fig. 3.19 Multiple tangential inlet Fig. 3.20 Axial inlet Fig. 3.21 Cylindric cyclone

The influence and the determination of the geometry of the separation chamber and the gas outlet section is extensively described in the appendix. Much less attention has been paid to the form of the dust discharge. Generally, in the case of dust separation, the form is long and tapered. This is to minimize the chance that the eddies, induced by a too strong change in direction of the gas flow, will reentrain dust particles from the wall. Other geometries exist but are therefore considered less effective.

3.4.4.3 Mist cyclones

1. Introduction

Although the principle of operation of mist cyclones is very similar to that of dust cyclones, there are differences that may lead to some characteristic design features. These will be discussed after description of the specific differences between the two types of separation. The factors that facilitate the separation process of gas/liquid mixtures are:

1. Droplets coagulate easier than dust particles and can, thus, be separated quicker.
2. When dust particles impinge on the inner cyclone wall they may bounce back into the main flow and consequently be reentrained. Droplets will tend to coalesce with the wall film in which their kinetic energy will be dissipated.
3. The long conical section underneath dust cyclones, necessary for the controlled discharge of the captured dust particles, has often a great influence on the efficiency of the cyclone. A liquid film, however, can be drained otherwise than through a central outlet without reentrainment or clogging hazards (figure 3.21). Experiments have confirmed that for gas/liquid mixtures cylindric cyclones performed as well as conical cyclones (Storch [1979], Ter Linden [1953a]).

The advantage of omitting the long conical section is twofold:

1. the cyclone can be built more compact.
2. the vortex is prevented to swirl out of the cyclone and into the discharge bin. This is of particular disadvantage in respect to the reentrainment of already separated droplets, for instance in multicyclones (3.4.4.4).

However, the factors that restrict the gas/liquid separation in comparison to gas/dust separation in a cyclone may also be of considerable influence:

1. The liquid film that facilitates the capturing of droplets can partly creep to areas of lower pressure. This may result in creeping of the film across the cyclone top, down the vortex finder and entering into the cleaned gas leaving the cyclone. This effect can be of considerable influence according to different sources: Pollak and Work [1942], Stairmand [1951], ter Linden [1953a]. Ter Linden found that the amount of film creep increases with increasing liquid viscosity, increasing pressure drop and decreasing diameter and that it is relatively independent of liquid content of feed stream.
2. Although the film prevents to a large extent the bouncing back of droplets, it is itself susceptible to reentrainment.

Apart from the above mentioned differences between separation of liquid and of dust there is one more general distinction:

- The presence of the film may alter the effective roughness of the cyclone wall and thus influence the pressure drop characteristics.

To prevent the second defect, reentrainment of the liquid film, the shear stresses between liquid and gas phase should not exceed a certain maximum.

In appendix A 3.4.4.3 some correlations are cited from literature, although none of these seems to extend into the high pressure area of the present field of study. Therefore, these phenomena will form an important subject in the last three chapters of this report.

With respect to the first defect it is possible to reduce the effects of film creep layer loss by a number of well chosen geometrical provisions added to or instead of the conventional dust cyclone design.

1. A concentric skirt around the exit pipe to lead the film back into the separation chamber of the cyclone where again it will be susceptible to the forces of separation (figure 3.22).
2. With the same objective, an obstructing ring around the vortex finder that extends down into the separation chamber (figure 3.23).
3. A circular slit in the vortex finder (figure 3.24) to extract the wall film in it.

With the pressure drop either available in the centre of the cyclone or generated with an additional venturi in the inlet line this liquid can be brought back into the separation chamber of the cyclone.

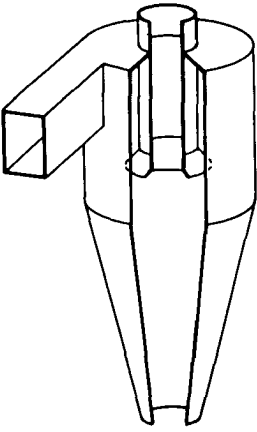


Fig. 3.22 Prevention of
creep I

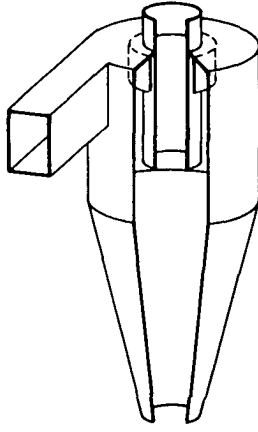


Fig. 3.23 Prevention of
creep II

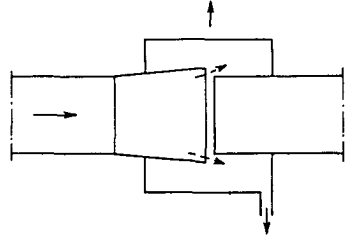


Fig. 3.24 Prevention of
creep III

4. Specially adapted design types for gas/liquid separation, of which the Webre cyclone is the most famous (figure 3.25) but of which the cyclone designed by Polyakov [1986] (figure 3.26) is also a good example.

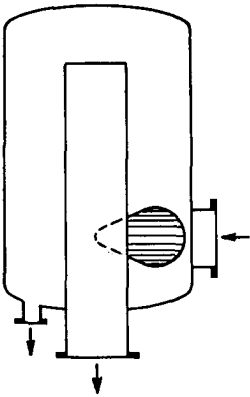


Figure 3.25 Webre cyclone

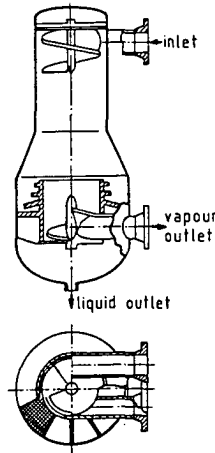
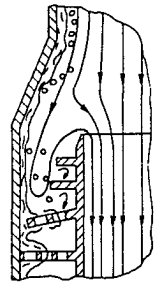


Figure 3.26 Polyakov cyclone



The merit of these types of special designs for gas/liquid separation in comparison to conventional designs is presented in figure 3.27A (Pollak and Work [1942], with respect to figure 3.25) and in figure 3.27B (Polyakov, with respect to figure 3.26). Unfortunately no such direct comparisons could be found for the other three kinds of adaptations.

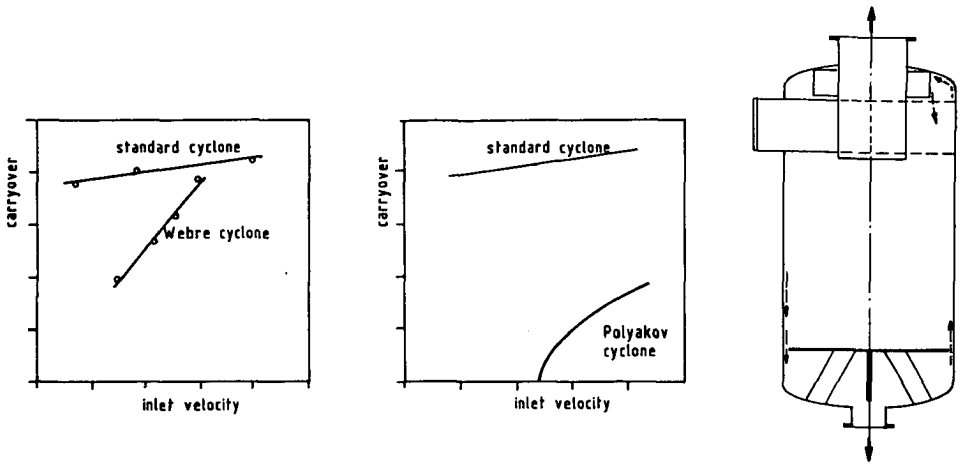


Fig. 3.27A Characteristics Webre cyclone Fig. 3.27B Characteristics Polyakov cyclone Fig. 3.28 Ter Linden cyclone

As an example of practical application of a conventional gas/liquid cyclone one could take the separator suggested by Ter Linden [1953a] (figure 3.28). In this case a solution has been chosen to process the total gas flow with one cyclone. This is a solution of simple geometry, but with a relatively high d_o , and pressure drop. The design procedure for these types of cyclone are listed in appendices A 3.4.4.2 - 3.4.4.3. It is apparent that at higher operating pressures a vane-type tangential inlet as depicted in figure 3.28 will be uneconomic and the overall length/diameter ratio will be influenced by the operating pressure (equation A.15, appendix A) as well.

These cyclones feature a splash ring around the vortex finder which extends down to the inlet height and a horizontal baffle plate to prevent interactions between vortex and separated liquid. From a practical point of view it is recommendable to replace the flat bottom plate by a slight angled cone to avoid renewed gas/liquid interaction. Storch [1979] recommends especially the straight through type cyclones for gas/liquid separation, as he found the creep loss with these cyclones minimal. Straight through cyclones will be discussed separately later.

In figures 3.29 and 3.30 the earlier described recycle type cyclones are depicted. A large scale practical application of the Webre type cyclone is presented in figure 3.31.

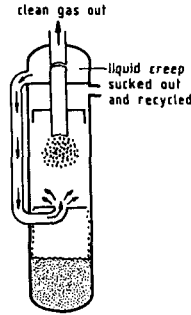
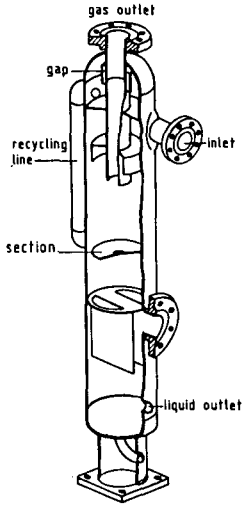
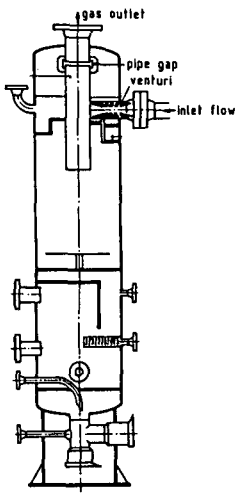


Fig. 3.29 Recycle cyclone I Fig. 3.30 Recycle cyclone II Fig. 3.31 Webre cyclone

3.4.4.4 Multi cyclones

The large disadvantage with single cyclones is the required extra pressure drop and accompanying erosion problems to maintain a certain collection efficiency when upscaling. This had led to the use of smaller cyclones placed in parallel. For not apparent reasons a two inch diameter cyclone with a double tangential inlet has been set to industrial standard. This is the most often encountered cyclonic gas/liquid separation method in the oil field industry. At least three or four different companies produce design variations on an identical theme (figure 3.32).

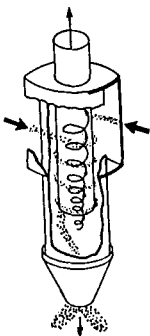


Figure 3.32 2" cyclone standard

The obvious advantage of an arrangement with very small cyclones is that with a lower pressure drop high efficiencies can be obtained. Figure 3.33 gives an example of a multi cyclone separator, mounted in a horizontal vessel. Figures 3.34 and 3.35 are examples of two possible configurations in a vertical vessel.

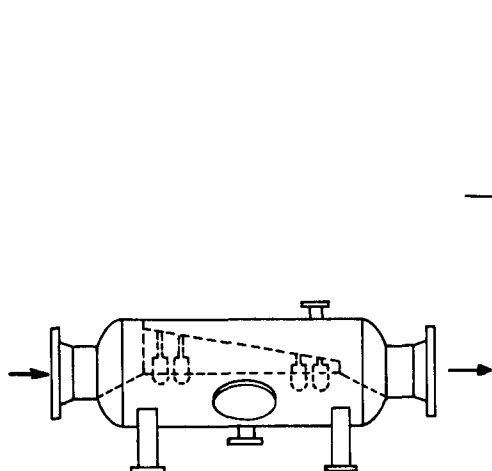


Fig. 3.33 Horizontal

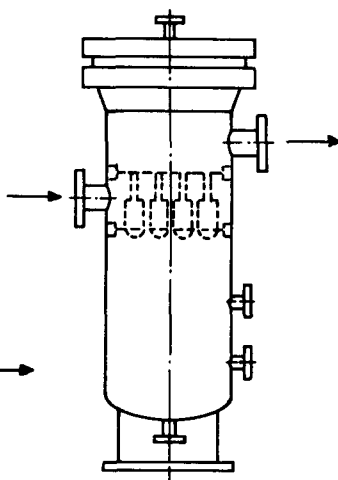


Fig. 3.34 Vertical I

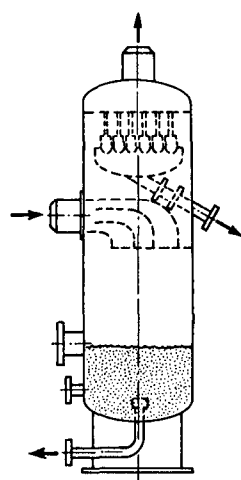


Fig. 3.35 Vertical II

The situation of figure 3.34 is encountered in applications in which no slugs are anticipated. Often in this case a number of cyclones directly in the front of the inlet has been omitted to facilitate the distribution. The two-stage configuration of figure 3.35 will be described more detailed with other such set-ups in section 3.6.

3.4.4.5 Straight through cyclones

1. Introduction

Another type of cyclone which may be successfully applied in high pressure gas/liquid separation is the straight through cyclone. Its basic form is depicted in figure 3.36. The gas enters the tube on the left side, the swirling flow is usually induced by a set of static vanes. Particulate matter is collected on the walls and discharged with or without the help of a purge stream which has to be cleaned afterwards. The cleaned gas stream leaves the tube through a vortex finder located in the centre.

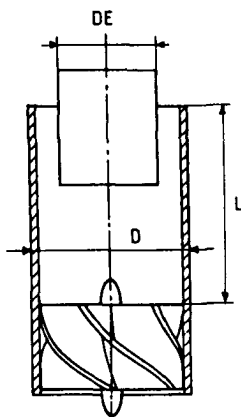


Figure 3.36 Straight through cyclone

Although it is much easier to predict the flow field inside this type of cyclone than inside the reverse flow cyclone, relatively little theoretical work has been performed to assist in design purposes.

Sofar, the field of application has essentially been the automotive industry where this cyclone is used as a precleaner in the air intake.

Principle advantages of the straight through cyclone compared to the reverse flow cyclone are:

1. Less susceptible to reentrainment, since less changes of direction with accompanying turbulence will be necessary;
2. A smaller pressure drop at the same collection efficiency;
3. More compact at the same collection efficiency;
4. Better suited to be grouped to a multicyclone (no danger of maldistribution and very compact).

Principle disadvantages:

1. The necessity of a very carefully designed outlet section, since cleaned gas and separated matter are drawn off very close to each other;
2. The need to make provisions for secondary cleaning if a purge gas stream is used to discharge the separated matter.

It appears from early literature, Ter Linden [1949] referring to Davidson, Daniels [1957] and Jackson [1963], that the reasons for employing straight through cyclones were not always the same: did Davidson mean to design a compact efficient separator with a high turn down ratio; Daniels misused the concept, according to Jackson, for a low pressure drop, low efficiency, compact separator. In a later publication Plekhov [1972] reports very

successful high efficiency applications of straight through cyclones at operating pressures from 0.1 to 120 bars.

Several inlet designs exist; figure 3.37 gives some examples. The tangential inlet depicted in figure 3.37 has been presented as a means to prevent one of the effects that influence the collection efficiency of a straight through cyclone negatively. With an axial swirl element large particles can hit the wall with a fairly large radial velocity, which can cause bouncing back in the gas stream. When a tangential swirl element is used these particles will be projected to the wall at a much shallower angle and bouncing will not take place. This effect will be much stronger in case of dust separation than in case of mist separation. One disadvantage of a tangential inlet is the fact that care has to be taken when designing a multicyclone, since maldistribution to the cyclones can take place again.

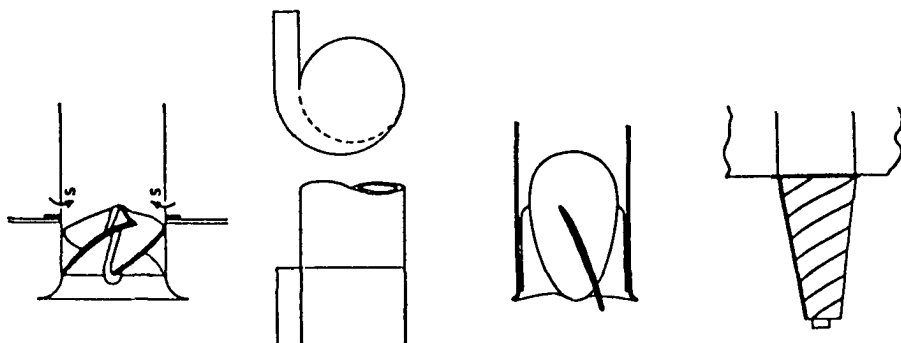


Fig. 3.37A Inlet I 3.37B Inlet II 3.37C Inlet III 3.37D Inlet IV

The function of the outlet section is to discharge the gas and collected solids or liquids without any remixing of the collected matter in the cleaned gas. In industrial practice two types of discharges can be found: the collected matter is discharged either axially, figures 3.38A and B, or radially, C and D. There seem to be some clear advantages attached to the use of radial discharges:

1. Collected matter is discharged in an early stage and reentrainment chances are reduced;
2. Collected matter is discharged more efficiently because of higher discharge pressure.
3. Lower pressure drop across outlet.

With respect to the last characteristic: it is usual to place an obstructing ring behind the longitudinal slits to prevent reentrainment. This will, of course, result in pressure drop increase.

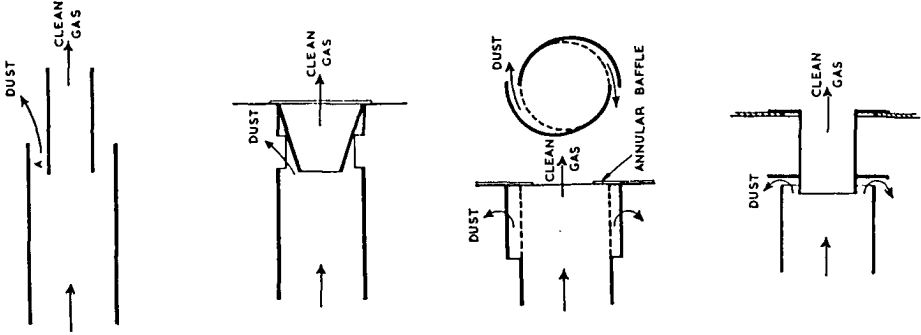


Fig. 3.38A Outlet I 3.38B Outlet II 3.38C Outlet III 3.38D Outlet IV

Plekhov [1972] found that concentric slots performed better than longitudinal slots supposedly because of smaller disturbances to the flow field. The main advantage of an axial outlet is probably its constructional simplicity.

The discharge of collected matter is often facilitated by a purge stream. Purge rates varying up to 40% of the total gas stream are reported by various authors: Jackson [1963], Plekhov [1972], Stenhouse [1979].

Usually a purged discharge leads to a considerable higher collection efficiency (figure 3.39, Stenhouse [1979]).

The cleaning of the purge gas can take place in a secondary separation stage of more or less intricate design. Sometimes it consists of a simple baffle above the discharge which causes some inertial forces. Sometimes, in case of a multicyclone, the purge gas is collected and fed to a separate reverse flow cyclone. The cleaning of the purge gas can also take place in the axial cyclone itself if use is made of the available underpressure inside the cyclone (see figure 3.40).

The obvious advantage of this arrangement is that no secondary cleaning stage will be necessary. Disadvantages have so far been the susceptibility to plugging of the underpressure channels and the negative influence on pressure drop and/or size characteristics.

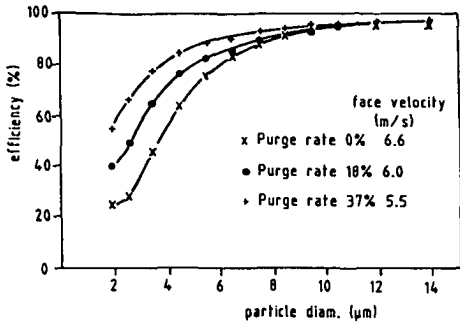


Figure 3.39 Effect of the purge gas rate

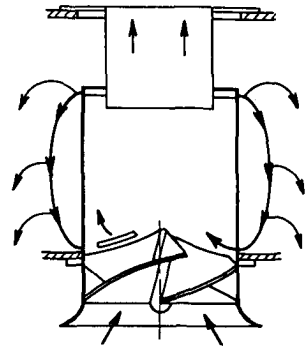


Figure 3.40 Recycled purge gas

Axial multicyclone

Like the earlier described reverse flow cyclones axial cyclones are often grouped together to operate in parallel, maintaining high efficiency and reasonably low pressure drop for high gas flows. The method of nesting is almost always the same: a bank of cells is contained by front- and backplates. Holes in both plates accommodate the inlet and gas outlet passages of the tubes. Maldistribution, with the accompanying decrease in separation efficiency, is by no means as acute as with reverse flow. Normally it will not be necessary to pay special attention to this effect.

3.4.4.6 Characteristics of cyclone type separators

As has been demonstrated in the previous sections, many design varieties of cyclone separators exist. This section gives an overview of the separation characteristics of five main types.

In the first place the following three existing designs are treated:

1. large single gas/liquid cyclones (figure 3.28);
2. large single gas/liquid cyclones of special design (figures 3.29-3.30);
3. conventional multicyclones (composed of typical dust cyclones, fig. 3.18)

Also two other, not often applied, multicyclones are characterized:

4. multicyclones composed of cylindrical reverse flow cyclones;
5. straight through multicyclones.

Although no quantitative data of existing straight through gas/liquid cyclones are available, expected characteristics are estimated from dust separating operation. The same applies to multicyclones of gas/liquid cyclones, although characteristics are estimated from the data available of single gas/liquid cyclones and conventional multicyclones.

A. Operating characteristics

For some of the quantitative data of the different designs given for the operating characteristics the following conditions apply:

mixture : water/air
operating pressure : 1 bar
droplet size distribution: > 8-10 μm

| | single cyclone | single cyclone special design | multicyclone of dust cycl. |
|---|---|---|--|
| 1. separation efficiency | low; $d_{50} \sim 50 \mu\text{m}$ | fairly low; $d_{50} \sim 25 \mu\text{m}$ | high $d_{50} \sim 5\text{-}7 \mu\text{m}$ |
| 2. flow per unit volume expressed as λ (*) | $\lambda \sim 0.2$ (*) | $\lambda \sim 0.25$ (*) | $\lambda \sim 0.3$ (*) |
| 3. turn down ratio | 0.4 | 0.35 | 0.3 |
| 4. pressure drop | 20-30 mbar | 20-30 mbar | < 20 mbar |
| 5. ability to separate non liquid constituents | very good | very good | very good |
| 6. installation and opera- tional costs | relate approximately inversely with λ | | |

| | multicyclone of gas/liquid cyclones | straight through multicyclones |
|---|---|---|
| 1. separation efficiency | high; $d_{50} \sim 5\text{-}7 \mu\text{m}$ | high; $d_{50} \sim 10 \mu\text{m}$ |
| 2. flow per unit volume expressed as λ (*) | $\lambda \sim 0.35$ (*) | $\lambda \sim 0.4$ (*) |
| 3. turn down ratio | 0.25 | 0.2 |
| 4. pressure drop | < 20 mbar | < 10 mbar |
| 5. ability to separate non liquid constituents | depending on geome- trical characteristics | depending on geome- trical characteristics |
| 6. installation and opera- tional costs | relate approximately inversely with λ | |

(*) For explanation see appendix A. It must be realized that the use of the load factor λ is inappropriate and only meant as a means to compare the specific capacities of the designs; again it is stressed that the values of λ will only apply under the above given circumstances.

B. Design characteristics

In table 3.IV the availability and expected reliability of the design procedures for reverse flow and axial cyclones have been summarized.

| | as a function of geometry | as a function of oper. press | as a function of liq. loading | as a function of liq. proport |
|------------------------|------------------------------|---------------------------------|----------------------------------|----------------------------------|
| separation eff. | | | | |
| availability | + | + | + | + |
| exp. reliability | +/- | +/- | - * | - * |
| max. capacity | | | | |
| availability | + | + | - | - |
| exp. reliability | +/- | - | - | - |
| turndown ratio | | | | |
| availability | + | + | - | - |
| exp. reliability | +/- | - * | - | - |
| pressure drop | | | | |
| availability | + | + | + | + |
| exp. reliability | +/- | +/- | - | -/NI? |

* crucial design information NI not of interest

Table 3.IV

3.5 Diffusional separation

1. Principle of operation

As described in section 3.2 very small particles in a gas stream will show Brownian movement. With equation 3.4 the trajectory the droplets travel under influence of this effect can be estimated. This equation makes clear that only the smallest droplets ($< 0.5 \mu\text{m}$) will be influenced perceptibly. In order to achieve a separation of these particles it will be necessary to create a large collection surface through which the gas must flow slowly, which gives the particles enough opportunity to reach this surface. If larger particles are separated as well by a separator relying on this principle, inertia has taken over as the main separation mechanism.

A practical form of a separation unit based on this principle is the often applied filter cartridge (see figure 3.41). The filter cartridge consists of a fiber bed that is packed between two concentric support rings. The fibrous matter in the bed is densely packed and in most cases made of fiber glass. The fibers are 15-30 μm in diameter.



Figure 3.41 Filter cartridge

The mist laden gas moves through the bed, whereby the mist particles coalesce on the fibers. The liquid film flows downward and out of the filter cartridge. Gas velocities are typically 20 cm/sec; collection efficiencies (for droplets $< 1 \mu\text{m}$ > 99.5%) and pressure drops for atmospheric water and air operation can range up to 75 mbar.

A second way of employing diffusional separation is permitting too high gas velocities inside the fiber bed. This will lead to reentrainment of the separated liquid in the cleaned gas stream. Since the reentrainment consists of coarse droplets, a fairly simple mist extraction device can be used for the final separation. Fiber beds applied as such are usually referred to as coalescers. It is a practical way of reducing a large disadvantage (large separator volumes) while maintaining the specific advantages (high separation efficiency of very small particles).

A practical separator that combines the two separation actions is suggested by Joseph [1984]. It consists of a bicomponent fiber bed made out of two layers of fiber packing. The first is of conventional design and the second of a much less densely packed material. If overfed, the first layer produces coarse reentrained droplets, that can easily be drained through the second layer. No specific maximal allowable gas velocities were reported.

2. Characteristics of diffusional separators

2.A Operating characteristics

- separation efficiency : very high ($d_{s,0} < 1 \mu\text{m}$)
- flow per unit volume : very low
- turndown ratio : no practical lower limit attached to separation principle
- pressure drop : high; approximately 50-60 mbar; atmospheric water/air operation

- ability to separate non-liquid constituents : very good, but operation under fouling conditions is only possible if the filter cartridges are regularly replaced.
- installation and operating costs : because of low throughputs and possibly necessary replacements of clogged cartridges: both high.

2.B Design characteristics

In table 3.V the availability and expected reliability of different design correlations are summarized.

| . | as a function of geometry | as a function of oper. press | as a function of liq. loading | as a function of liq. propert. |
|------------------|------------------------------|---------------------------------|----------------------------------|-----------------------------------|
| separation eff. | | | | |
| availability | + | + | - | - |
| exp. reliability | + | + | - | - |
| max. capacity | | | | |
| availability | + | - | - | - |
| exp. reliability | +/- | - | - | - |
| pressure drop | | | | |
| availability | + | + | - | - |
| exp. reliability | +/- | + | - * | - |

* probably necessary for geometrical optimization

Table 3.V

3.6 Existing separator types

In the previous section several possible components of practical separators have been discussed. In this section some meaningful and often applied combinations of different components are described. The most important factors that determine the general form of the separator are:

1. whether the separator is positioned horizontally or vertically;
2. whether the separator comprises one or more separation stages.

In the following more attention will be paid to the backgrounds of the various alternatives.

3.6.1 Horizontal or vertical position

1. According to De Graauw [1984] usually a vertical knock-out drum is preferred because:

- the plan area is smaller;
- the solids can be removed more easily;
- they are less susceptible for liquid surges;
- the liquid level is not critical for operation.

However, in most cases when one or more of the following circumstances are applicable, a horizontal knock-out vessel is chosen.

- If the liquid to gas ratio is high and at the same time the liquid viscous, then the size of the liquid interface determines the design (for example when viscosity of oil $\eta > 0.01 \text{ Ns/m}^2$);
- If the mixture foams easily;
- If liquid/liquid separation has to take place in the liquor sump.

In formulating these rules De Graauw [1984] assumes that it is mainly the larger gas/liquid surface in a horizontal separator which makes this type sometimes preferable to the vertical separator.

2. Arnold [1984] on the other hand states that the higher gas velocity allowed inside a horizontal separator, resulting in a smaller vessel volume, is the reason why in most cases a horizontal separator should be chosen. Arnold advises to use vertical separators only in case of limited floorspace (offshore applications).

Summarizing it can be concluded that the choice between the two types of separators depends in most cases on the operating pressure.

When floorspace is not a critical criterion, the operating pressure will be a determining factor in judging the economics of a horizontal separator and the convenient operating characteristics of a vertical separator.

3.6.2 Number of separation stages

This number is actually determined by the form and the quantity of the liquids offered to the separator and the maximal amount of liquid quantity permitted in the outlet of the separator. As an illustration: if a gas flow contains both slugs of liquid and fine mists and it is necessary to separate out only the slugs (for instance for the feed line to flare) a knock-out vessel will be sufficient. If mists are not permitted downstream of the separator (feed line to glycol dehydrator for instance) it will be necessary to accommodate both a knock-out and a mist extraction stage in the separator. If the gas must be virtually free of any liquids (sales gas) these two separation stages will be followed by a third; in which diffusional separation (filter cartridges) will either separate or coalesce the remaining fine mist particles. In the following, the general form and operating properties of several possible one-, two- or multiple stage separators will be described and illustrative practical examples of each type will be given.

One-stage

One-stage separators have been described in sections 3.3, 3.4 and 3.5.

Only one-stage separators based on gravity settling and inertial separation have found practical application in oil field operations.

Specific details have been described in sections 3.3 and 3.4.

Figures 3.5 and 3.6 give a trivial example of a practical form of both a horizontal and a vertical knock-out vessel. Figure 3.34 shows a one-stage mist eliminator with a multicyclone, figure 3.15A with a horizontally flowed through vane-pack. The latter two separators are referred to as 'in line' separators. They are only suited for operations in which no slugs are formed in the feed line. Figure 3.28 shows a single cyclone as one-stage separator. This cyclone will show a higher pressure drop and probably also a lower collection efficiency compared to the multicyclone, but on the other hand have better separation characteristics for slugs. Mesh type or upflow vane-type separators can physically only be applied in two-stage separators. Filter cartridges are hardly used in single stage separations because of their susceptibility to liquid overloading.

Two-stage

Two types of two-stage separators can be distinguished:

1. Those having an effective separation ability in the slug and mist ranges.
The general form of this kind of separator consists of a knock-out (section 3.2) and a mist extraction stage (either horizontally or vertically positioned) (section 3.4). Figures 3.16B and 3.35 give illustrative examples. The operating characteristics of these separators will be the summation of the characteristics of the single components. Apart from this form also slightly more exotic forms can be encountered as for instance the two-stage single cyclone separator (figure 3.42).

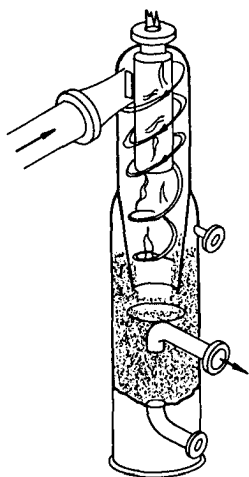


Fig. 3.42 Two-stage
single cyclone
separator

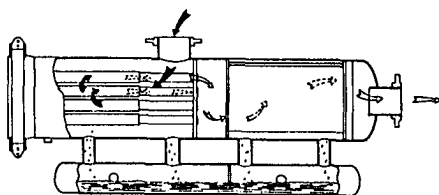


Fig. 3.43 Filter separator

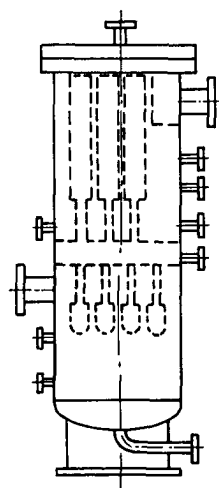


Fig. 3.44 Cyclone
filter
separator

2. Those aiming at an effective separation of mists and fine mists.

The general form of this kind of separator consists of a coalescing stage in which filter elements deliver coarse droplets to a mist extraction stage where usually a mesh-type or a vane-type demister is located (figure 3.43).

Also references to practical applications were found in which the position of the two stages are reversed and in which the demister acts as a precleaner and the filter elements as high efficiency separators (figure 3.44).

Three-stage

Although one would expect in this case a separator in which all three separation mechanisms would be delegated to provide a separation ability for a broad range of inlet conditions, this application is not very often encountered in practice. The reason is mainly that the internal structure of the separator vessel tends to get very complicated. A three-stage configuration that did find practical application found in separators that overload a mesh pad or a simple upflow vane-pack which then acts as a coalescing element. Downstream of this coalescer a relatively simple mist extractor can be mounted which does not need to have a high collection efficiency for fine mist particles (with its advantages to pressure drop and separator size).

3.7 Evaluation of present technology

In this section the most often applied separators (described qualitatively in 3.6) are compared and characterized with respect to:

1. their operating characteristics (table 3.VI);
2. reliability and versatility of their design procedures (tables 3.VII and 3.VIII).

These two inventories will give a representative overview of two important aspects in connection with separator technology.

The different separator types that will be discussed are:

1. Knock-out drum (section 3.3.2)
2. Mesh-type separator (two-stage) (sections 3.3.2, 3.4.2 and 3.6)
3. Vane-type separator
 - a. inline (one-stage) (section 3.4.3)
 - b. two-stage (sections 3.3.2, 3.4.3 and 3.6)
4. Cyclone type separator
 - a. single conventional cyclone (section 3.4.4.3)
 - b. inline (one-stage) multicyclone (section 3.4.4.4)
 - c. two-stage multicyclone (sections 3.3.2, 3.4.4.4 and 3.6)
5. Filter separator (sections 3.5 and 3.6)
(two-stage, filters as coalescers)

Although some practical use in this field of straight through cyclones is reported, this separation method can not be considered as generally applied. Because hardly any quantitative information is available about these (potential) gas/liquid separators, they have not been included in this inventory. For more specific information is referred to section 3.4.4.5.

The general impression that is given by the present design practice is of empiricism. This is caused particularly by the lack of exact knowledge of the physical phenomena that take place inside the separator.

The latter effect is the reason why at present it will not be possible to tailor a design for a particular application, even if one would have full knowledge of the operating conditions. Issues as the influences of high pressure, the presence of glycols in the feed stream or variations of geometry are still the subjects on which many lectures are given.

This has led to a situation in which only few innovative separator designs are applied. The industry rather holds on to traditional designs that have been proven in practice and with which operating experience exists. Few experiments are undertaken with new designs, that may be very promising in one or more aspects (compactness for instance). In itself this is a very understandable course of events, because the investments for possibly superfluous gas/liquid separation equipment are often minor in comparison to the damage that could be inflicted by a malfunctioning separator.

Most of the present separator technology finds its origin in the fifties and is relatively little developed. The popular multicyclone bundles described in 3.4.4 for instance have originally been developed for dust separation and have not at all benefitted from the advances made in the multiphase flow sciences.

| Operating characteristics Separator types | Separation efficiency | | | Flow per unit volume (expressed as λ) ¹⁾ | Turndown ratio (minimal capacity) | Pressure drop ¹⁾ | Suitability for high operation (> 100 bar) |
|--|-----------------------|-------|----------|---|--------------------------------------|-----------------------------|---|
| | mist | slugs | sand/wax | | | | |
| - Knock-out vessel | -- | ++ | - | hz: 0,12 vt: 0,8 | not limited | < 5 mbar | -- |
| - Mesh type sep. (two stage) | ++ | ++ | - | hz: 0,15 vt: 0,12 | 1/3 | < 10 mbar | - |
| - Vane type sep. in line | + | - | - | 0,3 | 1/3 - 1/3 ¹⁾ | < 10 mbar | +/- |
| two stage | + | ++ | - | 0,3 | 1/3 - 1/4 ¹⁾ | < 10 mbar | +/- |
| - cycl. type sep. single | - | ++ | + | (-) | 1/2,5 - 1/3 ¹⁾ | < 20-25 mbar | - |
| in line multi | + | - | + | 0,3 | 1/3 - 1/5 ¹⁾ | < 15-20 mbar | + |
| two stage multi | + | ++ | + | 0,3 ** | 1/3 - 1/5 ¹⁾ | < 15-20 mbar | + |
| - Filter sep. | ++ | -- | + | (-) | not limited | < 40 mbar | + |

* at the cost of higher erosion

¹⁾

with respect to atmospheric operation with air/water

** complicated vessel at higher operating pressures

Table 3.VI

| Design procedure Separator types | Determination of separation efficiency as a function of gas throughput and DSD | | | | Determination of maximum capacity | | | |
|-------------------------------------|---|------------------------------|---------------------------|-----------------------------|-----------------------------------|------------------------------|---------------------------|-----------------------------|
| | Influence of geometry | Influence of oper. press. | Influence of liq. load | Influence of liquid sort | Influence of geometry | Influence of oper. press. | Influence of liq. load | Influence of liquid sort |
| - Knock-out vessel | vt:r hz:rr | rr | NI | NI | rr | rr | NI | NI |
| - Mesh type sep. (two stage) | rr | rr | NI | rr | rr | rr | ur * | ur * |
| - Vane type sep. in line | ur * | ur * | ur | ur | ur * | ur * | ur * | ur * |
| two stage | ur * | ur * | ur | ur | ur * | ur * | ur * | ur * |
| - Cycl. type sep. single | rr/ur * | ur * | ur | ur | rr/ur * | ur * | ur * | ur * |
| in line | rr/ur * | ur * | ur | ur | rr/ur * | ur * | ur * | ur * |
| two stage | rr/ur * | ur * | ur | ur | rr/ur * | ur * | ur * | ur * |
| - Filter sep. | rr | rr | ur | ur | rr | rr | ur * | ur * |

* necessary knowledge for optimized practical operation

r reliable; rr reasonably reliable; ur unreliable; NI not of interest

Table 3.VII

| Design procedure Separator types | Determination of minimum capacity as a function of DSD | | | | Determination of pressure drop | | | |
|-------------------------------------|---|------------------------------|---------------------------|-----------------------------|--------------------------------|------------------------------|---------------------------|-----------------------------|
| | Influence of geometry | Influence of oper. press. | Influence of liq. load | Influence of liquid sort | Influence of geometry | Influence of oper. press. | Influence of liq. load | Influence of liquid sort |
| - Knock-out vessel | NI | NI | NI | NI | r | r | NI | NI |
| - Mesh type sep. (two stage) | rr * | ur * | NI | rr | r | r | rr/ur | rr/ur |
| - Vane type sep. in line | ur * | ur * | ur/NI | ur | ur | ur | ur | ur |
| two stage | ur * | ur * | ur/NI | ur | ur | ur | ur | ur |
| - Cycl. type sep. single | ur * | ur * | NI | NI | rr | rr | ur | ur/NI |
| in line | ur * | ur * | NI | NI | rr | rr | ur | ur/NI |
| two stage | ur * | ur * | NI | NI | rr | rr | ur | ur/NI |
| - Filter sep. | NI | NI | NI | NI | rr | rr | ur/rr | ur/rr |

* necessary knowledge for optimized practical operation

r reliable; rr reasonably reliable; ur unreliable; NI not of interest

Table 3.VIII

4. DESCRIPTION OF THE CURRENT RESEARCH PROJECT

4.1 Structure of chapter

In this chapter the objectives of this project are formulated and the project strategy and available tools are described. In section 4.2 is evaluated to what extent present separator technology can fulfil the requirements of modern separators. With the outcome of this inventory the overall research objectives can be described. In section 4.3 the strategy to reach these objectives is explained in detail and section 4.4 describes the extent to which this report covers the total project.

4.2 Formulation of research objectives

The evaluation of present technology with respect to modern separator requirements is based on the comparison of tables 2.I and 2.II (inventory of operating conditions and requirements) and tables 3.VI, 3.VII and 3.VIII (inventory of operating and design characteristics).

Possible discrepancies will be subdivided in two categories:

1. principle shortcomings of design procedures;
2. principle shortcomings of separator characteristics.

ad 1.

A. It appears from chapter 3 that present design procedures are hardly sufficient for practical use. In most cases design procedures consist of empirical correlations that are proprietary and based on practical experience, applicable to one particular separator type. Difficulties arise in situations in which a separator design needs to be optimized, as most procedures include large safety margins that are qualitatively determined.

When observing the three basic types of separators, it appears that those based on gravity and diffusion are best described; mainly because of the small influence of separator geometry variations.

Those based on inertial separation are hardly described reliably (with exception of dust cyclones, but they play no role in this chapter).

The inadequacy of some of the important practical design rules is demonstrated in sections 7.4-7.6. In these sections some of the experimental results described in chapter 6 combined with the physical knowledge acquired in chapter 7, are used to check the validity of existing design rules.

The most important relations that need to be quantified reliably are those between:

- separation efficiency and separator geometry, droplet size distribution, gas throughput and operating pressure;
- maximal capacity and separator geometry, liquid sort, liquid loading and operating pressure;
- minimal capacity and separator geometry, droplet size distribution and operating pressure;
- pressure drop and separator geometry, liquid loading, gas throughput and operating pressure.

B. As appears from chapter 2, the form of the liquid loading offered to the separator is often unknown. Little is known of this inlet condition that has a considerable influence on separator operation. To develop a more efficient design procedure it should be attempted to describe this quantity more exactly.

ad 2.

Apparently, a perfect separator has not yet made its appearance.

Most separators have drawbacks connected with their specific advantages.

In case of separators or separator modules based on gravity or diffusion these drawbacks (for instance necessary volume) are directly related to the principle of operation and can not be reduced easily. In case of separators based on inertial separation (the by far largest group of separators) much more design flexibility exists to minimize certain disadvantageous operating characteristics. Even so, in this group of separators no single type exists that combines all positive properties. Only cyclone and vane type separators will play a serious role as mesh type separators are rapidly losing popularity because of low capacity and fouling problems.

Traditional disadvantages of vanes

Vanes have a limited range of operating pressure (maximum 75-100 bar). The characteristics of most vane types in respect to fouling operations are questionable (although commercial exceptions exist).

Traditional disadvantages of reverse flow type cyclones

In many cases multicyclones can not be built in a vessel as compact as vane packs. At higher operating pressures the pressure drop across the cyclone bundle prevents drainage of the cyclones in the sump of the vessel through a liquid seal, which causes the need for a more expensive external drainage.

Traditional disadvantages of straight through type cyclones

Weak secondary separation of purge stream may result in low separation efficiencies.

4.3 Project strategy and tools

4.3.1 Introductory remarks

In this section the main research objectives are described. Considering the findings of the previous section there is apparently especially need of:

1. Development of generally applicable design procedures for vane and cyclone type separators;
- 2A. Development of a compact, low pressure drop, cyclone type separator;
B. Development of a vane-type separator with an extended operating pressure range;
Of both separators the traditional advantages should be maintained.
3. Development of relations to determine the inlet conditions of separators more exactly.

When considering the first two sets of objectives it is clear that the first necessity is the development of relations (or models) that describe the influence of issues as geometry and two-phase properties on the operating characteristics.

These models can then:

- a. easily be transformed to practical design procedures for existing separator types;
- b. be used for geometric optimization to assist in the development of the designs specified under the second objective.

The third objective stands apart and needs to be investigated separately.

Because experimental facilities for this specific purpose tend to be quite complicated and expensive, and because some experimental work carried out earlier seems directly transferable, it is expected that a literature investigation (reported in chapter 5) will suffice in first instance.

Further this section will be focussed on how to develop the separator behaviour models.

4.3.2 Project strategy and tools

The most important requirements of a general applicable model are that:

1. the gas flow field is predicted correctly for a broad range of geometries of a certain separator type;
2. the interaction between the gas and any liquid phase is correctly represented;
3. effects of upscaling are reproduced reliably.

Because the description of these quantities in the two separator types of interest can be very complex, it is necessary to make use of existing computer codes that are specialized in fluid dynamic problem solving. (In chapter 7 an extensive description is given of the theoretical background of these software packages, their uses and their limitations.) The code forms submodels in which the gas flow field inside a given geometry is calculated. These data are transferred and processed further to predict particle trajectories and secondary effects like reentrainment and creep. Thereafter the primary operating characteristics, separation efficiency and pressure drop are available (minimal and maximal capacity limits can be derived from these two).

Unfortunately, in spite of their convincing graphics, these fluid dynamic codes are not necessarily accurate. Much care must be taken to provide enough opportunity to verify predictions against experimental data, either acquired from literature or by own experiments.

The identification and quantification of the physical phenomena necessary to extend the gas flow field model is again acquired partially by literature searches and partially by own experiments.

The development procedure of the dedicated models of interest is represented in figure 4.1 and described subsequently.

This scheme will be carried out for vane (V), reverse flow (RFC) and straight through (or axial) cyclone (AC) separators.

The project is thus based on the use of three different 'tools':

1. Literature information; the results of several literature searches are described in chapter 5.
2. Experiments; the contents of the EXP blocks and the experimental facilities will be described extensively in chapter 6.
3. Modelling facilities; which encompass both software (from programmes in Basic to complex fluid dynamic codes) and hardware (from personal computers to a Cray supercomputer).

Detailed description of the activities to fill out the MOD blocks is given in chapter 7.

Since all blocks presented in figure 4.1 will be treated consecutively in the next three chapters sense of orientation with respect to the location of an individual block in the project structure might be lost. Therefore figure 4.1 and accompanying text is also printed on the innerside of the (folded) frontcover as a quick reference.

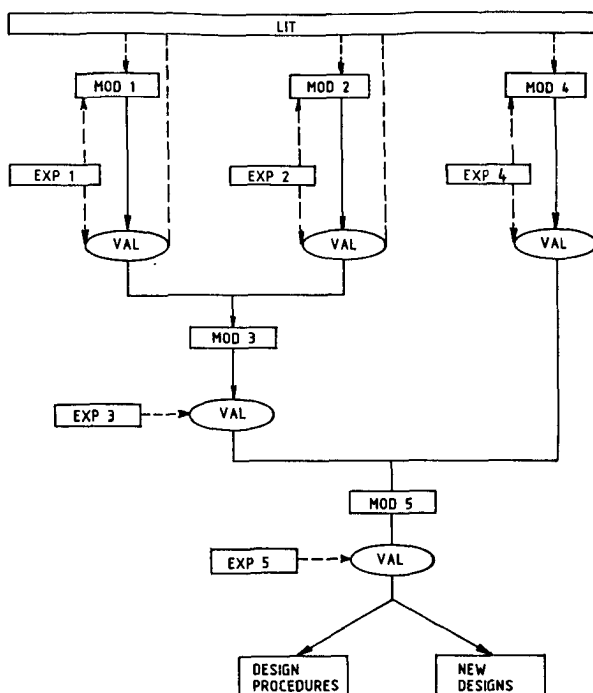


Figure 4.1

- MOD1 reproduces the gas flow field inside a basic separation unit;
 MOD2 describes the behaviour of the liquid phase (particle trajectories, reentrainment and creep phenomena);
 MOD3 describes the behaviour of a basic separation unit;
 MOD4 quantifies the measure of maldistribution across a full size separator; no need to model this with the earlier mentioned fluid dynamic codes;
 MOD5 combines the predictive powers of MOD3 and MOD4 and should therefore be able to describe the behaviour of an actual scaled separator over a broad range of operating conditions;
 EXP1 a. provides the fluid dynamic code with necessary physical information to start with (starting conditions) and
 b. provides the experimental data to validate MOD1 with (gas flow field measurements)
 EXP2 identifies and quantifies phenomena related to the liquid phase (reentrainment, creep, particle trajectories);
 EXP3 provides the experimental data to validate MOD3 with (operating characteristics of a basic separation unit over a broad range of operating conditions);
 EXP4 a. provides physical information (starting conditions) for MOD4;
 b. provides the experimental data to validate MOD4 with;
 EXP5 provides the experimental data to validate MOD5 with (operating characteristics of an actual scaled separator over a broad range of operating conditions);
 LIT represents the information acquired through literature investigation used for validating and supplementing models.
 VAL validation

4.4 Scope of present report

As this dissertation is the first of two in which the results of this project will be published, the following chapters are not complete for all separator types.

Table 4.I gives an overview which blocks have been realized. From this table it is apparent that special attention will be paid to straight through and reverse flow cyclones. It is expected that vane separators will be dealt with more completely later.

| | AC | RFC | V |
|------|----|-----|---|
| LIT | x | x | x |
| EXP1 | x | x | - |
| EXP2 | x | x | x |
| EXP3 | x | x | - |
| EXP4 | NA | x | x |
| EXP5 | NA | x | x |
| MOD1 | x | - | x |
| MOD2 | x | x | - |
| MOD3 | x | - | - |
| MOD4 | NA | x | x |
| MOD5 | NA | - | - |

x = completed

- = not completed

NA = not applicable

Table 4.I

5. RESULTS: LITERATURE SEARCH

For project structure and nomenclature see innerside of front cover.

5.1 Introduction

This chapter gives the conclusions of the two described literature searches.

1. Section 5.2 gives a short overview of different phenomena that influence the inlet conditions of a separator. Where possible, a short quantification is given. This section clarifies some of the uncertainties that are usually encountered when the inlet conditions of a certain separator are determined (third objective in section 4.3).

This information is also used in chapter 6 to determine the experimental droplet size distributions.

2. Sections 5.3-5.5 give the results of the literature searches described in chapter 4 as block LIT in the project strategy. Specific information that is necessary to set up and verify the models is collected.

Sections 5.3 and 5.4 quantify respectively the friction factor at a gas/liquid interface and the reentrainment behaviour of a liquid film (information necessary for MOD2). Section 5.5 gives characteristics of swirling flows under different conditions (information necessary for RFC/AC-MOD1).

5.2 Determination of the inlet conditions

The inlet conditions that exert the largest influence on the operating characteristics of the separator (see chapter 2 and 3) are:

1. operating pressure;
2. physical properties of liquid phase, liquid density, liquid viscosity and surface tension;
3. droplet size distribution;
4. gas to liquid ratio;
5. complicating characteristics (fouling: the presence of sand and wax in the gas and/or foaming).

ad 1, 2 and 4

Gas- and liquid density are important because the ratio of these properties determines the magnitude of the separating forces (section 3.2). Depending on the application, this ratio can vary considerably.

Liquid viscosity and surface tension often determine the maximum allowable gas and liquid loading of the separator prior to reentrainment or flooding (see for instance appendix A 3.4).

The liquid to gas ratio of the mixture not only influences the maximum allowable gas velocity through a separator but also determines the form of the liquids in front of the separator. The separator design is to a large extent determined by the form of the liquids. The separation of a slug puts other demands on the separator than the separation of a mist (see section 3.6).

At present, groups 1, 2 and 4 can be determined quite exactly if enough information is available about the composition of the reservoir fluids and about the production system. With the help of software packages to predict thermodynamic and physical properties of complex mixtures it is, for instance, possible to calculate the amount of retrograde condensation in a given gas mixture under a given pressure drop.

ad 3.

Unfortunately, the form of the liquid loading (droplet size distribution) seems much less easier predictable.

It depends on:

1. gas velocity;
2. liquid to gas ratio;
3. physical properties (viscosity, density, surface tension);
4. dissipated energy in the system.

In figure 5.1 Sakaguchi [1979] (Hetsroni [1982]) shows the influence of the first three groups on the form of a two-phase mixture in a horizontal pipe. Figure 5.2 (Hetsroni) shows the actual form of the different flow regimes encountered in figure 5.1.

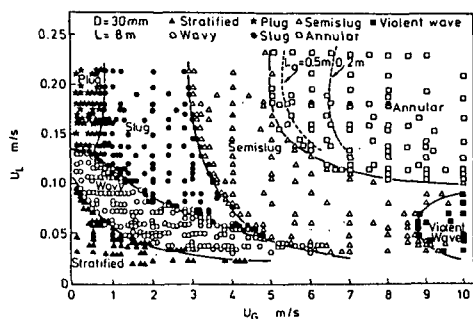


Figure 5.1 Flow pattern map

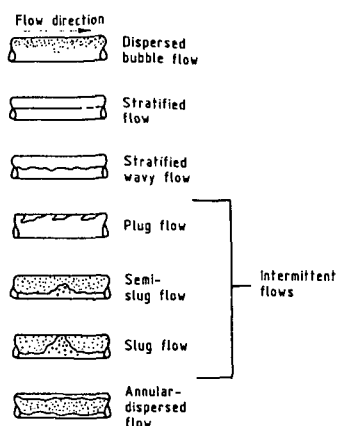


Figure 5.2 Flow patterns

Many authors have investigated the transition of flow regimes as a function of the parameters used in figures 5.1 and 5.2. Baker [1954], Schicht [1969], Mandhane [1974] and Taitel and Dukler [1976] are examples of authors who have suggested different flow charts. In order to account also for the different physical properties of other gas/liquid systems than water and air Baker suggests the following correction factors for the values on the two axes of the diagram (figure 5.3):

$$\lambda_B = \left(\frac{\rho_g}{\rho_A} \frac{\rho_l}{\rho_W} \right)^{0.5} \quad \text{and}$$

$$\psi_B = \frac{\sigma_W}{\sigma_1} \left[\frac{\mu_1}{\mu_W} \left(\frac{\rho_W}{\rho_1} \right)^2 \right]^{1/3}$$

The subscripts A and W refer to the corresponding physical properties of air and water; g and l to the properties of the gas and liquid in question.

Taitel and Dukler have set up a semi-theoretical derivation of the flow regime chart which has been found fairly consistent with experimental data and which is referred to as most reliable (Hetsroni [1982]) for predictions of flow regimes for unconventional gas/liquid systems.

The correlations that have been mentioned sofar apply to horizontally flowing gas/liquid mixtures. For inclined or vertical flows similar regimes can be encountered, but occur under completely different circumstances (see figure 5.4).

N_g and N_l are comparable to the corresponding variables of figure 5.3.

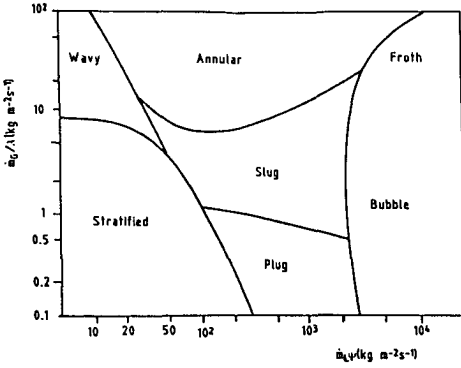


Figure 5.3 Flow pattern map of Baker, replotted in the form suggested by Bell (1969)

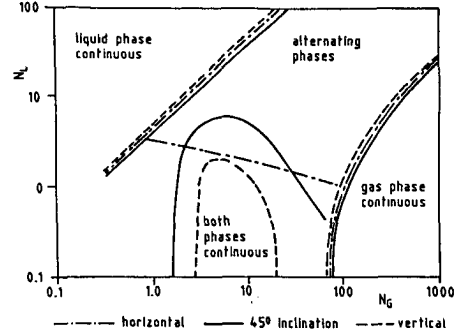


Figure 5.4 Vertical flow pattern map

The above clearly illustrates that with the present quantitative knowledge of these effects properties as maximum slug size or minimum droplet size are very difficult to predict, especially if one realizes that the approach of the gas/liquid mixture to a separator is often a bizarre combination of horizontal and vertical passages, alternated by bends in the pipeline.

It is apparently not possible to describe the liquid form quantitatively, completely and theoretically. Therefore, some phenomenological correlations will be cited that quantify the effects that determine the maximum stable droplet size. Hinze [1955] and Kolmogoroff [1949] developed, along different routes, the following expression for d_{\max} :

$$d_{\max} = C \left(\frac{\rho_g}{\sigma} \right)^{3/5} (\epsilon)^{2/5} \quad (5.1)$$

in which: $\epsilon = 2 \frac{f_{gi} v_g^3}{D}$, the dissipated energy per unit volume
 f_{gi} = friction factor between gas and liquid interface
 v_g = gas velocity
 C = dimensionless constant
 D = diameter of pipe

Sleicher [1962] derives a more empirical expression for d_{\max} :

$$We \left(\eta_g \frac{v_g}{\sigma} \right)^{1/2} = 38 \left(1 + 0.7 \left(\eta_l \frac{v_g}{\sigma} \right)^{0.7} \right) \quad (5.2)$$

in which the parameter We is defined as follows:

$$We = d_{\max} \rho_g \frac{v_g^2}{\sigma}$$

ad 5.

Fouling by sand or wax deposition can exert seriously detrimental effects on the operating characteristics of a separator, and thus be of influence on the choice of a particular separator. Possible wax problems can usually be predicted from the analysis of the reservoir fluids, although the exact extent to which waxing will occur is not always known and is often determined empirically. Sand can always be present in the feed of separators further upstream. The amount depends most often on reservoir characteristics but also on production rate.

Foaming is a second complicating property that can seriously hamper the separator operation.

In literature no specific references have been found that describe possibilities to predict this effect (semi-)theoretically.

5.3 Friction factors at gas/liquid interface

5.3.1 Form of gas/liquid interface

It is usually assumed that the separated liquid forms an evenly distributed film across the inner surface of the separator. In practice this is not always the case: when the liquid loading is low it will often appear that not all of the surface is wetted and that the liquid will run down in strings. If the liquid loading increases the whole surface will eventually be wetted with a smooth film. A further increase in the liquid loading will first result in ripples on the film surface and later in larger instabilities like 'roll-waves' (figure 5.5). In practical separation

situations all of the four mentioned regimes can occur, and each will be accompanied by a corresponding specific friction factor.

The following will largely deal with the fully wetted regimes, because hardly any information is available on string flows. Additionally, the computational techniques are not sufficiently refined. However, complex data, like those to describe the effects of string flow, could easily be incorporated in the envisaged models.

Hartley and Murgatroid [1964] developed a criterion for the minimal film thickness (b_{\min}) under which string flow would develop. This criterion has been modified by Bankoff [1971] to give the following equation:

$$b_{\min} = 1.72 (\sigma/\rho_l)^{1/5} (\rho_l/(\eta_l g))^{2/5} (f(\theta_o))^{1/5} \quad (5.3)$$

in which $f(\theta_o)$ is a function of the contact angle of the liquid phase and the separator material and varies between 0 and 1. For a contact angle of 60° (water and air) $f(\theta_o)$ amounts to $1/3$. As the correlation is not dimensionless it is important that correct dimensions of the parameters are used.

For this correlation: b_{\min} in cm
 σ in dyne/cm
 ρ_l in g/cm^3
 η_l in g/cm s
 g in m/s^2

It should be noted that in case of rotating flows g should be substituted by the local radial acceleration (g by $\frac{w^2}{r}$), in which w represents the tangential film velocity.

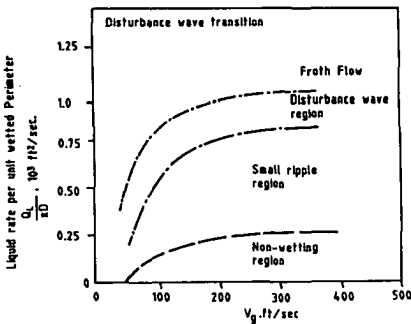


Figure 5.5 Interfacial regimes
 (Shearer et al. (1965))

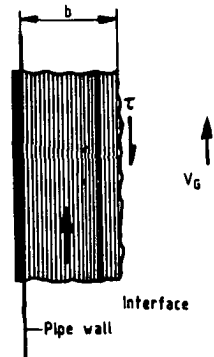


Figure 5.6 Nomenclature for interfacial phenomena

5.3.2 Friction factors of liquid film/gas systems

5.3.2.1 Introductory remarks

It is necessary to quantify the friction factor between the gas and liquid film in order to be able to:

1. predict the correct gas flow pattern with the models of chapter 7;
2. calculate the interfacial and wall shear stresses from which the liquid film velocity distribution can be derived.

For this reason correlations to determine the wall and interfacial shear stresses are collected.

The nomenclature used is explained in figure 5.6.

5.3.2.2 Wall friction factors of liquid films

From the wall friction factor, f_w , the shear stress at the wall is determined as follows:

$$\tau_w = f_w \cdot \frac{1}{2} \rho_1 v_1^2 \quad (5.4)$$

According to different authors there is no major difference between the wall friction factors of the full pipe flow and film flow (Wallis [1969], Ishii [1975], Popov [1986]). The following relation is recommended for smooth tubes:

$$f_w = 16/Re_1 \quad \text{for } Re_1 < 1000 \quad (5.5a)$$

$$f_w = 0.079 Re_1^{-0.25} \quad \text{for } Re_1 > 1000 \quad (5.5b)$$

The liquid film Reynolds number (Re_1) is defined as:

$$Re_1 = \frac{4 \rho_1 v_1 b}{\eta} \quad (5.6)$$

For higher Re_1 numbers and systems with a non-negligible wall roughness the friction factor can be determined conventionally, for instance with the well-known graph of Moody [1944].

5.3.2.3 Interfacial friction factor of liquid films

The interfacial friction factor can relate to either the gas or the liquid phase. In the first case the shear stress on the interface is calculated from f_{gi} , the interfacial friction factor related to the gas phase:

$$\tau_i = f_{gi} \cdot \frac{1}{2} \rho_g (v_g - v_i)^2 \quad (5.7)$$

In the second case τ_i relates to f_{li} , the interfacial friction factor related to the liquid phase, as:

$$\tau_i = f_{li} \cdot \frac{1}{2} \rho_l v_l^2 \quad (5.8)$$

v_g = superficial gas velocity

v_l = superficial liquid velocity

v_i = velocity of interface

I. First some correlations are cited that quantify f_{gi} .

Wallis [1969] proposed a correlation of the following form:

$$1. \quad f_{gi} = 0.005 (1 + C_1 b/D)^{C_2} \quad (5.9a)$$

in which D is the hydraulic diameter of the duct.

He found that the following values of the constants agreed with his experiments:

$$C_1 = 300 \text{ and } C_2 = 1 \quad (5.9b)$$

In later publications (cited in Hewitt and Hall-Taylor [1970]) he relates f_{gi} to f_w to generalize equation 5.9a for more geometries as follows:

$$2. \quad f_{gi} = f_w (1 + C_1 b/D)^{C_2}$$

$$\text{with } C_1 = 360 \text{ and } C_2 = 1 \quad (5.9c)$$

Bharatan [1978] on the other hand found values of:

$$3. \quad C_1 = 818200 \text{ and } C_2 = 2.04 \quad (5.9d)$$

substituted in equation 5.9 to describe his experimental results better. He attributed the discrepancies to geometrical differences in the testing equipment.

Measurements of Whalley et al. [1974] showed that C_1 and C_2 varied with the surface tension of the liquid phase.

Forde and Norstrud [1984] quantified the influence of surface tension and developed the following correlation to determine the equivalent roughness of the film (expressed in the ratio to the film thickness).

$$4. \quad \frac{k}{b} = 4 \sqrt{\left(\frac{\alpha}{1 - \alpha} \left(\frac{\sigma}{\mu_g v_g} \right)^{1/2} \right)} \quad (5.10)$$

in which: α = the liquid volume fraction.

k = height of instabilities on the film

With k/b (= interfacial roughness) the interfacial friction can be determined conventionally (for instance with the graph of Moody).

II. If the interfacial friction factor is related to the liquid phase (the second case mentioned at the start of this subsection) it can satisfactorily be quantified as follows:

$$(\text{Hughmark [1973]}) \quad f_{li} = (K_1 \text{Re}_1^m)^2 \quad (5.11)$$

in which: $K_1 = 3.730$; $m = -0.47$ for $2 < \text{Re}_1 < 100$
 $K_1 = 1.962$; $m = -0.33$ for $100 < \text{Re}_1 < 1000$
 $K_1 = 0.735$; $m = -0.19$ for $\text{Re}_1 > 1000$

5.3.3 Friction factors of rotating liquid film/gas systems

Hardly any reliable correlations have been developed to determine interfacial friction factors for rotating gas/liquid systems. It can be expected that the increased gravitational acceleration flattens out the film, causing a decrease of the film roughness. Loxham [1976] measured the apparent axial friction factor in an annular swirling gas/liquid flow. He found an increase of the friction factor with increasing film thickness, up to a certain value above which it remained constant. He compared the experimental values to those predicted by equation 5.9, without compensating for increased path length inside the tube and found the experimental values 4-5 times higher for small film thicknesses. However, when the tangential component of the gas/film contact is taken into account (angle of swirl at wall $\phi = 45^\circ$ and $v_{gcomp} = u/\sin\phi$) it appears that these friction factors obtain the same values as those predicted by equation 5.9. This is true for film thicknesses up to b/D of 0.005. Above this film thickness the gas/liquid friction factor remains constant. Apparently, only with thicker films the equalizing action of the increased gravitation becomes of considerable influence. This dependency of f_{gi} is depicted in figure 5.7. The dependency of f_{gi} on centrifugal acceleration is given in figure 5.8. Both figures are based on experimental data of Loxham [1976] for a swirl number of $S = 1$ (see section 5.5).

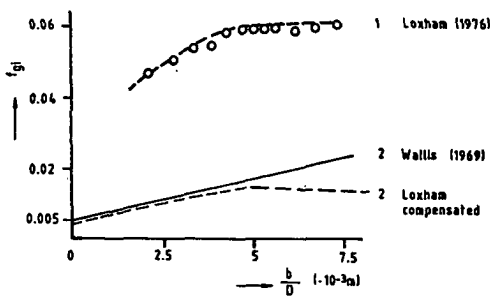


Fig. 5.7 Dependency of friction factors on film thickness

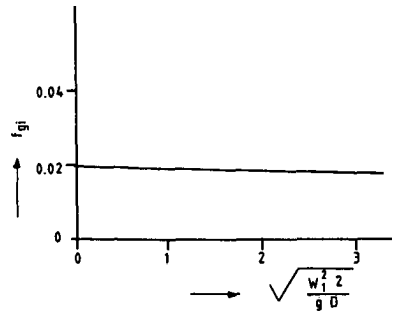


Fig. 5.8 Dependency of friction factors on tangential acceleration

$$f_{gi} = 0.005 \left(1 + \frac{b}{D}\right) \left(\frac{2w^2}{gD}\right)^{-0.05}$$

$$\text{for } \frac{b}{D} \left(\frac{2w^2}{gD}\right)^{-0.05} < 0.05 \quad (5.12)$$

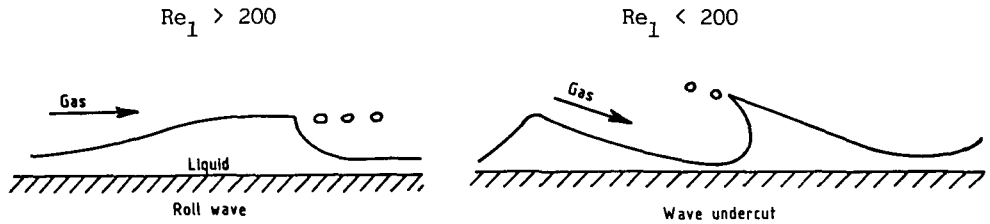
$$f_{gi} = 0.02 \left(\frac{2w^2}{gD}\right)^{-0.05}$$

$$\text{for } \frac{b}{D} \left(\frac{2w^2}{gD}\right)^{-0.05} > 0.05 \quad (5.13)$$

5.4 Reentrainment and related effects

5.4.1 Film break-up mechanisms

The break-up of the liquid film that is formed by the separated droplets is supposed to be the major source of reentrainment if the maximal capacity of the separator is exceeded. The two principal mechanisms that determine film break-up are depicted in figure 5.9.



Figures 5.9A and 5.9B Reentrainment mechanisms

The first mechanism (figure 5.9A) is strongly associated with roll waves. Roll waves appear at thick films and high liquid film Reynolds numbers (see figure 5.10). This has been described extensively by Cooper et al. [1985], Wallis et al. [1964], Hewitt and Hall-Taylor [1970], Ishii and Grolmes [1975]. Surface tension and hydrodynamic forces determine the shape and movement of a roll wave. Under certain conditions an extreme deformation of the top of the wave leads to the formation of numerous small drops.

The second mechanism is not often encountered and is usually referred to as "wave under cut". It can take place without the occurrence of roll waves. At a certain gas and liquid velocity the gas starts to cut under the wave; the wave starts to bulge and can eventually burst by the high pressure inside the half closed bubble (figure 5.9B). Droplets formed this way can be projected at high radial velocities.

Wave under cut is described by Hewitt and Hall-Taylor [1970] and Ishii and Grolmes [1975]. It takes place only at low liquid film Reynolds numbers.

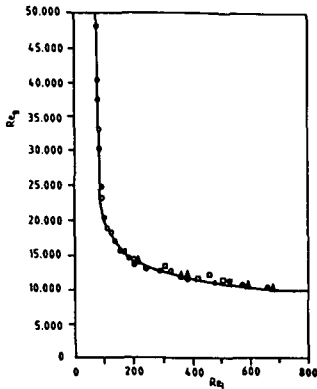


Fig. 5.10 Occurrence of roll waves
(Andreussi 1985))

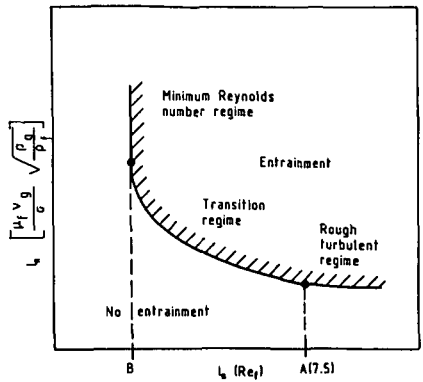


Fig. 5.11 Occurrence of reentrainment
(Ishii (1975))

5.4.2 Initiation criteria of reentrainment

The previous section made clear that the flow regime of the two-phase mixture has a strong influence on the onset of reentrainment. Figure 5.11 shows this effect. In this figure roughly three different regimes can be discerned:

1. Minimum Reynolds number regime; which represents the minimal liquid film Reynolds number under which no reentrainment will occur, irrespective of gas velocity;
2. Rough turbulent regime; to which a certain gas velocity is attached above which reentrainment of a liquid film will take place (irrespective of its Reynolds number);
3. A transition regime; which connects the two areas described above.

Regimes 1 and 2 are, within certain limits, independent (Ishii [1975]) of the direction of the gravity force (i.e. are identical for horizontal and vertical up- or down flow). Regime 3 on the other hand shows to be distinctly influenced by the direction of flow, and separate correlations have been developed to describe this effect on the reentrainment phenomena. For two-phase mixtures in cocurrent flow the transition regime starts at a certain minimum film Reynolds number ($Re_{1 \min}$). Rough turbulent regime starts from $Re_1 > 1500-1750$.

From literature it appeared that the experimental work of the different authors shows a large variability, as the inception criteria have not always been identical. As some authors have misunderstood the different reentrainment regimes, unjustified linearizations of sets of data have been carried out. Most of the correlations published before 1972 were purely empirical and, because of the reasons described above, not always very consistent.

Correlations that have been considered for use in the MOD2 framework, but will not be described in full in this section, are those of:

1. Zhivaikin [1962];
2. Chien and Ibele [1960];
3. Van Rossum [1959];
4. Wallis and Steen [1964].

These correlations were not dimensionless and general applicability is questionable.

Kutateladze [1972] proposes a correlation that depends on the gravity force direction for the full range Re_1 (see figure 5.13):

$$v_{gmax} = C \frac{\sigma}{\mu_L} \sqrt{\frac{\rho_1}{\rho_g}} N_\mu Re_1^{-1/3} \quad (5.14)$$

$C = 36$ horizontal

$C = 54$ vertical up

$$N_\mu \text{ (viscosity number)} = \frac{\mu_1}{(\rho_1 \sigma \sqrt{\frac{\sigma}{g \Delta \rho}})^{1/2}} \quad (5.15)$$

Ishii and Grolmes [1975] extended the range of applicability of the criterion formulated by Kutateladze. They derived for the minimum film Reynolds number under which no reentrainment can take place:

$$Re_{1 \min} = 155 \left(\frac{\rho_1}{\rho_g} \right)^{0.75} \left(\frac{\mu_g}{\mu_1} \right)^{1.5} \quad (5.16)$$

Up to $Re_1 = 2$ (for vertical down) or $Re_1 = 160$ (for vertical up and horizontal cocurrent flows) they derived the following reentrainment criterion:

$$\frac{v_{gmax}}{\sigma} \frac{\mu_1}{\rho_1} \sqrt{\frac{\rho_g}{\rho_1}} = 1.5 Re_1^{-1/2} \quad (5.17)$$

It is based on the reentrainment mechanisms of wave under cut (figure 5.9B). Above these film Reynolds numbers the other reentrainment mechanism takes over (see figure 5.9A). Now the crests of roll waves are sheared off. For film Reynolds numbers between 2 respectively 160 $< Re_1 < 1625$ (transition regime) Ishii and Grolmes [1975] derived the following criterion (see figure 5.13):

$$\begin{aligned} \frac{v_{gmax}}{\sigma} \frac{\mu_1}{\rho_1} \sqrt{\frac{\rho_g}{\rho_1}} = C; \quad C &= 11.78 N_\mu^{0.8} \quad \text{for } N_\mu < 1/15 \\ C &= 1.35 Re_1^{-1/3} \quad \text{for } N_\mu > 1/15 \end{aligned} \quad (5.18)$$

and for the rough turbulent regime ($Re_1 > 1625$):

$$\begin{aligned} \frac{v_{gmax}}{\sigma} \frac{\mu_1}{\rho_1} \sqrt{\frac{\rho_g}{\rho_1}} = C; \quad C &= N_\mu^{0.8} \quad \text{for } N_\mu < 1/15 \\ C &= 0.115 \quad \text{for } N_\mu > 1/15 \end{aligned} \quad (5.19)$$

N_μ = viscosity number (see equation 5.15)

Andreussi [1980] derived an other expression for v_{gmax} for the transition regime which does not vary much from the correlation of Ishii and Grolmes, but the experimental values to which he fitted his correlation seem to differ from most other published measurements (figure 5.12).

In figure 5.13 most of the other mentioned correlations are compared. It has been decided to use the correlations derived by Ishii and Grolmes as a basis for further developments in later chapters of this report.

The reentrainment mechanisms described by Ishii and Andreussi depend to a large extent on the presence of roll waves. With equation 5.25 Ishii assumes explicitly that above $Re_1 = 2$ for vertical down or $Re_1 = 160$ for vertical up and horizontal cocurrent flows roll waves will occur. It is very likely that in situations with increased gravitational forces (the centrifugal systems in cyclones and vane separators) the onset of roll waves will be delayed.

The result of a short survey with respect to roll wave formation is described below.

I. According to Ishii (Hetsroni [1982]) roll wave formation is well predicted by the Kelvin-Helmholtz instability. The Kelvin-Helmholtz stability arises at the interface of two fluid layers of different densities ρ_1 and ρ_g , flowing perpendicular to the gravitational fields with superficial velocities v_1 and v_g . The stability of the system is governed by three effects:

1. gravity force;
2. surface tension force;
3. relative motion.

The latter term accounts for the effect of pressure through the Bernoulli principle.

According to Helmholtz [1868], Kelvin [1871] and Lamb [1945] the flow is stable if:

$$\frac{g (\rho_1 - \rho_g)}{k (\rho_1 + \rho_g)} + \frac{\sigma k}{\rho_1 + \rho_g} > \rho_1 \cdot \rho_g \left(\frac{v_g - v_1}{\rho_1 + \rho_g} \right)^2 \quad (5.20)$$

in which: g = the gravitational acceleration

k = the wave number (m^{-1})

σ = surface tension

II. On the basis of the linear stability theory set up by Hershman and Hanratty [1961] to describe the initiation of roll waves, Andreussi [1985] developed a model for this purpose that shows excellent agreement with several collections of experimental data (see figure 5.10).

This model accounts for the most important physical two phase-parameters (ρ_g , ρ_1 , μ_1 , μ_g and flow rates), but does not describe the influence of increased gravitational forces on the stability of the liquid film.

The theory of Andreussi shows that at liquid film Reynolds numbers $Re_f > 200-300$ the critical gas Reynolds number above which roll waves will occur is independent of the physical properties mentioned above.

The most important forces that determine the stability of the film under these conditions are on one hand the gravitation forces; on the other hand the wave induced pressure variations that are directly proportional to the interfacial shear stress; $\tau_i = f_{gi} \frac{1}{2} \rho_g (v_g - v_l)^2$.

Each of the two theories described above assumes a relation of the following form between the stability criteria of a situation with and without increased gravitation:

$$\frac{(v_g - v_l)_{\text{increased gravitation}}}{(v_g - v_l)_{\text{normal gravitation}}} = \sqrt{\frac{2w_1^2}{gD}}$$

It is assumed that:

1. the stabilizing force of the surface tension can be neglected in case of roll waves induced by the Kelvin Helmholtz instability;
2. f_{gi} is constant in case of the second theory (see figure 5.7).

With this information the increased stability of the liquid film in cyclones can be quantified with respect to the necessary increase of the gas velocity to initiate roll waves. If for instance the liquid film rotates with a tangential velocity of $w_1 = 1.5$ m/s in a cyclone with $D = 0.05$ m, the differential velocity between the phases can be 3 times higher than in non centrifugal systems before roll waves occur.

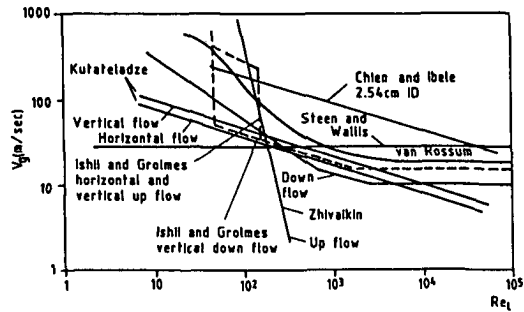
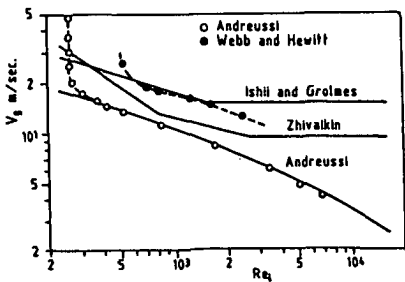


Figure 5.12 Reentrainment correlation of Andreussi (1980) Figure 5.13 Comparison of other reentrainment correlations

5.4.3 The rate of reentrainment

To this subject the same remarks apply as to the inception of entrainment. Many empirical correlations exist and many experiments have been carried out under different conditions. However, in this case no overlapping, general, physically based theory has yet been developed.

Correlations proposed by:

1. Wicks and Dukler [1960];
2. Paleev and Filippovich [1966];
3. Dallman and Hanratty [1979];
4. Ishii and Mishima [1981]

have been considered for use in MOD2 models, but are rejected because of their empirical nature (impossibility to account for higher g-forces) or basic assumptions. For instance, often the equilibrium is modelled between reentrained droplets and those redeposited by turbulence. However, in all cases under investigation the redeposition will be much stronger.

Whalley and Hutchinson [1974] proposed an annular flow model that accounts for both the processes of reentrainment and deposition. The difference of these forms the net fraction of reentrainment.

Although the model underpredicts the actual rate it gives correct trends. Whalley and Hewitt [1978] and Tattersson [1975] suggested improvements and variations of above model. The general form of this correlation (after the last modifications of Tattersson and Whalley is:

$$R_E = (u_g^* \cdot \rho_g^{0.5} \cdot \rho_l^{0.5} \cdot C_1 \left[\frac{\tau_i k}{\sigma} \right]^{C_2} \quad (5.21)$$

in which: $u_g^* = \sqrt{\frac{\tau_i}{\rho_g}}$ (friction velocity)
 k = height of instabilities on film
 C_1, C_2 = dimensionless constants
 R_E = reentrainment rate ($\text{kg/m}^2\text{s}$)

In figure 5.14 a comparison of experimental data and the predictions of some correlations is given.

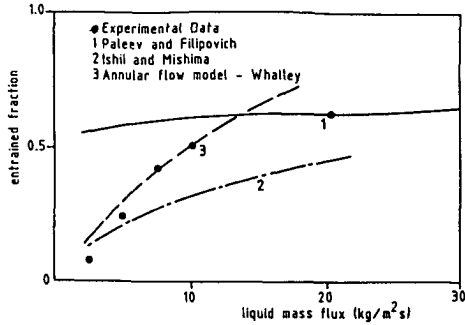


Figure 5.14 Comparison of correlations of reentrainment rate

For the circumstances that occur in a cyclone or vane separator, i.e. a horizontal flow under higher gravitational accelerations, only little information can be derived from the present correlations. Provisions should be made to account for the higher shear stresses in the film. In principle the approach of Whalley et al. [1974] offers this possibility. Therefore, this model is recommended for application in the MOD2 framework to describe reentrainment rates.

5.4.4 Droplet size distribution of reentrainment

Tatterson [1975] conducted experiments under atmospheric conditions with air and several liquids. He proved that the average drop size varied from 15 μm to 70 μm . The average drop size grew with an increase of gas velocity and with a decrease of surface tension. Tatterson found good agreement between a correlation of the following form and his experimental data:

$$d_{s,0} = C_1 D \left(\frac{R_E}{\rho_g u_g^2 D} \right)^{1/2} \left(\frac{D u_g \rho_g}{\eta_g} \right)^{C_2} \quad (5.22)$$

in which R_E is the rate of reentrainment in $\text{kg/m}^2\text{s}$.

Ishii [1975] proposed the following correlation:

$$d_{vm} = 9.9 \cdot 10^{-3} \left(\frac{\sigma}{\rho_g u_g^2} \right) \text{Re}_1^{2/3} \left(\frac{\rho_g}{\rho_1} \right)^{-1/3} \left(\frac{\eta_g}{\eta_1} \right)^{2/3} \quad (5.23)$$

Ishii assumed a symmetrical log-normal distribution in which d_{vm} is the median volume diameter.

Andreussi and Azzopardi [1983] found that the following correlation fitted the measured Sauter diameters ($\bar{d}_{3,2} = \sqrt{\frac{\sum(d^3 \cdot n)}{\sum(d^2 \cdot n)}}$)

$$\bar{d}_{3,2} = 1.91 D \frac{Re_g^{0.1}}{We_f^{0.6}} \left(\frac{\rho_g}{\rho_l}\right)^{0.6} + 0.4 \left(\frac{R_E}{v_g \rho_l}\right) \quad (5.24)$$

in which R_E = mass flow of reentrainment per unit area.

All mentioned correlations are derived on a purely empirical base and, therefore, not consistent. It is recommended to check these correlations with own representative experimental data. This way a suitable correlation can be derived to be fitted in the MOD2 framework.

5.4.5 Direction of and initial velocity of reentrained droplets

From the experimental investigations conducted by James et al. [1980], it appeared that reentrained droplets that were sheared of the crests of roll waves moved radially away from the film. These measurements concerned essentially droplets larger than 250 μm . Andreussi and Azzopardi [1983] discovered that the initial velocity and direction of the droplets are independent of the droplet diameter:

$$v_{radial} = 12 \left(\frac{\rho_g}{\rho_l}\right)^{1/2} u_g^* \quad (5.25)$$

in which u^* (friction velocity) = $\left(\frac{\tau_i}{\rho_g}\right)^{1/2}$

The initial axial droplet velocity is taken equal to the film velocity.

Again these empirical equations are in the first place set up for non-rotating flows.

5.5 Characterization of swirl elements and swirling flows

5.5.1 Introductory remarks

In the following two subsections attention is respectively paid to:

- a. a number of references in literature to the (experimental) characterization of swirling flows;
 - b. a procedure to characterize swirl elements in order to judge them on suitability for different applications.
- a. and b. will be used both in the process of building up and validating block AC-MOD1 and RFC-MOD1.

With some complementary experiments, reported in AC-EXP1, the outcome of b. assists in the selection of swirl elements for specific unconventional axial cyclones (chapter 8).

5.5.2 Examples of rotating flow fields

In appendix B representative examples of three different sorts of swirling flows are described:

- a. in a smooth pipe (Loxham [1976]);
- b. in an axial cyclone (Stenhouse [1979]);
- c. in a reverse flow cyclone (Mothes [1982]).

The swirling flow reported under a. is necessary to validate the assumptions on which the more complete models are based. These models are verified with the gas flow fields collected under b. and c.

5.5.3 Characterization of swirl elements and swirling flows

From section 3.4.4 it appeared that a number of possibilities exist to induce the swirling flow necessary for cyclone operation. In this section the literature concerning some representative swirl inducing devices is investigated for references to important characteristics. Missing data are supplemented from own experiments, reported in chapter 6.

Attention will be paid to the following swirler properties:

1. Form of the induced flow field (tangential and axial velocity profiles and swirl number);
2. Pressure drop across swirler;
3. Hydraulic efficiency of swirler;
4. Constructional aspects.

First the above mentioned swirler characteristics are explained shortly, then the different swirlers are described and judged.

Explanation of swirler characteristics

ad 1. Form of the induced flow field

The most important properties of a swirling flow are the magnitude of its velocity components in axial, tangential and radial direction at different radial cross sections. The former two components can to a great extent depend directly on the geometry of the swirler. These velocity components are of great influence on the separation characteristics of the cyclone: the tangential component determines the driving force of the separation; the axial component the residence time of the two-phase flow in the cyclone. The other component, the radial velocity, is in most cases determined by other geometric factors and relatively small, but it can be as important as the former components. Generally, its direction opposes the successful separation of a particle.

A useful parameter that has been introduced to facilitate the characterization of a swirling flow is the swirl number (S). The most popular definition of the swirl number describes this parameter as the ratio of the flux of angular momentum (M_θ) and the product of the flux of axial momentum (M_z) and the radius (R_0) of the flow.

$$M_\theta = \int_0^{R_0} \rho (u w + \langle u'w' \rangle) r 2\pi r dr \quad (5.26)$$

$$M_z = \int_0^{R_0} (\rho (u^2 + \langle u'^2 \rangle + (P - P_0))) 2\pi r dr \quad (5.27)$$

in which: $\langle u'w' \rangle$ and $\rho \langle u'^2 \rangle$ are the turbulent shear stresses
 $(P - P_0)$ is the axial pressure difference

$$S = \frac{M_{\theta}}{M_z R_o} \quad (5.28)$$

Loxham [1976] shows that S can be quantified by the following approximation (neglection of turbulent shear stresses and pressure contribution):

$$S = 2 \int_0^1 \bar{w} \bar{u} \bar{r}^2 d\bar{r} \quad (5.29)$$

in which: \bar{u} represents the dimensionless axial velocity ($= \frac{u}{V}$)
 \bar{w} represents the dimensionless tangential velocity ($= \frac{w}{V}$)
 \bar{r} represents the dimensionless radius ($= \frac{r}{R_o}$)

u, w and r are the actual time averaged values of above quantities

V represents the superficial gas velocity

Often a relation is assumed between vortex form and swirl number for a fully developed flow (Reydon et al. [1981], Loxham [1976]). This implies that for a certain swirl number of the flow its flow field is fixed, which will prove particularly useful when modelling results are evaluated (see chapter 7). Generally, the outer part of such a (combined or Rankine) vortex is of a free vortex type; the inner part of a forced vortex type (solid body rotation). Both vortex types are explained below.

- In a pure free vortex the tangential velocity is defined as follows:

$$w_r = w_{R_o} \cdot \frac{R_o}{r} \quad (5.30)$$

in which: w_r = tangential velocity at radius r

w_{R_o} = tangential velocity at the wall.

- In a pure forced vortex the tangential velocity is defined as follows:

$$w_r = w_{R_o} \cdot \frac{r}{R_o} \quad (5.31)$$

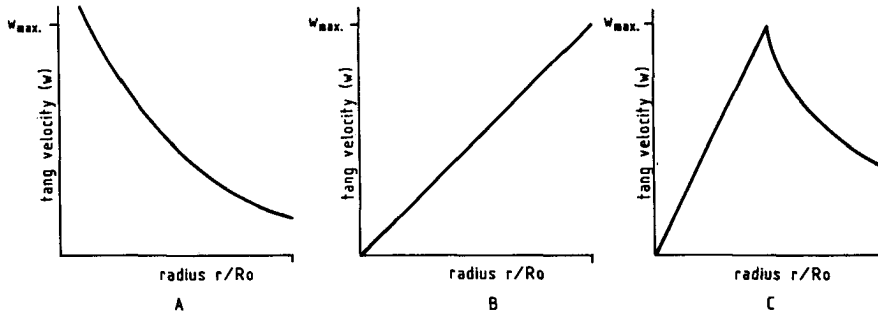
- In a combined vortex the part of the tangential velocity profile that connects the two above vortex forms is described as follows:

$$w_r = c \cdot r \cdot \exp(-\lambda r) \quad (5.32)$$

in which: c and λ are constants.

Figures 5.15A, B and C give examples of the free, forced and combined (or Rankine) vortices.

The maximum height, and the radius at which the tangential velocity reaches this maximum is considered as an important characteristic of an induced swirling flow.



Figures 5.15A, 5.15B and 5.15C Various vortex forms

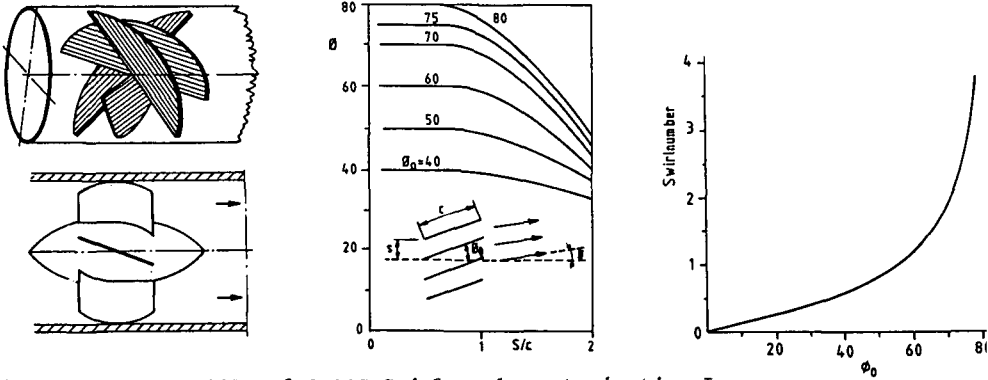
In literature practical relationships were encountered to predict the gas flow field of four of the five swirl inducing devices that are considered in AC-EXP1 (see A, B, C1, C2, D1 and D2 in figure 6.9).

In the relations to describe swirl elements the following variables are used:

- R = radius of swirl element
- R_b = radius of vane blade curvature
- R_i = radius of buff body of swirl element
- c = (projected) length of vane blades
- t = thickness of vane blades
- s = distance between vane blades
- n = number of vane blades
- ϕ = swirl angle of gas flow field
- ϕ_o = vane angle

The initial flow field and corresponding swirl number, induced by a swirl element with straight vanes (two examples are depicted in figure 5.16A), can be determined graphically with figures 5.16B and C (Fletcher [1973]).

Gupta [1984] advises to use these types of swirlers for swirl numbers smaller than $S = 0.7$, so ϕ_0 should not exceed 45° . According to this source, these swirlers become noticeably less efficient for higher swirl numbers due to flow separation around the blades. This results in increased downstream levels of turbulence and increased pressure drops.

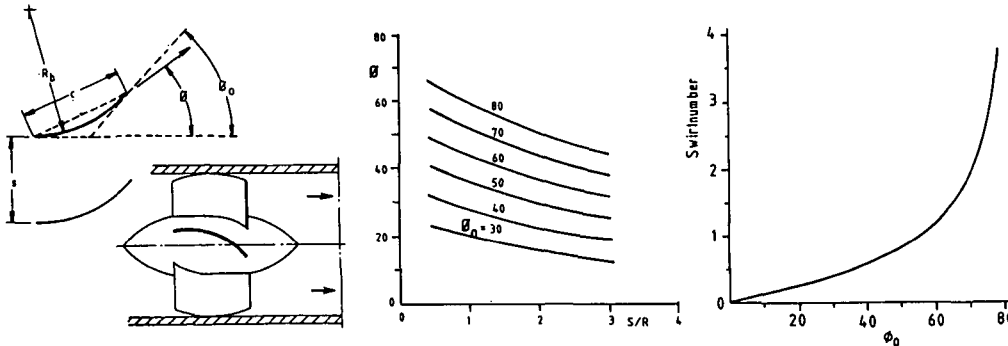


Figures 5.16A, 5.16B and 5.16C Swirler characterization I

For swirlers with constantly curved blades, as depicted in figure 5.17A, the following relation is often used to determine the induced initial flow field (swirl angle) and swirl number (Buckley et al. [1980]):

$$\phi = \phi_0 \left(1 - \frac{\sqrt{(s/R_D)}}{0.001 \phi_0 + 0.21 \sqrt{(2 \sin \phi_0 / 2)}} \right) \quad (5.33)$$

This relation is represented graphically in figure 5.17B. With figure 5.17C the swirl number can be determined.



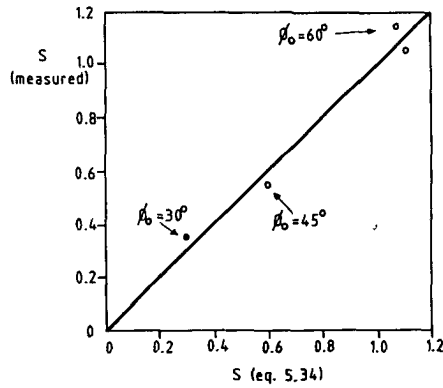
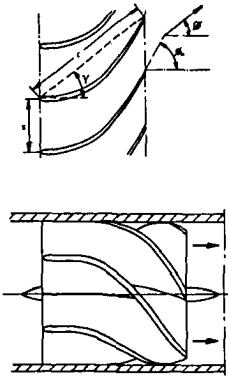
Figures 5.17A, 5.17B and 5.17C Swirler characterization II

For swirlers with variably curved blades (see figure 5.18A) Mather and McCallum [1967] proposed the following relation to describe the influence of the swirler geometry on the induced flow field:

$$S = \frac{1}{2(1 - \chi)} \cdot \frac{1 - (R_i/R)^4}{1 - (R_i/R)^2} \tan \phi_o \quad (5.34)$$

$$\text{in which: } \chi = \frac{n t}{2\pi R \cos \phi_o}$$

This relation is graphically represented in figure 5.18B in which results are shown of an experimental validation by Mather and McCallum. They advise these swirl elements to induce swirling flows of which $S > 1$ if low pressure drops are required.



Figures 5.18A and 5.18B Swirler characterization III

ad 2. Pressure drop across swirler

In some applications the separator pressure drop is an important operating characteristic. ξ_{sw} will represent the pressure drop across the swirl element. It is defined as:

$$\xi_{sw} = \frac{\Delta P_{sw}}{0.5 \rho v_s^2} \quad (5.35)$$

in which: ΔP_{sw} = the pressure drop across the swirler
 v_s = the superficial velocity

ad 3. Hydraulic efficiency of swirler

An important characteristic to compare different swirler types is the hydraulic efficiency. Only part of the pressure drop across a swirler will result in an increase of kinetic energy of the flow; the rest will be lost by friction. In other words (Leuckel [1968]):

$$\dot{E}_{kin.in} + \dot{E}_{stat.in} = \dot{E}_{kin.out} + \dot{E}_{stat.out} + \dot{E}_{loss} \quad (5.36)$$

in which: $\dot{E}_{kin.in}$ represents the total incoming flux of kinetic energy;

$$\dot{E}_{kin.in} = \int_0^R \frac{1}{2} \rho (w_{in}^2 + u_{in}^2) u_{in} 2\pi r dr \quad (5.37)$$

in which: u = the local axial velocity

w = the local tangential velocity

$\dot{E}_{kin.out}$ correspondingly the outgoing kinetic energy flux

$\dot{E}_{stat.in}$ represents the total incoming static pressure energy flux and is quantified as follows:

$$\dot{E}_{stat.in} = \int_0^R P_{stat.in} u_{in} 2\pi r dr \quad (5.38)$$

$\dot{E}_{stat.out}$ correspondingly the outgoing static pressure energy flux

\dot{E}_{loss} flux of loss energy

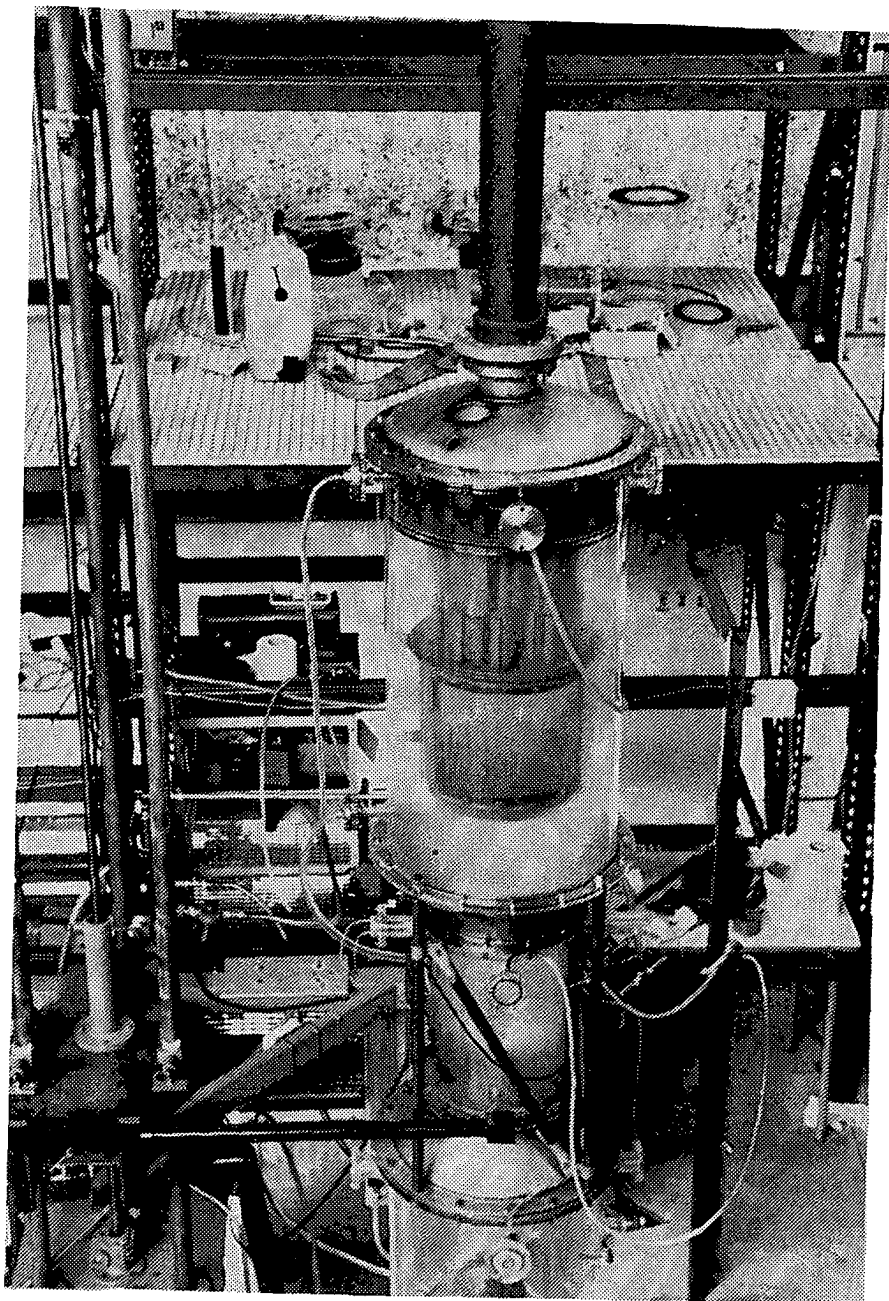
The hydraulic efficiency, ϵ_h , can be defined as follows:

$$\epsilon_h = \frac{\dot{E}_{tot.in}}{\dot{E}_{tot.in} - \dot{E}_{loss}} \quad (5.39)$$

Except for the consequences for the pressure drop one should bear in mind that the dissipated energy that accompanies a low ϵ_h will lead to turbulence which can seriously distort the flow field or cause dispersion of droplets.

ad 4. Constructional aspects

One of the characteristics a cyclone will be judged on is its economic feasibility: it should preferably be possible to take the swirler in mass-production without high costs. Another aspect is the behaviour under fouling operation: the swirler should preferably have no narrow passages that will easily plug.



6. TEST FACILITIES AND EXPERIMENTAL RESULTS

For project structure and nomenclature see innerside of front cover.

6.1 Structure of chapter

In this chapter the results of the EXP-blocks of the project structure are presented. In paragraph 6.2 the different test-rigs used for the experiments are described. In paragraph 6.3 three subparagraphs are devoted to each of the three separator types under investigation. In these subparagraphs all experiments relevant to the separator type in question are reported.

In case of experiments that result in vast collections of numeric data references are made to corresponding appendices.

At the beginning of the description of each EXP block a short overview is given of the purpose(s) of the experiments, the conditions under which they have been carried out, and, if applicable, where in the appendices the results can be found.

6.2 Test facilities

6.2.1 Introduction

In the collection of experiments, necessary to produce the results specified by the EXP blocks, three groups can be discerned which each set specific demands to the test facility:

1. Easy optical and physical accessibility of the equipment to be tested (EXP1).
2. Reproduction of practical operating conditions as reliable as possible (EXP2,3) for a basic separation unit.
3. Reproduction of actual operation scale as reliable as possible (EXP4,5).

Unfortunately, it appeared not economical or practically feasible to combine these, sometimes conflicting, demands in one test-rig. Therefore, it was decided to build three test-rigs; each an exponent of each of the three

above mentioned properties. There is one exception: it proved financially not feasible to design a large scale test-rig that could function under high pressure. Therefore, EXP5 has been split up in two parts: the large scale investigations are done on a large atmospheric test-rig and will be extrapolated according to the results of specific experiments on a smaller scaled test-rig that operates under actual operating conditions.

For each EXP-block specific modifications to the test sections appeared to be necessary, which demanded a flexible design of the test-rigs.

In the following three subparagraphs a short characterization is given of the framework of the three adjustable test-rigs.

It consists of a description of:

- I) the research purposes;
- II) the general form and range of experimental conditions;
- III) the measurement and control sections.

6.2.2 Test-rig 1 (block EXP1, EXP2)

Research purposes

In the first place this test-rig has been designed for the many gas flow field determinations that have to be carried out in EXP1. These velocity measurements serve either for defining starting conditions for the models to be set up in MOD1 or for validating predictions from these models.

A second application of this test-rig has been found in the observation of the interaction between the liquid film (formed in the separation units) and the main gas stream. These experiments resort under EXP2.

Description of test-rig 1 and range of experimental conditions

The central part of the test-rig is the section that is intended for the velocity measurements. This central measuring section is designed as such that an unperturbed gas flow is offered to the separator, which can easily be replaced or modified. Experiments have been carried out only with atmospheric air and water. Variation of the gas density is not possible, and with respect to the EXP1 experiments not necessary.

In this test-rig velocity flow fields have been measured mainly in axial and reverse flow cyclones of 50 mm ϕ .

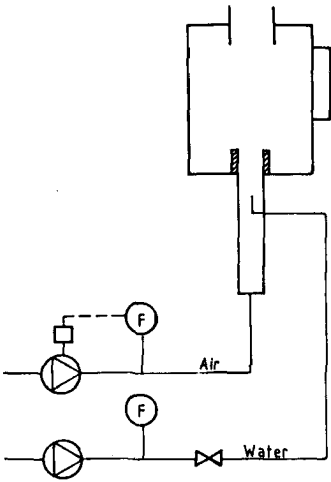


Figure 6.1 Flowsheet of test-rig 1

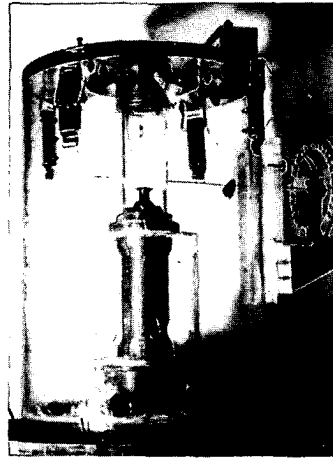


Figure 6.2 Test-rig 1

| | |
|--|----------------------------|
| Range of experimental conditions: air flow | 0 - 75 m ³ /hr |
| : maximal pressure drop | 100 mbar |
| : water flow | 0 - 0.1 m ³ /hr |
| : d _{s,0} | ~ 25 μm |

Measurement and control sections of test-rig 1

Gas and liquid flow are measured by ordinary Rotameters; pressure drops (except for the pitot tube) by water filled U-tube manometers. Therefore, all operating conditions have to be controlled and adjusted manually. This does not cause any delay, because the measurement of the gas flow field in the separation unit demands much more time. The gas velocities have been measured with a pitot tube of 1 mm ϕ connected to a Setra 0-14 mbar pressure transducer.

The pitot tube velocity measurement was preferred to Laser Doppler Velocimetry (LDV) because of its relatively simple way of operation, its versatility and relative insensibility to flaws in the experimental set-up. Moreover, it was assumed that if highly swirling flows were investigated the seeding particles, necessary for LDV operation, might be distinctly influenced by inertial forces. More thorough investigation of the availability of small seeding particles and dispergating mechanisms is necessary before a definite conclusion can be drawn with respect to instrumentation for the follow-up of this work.

Two large disadvantages of pitot tube velocity measurements are:

- 1) the presence of the pitot tube in the gas flow influences the gas flow;
- 2) the pitot tube is not able to measure turbulence spectra.

The first disadvantage has been minimized by designing a pitot tube with a much smaller diameter than that of the measured objects ($< 2\%$).

6.2.3 Test-rig 2 (block EXP2, EXP3, EXP5)

Research purposes

This test-rig has been designed to carry out the experiments:

1. (of EXP2) that characterize the behaviour of the liquid phase. The identification of the physical phenomena provides in the first place starting conditions to the models of block MOD2. Moreover, with these experimental results the predictions of these models can be validated.
2. (of EXP3) that characterize the behaviour of the basic separation unit (one cyclone or set of vane blades) under the same operating conditions as in practice. With these results the MOD3 models can be validated.

In one experiment the test-rig will be used to contribute to block RFC-EXP5.

Description of test-rig 2 and range of experimental conditions

The central section of this test-rig is formed by a vessel that contains a basic separation unit of which the operating conditions can be carefully controlled and adjusted. The operating characteristics of the separation unit can be monitored accurately as well.

Because many different separation units needed to be tested in different ways, the test-rig is designed in such a way that the central measuring section can easily be modified or interchanged for another vessel to ensure optimal accommodation of the separation unit.

The flowsheet of the test-rig (figure 6.3) basically consists of a closed gas- and liquid-loop. The liquid is sprayed in the gas just in front of the measuring vessel. The mist is separated partly by the separation unit and partly by a mist stripping vessel (containing filter cartridges) further downstream. The latter device extracts the liquid that has passed through the separation unit.

Other important parts of the gas loop are:

1. A roots blower as driving force of the gas stream. One of the requirements of the test-rig is the possibility of pressurization in order to achieve higher gas densities. It appeared to be difficult to find a roots blower that could withstand internal pressures higher than 5 bar. After some fruitless experiments with special shaft seals it was decided to place a conventional unit inside a pressurized vessel. This necessitated a special heat exchanger to remove the dissipated energy of the blower engine from the recirculating gas stream.
2. A heat exchanger to regulate the gas temperature (see 1.).
3. Control equipment to regulate the gas flows through the measuring vessel and the heat exchanger.

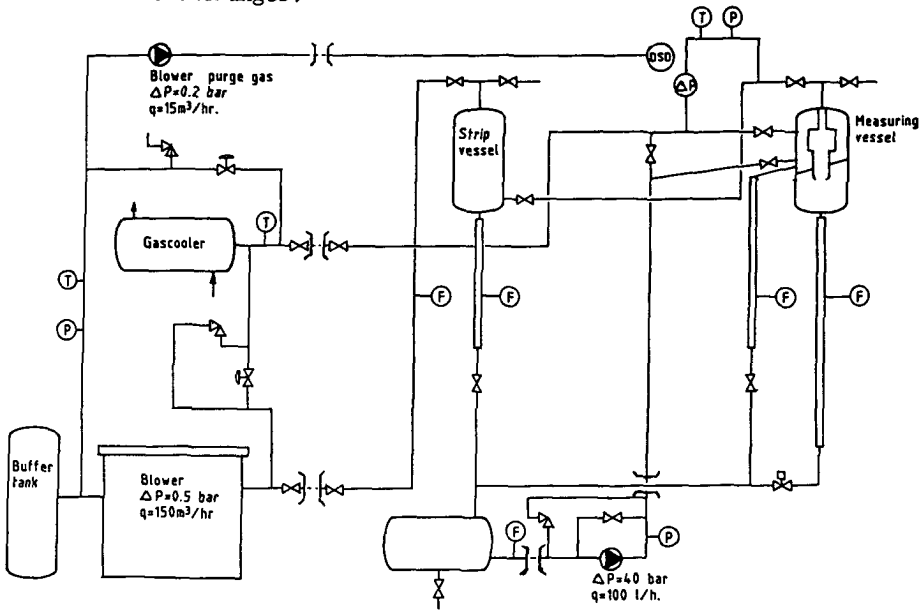


Figure 6.3 Flowsheet of test-rig 2

To achieve the same gas density as reported in section 5.2 it has been decided to fill the test-rig at medium pressures with a heavy gas. The most economical and practical gas appeared to be SF_6 (sulfur hexafluoride) with a density of 6.5 kg/m^3 and a vapour pressure of over 40 bars at room temperature. Gas densities of over 60 kg/m^3 are possible at an operating pressure of 10 bar, for which pressure the test-rig has been designed.

To be able to transport the test-rig to even bulkier equipment it has been built on two more or less mobile carriages. (In an early stage of the project it was considered to use measurement equipment consisting of a set of rigidly fixed large pulse-lasers to create holographic images of disperse phase systems.) One carriage contains all the driven, and thus vibration generating, equipment. The other contains the measuring vessel and equipment necessary to characterize the separation unit. The carriages are connected with 5 m long flexible hose pipes (see figures 6.4 and 6.5).



*Figure 6.4 Driven equipment of
test-rig 2*

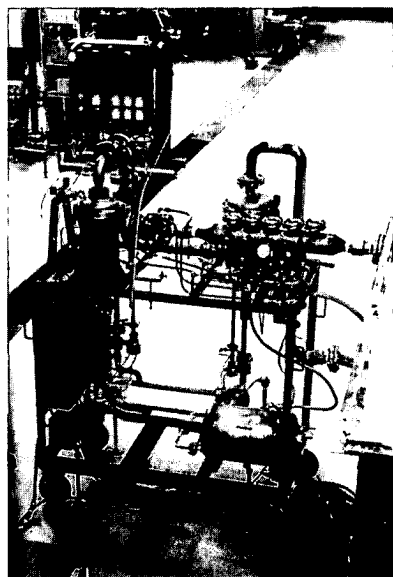


*Figure 6.5 Measuring section of
test-rig 2*

The experimental conditions that can be varied and the range over which this is possible are listed below:

| | |
|--|-----------------------------|
| gas flow | 20 - 120 m ³ /hr |
| maximal pressure | 10 bar |
| gas density | 1.3 - 60 kg/m ³ |
| maximal allowable pressure drop across separator | 1 bar |
| liquid flow | 1 - 0.04 l/hr |
| droplet size distribution, d ₅₀ | 10 - 100 μm |

As shown by the relations in section 5.2, in practice the droplet size distribution will most often lie above $5\text{ }\mu\text{m}$. The d_{50} of the mist can be adjusted either by varying the ratio between flow rate and pressure drop across a spray nozzle, or by using differently sized nozzles.

Almost any liquid can be used in this test-rig to vary physical properties. The physical properties of the used liquids are given in appendix C, page C.1.

Measurement and control sections of test-rig 2

To characterize a separator the separation efficiency and pressure drop have to be determined as a function of the following operating conditions:

1. gas flow;
2. gas density;
3. liquid loading of gas;
4. physical properties of liquid;
5. drop size distribution of mist.

It is quite simple to monitor real time the separation efficiency and pressure drop of the separator and at the same time the first three mentioned variables. A software driven data collection/process control unit has been used that monitored the process and adjusted the experimental key conditions automatically. The flow meters and pressure transducers could be coupled directly to the data collection device.

It proved to be more difficult to automatize the measurement of drop size distributions of the mist. A measurement technique has been used that derived the particle size distribution of a dispersion by interpreting its diffraction pattern, described by for instance Felton et al. [1985]. The practical embodiment of this measuring principle was formed by a Malvern 2600D apparatus that has been put at the disposal of this project against a reduced rate.

Each measurement had to be preceded by careful preparation and required much manual labour (especially the cleaning and aligning of the glasses through which the measurements were carried out). Therefore, the determination of droplet size distributions took place in special sessions, while the routine characterizations were carried out unattendedly.

6.2.4 Test-rig 3 (EXP2, EXP4, EXP5)

Research purposes

The experiments on this test-rig contributed to the following objectives:

1. (of EXP4) the identification of the physical phenomena that accompany the scaling up of a basic separation unit to a real scale separator (EXP4);
2. (of EXP4) the validation of the predictions of the models (MOD4) that specifically describe these effects;
3. (of EXP5) the formation of an extensive database for which several sorts of separators have to be characterized under varying (atmospherical) conditions in order to validate the atmospherical part of the (MOD5) models.

Because test-rig 2 was constantly in use for cyclone experiments, test-rig 3 has also been used for some experiments of the V-EXP2 block .

Description of test-rig 3 and range of experimental conditions

This test-rig is very similar to test-rig 2, except for two important differences: it is twenty times larger and it can not be pressurized.

The central section of this test-rig is a vertically orientated vessel, size and shape adjustable, in which the separator unit can be accommodated optimally. In figure 6.6 three different configurations of the measuring vessel are presented. To prevent periods of stand-still, necessary to change over to other configurations, the measuring section has been executed in twofold. This way, one section can be used for test runs, while the other is prepared for the next experimental session.

Also this test-rig consists of a closed, partially entwined, gas and liquid loop (see figure 6.8). The most important components of the gas loop are:

1. a demister vessel that extracts the unseparated mist from the gas flow (downstream of the measuring section);
2. a roots blower as driving force of the gas (because the test-rig can not be pressurized, special preparations like those for the blower of test-rig 2 are not necessary);
3. a heat exchanger to control the gas temperature in the closed loop;
4. control equipment to regulate the gas flows through heat exchanger and measuring section.

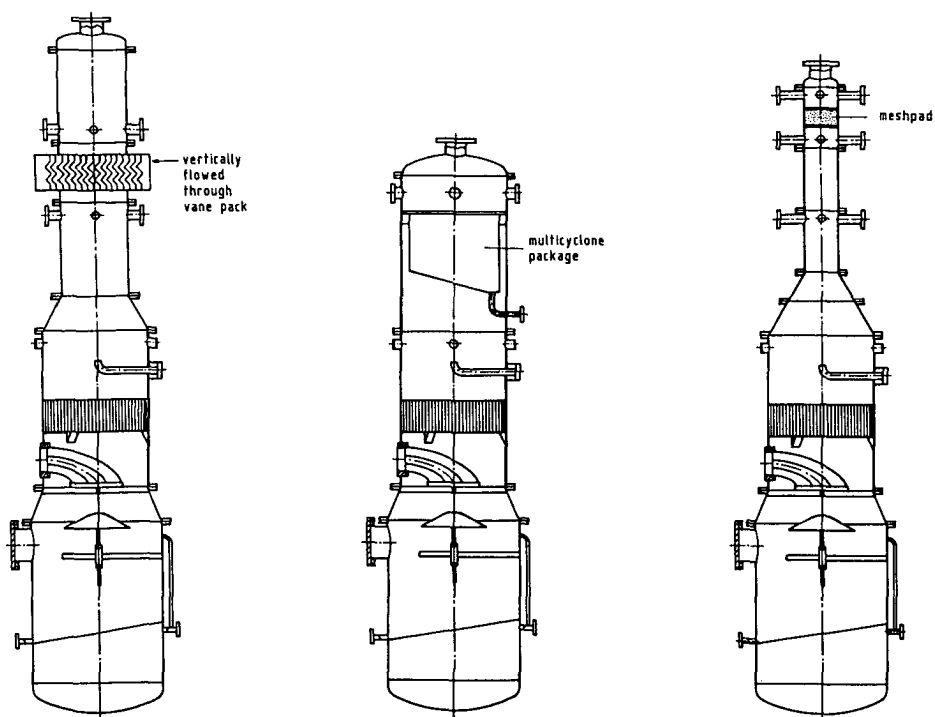


Figure 6.6 Possible test configurations of test-rig 3

The most important components of the liquid loop are:

1. the spray nozzles, of which two types were used:
 - a. Ultrasonic nozzles, in case vertically flowed through separation units were tested and fine droplet size distributions had to be achieved.
 - b. Direct impact nozzles for all other cases.

When ultrasonic nozzles were used, a separate high pressurized air flow appeared to be necessary to drive them. The air pumped in the system was bled downstream of the mist extraction vessel.

2. a high pressure (twenty stage) centrifugal pump as driving force of the liquid flow. It was chosen powerful enough to attain reasonably fine mists even when direct impact nozzles were used.

3. control equipment (valves) to regulate the liquid flow over a wide range. Although the test-rig can not be pressurized, it has been prepared to run with different gas fillings (SF_6). This way, gas densities may be raised at atmospherical, or near atmospherical conditions to approximately 10 kg/m^3 . However, no experiments have been carried out with this option yet.

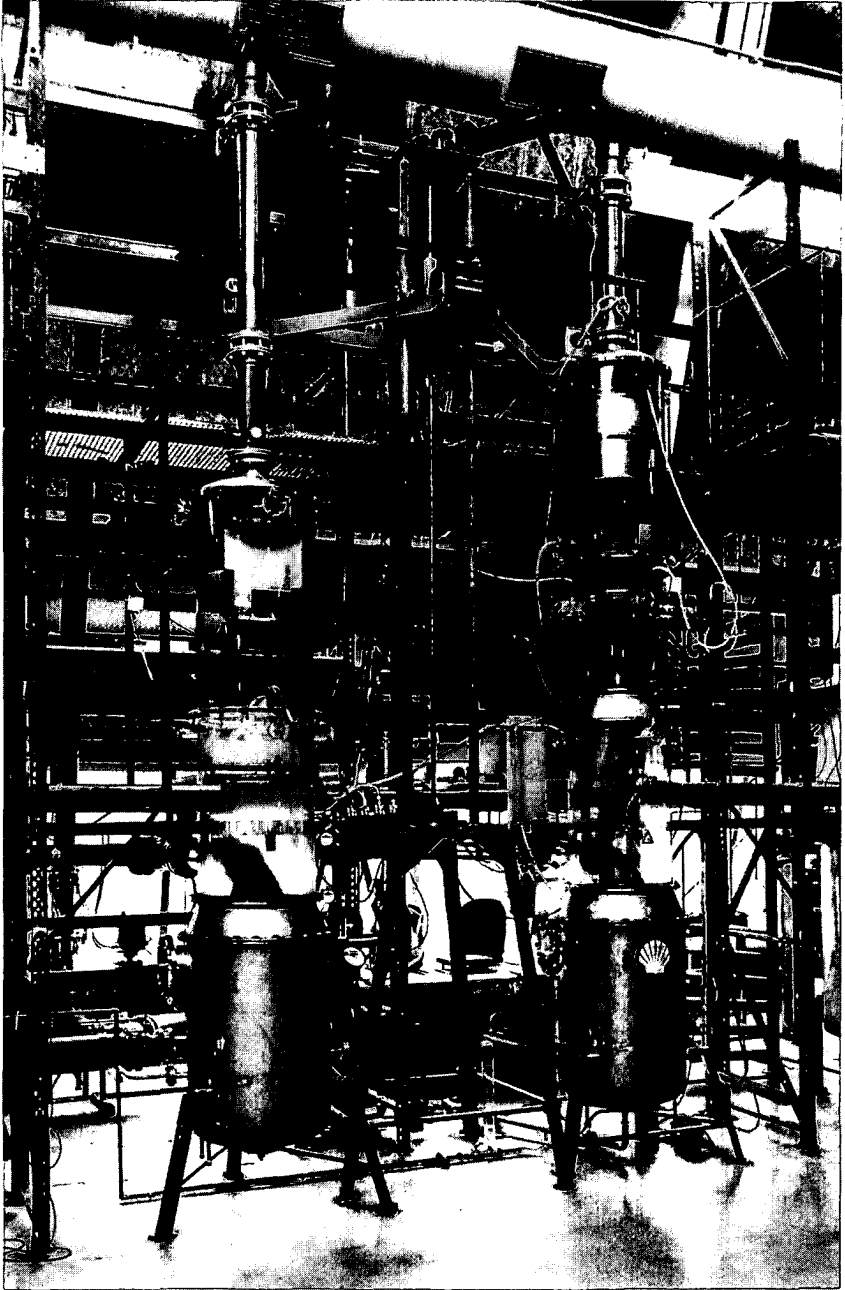


Figure 6.7 Test-rig 3

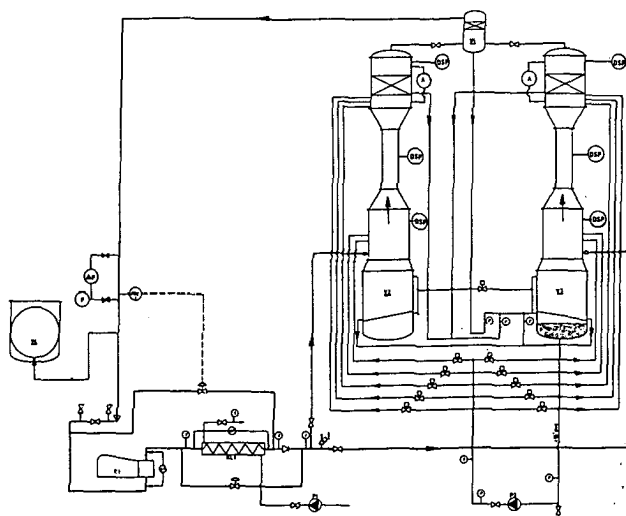


Figure 6.8 Flowsheet of test-rig 3

The experimental conditions covered by this test-rig are listed below:

| | |
|--|---------------------------------------|
| gas flow | 450 - 2400 m ³ /hr |
| maximal operating pressure | 1.5 bar |
| gas density | 1.3 - 10 kg/m ³ |
| maximal allowable pressure drop across separation unit | 500 mbar |
| liquid flow | 0.01 - 0.5 m ³ /hr |
| droplet size distribution, d_{50} | 15 μ m (ultrasonic) - 100 μ m |

To vary the liquid properties every liquid that does not affect plexiglass can be used. (The used liquids are listed in appendix C, page C.1.)

Measurement and control sections of test-rig 3

Because the operating principle of this test-rig is similar to that of test-rig 2 the measurement and control is carried out in the same way. For more information is referred to the corresponding section of test-rig 2.

During its unattended runs test-rig 3 could establish a modem connection to a remote operator for intervention. Even better than test-rig 2, this test-rig could achieve a very large number of useful running hours (one time it runned continuously over three weeks, testing four different geometries).

6.3 Experimental results

6.3.1 Axial cyclones

Block AC-EXP1

In first instance the experimental results of this block were meant for validation purposes only. The subject of validation would be the model that describes the gas flow inside an axial cyclone as a function of its geometry (MOD1). The gas flow pattern inside an axial cyclone depends on the type of swirl element. It appeared that with the literature information and software facilities at hand (see section 5.5) it was hardly possible or practical to model the influence of the geometry of a swirl element reliably. Therefore, it has been decided to carry out measurements to characterize a group of different practical swirl elements first, so that with these results can be determined which swirl element will meet the requirements that follow from the starting conditions of the rotating flow simulations (see chapter 7). The swirl elements in question are represented in figure 6.9.

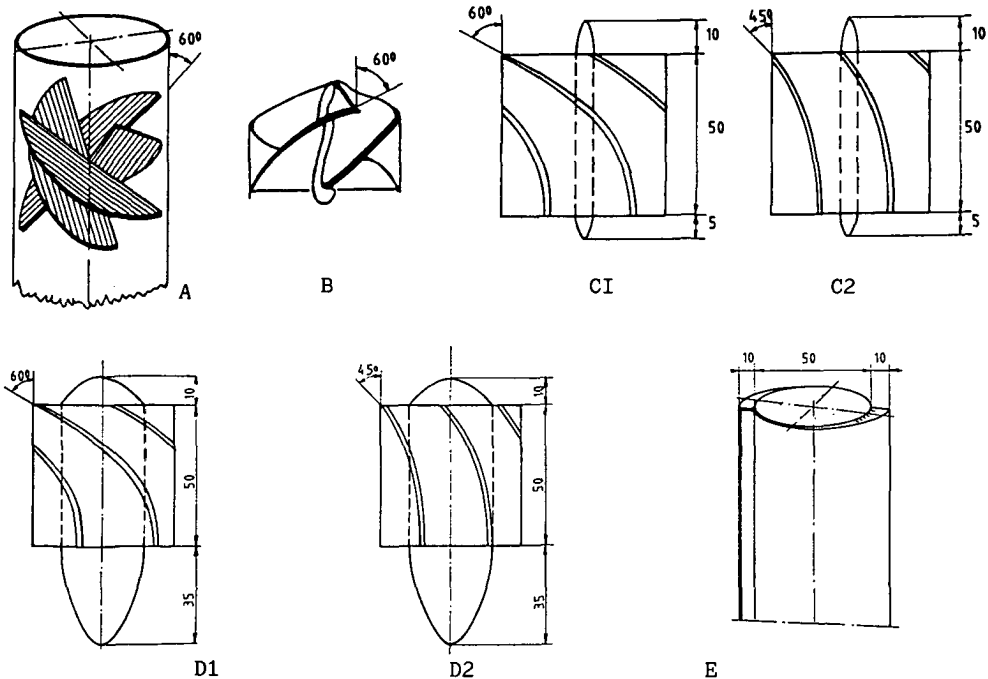


Figure 6.9 Tested swirl elements

Apart from this swirler characterization, which mainly served to provide the starting conditions of MOD1, many measurements have been carried out further downstream of the swirl elements at different locations in different types of geometries.

The main difference in test geometries lies in the liquid discharge section, which can either be coaxial or radial (for the exact description of this aspect see the corresponding paragraphs in section 3.4.4.5). Other important geometrical variations that have been characterized are the purge gas rate and the gas outlet diameter.

With these measurements the predictions of the MOD1 models were validated.

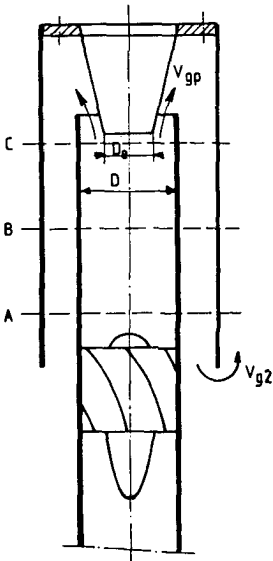


Figure 6.10A Coaxial liquid outlet

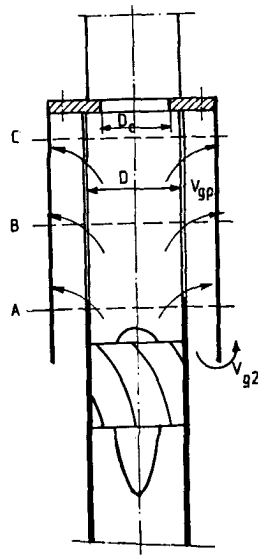


Figure 6.10B Radial liquid outlet

In figures 6.10A and B the nomenclature for each type of axial cyclone is given. The locations downstream of the swirl element at which the gas flow field has been determined, are also indicated.

In table 6.I the different swirl elements are characterized according to the structure proposed in section 5.5. The basic operating characteristics like the swirl number, hydraulic efficiency and pressure drop coefficient are given in the table. The gas flow fields downstream of the swirl element are depicted in appendix C and referred to in table 6.II.

| swirl element (figure 6.9) | swirl number, S | hydraulic efficiency, ϵ_h | pressure drop coefficient, ξ |
|-------------------------------|--------------------|---------------------------------------|-------------------------------------|
| A | 1.0 | 0.4 | 12.2 |
| B | 1.2 | 0.5 | 6.1 |
| C1 | 0.8 | 0.6 | 3.2 |
| C2 | 0.5 | 0.9 | 1.1 |
| D1 | 2.0 | 0.7 | 9.1 |
| D2 | 1.2 | 0.9 | 2.7 |
| E | 1.1 | 0.8 | 5.6 |

Table 6.I

In table 6.II the experimental conditions and specific geometrical properties of the flow field determinations for validation purposes are listed according to the nomenclature of figure 6.10. The results (gas flow field distribution) are printed in appendix C.

In this table at some locations a coaxially purging cyclone is defined with zero percent purge rate and a gas outlet diameter corresponding to the diameter of the cyclone. These measurements have been used to determine the unimpeded flow fields behind several swirl elements.

| exp. no. | type of liquid discharge | type of swirl element (figure 6.9) | diameter of gas outlet D_e/D | purge rate % | location of measurement | results in appendix C page |
|-------------|--------------------------------|--|--------------------------------------|--------------------|-------------------------------|----------------------------------|
| 1 | C | A | 1 | 0 | B | C.1 |
| 2 | C | B | 1 | 0 | B | C.1 |
| 3 | C | C1 | 1 | 0 | B | C.1 |
| 4 | C | C2 | 1 | 0 | B | C.1 |
| 5 | C | D1 | 1 | 0 | B | C.2 |
| 6 | C | D2 | 1 | 0 | B | C.2 |
| 7 | C | E | 1 | 0 | A | C.2 |
| 8 | C | C1 | 0.5 | 10 | A,B,C | C.2 |
| 9 | C | C2 | 0.5 | 15 | A,B,C | C.2,C.3 |
| 10 | R | C1 | 0.5 | 15 | A,B,C | C.3 |
| 11 | R | D1 | 0.6 | 10-15 | B,C | C.3 |

Table 6.II

Block AC-EXP2

The results of this block provide starting conditions and means of validation to model the liquid phase. Because the most important internal phenomena are similar for reverse flow and axial cyclones and because the necessary experiments have been carried out extensively for reverse flow cyclones, it is referred to these experiments (RFC-EXP2) to determine:

1. the measure of wetting of the internal surface of the cyclone as a function of liquid load and liquid physical properties, gas load and - density and centrifugal acceleration;
2. the film regime as a function of the same variables;
3. the inception point of reentrainment as a function of the same variables.

The experiments, specifically carried out for axial cyclones, that resorted under this block were very practical and qualitative. The major part took place on test-rig 1 and concerned the preliminary investigations into the influences of several geometrical variations with respect to the liquid outlet (see figures 6.10A and B). All experiments were carried out with atmospheric air/water mixtures. They were performed in the first place to come to a more or less representative design for a cyclone with a radial liquid discharge. However, a limiting phenomenon inside the coaxially discharging cyclone has been identified as well. At high liquid loadings the interfacial friction in the discharge section is not high enough to carry all the liquid out of the cyclone. Heavy reentrainment might be caused just underneath the vortex finder (see figure 6.11A).

Starting from the values for L/D and D_e/D , recommended by Stenhouse [1984] (see section 3.4.4.5) for a cyclone with a coaxial liquid discharge, a preliminary design for a radially purging cyclone has been developed. This cyclone is tested thoroughly in block AC-EXP3 as a representative of the axial cyclone type with radial liquid discharge. The influences of the following geometrical variables were investigated:

1. number of slits across the circumference of the tube;
2. height of the slits (as such that the distance between the swirl element and the beginning of the slits was varied);
3. form of the slits (see figures 6.11B and C);
4. swirl element.

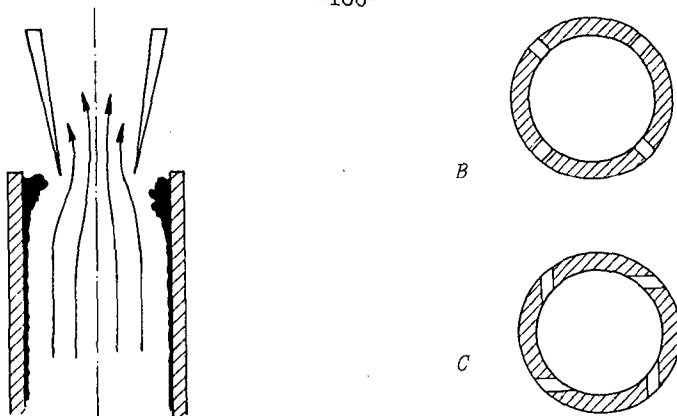


Fig. 6.11A Reentrainment in coaxial discharge Fig. 6.11B,C Slit geometries

The most important conclusions are:

1. With all swirl elements that induce flows of which the swirl number > 0.9 , 85-90% of the liquid in the gas was flung out in the first centimetres above the swirl element (approximate d_{50} of mist amounted to $25 \mu\text{m}$).
2. With the swirl elements with no or only a small buff-body (elements A, C1, D1) extensive reentrainment occurs from the downstream side of the buff-body because of liquid creep in the swirl element towards its center. This affects the separation efficiency very disadvantageously.
3. With swirl elements A, C1 and D1 liquid strings can 'escape' between the slits if only three slits are present in the circumference of the tube. This effect does not take place if the tube has four discharge slits, or at purge rates above 25%.
4. The form of the slit also determines the efficiency of the liquid discharge. Configuration B (figure 6.11C) provides a considerable more efficient discharge than configuration A. In case of configuration A droplets have been observed to jump across discharge slots.

In order to be able to verify the predictions of AC-MOD2 with respect to the particle trajectories it was attempted to measure the drop size distribution of the non-separated mist downstream of the cyclone on test-rig 2. With this information fractional efficiency curves could be calculated.

In case no reentrainment, creep or shortcircuiting of the purge air occurs, the d_{50} of a reasonably well designed cyclone results generally in overall separation efficiencies up to 99.5%. With the available equipment it is impossible to measure accurately this very low carry-over.

Block AC-EXP3

The experiments carried out in this block are used to characterize representative axial cyclones under practical oil field conditions. On test-rig 2 experiments took place with water and SF₆ under varying pressures.

The geometries that have been tested (nomenclature according to figure 6.10) are given in table 6.III. The corresponding experimental conditions and the figures in which the results are reported are given in table 6.IV. Figure 6.12 shows the influence of gas density on the operation of cyclone type II.

| type of liquid discharge | diameter D (mm) | length of separation zone, L (mm) | swirl element type | diameter of gas outlet D _e (mm) | secondary separation device B (mm) |
|--------------------------|-----------------|-----------------------------------|--------------------|--|------------------------------------|
| I coaxial | 50 | 125 | C2 | 30 | 10 |
| II radial | 50 | 125 | A | 30 | 10 |
| III radial | 50 | 125 | C2 | 30 | 10 |

Table 6.III

| run | type | gas density (kg/m ³) | gas throughput (m ³ /hr) | liquid loading (10 ⁻⁵ v%)* | pressure drop coefficient (ξ) | efficiency curves in app. C, page |
|-----|------|----------------------------------|-------------------------------------|---------------------------------------|-------------------------------|-----------------------------------|
| 1-3 | I | 15, 20, 40 | 30-100 | 12 | 13 | C.4 |
| 4-6 | II | 15, 20, 40 | 30-100 | 12 | 24 | C.4 |
| 7-9 | III | 15, 20, 40 | 30-100 | 12 | 14 | C.4 |

* the corresponding droplet size distribution is given in app. C, page C.4.

Table 6.IV

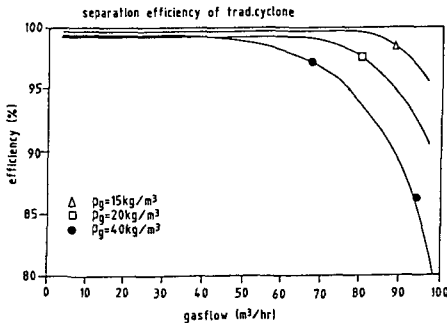


Fig. 6.12 Example of axial cyclone characterization: run 4-6 table 6.IV

Blocks AC-EXP4 and AC-EXP5

It is assumed that no detrimental secondary effects (maldistribution) of any scale will take place in an axial multicyclone. Therefore, no experiments were planned in these blocks.

6.3.2 Reverse flow cyclones

Block RFC-EXP1

The experimental results in this block supplement the information gathered in section 5.5.2 necessary to validate the gas flow field model of a reverse flow cyclone. Much information is available on the conventional reverse flow cyclone with a single tangential inlet. A reverse flow cyclone that is often used in the oil field industry is the double tangential inlet type. Of this type hardly any quantitative information exists (for a more elaborate description see section 3.4.4.4). Therefore experiments in this block were carried out to characterize also this reverse flow cyclone type.

The physical information necessary to set up the fundamentals of the flow field model (swirling flows in straight tubes) can in principle be deduced from the corresponding AC-block.

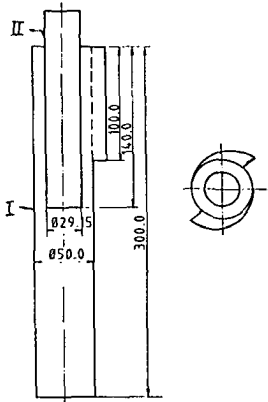


Figure 6.13A Test cyclone A

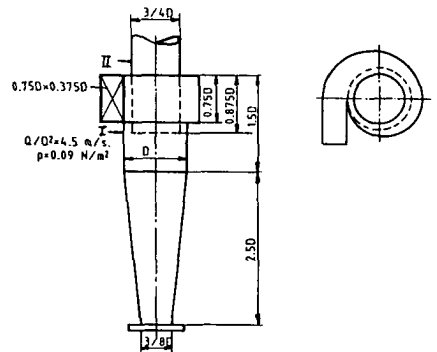


Figure 6.13B Test cyclone B

Gas flow field measurements have been carried out on two geometries (depicted in figures 6.13A and B). Figure 6.13A was chosen as a geometrical averaged version of two similar industrially applied cyclones (fabricators: Paladon and Burgess Manning). Figure 6.13B is an example of a conventional high throughput cyclone (Stairmand [1951], see appendix A 3.4.4.2). The locations at which the gas velocity distributions have been measured are indicated in the figure. The flow field measured at location I has served as starting condition of a version of RFC-MOD1. The flow fields measured at the other two locations were planned for validation purposes.

Table 6.V summarizes the conditions of the experiments and the location of the graphical results. (ξ refers to the cross sectional area of the cyclone)

| exp. nr. | geometry (fig. 6.13) | location of measurement | throughput (m^3/hr) | pressure drop coefficient (ξ) | flowfields depicted in app. C, page |
|----------|----------------------|-------------------------|---------------------------------------|-------------------------------------|-------------------------------------|
| 1 | A | I | 50 | 27 | C.5 |
| 2 | A | II | 50 | - | C.5 |
| 3 | B | I | 50 | 45 | C.5 |
| 4 | B | II | 50 | - | C.5 |

Table 6.V

Block RFC-EXP2

The experiments described in this block have supported in the formulation of models that describe the behaviour of the liquid phase in reverse flow cyclones (to a large extent also applicable to axial cyclones).

The liquid phase occurs in the cyclone in two forms:

1. the original mist phase;
2. the liquid film that has been formed by separated mist particles.

The major part of the experiments in this block have been carried out with respect to the latter.

Experiments with respect to the liquid film behaviour

These experiments have pursued two objectives:

1. Determination of the film properties in different sections of the cyclone (film thickness, flow regime);
2. Identification of conditions and locations of detrimental effects inside the cyclone.

With this information it is possible to provide the reentrainment models listed in sections 5.3 and 5.4 with data. It is then possible to check their validity for centrifugal systems, or modifying them to describe these systems. If the phenomenological model of Ishii [1975] is taken as the most versatile and reliable of those listed in chapter 5, and therefore most suited to be embedded in RFC (and AC) MOD2, the minimal physical data necessary to collect are:

1. the film thickness distribution in the cyclone;
2. the liquid Reynolds number (or, with 1: the film velocity);
3. gas phase properties, supplied by EXP1 or MOD1.

The film characteristics that are the object of investigation (and of prediction) are:

1. the film flow regime;
2. the occurrence of reentrainment;
3. the occurrence of creep.

The last aspect is not covered by the models of sections 5.3-5.5.

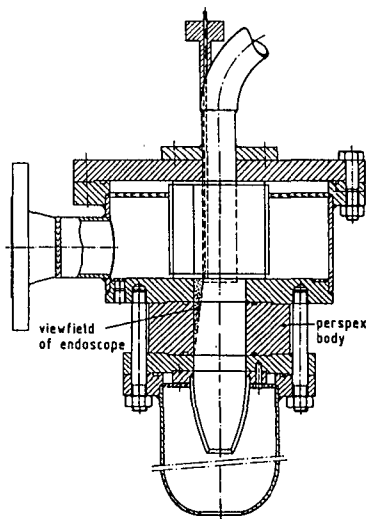


Figure 6.14 Visually accessible
test vessel

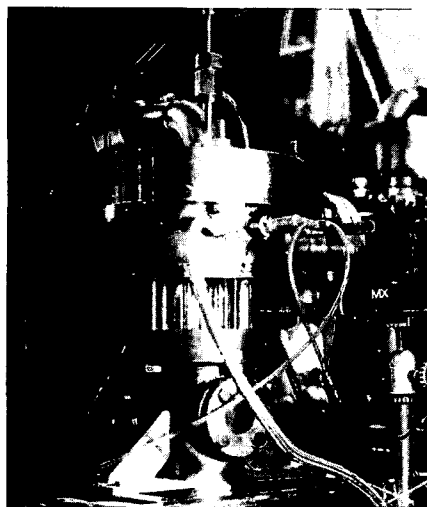


Figure 6.15 Test vessel in actual
operation

These experiments have been carried out with a specially designed measuring vessel which enabled close observation of the internal phenomena of a cyclone. The measuring vessel consisted of a central plexiglass section which forms the separation or settling zone of a reverse flow cyclone (see figures 6.14 and 6.15). The (double) tangential inlet was accommodated in the stainless steel 'head' of the vessel in which the mist was sprayed.

Observations were possible:

1. through an endoscope that was embedded in the vortex finder of the cyclone. This way the internal surface of the liquid film in the separation zone could be visualized;
2. through the plexiglass section of the general appearance of this liquid film and other internal phenomena (for instance the film behaviour on the vortex finder).

The separation efficiency, pressure drop and experimental conditions could be measured simultaneously. To transpone the results of the determinations (on a plexiglass surface) to a situation in which the inner surface of a cyclone consists of steel, the angle of contact of the test liquids has been determined on respectively plexiglass, smooth steel and corroded steel. The inner surface of the plexiglass part was perfectly smooth.

Experiments have been carried out with air/water mixtures with gas densities up to 10 kg/m^3 . Experiments with glycol and SF_6 are planned for the near future; they have not been carried out yet because of the rare availability of the necessary high speed video equipment. It is, however, not expected that the general findings of these experiments will be drastically changed. From the results of the next block (RFC-EXP3) it appears that the operating characteristics of a cyclone are similar for different liquid and gas properties. Qualitatively, this probably means that the mechanisms that have been found to limit cyclone operation with air/water mixtures also limit cyclone operation under other conditions.

In the following presentation of results the qualitative findings are described (1-5). In table 6.VI the experimental conditions and measured quantities are summarized. The geometry of the test cyclone is depicted in figure 6.17 and corresponds largely (except for the extended separation zone) to a Burgess-Manning type cyclone. Therefore, the overall operating characteristics of this cyclone are very similar to that of cyclone type D (figure 6.18B) tested in the next block. Under most circumstances the full inner perimeter of the cyclone is wetted.

1. The liquid flow, however, is to a large extent concentrated in two channels that start from the lower downstream end of each tangential inlet. This effect does not take place at high gas and liquid loading.
2. Just underneath the vortex finder an accumulation of liquid takes place, which results in a substantially thicker film. A bit lower (10-30 mm, depending on conditions) the accumulation spreads out, and surprisingly, the two thicker channels that originally flowed into this accumulation, seem to flow out of it seemingly unchanged. The accumulation is apparantly caused by a change in the ratio of local axial and tangential

gas velocities, as the angle of inclination is much smaller in the accumulation than up- or downstream of it (see figure 6.16).

3. Significant reentrainment of the liquid film in the cleaned gas seems to take place only from this band of accumulated liquid. If reentrainment takes place further down, reentrained drops seem to be deposited directly afterwards. Disturbances in the liquid film downstream of the band of accumulated liquid seem to be minimal in comparison to the disturbances in the band itself.
4. Reentrainment from this band occurred only when large disturbance waves appeared.
5. During all observations a certain amount of liquid crept along the vortex finder into the cleaned gas stream. The estimated quantity amounts from 0.5-1.0% of the total liquid throughput.

In table 6.VI the results are summarized with the corresponding experimental conditions under which they have been measured.

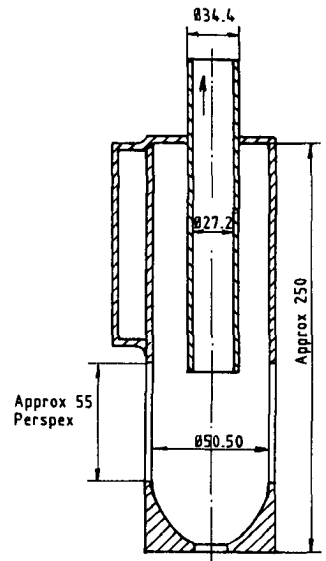
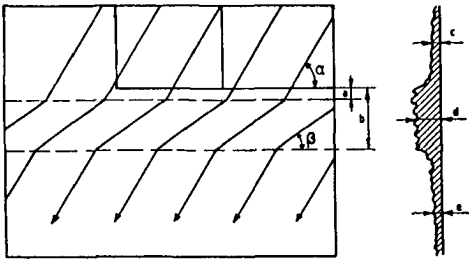


Fig. 6.16 Observed phenomena in cyclone Fig. 6.17 Geometry of test cyclone

The endoscope was put at the disposal of the project by Wolf GmbH.
Koninklijke/Shell-Laboratorium, Amsterdam assisted in the measurements.

| exp. run | gas density (kg/m ³) | liquid loading ($\cdot 10^{-5}$ v%) ($d_{50} \sim 20\mu\text{m}$) | channels disappear at (m ³ /hr) | band fully turbulent at (m ³ /hr) | reentrainment observed at (m ³ /hr) | efficiency curves and film velocity app. C, page |
|----------|----------------------------------|--|--|--|--|--|
| 1 | 1.3 | 3 | 90 | 60 | 65 | C.6 |
| 2 | 1.3 | 6 | 80 | 60 | 60 | C.6 |
| 3 | 1.3 | 12 | 65 | 60 | 60 | C.6 |
| 4 | 5 | 3 | 80 | 60 | 55 | C.6 |
| 5 | 5 | 6 | 80 | 55 | 55 | C.6 |
| 6 | 5 | 12 | 55 | 60 | 60 | C.6 |
| 7 | 10 | 3 | 75 | 55 | 50 | C.6 |
| 8 | 10 | 6 | 70 | 50 | 55 | C.6 |
| 9 | 10 | 12 | 50 | 55 | 55 | C.6 |

Table 6.VI

Experiments with respect to the behaviour of mist phase

Like in block AC-EXP2, it was also tried here to measure fractional efficiency curves. Unfortunately, the same negative results were achieved. In this case not only because of the very low concentrations of mist particles in the cyclone outlet, but particularly because the particles appeared to be large and probably originated from sheared off creeping film. After these measurements it was clear that it would be necessary to measure primary fractional efficiency curves with dust in order to prevent distortion because of creep. (This has not been carried out sofar.)

Block RFC-EXP3

The experiments in this block are necessary to form a general database to verify the predictions of the general RFC-MOD3 model, that is intended to describe the full behaviour of a cyclone. Therefore, experiments were carried out with four different cyclone geometries (two of which were designed according to guidelines collected in section 3.4.4.2; and two of which were cyclones that are popular in practical operation). These four geometries are depicted in figures 6.13B and 6.18A-C.

Table 6.VII lists the experimental conditions under which each of these cyclones was characterized and where the results can be found in appendix C. Each run consists of a variation of the gas flow from 30-100 m³/hr and of the liquid load from $2-12 \cdot 10^{-5}$ v%. In appendix C cyclone types B, C, D and E are referred to as cyclones I, II, III and IV.

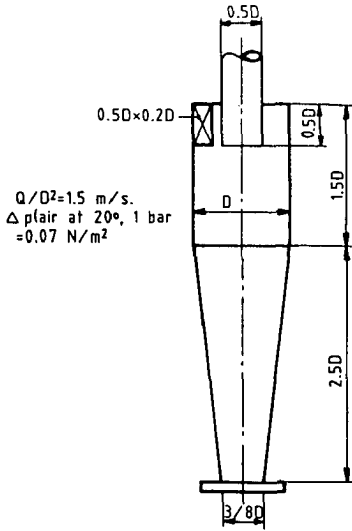


Figure 6.18A Cyclone
geometry C

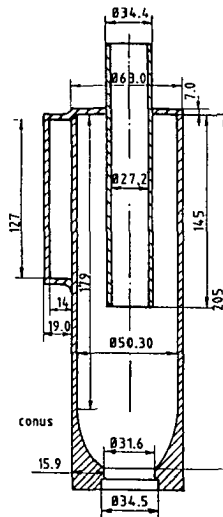


Figure 6.18B Cyclone
geometry D

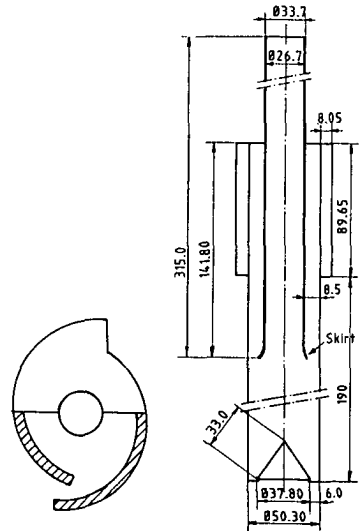


Figure 6.18C Cyclone
geometry E

| exp. run * | cyclone type (fig.6.13/18) | gas density ρ_g - kg/m ³ | liquid sort ** | pressure drop (ξ)*** | eff. curves app. C. page |
|------------|----------------------------|--|----------------|----------------------------|--------------------------|
| 1 | B | 1.3 | wa | 45 | C.7 |
| 2 | B | 4 | wa | - | C.7 |
| 3 | B | 6.5 | wa | - | C.7 |
| 4 | C | 1.3 | wa | 65 | C.7 |
| 5 | C | 4 | wa | - | C.7 |
| 6 | C | 6.5 | wa | - | C.7 |
| 7 | C | 10 | wa | - | C.7 |
| 8-10 | D | 1.3 | wa,bu,gl | 24 | C.7,C.8 |
| 11-13 | D | 4 | wa,bu,gl | - | C.8 |
| 14-16 | D | 6.5 | wa,bu,gl | - | C.8 |
| 17-19 | D | 10 | wa,bu,gl | - | C.9 |
| 20 | D | 13 (SF ₆) | wa | - | C.9 |
| 21 | D | 25 (SF ₆) | wa | - | C.9 |
| 22 | E | 1.3 | wa | 29**** | C.9 |
| 23 | E | 4 | wa | - | C.9 |
| 24 | E | 6.5 | wa | - | C.9 |
| 25 | E | 10 | wa | - | C.10 |

* in each experiment the gas flow is varied from 30-100 m³/hr at liquid loadings of 2-12 vol%.

** droplet size distributions depicted in appendix C, page C.10.

*** ξ relates to cross sectional area of cyclone ($0.25 \pi D^2$).

**** pressure drop curves given for measurements with water in appendix C, page C.10.

Table 6.VII

Block RFC-EXP4

The experiments carried out in this block serve to identify and quantify the detrimental effects that accompany the scale-up of a single cyclone to a multicyclone package. With this information it is possible to form a basis for the MOD4 blocks and their validation. As was the case with other EXP-blocks (AC-EXP1 and RFC-EXP1) part of the data are used as starting information for MOD4 and part for its validation. The results envisaged in the first objective are:

1. Determination of the variation of inlet conditions of individual cyclones across a multicyclone package;
2. Determination of the influence of the multicyclone geometry on this variation.

The results envisaged in the second objective are:

1. Comparison of the operating characteristics of a single cyclone to those of the average individual cyclone in a multicyclone package;
2. Comparison of the operating characteristics of a single cyclone to those of the average individual cyclone in a special multicyclone package. This package has been designed in such a way that every single cyclone is positioned identically.

The set-up of the experiment clearly implies that of all detrimental effects mentioned in section 3.4.4.4, the effect of maldistribution of gas and liquid phases across a package will be investigated especially. The other effects are mainly constructional or mechanical and can easily be avoided. The different multicyclone geometries that have been tested are depicted in figure 6.19. Test bundles B and C (Paladon) are composed of cyclones of type E (figure 6.18C). Testbundle A (Burgess Manning) consists of cyclones of type D (figure 6.18B).

This multicyclone has been specially prepared to measure the operating conditions of the individual cyclones in the multicyclone bundle.

Provisions were made to measure:

- a. the liquid loading of a number of cyclones;
- b. the gas flow through the vortex finder of these cyclones.

The cyclones that have been measured individually are situated at representative locations across the multicyclone and are indicated in figure 6.19. Figure 6.20 shows a picture of the multicyclone under investigation.

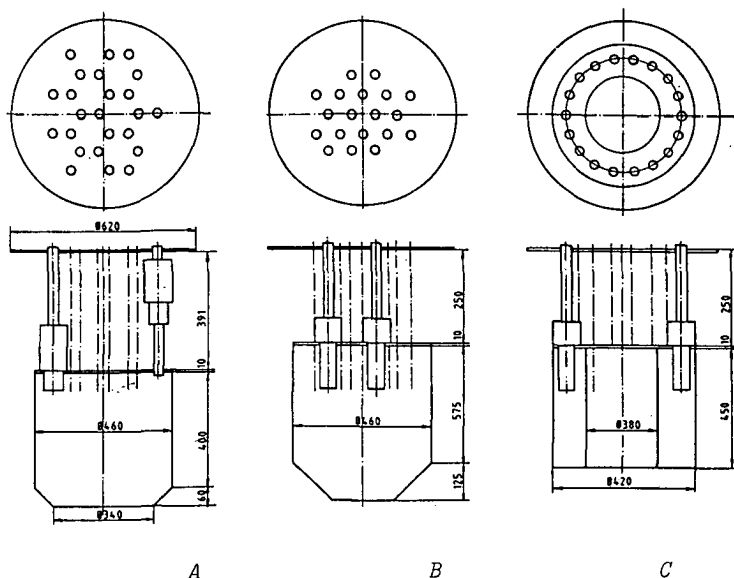


Figure 6.19 Multicyclones A-C

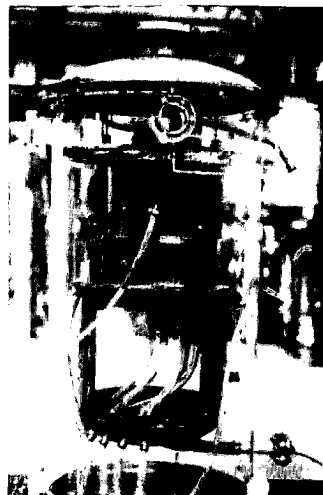


Figure 6.20 Multicyclone A

Test bundles B and C consist of only one layer of cyclones. Test bundle A features a double layer. This appears to be a practical method to minimize the diameter of the vessel; a practice sometimes also carried out by the other manufacturer. Test bundle C is a cyclone package with one cyclone less than B in which all cyclones are positioned identically to minimize maldistribution. The experiments of this block are listed in table 6.VIII as numbers 1-9. Figure 6.21A gives an example of the 'multicyclone' effect.

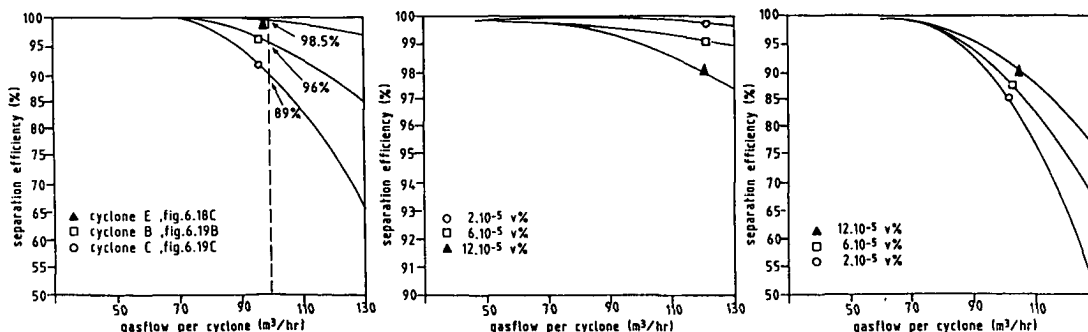


Fig. 6.21A Multicyclone effect Fig. 6.21B Multicyclone A Fig. 6.21C Multicyclone B

Block RFC-EXP5

The results of this block are used to form a database with which the general multicyclone describing model (MOD5) can be verified.

The measurements to quantify the multicyclone effect have already resulted in a vast amount of atmospheric data that can fulfil this function. Therefore, the only extra experiments specifically carried out for this block consisted of the determination of the operating characteristics of the multicyclones presented in figure 6.19 with another two phase system, glycol/air.

The particulars are summarized in table 6.VIII.

| exp. run * | multicyclone type | liquid sort ** | extra carry-over of multicyclone w.r.t. single cyclone *** | results in |
|------------|-------------------|----------------|--|---------------------------------------|
| 1- 3 | A | water | ca. 17x | Nieuwenhuis [1987] and Besemer [1988] |
| 4- 6 | B | water | ca. 11x | |
| 6- 9 | C | water | ca. 2.5x | |
| 10-12 | A | glycol | - | |
| 13-15 | B | glycol | - | |

* each run consists of determination of separation efficiency and pressure drop from approximately 30-100 m³/hr with $2-12 \cdot 10^{-5}$ v% of liquid.

** inlet droplet size distributions: d_{50} varies between 25 - 75 μ m.

*** measured at 100 m³/hr.

Table 6.VIII

In figures 6.21B and C examples are given of the characterizations of multicyclones A and B. It appears that the separation efficiency of A decreases with decreasing liquid load, while the separation efficiency of B increases. This effect will be explained in chapter 7.

For test-rig 2 a test vessel has been designed in which two single cyclones can be accommodated. The operating conditions offered to each of the cyclones can be carefully controlled. Also the operating characteristics can be monitored separately. This vessel is depicted in figure 6.22.

With these experiments, which are not finished yet, it is expected to extend the validation of the relations to be set up in MOD⁴ to all operating conditions.

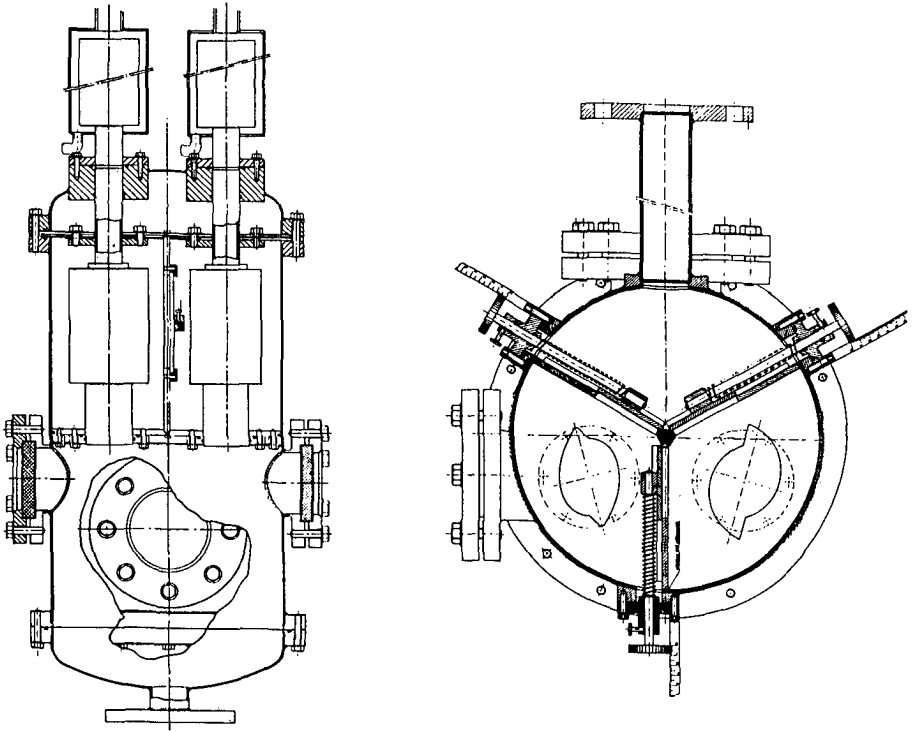


Figure 6.22 Test vessel for two cyclones

6.3.3 Vanes

As already mentioned in chapter 4, the emphasis of the present research project has been put on the investigations of the cyclone-type separators. Large parts of the logical project structure for these separators have been completed. The completion of the project structure for vanes is much less advanced. Therefore the emphasis of the follow-up project will be put on these separators. These results will be included in the thesis of Verlaan [planned to be published in 1990]. Experimental results have already been obtained, sometimes even in vast amount, but the whole collection looks somewhat fragmented as still some important data lack.

Block V-EXP1

The results of the experiments of this block are used to validate the MOD1 predictions of the gas flow field between vane blades. Unlike the other EXP1 blocks no information needs to be collected to start the models with, because the modelling of vanes appeared to be much more straight forward than that of cyclones. Anticipating the already mentioned follow-up thesis of Verlaan, preliminary experiments lead to the following measured gas flow field distributions between vane blades of a geometry as depicted in figure 6.23A. Velocities are measured with the pitot tube as described in earlier EXP1 blocks. In figure 6.23B the corresponding gas flow lines, visualized with smoke, are shown (De Kort [1987]).

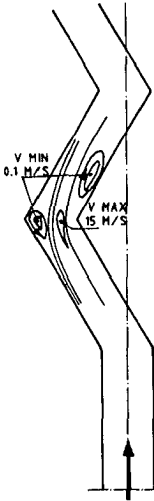


Fig. 6.23A Indicative example of measured velocity distribution between vanes

Fig. 6.23B Flow field visualization

Block V-EXP2

The experiments in this block are necessary to check the models that describe the behaviour of the liquid phase. As encountered with the other separator types this means that the behaviour of i) the liquid film and ii) the disperse phase (droplets) has to be characterized through experiments.

Experiments with respect to the liquid film behaviour

One experiment has already been carried out on test-rig 3. For this purpose a commercial vane package was prepared for internal investigations. One of the more or less hollow blades of this vane package (Burgess Manning 625) has been provided with a longitudinal slit, in which an endoscope could be embedded unobstrusively to view the opposite blade (for precise description of geometry see section 3.4.3). The location of this slit was chosen so that the second drainage slit of the opposite blade could be observed (see figure 6.24A). The endoscope was put at the disposal of the project by Wolf GmbH. Koninklijke/Shell-Laboratorium, Amsterdam assisted in the measurements.

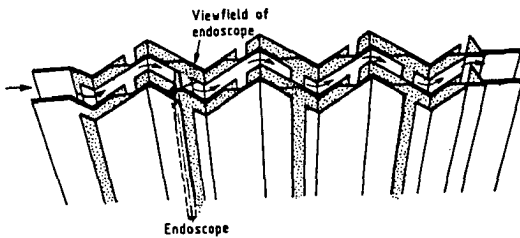


Figure 6.24A Field of view

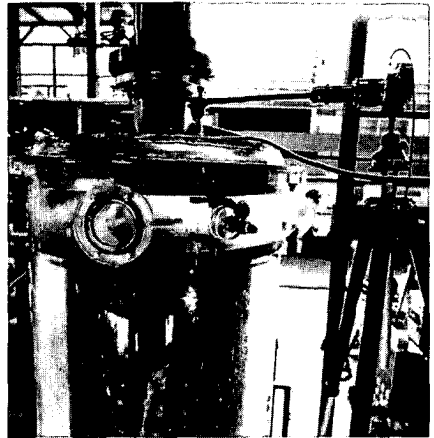


Figure 6.24B Experimental set-up

The important observations of these investigations were:

- 1A. At superficial gas velocities (referred to the frontal area of the vane) lower than 3-5 m/s and liquid loadings $< 5 \text{ m\%}$ most of the liquid offered to the vanes (80-90%) did not reach the second bend and had apparantly, been separated in the first bend.
- 1B. At liquid loadings $> 5 \text{ m\%}$ and/or at superficial gas velocities above 3-5 m/s a substantial amount of liquid is drained through the slit behind the second bend.
2. Also a substantial amount of liquid was drained in the top section of the bend in the vane plate (see figure 6.25).
3. The liquid film enters the drainage slit flowing around the upstream lip of the slit (see figure 6.25).

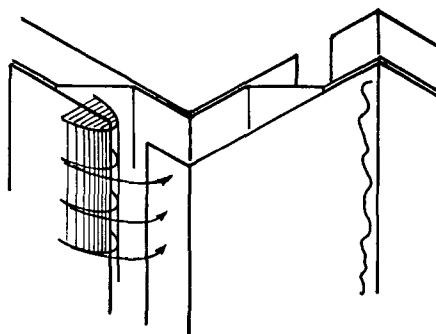


Figure 6.25 Observed phenomena inside vane

4. At liquid loadings < 5 m% and at superficial gas velocities > 7 m/s the thin (0.03-0.08 mm) laminar liquid film changed to a pulsating, at times, thick film (0.1-0.25 mm) with a very wavy surface. In this film regime reentrainment of drops could often be observed.
5. Reentrainment took always place from the sharp irregularities at the edge of the upstream lip of the slit, around which the film flowed into the slit (see figure 6.25).
6. Reentrained drops were at most times deposited again under the conditions mentioned under 4. Reentrained drops of $30 \mu\text{m}$, the smallest drops that could be recognized with the optical system used, were deposited halfway between the slit and the next bend. Reentrained drops of $100 \mu\text{m}$ and larger directly behind the slit. This phenomenon appeared as droplets 'jumping' across the slit.
7. At high liquid loadings and gas velocities, when the downstream side of the slit was wetted substantially in the above described way, a very thin film ($20\text{-}30 \mu\text{m}$) was observed creeping against the gas direction into the slit (bending itself around the edge of the downstream lip).

Table 6.IX gives a summary of the experimental conditions and measured results. Experiments have been carried out only with water and air.

| exp. run | liquid loading ($\cdot 10^{-5}$ vol%) | gas velocity (m/s)* at which second slit was first wetted | gas velocity (m/s)* at which film showed first instabilities |
|----------|--|---|--|
| 1 | 2 | 5,5 | 8 |
| 2 | 5 | 5,0 | 8 |
| 3 | 10 | $< 3,5$ | 4 - 4,5 |

| exp. run | film thickness (μm) at minimum gas velocity* | film thickness (μm) at maximum gas velocity (13 m/s)* |
|-------------|---|--|
| 1 | 30 | 80 |
| 2 | 40 | 80 |
| 3 | 40 | 80 - 120 |

* gas velocities refer to the superficial velocity in front of the vane.

Table 6.IX

Experiments with respect to the behaviour of the disperse phase

On test-rig 3 it appeared to be possible to determine downstream droplet size distributions of mists that had penetrated untouched through the vane blades and that did not contain larger droplets caused by creep or reentrainment. This enabled the direct determination of the fractional efficiency curve of vane separators with geometries as presented in figure 6.29 in V-EXP4. Table 6.X summarizes experimental conditions and refers to the figures.

| exp. run | geometry (fig. 6.28) | superficial gas velocity (m/s) | graphs app. C, page |
|-------------|-------------------------|-----------------------------------|------------------------|
| 1 | A | 4 | C.11 |
| 2 | A | 8 | C.11 |
| 3 | B | 4 | C.11 |
| 4 | B | 8 | C.11 |
| 5 | C | 4 | C.11 |
| 6 | C | 8 | C.11 |
| 7 | D | 4 | C.11 |
| 8 | D | 8 | C.11 |

Table 6.X

Block V-EXP3

With vane separators no experiments under actual oil field conditions have been carried out yet. With respect to these experiments is referred to the thesis in preparation of Verlaan.

Block V-EXP4

The experiments in this block will be used to quantify the effects that accompany upscaling of vane separators. The most noteworthy effect that was expected (see also section 3.4.3) was the maldistribution of the two-phase mixture across the frontal surface of the vane separator.

This will especially be the case with vane separators that have a large ratio of length and width of their frontal surface. One of the measures to counteract this maldistribution is to place perforated plates up- and downstream of the vane pack to build up an equalizing pressure. The experiments planned in this block consisted of the:

1. determination of the effect of varying length/width ratios of the frontal surface of the vanepack;
2. determination of the secondary effect of perforated plates with respect to their influence on the liquid phase.

During these investigations it appeared that unexpected separation mechanisms downstream of the vanepack played an important role and impeded with the characterization of the vane pack itself. These effects are described first.

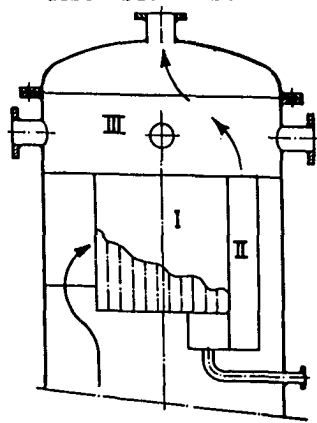


Fig. 6.26 Secondary separation

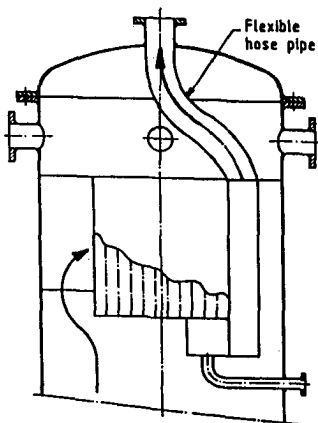


Fig. 6.27 Alternative set-up

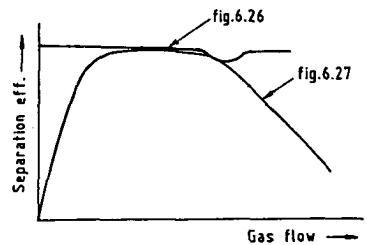


Fig. 6.28 Effect of alternative set-up

The usual way to install a horizontally flowed through vane pack is depicted in figure 6.26. This way of installation necessitates two sharp turns of the gas flow after exiting between the vane blades. Under conditions of overloading, relatively large droplets $d_{s,} > 200 \mu\text{m}$ are reentrained from the vane pack and are subsequently separated in the two zones indicated in figure 6.26. In the first zone because of the sharp bend the gas has to make; in the second also because of a relatively sharp bend, but mainly because of the reduction in actual velocity above the vane pack.

The liquid separated in second instance has been observed to flow back in sheltered zones against the gas stream in the space directly behind the vane (zone I). From here it flows over into the sump underneath the vane pack from which the separated liquid is drained.

To quantify these effects measurements have been carried out in which the gas flowing out of vane pack, flowed directly in a flexible hose out of the separation zones (see figure 6.27). Figure 6.28 gives an illustrative example of the operational differences of this configuration with respect to the usual vane pack installation.

Hereafter the experiments, originally planned in this block, were carried out.

Determination of the influence of varying length/width ratios

A qualitative experiment has been carried out with vane pack type A (figure 6.29) in which the length width ratio of its frontal inlet area was increased from 50 cm/26 cm (I) to 50 cm/13 cm (II). In this way the effect of both detrimental mechanisms that act during this kind of upscaling can be determined.

| exp. run | superficial gas velocity (m/s) | liquid loading ($\cdot 10^{-5}$ vol%) | % more carry-over of situation II |
|----------|--------------------------------|--|-----------------------------------|
| 1 | 8 | 2 | 2 |
| 2 | 8 | 6 | 1 |
| 3 | 8 | 12 | 8 |

Table 6.XI

The measurements have been carried out with the vane separator configured as in figure 6.27. It has not been quantified whether the decrease of the separation efficiency with the increase of L/D ratio is caused by the overflowing of the lower parts of the drainage slits or by the maldistribution of the gas across the longitudinal cross section. The fact that the effect is most distinct at high liquid loadings favours the first mechanism.

Determination of the secondary effects of perforated plates

Apart from the positive effects that the popular perforated plates might exert with respect to enhancing of the distribution, it was felt that also negative aspects might cling to the use of them. Especially the break-up of large droplets at the downstream side might spoil the secondary separation mechanisms which have been mentioned before. Therefore, a simple experiment has been carried out in which a vane pack with a more or less square inlet surface (so that maldistribution will not take place) has been provided with different sorts of perforated plates. It was expected that the smaller the net free area was chosen, the larger the shear forces on the droplet would be and the smaller the droplet, the higher the carry over (the smaller the separative force of zone I and II). This was confirmed by the experiments. However, the quantification of this effect lies slightly outside the scope of this project. Only an illustrative example is presented in figure 6.30 and no reference to it will be found in the corresponding MOD4 block. The vane pack, according to type B of figure 6.29, has been tested in its original form (no modifications as in figure 6.27).

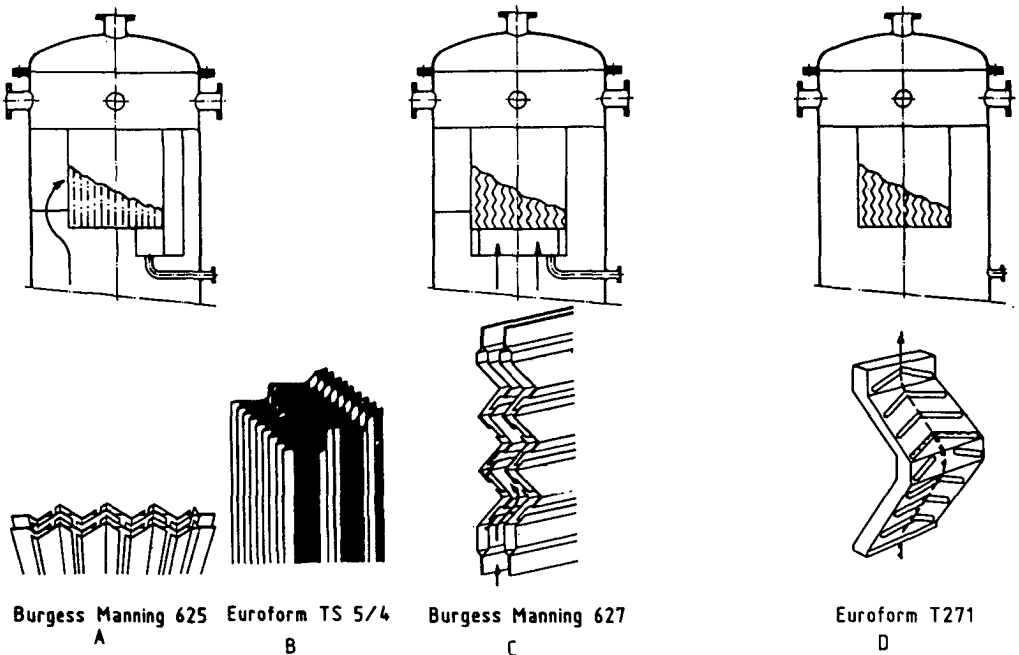


Figure 6.29 Tested vane geometries

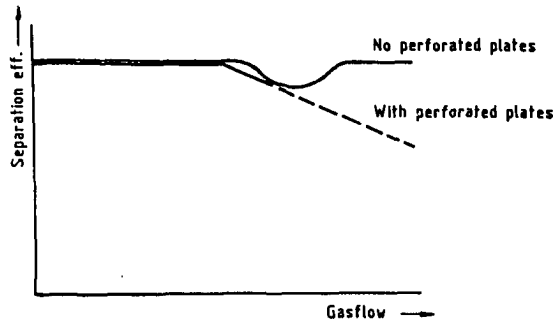


Figure 6.30 Effect of perforated plates

Block V-EXP5

In this block four types of actual scaled vane separators have been tested under varying conditions. These results form a database from which the atmospherical part of the MOD5 models can be verified. The four vane separators are presented in figure 6.29. Type A and B are two commercial horizontally flowed through vanes with shielded liquid drainage. Type C and D are two commercial vertically flowed through vanes, of which type C features a shielded internal drainage. For the specific description of these aspects, see section 3.4.3.

The reason why only the horizontally flowed through vanes have been the subject for scaling up characterizations is that the test section of test-rig 3 is positioned vertically. (Under this condition vertical flowed through separators will not show effects of maldistribution.)

Table 6.XII summarizes the experimental conditions and refers to the location of the test results.

| exp.* run | vane type | liquid sort ** | results in |
|--------------|-----------|-------------------|--|
| 1 | A | water | Vemer [1987] and Overgaag [1988] |
| 2 | B | water | |
| 3 | C | water | |
| 4 | D | water | |
| 5 | A | glycol | |
| 6 | B | glycol | |
| 7 | C | glycol | |
| 8 | D | glycol | |

* each run consists of a variation of the superficial gas velocity from approximately 3-15 m/s at variation of the liquid load from $2 \cdot 10^{-5}$ v%.

** inlet droplet size distribution: $d_{50} \sim 25-75 \mu\text{m}$.

Table 6.XII

In figure 6.31 the characterizations of the two vertical vane packs are given as illustration. Figure 6.31A gives the test results of vane C; figure 6.31B of vane D.

The difference in capacity limitation (see section 3.4.3) is clearly demonstrated.

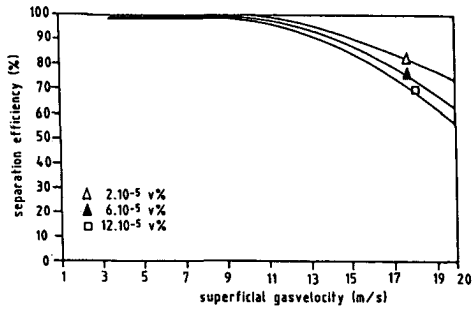


Figure 6.31A Test results of vane C

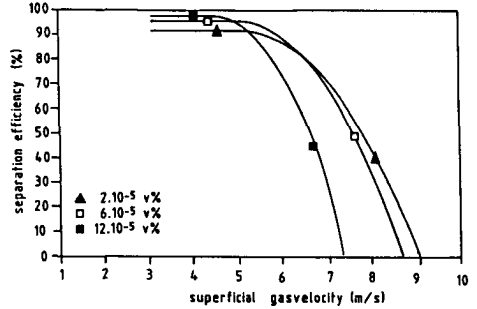


Figure 6.31B Test results of vane D

7. MODELLING RESULTS

7.1 Introduction

7.1.1 Structure of chapter

In this chapter models are formulated with which it is possible to predict the characteristics of the separators under investigation. These models lead to the introduction of new separator designs and improved design equations for existing separators (in chapter 8).

The following operating characteristics are the subject of modelling:

1. separation efficiency, thus also:

- a. maximal capacity
- b. minimal capacity

2. pressure drop

as a function of separator geometry and operating conditions.

In sections 7.2 and 7.3 common components of the models are described.

Sections 7.4-7.6 give an overview of the models that have been developed sofar, per separator type under investigation.

7.1.2 Modelling techniques

The models that are envisaged consist of several submodels as explained in chapter 4. Submodels are formulated that describe the gas phase (MOD1) and the liquid phase (MOD2). See innerside of the front cover for explanation of the codes.

Predicting a gas flow field puts other demands on modelling techniques than predicting a gas/liquid interaction under given conditions.

The former model type performs only adequately if a numerical scheme is set up with which it is attempted to describe the gas flow field as accurately as possible. Grave simplifications of the gas flow field, as shown in for instance appendix A 3.4.4.2, will almost immediately result in an unallowable degree of inaccuracy. Powerful computing facilities are necessary to perform these extensive numerical computations.

The prediction of the behaviour of a two-phase system under given conditions is much more subsisted by physical or phenomenological modelling: certain observed phenomena are used as a start for further models. A good example is the reentrainment model of Ishii [1975], described in section 5.3.

The approach chosen in this chapter is one of model clustering. With assumed boundary conditions (depending on the liquid phase) the gas flow field (in MOD1) is calculated. These results are used to predict the behaviour of the liquid phase (in MOD2), from which the assumed boundary conditions with respect to the gas phase can be verified. If necessary a valid solution is obtained after some iterations. MOD3 forms the framework in which this interaction takes place. Sometimes the influence of scale has to be taken into account. The results of the model that predicts maldistribution across the separator (MOD4) are used to verify the boundary conditions of MOD3, the model that describes the basic separation unit. This interaction plays in MOD5, the model that describes the full separator.

In the following sections attention is paid to common elements in the MOD1 and MOD2 blocks of the three separator types under investigation. In section 7.2 specific attention is given to the numerical prediction of gas flow fields and in section 7.3 to the gas/liquid phenomena that form the core of the MOD2 models.

7.2 Numerical modelling of gas flow fields

7.2.1 Physical background

Laws of conservation

The equations that govern incompressible, time-independent, isothermal, single phase fluid flow are: (see figure 7.1 for coordinate notation)

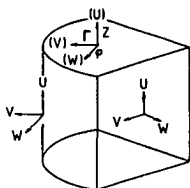


Figure 7.1 Notation for coordinate system

1. the law of conservation of matter:

$$\frac{\delta(\rho V)}{\delta r} + \rho \frac{V}{r} + \frac{\delta(\rho W)}{r \delta \phi} + \frac{\delta(\rho U)}{\delta z} = 0 \quad (7.1)$$

2. the law of conservation of momentum:

in the direction of r:

$$\begin{aligned} \rho_g \left(\frac{\delta V}{\delta t} + V \frac{\delta V}{\delta r} + \frac{W}{r} \frac{\delta V}{\delta \phi} - \frac{W^2}{r} + U \frac{\delta V}{\delta z} \right) = \\ - \frac{\delta P}{\delta r} + \mu_g \left(\frac{\delta^2 V}{\delta r^2} + \frac{1}{r} \frac{\delta V}{\delta r} - \frac{V}{r^2} + \frac{1}{r^2} \frac{\delta^2 V}{\delta \phi^2} - \frac{2}{r^2} \frac{\delta V}{\delta \phi} + \frac{\delta^2 V}{\delta r^2} \right) \end{aligned} \quad (7.2)$$

in the direction of ϕ :

$$\begin{aligned} \rho_g \left(\frac{\delta W}{\delta t} + V \frac{\delta W}{\delta r} + \frac{W}{r} \frac{\delta W}{\delta \phi} - \frac{VW}{r} + U \frac{\delta W}{\delta z} \right) = \\ - \frac{\delta P}{r \delta \phi} + \mu_g \left(\frac{\delta^2 W}{\delta r^2} + \frac{1}{r} \frac{\delta W}{\delta r} - \frac{W}{r^2} + \frac{1}{r^2} \frac{\delta^2 W}{\delta \phi^2} - \frac{2}{r^2} \frac{\delta W}{\delta \phi} + \frac{\delta^2 W}{\delta r^2} \right) \end{aligned} \quad (7.3)$$

in the direction of z:

$$\begin{aligned} \rho_g \left(\frac{\delta U}{\delta t} + V \frac{\delta U}{\delta r} + \frac{W}{r} \frac{\delta U}{\delta \phi} + U \frac{\delta U}{\delta z} \right) = \\ - \frac{\delta P}{\delta z} + \mu_g \left(\frac{\delta^2 U}{\delta r^2} + \frac{1}{r} \frac{\delta U}{\delta r} + \frac{1}{r^2} \frac{\delta^2 U}{\delta \phi^2} + \frac{\delta^2 U}{\delta z^2} \right) \end{aligned} \quad (7.4)$$

U, V and W are the momentary velocities in the directions denoted in figure 7.1, P is the momentary pressure, μ the laminar dynamic viscosity.

These equations are generally applicable to turbulent and laminar flows. In laminar flows the momentary values of velocity components and pressure equal the average values.

The Reynolds decomposition

In turbulent flows the momentary values of velocities and pressure fluctuate. The scale at which these fluctuations occur is often much smaller than the macroscopic gas flow field. According to Colenbrander [1988] a typical scale of length at which mass and momentum are transferred in a

turbulent gas flow is 0.1 mm. It has tremendous implications for the computing facilities if a macroscopic gas flow field is modelled with a resolution of this order of magnitude. Therefore, fluid flow calculations are often based on the time averaged value of velocities and pressure and the momentary value of their fluctuations. This is called Reynolds decomposition (after Reynolds [1877]).

$$U_i = u_i + u'_i \quad (7.5)$$

in which:

U_i = momentary value of variable U_i (velocity component or pressure)

u_i = time averaged component

u'_i = fluctuating component

$$u_i \text{ is defined as } u_i = \lim_{\theta \rightarrow \infty} \frac{1}{\theta} \int_{t_0}^{t_0 + \theta} U_i \, dt \quad (7.6)$$

the averaged value of u'_i equals zero, as per definition:

$$\overline{u'_i} = \lim_{\theta \rightarrow \infty} \frac{1}{\theta} \int_{t_0}^{t_0 + \theta} (U_i - u_i) \, dt = 0 \quad (7.7)$$

This decomposition is only of practical use if the rate of fluctuation of u_i is small in comparison to that of U_i . In other words, u_i should be independent of t_0 . This is the case in stationary flows.

If this decomposition is applied to U , V , W and P in equations 7.1-7.5 and it is assumed that:

1. the gas flow fields under investigation are axially symmetric (cyclones),
thus $\frac{\delta}{\delta \phi} = 0$;
2. the flow field is stationary;

then the continuity equation is transformed to:

$$\frac{\delta u}{\delta z} + \frac{1}{r} \frac{\delta(rv)}{\delta r} = 0 \quad (7.8)$$

and the equations that describe the conservation of momentum:

in the direction of z:

$$u \frac{\delta u}{\delta z} + v \frac{\delta u}{\delta r} = - \frac{1}{\rho} \frac{\delta p}{\delta z} - \frac{\delta}{\delta z} \langle u'^2 \rangle - \frac{1}{r} \frac{\delta}{\delta r} r \langle u'v' \rangle + v_g \left(\frac{\delta^2 u}{\delta z^2} + \frac{1}{r} \frac{\delta}{\delta r} r \frac{\delta u}{\delta r} \right) + \frac{F_z}{\rho g} \quad (7.9)$$

in the direction of r:

$$u \frac{\delta v}{\delta z} + v \frac{\delta v}{\delta r} - \frac{w^2}{r} = - \frac{1}{\rho} \frac{\delta p}{\delta z} - \frac{\delta}{\delta z} \langle u'v' \rangle - \frac{1}{r} \frac{\delta}{\delta r} r \langle v'^2 \rangle + \frac{\langle w'^2 \rangle}{r} + v_g \left(\frac{\delta^2 v}{\delta z^2} + \frac{1}{r} \frac{\delta}{\delta r} r \frac{\delta v}{\delta r} - \frac{v}{r^2} \right) + \frac{F_r}{\rho g} \quad (7.10)$$

in the direction of ϕ :

$$u \frac{\delta w}{\delta z} + v \frac{\delta w}{\delta r} - \frac{vw}{r} = - \frac{\delta}{\delta z} \langle u'w' \rangle - \frac{1}{r} \frac{\delta}{\delta r} r \langle v'w' \rangle - \frac{\langle v'w' \rangle}{r} + v_g \left(\frac{\delta^2 w}{\delta z^2} + \frac{1}{r} \frac{\delta}{\delta r} r \frac{\delta w}{\delta r} - \frac{w}{r^2} \right) + \frac{F_\phi}{\rho g} \quad (7.11)$$

The products of velocity fluctuations, enclosed by the triangular brackets, $\langle u'_i u'_j \rangle$ are time averaged values. If multiplied by ρg , the product $\langle u'_i u'_j \rangle$ represents the transfer of x_i momentum in x_j direction by turbulence (fluctuating velocities):

$$\tau_{ij} = - \rho \langle u'_i u'_j \rangle.$$

These are called Reynolds stresses. Figure 7.2 shows their nomenclature in a cylindrical coordinate system.

It can be proven (for instance Leijdens [1984]) that $\tau_{ij} = \tau_{ji}$, so that in total six Reynolds stresses are defined.

F_z , F_r and F_ϕ are external forces which can for instance represent the effect of droplets with which the gas phase exchanges momentum. As the formulated models are in first instance assumed to concern a single gas phase, these forces can be taken equal to zero.

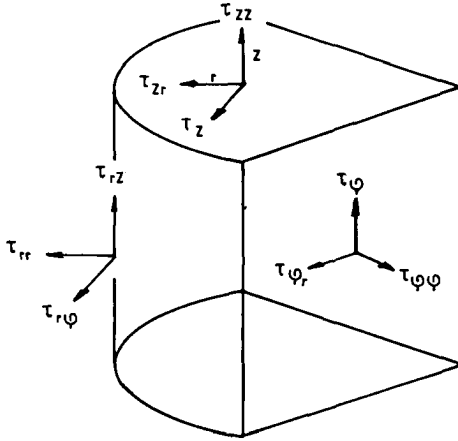


Figure 7.2 Nomenclature for Reynolds stresses

Closure problem

It appears that equations 7.8-7.11 are coupled and non-linear. They describe the gas flow completely, because no simplifications have been made in the derivation of any of the terms. With 10 unknown variables and 4 equations, they obviously do not form a closed system.

Herewith the well-known closure problem is introduced, which has been the subject of many investigations since its creation by Reynolds [1877].

The solution for this closure-problem is formed by turbulence models, which somehow quantify the six Reynolds stresses as a function of velocities and pressure. The importance of the turbulence model on the reliability of the gas flow field predictions is demonstrated extensively in sections 7.4-7.6. Strongly rotating flows are anisotropic, which means that the Reynolds stresses will have to be solved individually. They should not be assigned a collective equal value, which takes place in the most popular simpler turbulence models that are presently in use.

In appendix D the characteristics of the turbulence models that play a role in the models described in sections 7.4-7.6 are explained.

7.2.2 Mathematical background

The numerical technique to solve the fundamental equations, governing fluid flow and the additional equations expressing the conservation of the parameters of the turbulence model, involves (Patankar [1980]):

- subdivision of the domain of interest into a finite number of control volumes ('grid cells');
- discretisation of the partial differential equations over these volumes to obtain sets of algebraic relations;
- the use of an iterative solution procedure since the differential equations are coupled and non-linear.

Discretisation of conservation laws

The discretisation equation (or finite difference equation) has the following general form to determine the value of a variable ϕ in a stationary system:

$$\phi_p = \frac{a_1\phi_1 + a_2\phi_2 + a_3\phi_3 + a_4\phi_4 + a_5\phi_5 + a_6\phi_6 + S_c}{a_1 + a_2 + a_3 + a_4 + a_5 + a_6 + S_p}$$

in which:

ϕ_p : the value of ϕ in grid cell p;

1-6 : refer to the bordering grid cells in case of a 3D grid;

a : the coefficient that determines the contribution to ϕ_p by ϕ in a neighbour cell. 'a' is a function of the mass flow rate between the cells and the diffusion coefficient;

S : the contribution to ϕ_p by external sources

$$S_p = S_c + S_p \phi_p$$

Apart from this equation the mass balances (continuity equation) is calculated for each grid cell as well.

Iterative solution procedure

It is referred to Patankar [1980] for a full description of the iterative methods that are used to solve the above mentioned coupled linear equations.

7.2.3 Fluid dynamic codes used

Two existing codes were used:

- i) Phoenix, by Cham Ltd.
- ii) Fluent , by Creare Inc.

The numerical solution procedure of both codes is based on the earlier described 'control volume' method.

Phoenix was available through the University software library and, moreover, placed at the disposal of final year students by Neratoom B.V.

Because the installed version (1.3) still featured some bugs of which the identification proved to be time consuming and because Phoenix did not have built-in anisotropic turbulence models, the results achieved with the package for highly swirling flows (cyclones!) were very disappointing. Especially with respect to the number of CPU hours used. Satisfying results were achieved when modelling the gas flow field between vane blades.

Fluent was temporarily placed at the disposal of final year students by Koninklijke/Shell-laboratorium, Amsterdam. This code is much better equipped to model rotating flows as it offered possibilities to simulate anisotropic gas flow fields. The modelling results (or attempts) are described in the MOD1 blocks in sections 7.3-7.5.

7.3 Physical modelling of gas/liquid interactions

7.3.1 Introductory remarks

In this section physical models are formulated that form common elements in the MOD2 blocks. These blocks describe the behaviour of the various forms of the liquid phase during the process of separation.

Two forms of the liquid phase that are present in all separator types under investigation and for which general relations are derived in this block are:

- a. the original mist phase;
- b. the film formed by separated liquid under centrifugal accelerations.

7.3.2 Behaviour of droplet phase

The behaviour of a disperse phase can be predicted with numerical methods either by:

1. viewing the disperse phase as a continuum and modifying the laws of conservation as such that they describe this disperse phase (Eulerian approach, see for instance Hinze [1975]);
2. viewing the disperse phase as discrete particles of which the dynamics are determined by interactions with the continuum (Langrangian approach).

The second approach is chosen. If it is assumed that the particle does not influence the gas phase momentum, the time consuming and expensive simulation of a gas flow field has to be carried out only once. With the results it is possible to determine the trajectory of droplets in this particular gas flow field in a simple way. The assumption mentioned above is valid throughout the largest part of the cyclone as the slip velocity between particle and gas is very small.

Complications might arise in the inlet section of the cyclone at high concentrations of the disperse phase. Then the momentum, necessary to accelerate the mass of particles, might result in a considerable decrease of the gas phase momentum, leading to lower tangential velocities throughout the cyclone than originally simulated.

When it is assumed that:

1. droplet-droplet interactions are absent (which is the case in dilute mists);
2. only drag forces will play a role in the determination of the particle trajectory (which is the case if the droplet size is between $1 \mu\text{m} < d_d < 100 \mu\text{m}$ and $\rho_l - \rho_g > 500 \text{ kg/m}^3$)

the relations to characterize droplet motion in cylindrical coordinates are easily derived (see equation 3.3 and figure 3.4):

$$\frac{d U_d}{dt} = - \gamma (U_d - U_g) [U_d - U_g] - g \quad (7.12)$$

$$\frac{d V_d}{dt} = \frac{w_d^2}{r} - \gamma (V_d - V_g) [V_d - V_g] \quad (7.13)$$

$$\frac{d W_d}{dt} = 2 \frac{V_d W_d}{r} - \gamma (W_d - W_g) [W_d - W_g] \quad (7.14)$$

In these equations:

$$\gamma = \frac{3}{4} \frac{\rho_g}{d_d(\rho_l - \rho_g)} C_d \quad (7.15)$$

U_d, U_g = axial velocity of respectively droplet and gas

V_p, V_g = idem, radial velocity

W_p, W_g = idem, tangential velocity

$$C_d = a_1 + a_2/Re + a_3/Re^2 \quad (7.15a)$$

with $a_1 - a_3$ quantified according to Morsi and Alexander [1972].

It can be reasoned that in case of droplet trajectories in highly swirling flows C_d must be quantified as $C_d = 24/Re$. In this case $(U_d - U_g) \sim 0$ and $(W_d - W_g) \sim 0$. Only the radial differential velocity will then contribute to the droplet Reynolds number. Re_d may under practical circumstances amount up to $Re \sim 10-20$ which would normally not justify the assumption that Stokes' Law applies. However, as the amount of turbulence that can form in radial direction is very limited because of the stabilizing action of the centrifugal field, it is not probable that flow separation and wake formation behind the droplet will take place.

From equations 7.14 and 7.15 it becomes clear that this has strong implications for the dependency of the minimal necessary gas velocity in a separator on the operating pressure. If Stokes' Law applies there is only a weak dependency through the group $(\rho_l - \rho_g)$. If Stokes' Law does not apply the constant a_1 in equation 7.15a becomes non zero and a much stronger dependency is created. Although not yet quantified, one can expect that in case $\langle w' \rangle$ is very small (cyclone operation) $C_d \sim 24/Re$. With this relation the particle trajectories have been calculated in section 7.4. In vane packs the situation is more complicated as a centrifugal field will be alternated by a straight gas flow field.

The effect on the mist particles will strongly depend on where the mist particles occur. The simulation described in section 7.6, in which particle

trajectories between the vanes are calculated, have made use of a conventionally calculated value for C_d (equation 7.15a).

The fluctuating components $\langle u' \rangle$, $\langle v' \rangle$ and $\langle w' \rangle$ are neglected. From the results of MOD-AC1 appeared that in most cases the turbulent kinetic energy, k , remained smaller than $1 \text{ m}^2/\text{s}^2$. This means that $\langle u' \rangle^2 + \langle v' \rangle^2 + \langle w' \rangle^2 < 2 \text{ m}^2/\text{s}^2$. It can also be assumed that the influence of the droplets on the gas can be neglected (dilute concentrations). The latter assumption is verified in AC-EXP3 and RFC-EXP4.

The grid that has been set up for the flow field calculations and the resulting values of the velocity components are used as a framework for the droplet trajectory calculations. It is assumed that the velocity of the droplet remains constant when traversing a grid cell; its new velocity will be determined when it crosses a radial plane. The total gas flow field has been divided into sufficiently small calculational volumes (totalling to more than 1200 grid cells in one axial plane). Therefore it is assumed that this procedure will prove adequately accurate.

7.3.3 Behaviour of the liquid film

From sections 5.2-5.3, it appears that no earlier research has been reported concerning the liquid films presently investigated. For this reason some of the models and correlations cited in chapter 5 will be modified so that their validity extends to conditions of high centrifugal accelerations and high gas densities.

The specific objective of this section is to determine the upper limit of the stability range (onset of reentrainment) of the internal liquid films under centrifugal acceleration. The logical structure of the determination of these conditions consists of the following elements:

1. First it is determined when the liquid film breaks up in strings or rivulets, in order to ensure that the liquid will reach the onset of reentrainment in the form of a film (description of rivulets would necessitate a completely different model);

2. A stability criterion for the onset of roll waves will be derived as these are necessary elements in the reentrainment mechanism.
3. On the basis of the phenomenological models of Ishii [1975] and Kutateladze [1972] a model will be described that accounts for the modified roll wave criterion and for changes of the gas/liquid interface.

ad 1. Minimal film thickness to ensure full wetting

The criterion (equation 5.3) in section 5.3 derived by Bankoff [1971] is compared to experimental results of block RFC-EXP2. The gravitational constant in his criterion is replaced by the tangential acceleration (w_1^2/r). It appears that for low gas velocities the prediction agrees well with the experimental observations. For higher gas velocities the discrepancy increases and nearly always a continuous film is observed. This is obviously due to the increasing shear stress that is exerted on the liquid surface, which is not taken into account by Bankoff. Because this effect appears to be very strong, it is decided to assume that for the gas velocities at which reentrainment can occur, there will always be a fully wetted inner perimeter with an evenly distributed film. As the experiments of RFC-EXP2 showed, there can always be a variation in film thickness because of radial assymetry in the location of the entrance slits.

ad 2. Modified criterion for roll wave formation

If the reentrainment criteria are observed that Ishii and Kutateladze (equations 5.14-5.19) derived for liquid films of which the Reynolds number exceeds 160, reentrainment is supposed to take place by shearing off the crests of roll waves.

In section 5.4.2 it has been shown that for liquid film Reynolds numbers of $Re_1 > 200-300$ the critical gas Reynolds number becomes independent of most physical properties of the two-phase mixture. This critical value of Re_g is influenced by the increased gravitation induced by film rotation in the following way:

$$\frac{(\bar{v}_g - \bar{v}_1)_{rot}}{(\bar{v}_g - \bar{v}_1)_{lin}} = \sqrt{\frac{2w_1^2}{gD}}$$

in which the subscripts rot and lin signify rotating film, respectively non-rotating film.

If it is assumed that the other conditions remain constant on basis of the model of Andreussi [1980] it can be stated that:

$$\text{Re}_{\text{gwc}} = 11.10^4 \sqrt{\frac{2w_1^2}{gD}} \quad \text{for } \text{Re}_1 > 200. \quad (7.16)$$

In which Re_{gwc} = critical gas Reynolds number at which roll waves occur. Figure 7.3 shows the effect of an increasing factor $G = \sqrt{\frac{2w_1^2}{gD}}$ on the inception of roll waves. The dotted lines at $\text{Re}_1 < 200$ represent the divergence of the two theories investigated in section 5.4. (a) for the Kelvin-Helmholtz instability-theory and (b) for the linear stability theory refined by Andreussi (see section 5.4.2).

To determine a stability criterion for the liquid film in centrifugal separators the following line of reasoning is followed:

- a. A relation is derived with which the film velocity can be derived from the local gas velocity (Re_g) inside a centrifugal separator;
- b. A relation is derived with which the film thickness can be derived from the local gas velocity (Re_g);
- c. Combination of the two above relations gives:
 - a relation between Re_1 and Re_g inside a cyclone;
 - a relation between the film stabilization as a function of Re_1 or Re_g .

With the last two relations it is possible to determine under which operating conditions roll waves will occur on the liquid film.

ad a. The film velocity can be determined combining equations 5.7 and 5.8 which leads to:

$$v_1 = \sqrt{\left(\frac{f_{gi}}{f_{li}} \frac{\rho_g}{\rho_l} \right)} (v_g - v_1) \quad (7.17)$$

in which: $f_{gi} = 0.02$ (see equation 5.12)

$$f_{li} = (K_i Re_f^m)^2 \quad (\text{see equation 5.11})$$

$$K_i = 1.962$$

$$m = -\frac{1}{3}$$

for $100 < Re_1 < 1000$

$$f_{li} \sim 0.03$$

for $Re_1 > 1000$

as v_l/v_g is in most cases smaller than 0.03, v_l is neglected with respect to v_g .

This relationship compared against experimental data is shown in figure 7.4.

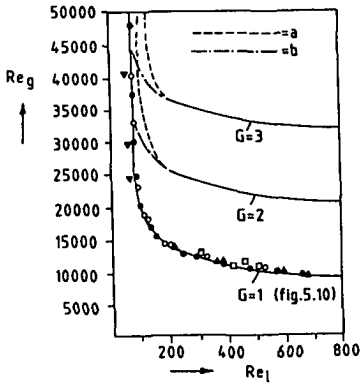


Figure 7.3 Influence of centrifugal force

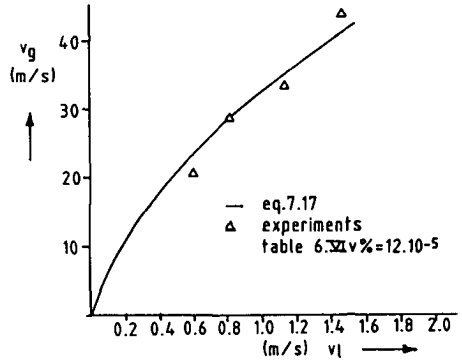


Figure 7.4 Relation between v_g and v_l

ad b. The film thickness depends on:

- the amount of liquid separated from the gas (ϕ_l);
- the internal wetted perimeter (πD);
- the axial film velocity (discharge rate) (u_l).

$$b = \frac{\phi_l}{\pi D u}$$

(7.18)

When the gas flow increases through a cyclone the amount of separated liquid will increase accordingly (assuming full separation). The swirl angle of the gas flow will not change (see section 5.5). It appeared that for most film thicknesses the liquid film velocity depends linearly on the gas velocity. Therefore, it can be concluded that the axial liquid film velocity (or the liquid discharge rate) increases linearly with an increase of the gas flow through the cyclone.

As the increase of discharge rate compensates for the increase of separated liquid in the cyclone the film thickness in the cyclone is largely independent of its gas throughput and will mainly be determined by the liquid loading of the gas.

ad c. From the two previous derivations it appears that for a certain liquid loading of the gas and a certain operating pressure (p_g) the increase of Re inside a cyclone as a result of the increase of Re will only be caused by an increased film velocity. At other gas densities the new relation between Re_l and Re_g can be determined according to equation 7.17. At other liquid loadings of the gas also changed values of the film thickness (equation 7.18) should be considered in the determination of Re_l . This is depicted indicatively in figure 7.5.

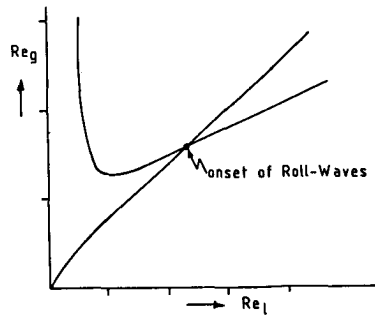
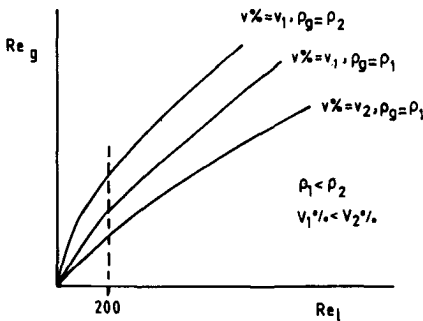


Figure 7.5 Relation between Re_l and Re_g Figure 7.6A Roll wave inception in cyclones

With this information it is possible to couple the stability criterion for roll waves derived in section 5.4 (equation 7.16) to the relation between Re_g and Re_l inside a cyclone.

An increase in Re_1 at constant gas density and liquid loading means a corresponding increase of liquid film velocity. As the swirl angle remains constant, a corresponding increase of the tangential film velocity, and thus of G , will be effected. So, for a certain geometry, G will only depend on Re_1 (at constant ρ_g and liquid loading). Because the relation between Re_1 and Re_g inside a cyclone is known, the onset of roll waves inside a particular geometry can be determined. This is depicted indicatively in figure 7.6A. Figure 7.6B gives a graphical example of the effect of increase of the operating pressure. The film velocity increases according to equation 7.17, resulting in an increase of G (tangential component) and of the discharge rate (axial component). Therefore the film thickness decreases (equation 7.18) correspondingly, resulting in an unchanged Re_1 . It appears that at the new combination of Re_1 and Re_g (point II) roll waves will occur. If one would like to prevent this, Re_g should be decreased through lowering the gas velocity to the level at which the inception criteria is not longer met (point III). The absolute value of the necessary decrease depends on the local angle of swirl that determines which part of the increased film velocity is attributed to the tangential velocity. Figure 7.6C gives a graphical example of the effect of an increase of the liquid loading of the gas processed by a cyclone. The liquid film thickness will increase (equation 7.18), but the liquid film velocity (and thus also G) will remain approximately constant (equation 7.17). Therefore, from a situation that just not meets the roll wave criterion an increase of liquid loading of the gas will not lead to the onset of roll waves.

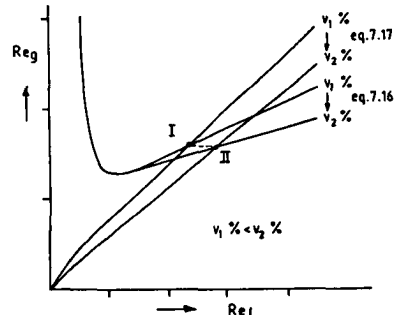
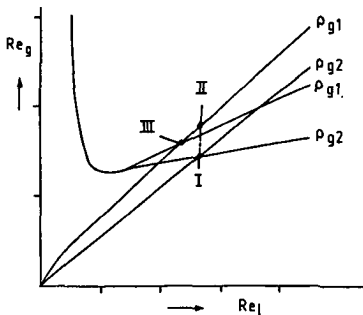


Figure 7.6B Influence of gas density Figure 7.6C Influence of liquid loading

ad 3. Modified criterion for the onset of reentrainment

Sofar only a criterion is given for the occurrence of roll waves. Ishii [1975] and Kutateladze [1972] set up the following relation to describe the onset of reentrainment in the presence of roll waves in which the forces act that are depicted in figure 7.7.

$$\frac{u_1 (v_g - v_l)}{\sigma} * \sqrt{\frac{\rho_g}{\rho_l}} \geq \frac{C_s \sqrt{f_{gi}}}{C_D C_W (N_u)} \frac{1}{\sqrt{f_{li}}}$$

C_D = drag coefficient of wave

C_S = interfacial shape coefficient

C_W = factor to account for the internal flow in the wave as a function of N_u
(viscosity number: see equation 5.15)

In order to derive a useful relation Ishii proposed to:

1. quantify f_{gi} with the relation of Wallis [1969] (equation 5.9) and because of small values of the film thickness he proposed to approximate this relation by assuming $f_{gi} = 0.005$;
2. quantify f_{li} with the relations of Hughmark [1973] (equation 5.11);
3. neglect v_l with respect to v_g so that $(v_g - v_l) \sim v_g$.

The second and third quantification seem reasonable in the present situation, but the approximation of f_{gi} by assuming $f_{gi} = 0.005$ is not realistic.

As $\frac{b}{D}$ can amount to values of $\frac{b}{D_H} = 0.05$ and is in nearly all cases larger than $\frac{b}{D_H} > 0.01$ it is more advisable to use the relation that quantifies f_{gi} for rotating (water/air) systems derived from the experimental results of Loxham [1976]). Assuming that $\frac{b}{D_H} > 0.01$ this leads to $f_{gi} = 0.02$.

Because Re_l will in all cases amount to $Re_l > 160$, the criteria of Ishii to describe the onset of reentrainment will have the following form for rotating flow systems with roll waves (for $\sqrt{\frac{2w_1^2}{gD}} > 1$):

$$\frac{\mu_1}{\sigma} \frac{v}{g} \sqrt{\frac{\rho_g}{\rho_1}} \geq 23.6 N_\mu^{0.8} Re_1^{-1/3} \text{ for } Re_1 < 1600 \text{ and } N_\mu \leq \frac{1}{15}$$

$$\frac{\mu_1}{\sigma} \frac{v}{g} \sqrt{\frac{\rho_g}{\rho_1}} \geq 2 N_\mu^{0.8} \text{ for } Re_1 > 1600 \text{ and } N_\mu \leq \frac{1}{15} \quad (7.19)$$

This is the only way to account for the increased gravitation force as all forces that play a role in the mechanism depicted in figure 7.7 act perpendicular to and are independent of the gravitation force.

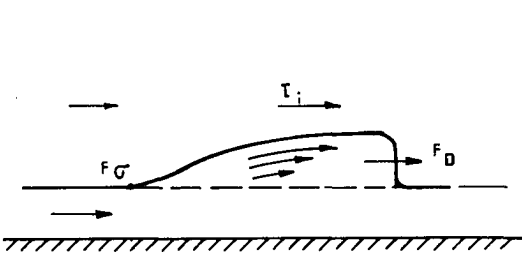


Figure 7.7 Forces on wave crest

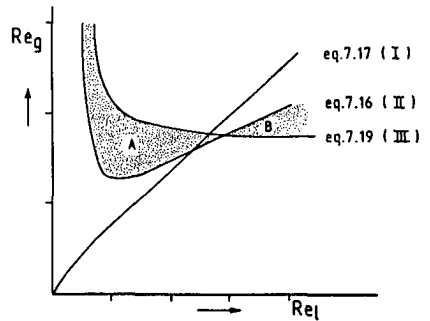


Figure 7.8 Graphical representation of proposed model

In order to determine whether reentrainment will take place in a cyclone, the graph depicted in figure 7.8 has to be considered. Lines I and II are described before and depend on cyclone geometry and operating conditions. Line III is the reentrainment criterion given in equation 7.17.

Two distinctly different regions can be discerned:

1. at lower film Reynolds numbers: it appears that above the onset of roll waves the gas Reynolds number can still be increased prior to the onset of reentrainment (region A in figure 7.8).
2. at higher film Reynolds numbers: it appears that the criterion for the onset of reentrainment sets a more conservative limit to Re_g than for onset of roll waves. This implies that an unstable region exists (between lines III and I) in which momentary film instabilities can be reentrained immediately (as the operating conditions conform to the reentrainment criterion). When line II is exceeded roll waves are initiated from which reentrainment will take place immediately (region B in figure 7.8).

With the combination of the information to which is referred in figure 7.8, it can be determined in which stability region the film is inside a particular cyclone geometry.

This model, which is still conceptual, has reasonably reliably been confirmed by the results of RFC-EXP2 in which reentrainment experiments have been carried out.

The only important differences between model and experiments were the higher predicted values of the critical Re_g at which actual reentrainment took place and the lower dependency of this Reynolds number on the gas density. This can be explained adequately by the already mentioned irregular distribution of the film across the perimeter that is caused by geometrical assymetry of the inlet section.

Figure 7.9 shows an example of the predicted and measured influence of liquid loading. Figure 7.10 of the predicted and measured influence of the pressure drop.

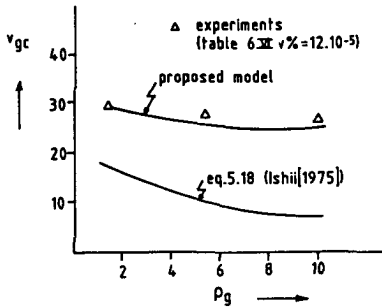


Figure 7.9 Validation of model I

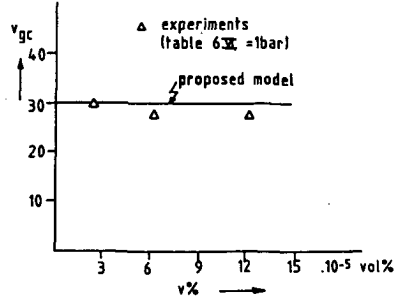


Figure 7.10 Validation of model II

7.4 Axial cyclone models

For the project structure and nomenclature see innerside of the front cover.

7.4.1 Block AC-MOD1

Objective: Formulation of a model that describes the gas flow field inside an axial cyclone as a function of its geometry.

Summary : The attempts based on the Fluent code have been very successful; a good agreement between simulation and experiment has been achieved. Before the actual cyclone model is set up and validated two exercises are carried out.

1. The validity of Fluent for simulating rotating flows is verified.
2. A simplified procedure to represent swirl elements is conceived.

The disappointing results from the Phoenix simulations are not described. These simulations were in the first place less successful because of the earlier mentioned inadequacy of the built-in turbulence models for swirling flows.

The Fluent and Phoenix codes are introduced in section 7.2.3.

ad 1. Setting up Fluent to model rotating flow fields

An experimentally very well characterized rotating flow has been the subject of simulation to:

1. verify the validity of the gas flow field simulation procedure for rotating flows;
2. formulate the boundary conditions specifically to the simulation of rotating flows.

The measurements used for this purpose were carried out by Loxham [1976] and are reported in section 5.5.2 (appendix B.1). These results were particularly suited since they characterized the free evolution of a rotating flow in a long straight tube without geometrical complexities.

Of the following aspects the influence on the reliability of the simulation has been investigated:

- i. grid geometry;
- ii. outflow conditions;
- iii. turbulence model.

ad i. Grid geometry

The two-dimensional, axially symmetrical grid that proved to be adequate for a satisfying simulation comprised:

- a. condensed axial grid lines at the locations where the largest velocity gradients were expected to occur; thus at the wall and in the centre;
- b. a downstream elongation of the tube to achieve a further decay of the swirl to a level at which backflow would not occur anymore in the centre of the outlet. Central regions in rotating flows in which backflow occurs are observed at swirl numbers larger than $S = 0.6$ (Schetz [1980]); this effect can easily be explained and is caused by rapid decay of swirl intensity (see figure 7.6A).

If the latter provision was not included, the simulation would almost immediately diverge when the developing area of backflow reached the exit of the tube. When this happened, inflowing gas would import angular momentum, leading to steadily increasing velocity gradients on the axis. At a certain stage these could no longer be handled by the simulation code, and the iteration procedure would be terminated.

With the elongation of the tube a practical situation was modelled in which the swirl was decayed to such an extent that no backflow occurred any longer at the outlet plane. The upstream consequences of this elongation were investigated by Kerstjens [1988] and proved to be negligible. In this reference an exact description of the grid geometry is given as well.

ad ii. Outflow conditions

The outflow conditions that appeared to be adequate set the axial velocity gradient at the output cells to zero. No other options have been tested.

ad iii. Turbulence model

It is referred to appendix D for explanation of the properties of the turbulence models mentioned below.

The standardly built in algebraic stress model proved to be reasonably suitable. It has been attempted to decrease (small) discrepancies between simulation and experiments by adjusting some parameters of the turbulence model. Below, these attempts will be described in detail.

Because the tangential shear stresses in the centre of the radial plane ($\langle v'w' \rangle$) proved to be very low in comparison to the axial shear stresses at

these locations ($\langle u'w' \rangle$), the isotropic $k-\epsilon$ turbulence model in its original form is useless. Making use of the $k-\epsilon$ model the effective (isotropic) turbulent viscosity is calculated much too high with respect to the actual angular momentum transfer. This results in a simulation that predicts a too rapid decrease of swirl intensity. Because of this effect simulated highly swirling (combined vortex) flows will be transformed very quickly into weak solid body rotations. (For a more elaborate description of these effects, see Pelsma [1987], Karvinen [1987], Boysan [1985].)

The results of the simulations based on the experiments of Loxham are depicted in figures 7.10 A,B and C.

Accuracy of axial flow field predictions

The simulated evolution of the axial velocity profile in axial direction looks very similar to the experimentally determined evolution.

The simulated profiles tend to depict larger velocity gradients. However, this discrepancy is probably partly caused by experimental inaccuracy.

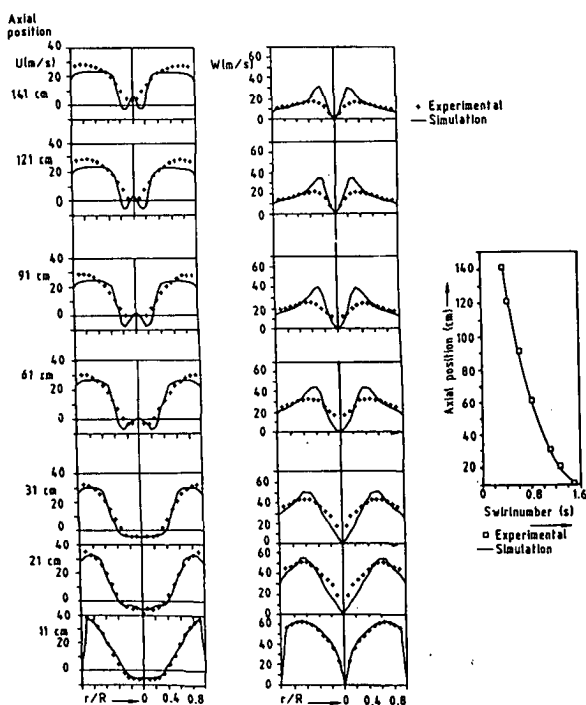


Fig. 7.10A, B and C Verification of predicted swirling flows in a straight tube

From the experimental results of Loxham [1976] it appears that the throughput at a certain stage (at the radial plane $z = 121$, see appendix B) is for instance 11% lower than the original input (at the radial plane $z = 11$). These throughputs have been calculated by integration of the axial velocity profiles. In the case of simulated gas flow field another clear difference is the reversal of gas flow direction on the axis in the central back flow area. Whether this effect is caused by an anomaly in the simulation procedure or whether it is an actually occurring phenomenon, for which the measurement techniques used by Loxham (pitot tube) were too coarse, has not been investigated. It has been noticed that this effect also occurred in other rotating flow simulations (Karvinen [1985]).

Accuracy of tangential flow field predictions

The decay of the swirl intensity is almost exactly predicted. This is a very convincing sign that some fundamental laws are reliably represented. The tangential flow fields are less strikingly similarly simulated, although generally the form and axial development of the velocity profiles are much alike. The most important difference between simulation and experiment seems to be the radius at which the free vortex form takes over from the forced vortex. This point is located too close to the centre. Related to this effect are the too high simulated values of the tangential velocity maximum and the rotation speed of the forced vortex.

The reason of these phenomena might be caused *) by too low calculated $\langle v'w' \rangle$ shear stresses.

The forced vortex does not export enough angular momentum in radial direction to expand itself to a larger radius (thereby reducing its speed of rotation). Two attempts have been carried out to modify the constants of the turbulence model to decrease the discrepancy:

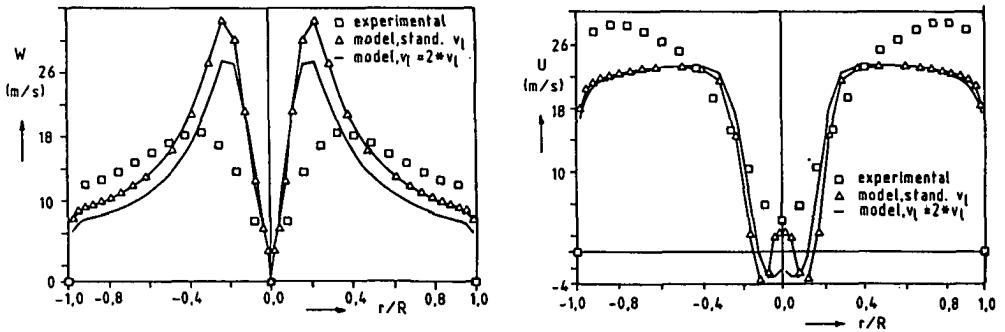
*) This effect might also be caused by experimental inaccuracy. Precessing of the vortex might lead to the same observed discrepancy if velocity measurements are carried out with pitot-tube (for a more complete explanation see Kerstjens [1988]).)

- The laminar viscosity has been doubled. Because the turbulence shear stresses and corresponding turbulence viscosity in this region are very low this increase may lead to the desired effects (see eq. 7.9-7.11).
- The constant α has been decreased in equation D.19 in order to increase angular momentum transport (constant c_2 was chosen $c_2 = 1.1$ instead of $c_2 \approx 0.55$).

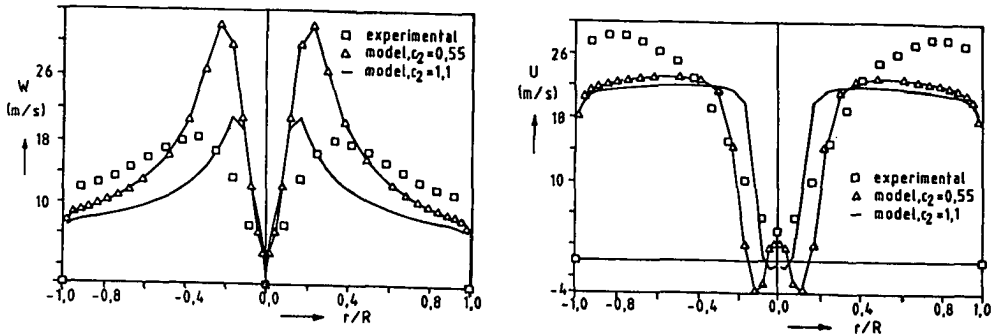
Increasing the laminar viscosity leads to an evenly decreased tangential velocity on the free vortex side; the point of vortex form change-over and forced vortex rotation speed is left unchanged (see figures 7.11A and B).

This means that the $\langle u'w' \rangle$ stresses in the forced vortex are very small (which is to be expected for solid body rotations).

Facilitating the transport of the Reynold stresses the second option leads to comparable results (figures 7.12A and B).



Figures 7.11A and B Effect of increase of v_{lam}



Figures 7.12A and B Effect of increase of C_2

The tangential velocities are reduced on the free vortex side, but the point of vortex form changeover and forced vortex rotation speed is not influenced. The necessity of a turbulence model that accounts for anisotropy when simulating this type of rotating flow is clearly indicated by figures 7.11A and B). The tangential velocity profile is influenced quite strongly by doubling the laminar viscosity. This means that the turbulence component in this direction is so low that the share of viscous forces in the momentum transportation is of the same order of magnitude as the share of turbulence stresses. The axial profile on the other hand, shows hardly any significant changes by these adjustments, which means that the viscous forces play a subordinate role; an indication of a high level of turbulence.

From figure 7.11 it can be concluded that the maximal $\langle v'w' \rangle$ stresses take place at the vortex change-over point. They are minimal on the forced vortex side, and decrease steadily to the wall on the free vortex side.

Unfortunately financial and time limitations prevented further investigations to discover possibilities to decrease the rotation speed of the forced vortex.

Ad 2. A simplified procedure to determine the initial flow field of a swirl element

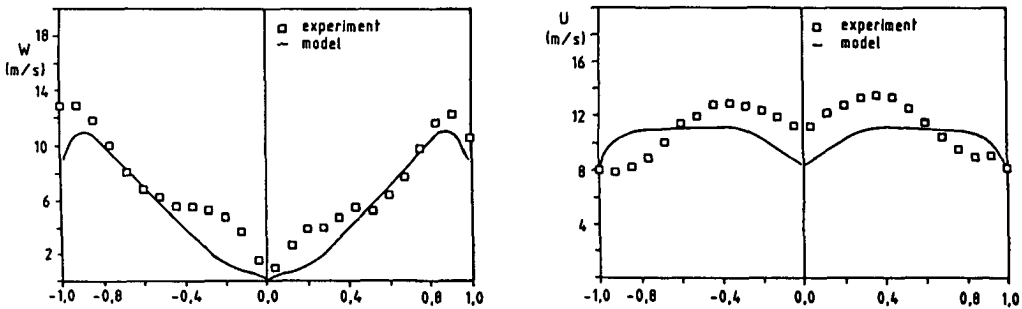
Modelling of the swirl element has been prevented. Firstly this would cause the need to run three instead of two dimensional simulation models (sharp increase of computer running time). Secondly, every time another swirl element would be simulated, a completely new (three dimensional) grid would have to be puzzled together (lengthy model set-up times).

It appeared that most types of axial swirl elements (in section 5.5.3 all except type A) initially induced pure solid body rotations. This is a direct consequence of the swirler geometry. This velocity distribution then evolves further downstream under influence of hydrodynamic and drag forces. The angular momentum immediately downstream of the swirl element is either measured directly or calculated from measurements further downstream and from swirl decay data. With the knowledge of the angular momentum somewhere downstream of the swirl element and with the assumption of an evenly distributed axial flow the flow field just above the swirler can be reconstructed quite easily.

In figures 7.13A and B the validation of this procedure is demonstrated. From a velocity profile, measured at 1.5 diameters downstream of the swirl element, the angular momentum was calculated. This angular momentum was corrected for the amount of swirl decay that had occurred in the 1.5 diameters length from the swirl element. A solid body rotation with the calculated angular momentum was used as starting condition in a simulation. The velocity profile 1.5 diameter downstream was simulated and compared to the original measured profile.

The simulations that were run from this point onwards characterize a swirl element by assigning to it a certain swirl number. Under the assumptions described above the initial flow field can easily be reconstructed.

The corresponding swirler geometry can be deduced from the required swirl number, allowable pressure drop and the information presented in block AC-EXP1.



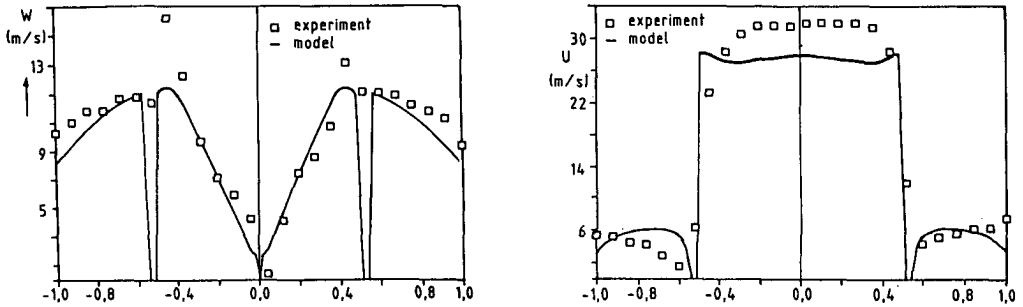
Figures 7.13A and B Validation of simplified swirl element representation

Verification of gas flow field predictions of an axial cyclone

With the elements described before, it is a minor step to describe the full gas flow field inside an axial cyclone with a coaxial liquid discharge (see section 3.4.4.5). The modelling of a cyclone with a radial liquid discharge will be less straight forward, because the decrease in axial symmetry will cause the need to model three-dimensionally. In first instance only the former cyclone type has been simulated with the expectation that the flow fields of the other cyclone type could be deduced from this in a reasonably simple way.

Coaxially purging axial cyclone

In figures 7.14A and B an example is given of the validation scheme: the prediction of the gas flow field just underneath the outlets is compared to actual measurements. Both tangential and axial velocity profiles are reported sufficiently exact.



Figures 7.14A and B Validation of gas flow field predictions in coaxially purging axial cyclones at location C (figure 6.10A)

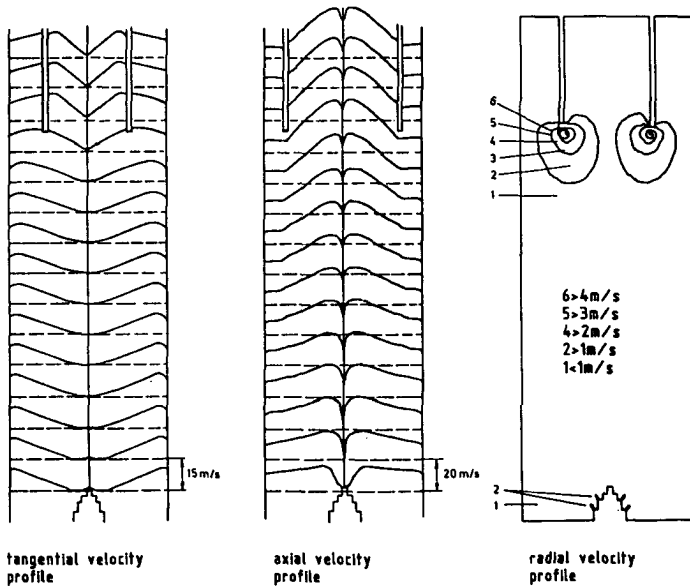


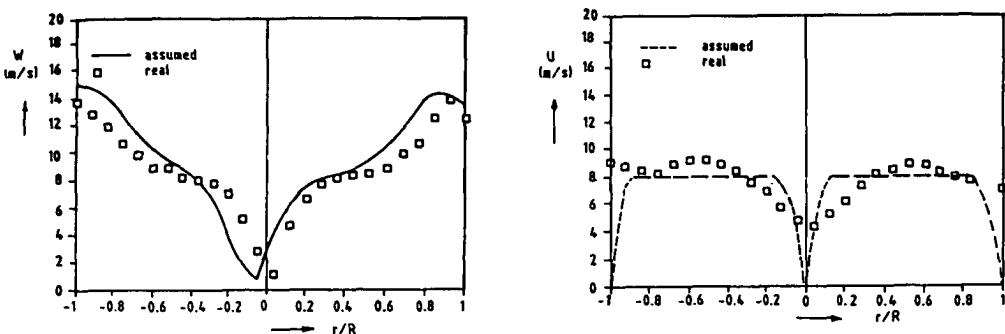
Figure 7.14C Example of a full flow field simulation at $S = 0.55$

Radially purging axial cyclone

As the exact simulation of this geometry type would necessitate a three dimensional, and thus expensive, approach it has been attempted first to derive acceptable results from the simulated flow fields of otherwise corresponding coaxially purging cyclones.

From earlier reported studies (see section 5.5) it can be concluded that the radial location of the tangential velocity maximum is mainly determined by the swirl number of a rotating flow. In case of a radially purging axial cyclone it can therefore be expected that, if not too much angular momentum is lost with the purge gas, the location of the tangential velocity maximum will not lie at significantly different locations than in otherwise corresponding coaxially purging axial cyclones.

The axial velocity profile determines the superficial volume rate and is not so much effected by characteristics of the swirling flow. The profile of this velocity component will therefore be determined in a radially purging cyclone, on one hand by the radial inflow imposed by the constriction of the vortex finder and on the other hand by the radial outflow imposed by the radial purge. Based on the results from simulations of the previous cyclone geometry, simulations of the behaviour of this cyclone have been carried out. In figures 7.15A and B the measured and assumed velocity components in the two cyclone types are compared. The agreement is satisfiable for the purpose of simulation.



Figures 7.15A and B Justification of assumptions with respect to radially purging axial cyclones

7.4.2 Block AC-MOD2

Objective: Formulation of relations that describe the behaviour of the liquid phase inside an axial cyclone.

Summary : The various forms of the liquid phase and their origins are identified. For each of these forms relations are set up to describe the behaviour and to predict possible critical effects.

In an axial cyclone the liquid phase can occur in one of the following forms (see figure 7.16):

- a. as the original mist phase (I);
- b. as the liquid film formed by separated droplets (II);
- c. as the droplets that are reentrained from this film (III);
- d. as drops/droplets formed during the discharge action in the secondary separation zone (IV).

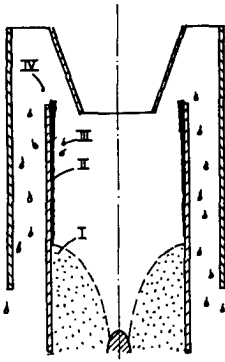


Figure 7.16 Forms of liquid in an axial cyclone

ad a. Behaviour of mist phase

In section 7.3.2 adequate relations are given to predict the trajectories of mist particles in a rotating flow field.

ad b. Behaviour of film

In section 7.3.3 adequate relations are given to predict the behaviour of the liquid film in a centrifugal force field.

ad c. Behaviour of droplets that are reentrained from separated film

To draw any conclusions as to what respect reentrained droplets exert detrimental effects on the separation efficiency, both droplet size distribution and initial velocity of these droplets must be evaluated with respect to the local gas flow field characteristics. In section 5.4 relations have been derived for both quantities.

If the droplet size distribution is determined according to equations 5.22-5.25 and R_E in these equations according to equation 5.21 values of reentrained droplet diameters are found between 30 and 300 μm , depending on correlation and specific operating conditions. It is recommended to consider these values as indicative because the cited correlations are by no means consistent to each other.

Equation 5.25 gives an indication of the initial velocity of the reentrained droplets perpendicular to the film surface. Maximal values of v_{rad} between 2-3 m/s are found independent of drop size but depending on u^* .

ad d. Behaviour of droplets in the secondary separation zone

The separation mechanism of this step is supposed to be the fall-out of the droplets against the relatively low gas velocities between the axial cyclones (see figure 7.16). In order to determine whether these gas velocities are low enough for a successful secondary separation it is necessary to quantify the sizes of the droplet that are created when the film is discharged from the separation zone. For this purpose simple indicative relations will be provided to determine these diameters for both liquid discharge principles under investigations.

Coaxial liquid discharge

The sizes of the droplets that are created during the discharge process are determined by the balance of break-up forces (centrifugal acceleration over the cyclone top and interfacial forces) and containing forces (surface tension). This balance is depicted in figure 7.17.

It is assumed that the interfacial forces are small in comparison to the centrifugal forces. The balance reduces to:

$$\rho_1 \frac{2w^2}{D} b^2 \delta = 2\sigma b \quad \left(\text{if } \frac{b}{r} \ll 1\right) \quad (7.20)$$

so that $\delta = \frac{\sigma D}{b \rho_1 w^2}$

If an equivalent drop diameter d_{eq} is defined as $d_{eq} = \sqrt{\frac{4b\delta}{\pi}}$, then:

$$d_{eq} = \frac{2}{w} \sqrt{\frac{\sigma D}{\rho_1 \pi}}$$

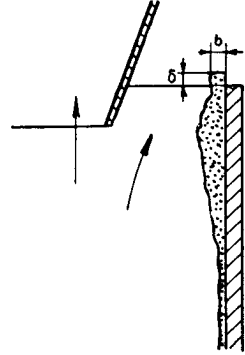


Figure 7.17 Balance of forces I

Radial liquid discharge

In this case interfacial forces will be much higher as the gas actually drives the liquid film through the slots. A balance between the interfacial (break-up) force and the surface tension (containing force) determines the minimal stable droplet size (see figure 7.18).

$$\frac{1}{2} \rho_g v_{gp}^2 \cdot C_D b \delta = 2\sigma b$$

in which v_{gp} is the average purge gas velocity through the slits.

Assuming a drag coefficient of $C_D = 1$, then:

$$\delta = \frac{4\sigma}{\rho_g v_{gp}^2}$$

Thus: $d_{eq} \sim \frac{4}{v_{gp}} \sqrt{\frac{b\sigma}{\pi \rho_g}} \quad (7.21)$

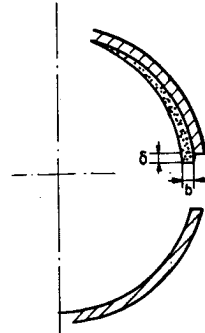


Figure 7.18 Balance of forces II

7.4.3 Block AC-MOD3

Objectives: Formulation of practical relations that describe the operating characteristics of an axial cyclone as specified in sections 4.3 and 7.1.

Summary : The models of AC-MOD1 and AC-MOD2 were joined and the predictions of this model cluster were compared with the measured operating characteristics of various axial cyclone geometries. The predictions with respect to the primary efficiency could only be verified indirectly because of experimental complications. The predictions with respect to maximal capacity and pressure drop agreed well with experimental results.

7.4.3.1 Structure of model

The following operating characteristics have been the subject of modelling:

1. primary separation efficiency;
2. maximal capacity.

Of both the modelling procedure is shortly explained and the results of the modelling efforts are compared with experimental results.

It is assumed that the pressure drop is determined simultaneously with the gas flow field in AC-MOD1.

7.4.3.2 Primary separation efficiency

The determination of the primary separation efficiency consisted of the procedure explained before: particle trajectories were calculated with the equations of motion described in AC-MOD2 on basis of the gas velocities that had been assigned to the grid cells in which the axial cyclone had been subdivided. An example of this calculation is depicted in figure 7.19.

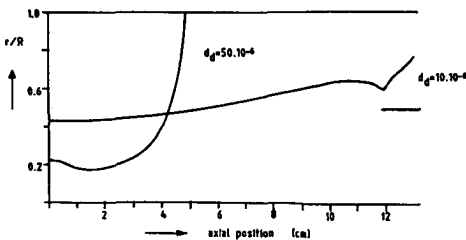


Figure 7.19 Example of simulated particle trajectories

The most important assumptions of AC-MOD1 seemed to be justified:

- The influence of the presence of the liquid phase on the gas flow field was negligible as separation efficiency and pressure drop did hardly vary when the liquid load was raised from 0.5 mass% to 10 mass% (see corresponding results in chapter 6).
- From the simulations (this has not been confirmed by experiments because of inadequate measuring equipment) it appeared that the turbulent fluctuations of the velocity components were sufficiently small to justify the neglect of turbulence on the particle motion.
($\langle v \rangle < 1$ m/s; $\langle u \rangle$, $\langle w \rangle < 1$ m/s at superficial velocities through the cyclone of approximately 15 m/s.)

It has not been possible to measure grade efficiency curves of axial cyclones: the carry-over was too dilute to measure exactly. Therefore an alternative, somewhat less direct, approach has been chosen to verify the prediction.

Through simulation runs the theoretical grade efficiency curve for a certain cyclone geometry could be determined for certain operating conditions. From the corresponding physical experiment the overall separation efficiency was determined. This measured efficiency was compared to the theoretical overall separation determined by multiplying the matrices of the measured incoming drop size distribution and the predicted grade efficiency curve. Such a validation procedure has been carried out only once. The results are summarized in table 7.I. For the conditions of the experiments is referred to table 6.IV, section 6.3.1 and appendix C, page C.4.

| run | measured separation efficiency | calculated separation efficiency | d_{50} (simulated) cyclone | d_{50} coming mist |
|-----|--------------------------------|----------------------------------|------------------------------|----------------------|
| 1 | 99,5 % | 99,1 % | 8 μ m | 28 μ m |

Table 7.I

Although the results seem to agree fairly well, it must be realized that the simulated amount of carry-over is almost twice the measured amount. The probable reason is coagulation of the smaller droplets between location of measurement and entry into the cyclone, as one would rather expect an opposite discrepancy with the assumptions made in the simulation.

7.4.3.3 Maximal capacity

Two mechanisms that may limit the range of operation are:

1. reentrainment of the separated liquid;
2. malfunctioning of the secondary separation zone.

As the discharge geometry of the cyclone can be of influence on the amount of carry-over that is caused by these mechanisms, each will be quantified for both discharge types separately.

ad 1. Consequences of reentrainment

In section 7.3.3 the submodel that predicts the onset of reentrainment in rotating gas/liquid systems has been verified adequately. This will not be repeated for the geometry of an axial cyclone.

Radially purging cyclones

With an example will be demonstrated that this mechanisms will not play a significant role in the limitation of the capacity of this cyclone type. From the modified reentrainment model appears that at gas densities of 60 kg/m^3 reentrainment takes place at superficial gas velocities of approximately 7.5-12.5 m/s. The tangential acceleration at this location will, depending on the swirl number, amount to approximately 3.000 m/s^2 .

If droplets are reentrained even with escape velocities of 5 m/s it can easily be calculated that they are redeposited (assuming axial plug flow, neglecting drag forces on the particle and assuming immediate acceleration of the droplet to the tangential velocity of the gas) in approximately $2 \cdot 10^{-3}$ sec. In this time the droplet will not traverse a meaningful axial distance. This calculation illustrates the observations described in chapter 6 that reentrainment of the separated film does generally not seem to limit the capacity in axial cyclones (although these experiments have been carried out at gas densities only up to 10 kg/m^3).

Coaxially purging cyclones

For the bulk of the film exactly the same calculation applies as above. However, the presence of the vortex finder can cause a considerable decrease in axial velocity at the wall at the height to which it extends (see for instance figure 7.10A). The tangential gas velocity does not decrease all that sudden (see figure 7.10B).

This results in the behaviour (depicted in figure 6.11) that the wall film thickens just underneath the vortex finder while its angle of rotation increases sharply. This way, very unfortunate separation circumstances are created. Suppose that reentrainment takes place: then droplets immediately enter the zone of high radial velocities (see figure 7.10C) and redistribution will not take place easily. The balance of drag forces inwards and centrifugal forces outwards can easily be calculated with the information presented in AC-MOD1/2 (no quantitative relations will be given here).

ad 2. Consequences of malfunctioning of secondary separation zones

As shown in AC-MOD2 the liquid that is discharged from axial cyclones can be so fine that it is questionable if a simple gravitational separation step would be sufficient to prevent these droplets from reentering the main flow.

In the following a practical criterion will be given to quantify the detrimental effects on the total separation efficiency.

If it is assumed that the axial cyclones are grouped in squares (figure 7.20) the space between the cyclones is $D^2 \left(1 - \frac{C_A}{T_A}\right) = 0.215 \cdot D^2$ (see also figures 6.10A and B).

The superficial velocity in this space (v_{g2}) amounts to $v_{g2} = \frac{(p\% \phi_g)}{0.215 D^2}$ in which $p\%$ is the purge rate and ϕ_g the throughput of the cyclone.

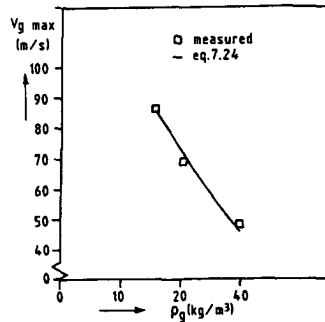
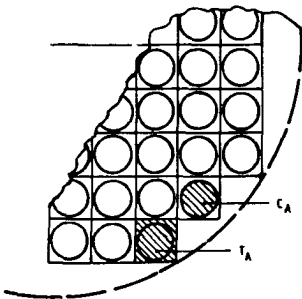


Fig. 7.20 Composition of multicyclone Fig. 7.21 Validation of equation 7.24

Coaxially purging cyclones

To determine whether droplets, that are formed during discharge, are taken with the purge gas to the main stream the following applies (under Stokes' law):

$$v_{g2} \geq \frac{(\rho_l - \rho_g) g d_{eq}^2}{18 \rho_g \mu} \quad (7.23)$$

in which d_{eq} is determined according to equation 7.20.

This relation has not been verified against experimental results.

Radially purging cyclones

The same carry-over criterion (equation 7.22) applies to radially purging cyclones, but in this case d_{eq} is determined according to equation 7.21.

When this equation for d_{eq} is substituted in the carry-over criterion the following relation is derived:

$$v_{gp}^3 \rho_g^2 \leq C \frac{b \sigma g (\rho_l - \rho_g)}{\mu_g} \quad (7.24)$$

This relation has been verified for a cyclone of which $S_A = 32.10^{-4} \text{ m}^2$ and $p\% = 20$. The results of the experiments are represented in figure 7.21. From this figure it appears that for the tested geometry the limitation in gas throughput is purely set by inadequate secondary separation. This effect is not as much specific for this particular geometry but rather for the usual way in which axial cyclones are operated.

7.4.4 Blocks AC-MOD4/MOD5

It is expected that banks of axial cyclones will not show other detrimental effects with respect to operating characteristics than those observed with single axial cyclones. Maldistribution, for instance, is an effect that is not likely to occur. Therefore, the interpretation of the experiments and subsequent modelling for axial cyclones is concluded.

7.5 Reverse flow cyclones

7.5.1 Block RFC-MOD1

Objective: Formulation of a model that describes the gas flow field inside a reverse flow cyclone as a function of its geometry.

Summary : No satisfying results have been achieved.

Unfortunately the Fluent code has not been available to model reverse flow cyclones. Instead the Phoenix code was used, which is much less equipped to model swirling flows.

One of the most important deficits of Phoenix is the lack of an advanced turbulence model which is necessary to model anisotropic flows. This was the principle cause of the failure to formulate a generally applicable model.

In figure 7.22 an example is given of the comparison of a simulated flow field to an experimentally determined one. Although this simulation has been carried out with a for this purpose modified Prandtl-mixing length turbulence model (suggested by Pericleous [1984]), the agreement is still very poor.

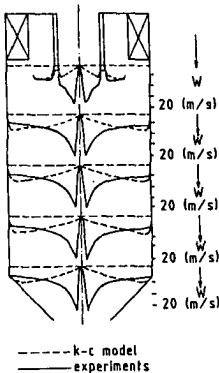


Fig. 7.22 Simulated axial development of the tangential velocity profile in a reverse flow cyclone with $k-\epsilon$

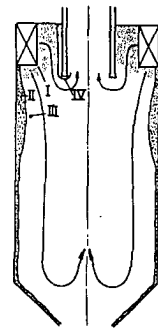


Fig. 7.23 Manifestations of the liquid phase in a reverse flow cyclone

7.5.2 Block RFC-MOD2

Objective: Formulation of models that describe the behaviour of the liquid phase inside a reverse flow cyclone.

Summary : The various forms of the liquid phase and their origin are identified. Because the conditions inside a reverse flow cyclone are very similar to those in axial cyclones it is possible to refer in most cases to the corresponding relations formulated for these cyclones.

In a reverse flow cyclone the liquid phase can occur in one of the following forms (see figure 7.23):

- a. as the original mist phase (I);
- b. as the film formed by the separated liquid (II);
- c. as droplets reentrained from this film (III);
- d. as boundary layer creep towards the vortex finder (IV).

The first three phases can be described with the corresponding relations derived in AC-MOD2, as these relations take the same effects into account that are of influence in reverse flow cyclones. Boundary layer creep is caused by the short circuiting gas flow that flows directly into the vortex finder upon entry (see figure 7.23).

The amount of liquid that is transported this way can be quantified when the interfacial shear stresses and the film thickness are known:

- the interfacial shear stress τ_i amounts to $\tau_i = f_{gi} \cdot \frac{1}{2} \rho_g v_g^2$;
- when assuming a thin laminar film the average film flow rate can be quantified as $\phi_v = \bar{v}_1 L = \frac{\tau_i b L}{2\mu}$,

in which: b = the film thickness

\bar{v}_1 = the average film velocity

L = the width of the surface across which creep takes place

7.5.3 Block RFC-MOD3

Objective: Formulation of models that describe the practical operating characteristics of a reverse flow cyclone.

Summary : The characteristics to which attention will be paid are:

1. primary separation efficiency;
2. maximal capacity;
3. pressure drop.

Because RFC-MOD1 has not been completed, it is not yet possible to formulate an encompassive model cluster as has been done in AC-MOD3. Still, some limiting phenomena have been identified for which qualitative models are formulated. The reliability of these models will be verified for specific cases that are experimentally well characterized.

7.5.3.1 Primary separation efficiency of a reverse flow cyclone

Because no gas flow fields have yet been produced from simulations it has been attempted to relate the determination of the primary separation efficiency of a reverse flow cyclone to that of an axial cyclone. This seems to be justified because the conditions in the separation zones of both cyclones are very similar.

The primary separation efficiency of a reverse flow cyclone was simulated by determining the primary separation efficiency of an axial cyclone that:

1. had an equal diameter of the vortex finder;
2. had a swirl number that equalled the swirl number of the gas flow in the separation zone;

and implicitly it was assumed that the tangential velocity profiles would only depend on the actual swirl number and would not be influenced by the axially reversed core.

The experimental validation has the same set-up as described for the corresponding experiment in AC-MOD3. The results are given in table 7.II.

| run | measured separation efficiency | simulated separation efficiency | simulated d_{50} of cyclone | d_{50} of incoming mist |
|-----|--------------------------------|---------------------------------|-------------------------------|---------------------------|
| 1 | 99,1% | 99,6% | 4 μm | 28 μm |

Table 7.II

Although the predicted seems to agree fairly well with the measured separation efficiency it must be realized that the amount of measured carry-over is more than two times the amount that is predicted. Probably the reason for this effect is that it is not accounted for short circuiting gas flow just underneath the vortex finder which takes particles outside the reach of the separation zone (see figure 7.25, IV).

7.5.3.2 Maximal capacity of a reverse flow cyclone

With respect to the determination of the maximal capacity of a reverse flow cyclone, two limiting phenomena will be described:

1. the effect of reentrainment;
2. the effect of creep.

ad 1. Effect of reentrainment

From the description of RFC-EXP2 it appears that just underneath the vortex finder of the cyclone under investigation a comparable build-up of liquid took place as described for coaxially purging cyclones. Apparently the radial inflow of the shortcircuiting gas flow to the vortex finder caused a momentary decrease of the axial velocity. This effect is for instance confirmed by gas flow field determinations of Boysan [1982].

The observed phenomena can be explained by the fact that the tangential velocity does not show this dip at the wall. These effects result in a thickened film rotating at a sharper angle (see figure 6.16).

This is a very unfortunate situation as the reentrainment that will take place at this location will not be redeposited further downstream in the cyclone. Instead it will be picked up by the high inward radial velocities and brought into the exiting cleaned gas flow.

When the gas flow field can be predicted it will be straight forward to determine the effect of reentrainment with the relations formulated in AC-MOD3 with respect to coaxially purging axial cyclones.

ad 2. Effect of creep

Creep is an effect of which the quantity, according to RFC-MOD2, does not depend on liquid loading of the gas. Therefore, creep is often the reason why at lower liquid loadings the separation efficiency seems to deteriorate,

as the absolute amount of creep stays constant. Unfortunately, yet no information is available on the boundary layer gas flow rate, so no quantitative predictions can be given. However, the test results of cyclone type B, figure 6.21C demonstrate this effect very clearly.

7.5.3.3 Pressure drop of a reverse flow cyclone

In case of axial cyclones it has been established that the liquid phase exerts little influence on the pressure drop and therefore, it is relied on the gas flow field simulations only to give predictions of the pressure drop.

In case of reverse flow there is a clear influence of the liquid phase, as is demonstrated by, for instance, the pressure drop curves of cyclone IV (type E, figure 6.18C) page C.10 in appendix C.

On one occasion (cyclone type E, figure 6.18C) a reduction up to 15% of the pressure drop has been measured when the liquid loading was increased from 0 to 10%. This reduction can be explained by:

1. A reduction of the tangential velocity by a decrease in angular momentum of the gas (swallowed by the droplets);
2. A reduction of effective turbulence by the presence of particles;
3. A reduction of wall friction by the formation of the wall film.

Because the first two effects would have been apparent for axial cyclones as well, the third explanation is the most probable. The surface covered by wall films is much smaller in radially discharging cyclones to which the original experiments relate.

7.5.4 Block RFC-MOD4

Objective: Identification of the effects that influence the reduction in separation efficiency of a multicyclone in comparison to a single cyclone.

Summary : A simplified conceptual model of a reverse flow cyclone will be set up with which the observed behaviour of a multicyclone can be explained.

The results of the experiments with multicyclone A, described in RFC-EXP4, show an apparant contradiction: although there is a high maldistribution of liquid across the cyclone, the gas flow that is measured at the outlet of the individual cyclones is constant*) (see table 6.VIII).

One would rather expect a higher gas flow through the cyclones that separate higher amounts of liquid, as the increase of liquid should have resulted in a decrease of the pressure drop (RFC-MOD3). A valid explanation of this effect is the assumption that the reduction of wall friction causes the reduction in pressure drop and that a free exchange of gas between the cyclones is possible in the discharge bin. The reduction in pressure drop is in this case only created between the inlet and liquid outlet of the cyclone, causing extra gas to travel this trajet through the cyclone if extra liquid is processed. This relative advantage is lost, though, upon reversal of the gas direction, as much less liquid is available to smooth the wall roughness in the vortex finder. Therefore, in the discharge bin, a redistribution of the gas will take place as such that the pressure drop across all the individual vortex finders is equal (see figure 7.24). This redistribution will cause already separated droplets to enter the cyclones again, after which they will pass very fast through the vortex finder.

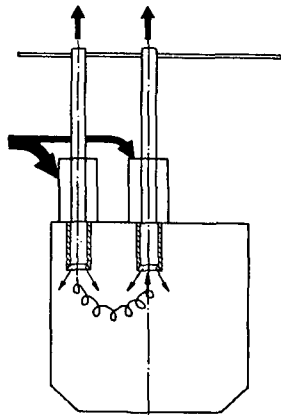


Figure 7.24 Multicyclone effect induced by wall roughness and variation of liquid loading

*) The reason that cyclones II and IV show lower velocities is caused by their longer vortex finder. The effect hereof is explained in the course of the text.

The influence of this effect on the separation efficiency depends on:

1. The rate of gas redistribution under the cyclones, which is determined by:
 - a. the rate of liquid maldistribution across the cyclone;
 - b. the absolute wall roughness of the separation zones of the individual cyclones, as this determines the amount of liquid that is necessary before extra liquid will no longer result in extra gas through the inlet. An example: if a very thin film is already enough to cover the wall roughness, the pressure drop across the cyclone becomes independent of the liquid loading across the cyclone (see equations 5.12 and 5.13) and the amount of extra processed gas and subsequent redistribution stays limited.
2. The droplet size of the discharged liquid. As the same balance of forces plays a role as depicted in figure 7.22 for coaxially purging cyclone it is referred to this section of AC-MOD2.

The quantification depends very much on the yet uncompleted gas flow field model of RFC-MOD1 and the models that quantify the liquid maldistribution across the package and the gas velocities in the discharge bin, as the latter will determine how much liquid will reenter the cyclones. These models have not yet been formulated.

One conclusion can be drawn: if the wall friction factor of the separation zone is smaller than the interfacial (gas) friction factor, the described mechanism can not occur and the separation efficiency of the multicyclone is quite easily improved considerably - up to 10% as shown by RFC-EXP4. (After these experiments one of the cyclones of bundle II was sacrificed for internal examination: it appeared that chunks of rust protruded up to 3 mm into the separation zone.)

7.5.5 Block RFC-MOD5

Objective: Formulation of practical relations that predict the behaviour of multicyclones.

Because of the qualitative character of MOD4, no attempts have yet been undertaken to set up relations for MOD5.

7.6 Vanes

7.6.1 Block V-MOD1

Objective: To set up a model that describes the gas flow field inside a vane.

Summary : A suitable model has been developed on basis of the Phoenix code. The validation of this model is described.

It was assumed that the measure of rotation between the vanes is low enough to model the system with the $k-\epsilon$ turbulence model. The first results did not show the vortices that are developed in the top section of and behind the bends (figure 6.23). After the grid had been refined the simulation did show these vortices and a satisfying agreement was reached between prediction and experiment. The outflow conditions set the velocity gradients at the exit plane to zero. The grid and other simulation parameters are described more extensively by Waterreus [1988]. In figures 7.25 and 7.26 an example is given of the comparison of simulation and experimental results. The discrepancy was thought to be small enough to be able to rely on this model for the geometrical optimizations that will be described in chapter 8.

The elongation of the vortex behind the bend can be explained by the same effect described with one of the preliminary AC-MOD1 models: angular momentum is imported by inflow of outside gas. If the grid would have been chosen longer, this effect would no longer be present.

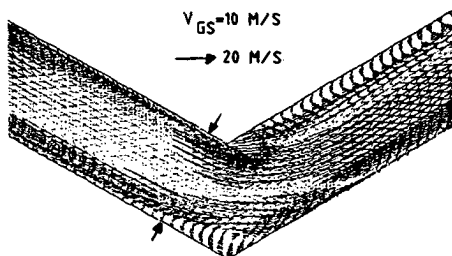
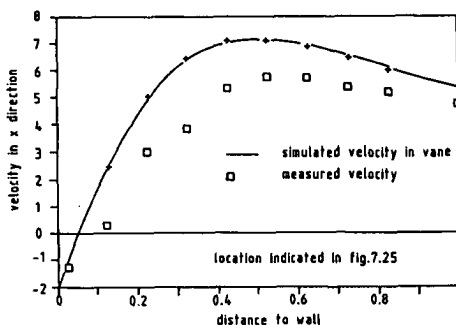


Figure 7.25 Simulated flow field between vanes



Figures 7.26A and B Validation of V-MOD1

The vortex behind the bend can be explained by the after effects of the radial pressure gradient that is formed in the bend. The low pressures at the inner side of the bend cause an axial pressure gradient that is directed against the overall flow direction when the bend ends.

7.6.2 Block V-MOD2

Objective: Formulation of relations that describe the behaviour of the liquid phase between vane blades.

Summary : The various forms of the liquid phase and their origin are identified. For each of these forms relations are set up to describe behaviour and to be able to predict possible critical effects.

The liquid can occur in one of the following forms (see figure 7.27):

1. as the droplets of the original mist phase (I);
2. as the film that is formed by the separated droplets (II);
3. as the droplets reentrained from the film (III).

ad 1. Behaviour of mist phase

It is referred to section 7.3.2 in which the relations are derived that have been used in the previous sections for determining particle trajectories.

ad 2. Behaviour of liquid film

Distinction will be made between vane separators in which the separated liquid is drained through shielded channels or in which the separated liquid is drained against the upflowing gas.

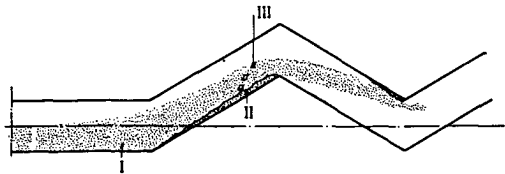


Figure 7.27 Manifestations of the liquid phase in a vane-type separator

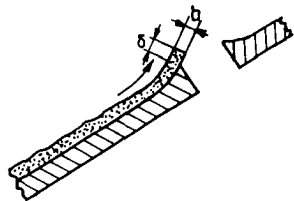


Figure 7.28 Balance of forces on the liquid film

In case of shielded liquid drainage

There are two mechanisms that can cause reentrainment of the film:

- shear off of film from geometrical irregularities (see EXP-V2);
- shear off of interfacial instabilities (see previous MOD2 blocks).

The first mechanism has been observed to take place extensively on vane blades of type A in figure 6.29. The droplet size that is created can be estimated with the balance of forces depicted in figure 7.27, in which the break up of the film is caused by interfacial forces, while the containing force is formed by the surface tension:

$$C_D \cdot \frac{1}{2} \rho_g v_g^2 \delta b = \sigma b$$

assuming $C_D = 1$ and $d_{eq} = \sqrt{\frac{4b\delta}{\pi}}$

$$d_{eq} = \frac{4}{v_g} \sqrt{\frac{b\sigma}{\pi\rho_g}} \quad (7.25)$$

In case of the second mechanism, the reentrainment model given in section 7.3.3 can be used for predictions if the local tangential film velocity and the friction velocity of the gas phase are known (both can be determined from the predictions of V-MOD1). It is assumed that the film velocity can be determined according to equation 7.17:

$$\bar{v}_l = \sqrt{\frac{f_{gi}}{f_{li}} \cdot \frac{\rho_g}{\rho_l} \cdot \bar{v}_g^2}$$

In case of unshielded liquid drainage in vertically flowed through vanes

The mechanism that limits the capacity is fully different. Mist is offered to the vane, liquid is separated and drained against the upflowing gas. The capacity of the drainage depends on the gas friction velocity, gas density and liquid properties. If at a certain moment the amount of liquid offered to the separator surpasses this maximal drainage capacity, the separator will rapidly flood internally and the maximal capacity will be reached abruptly. Pressure drop and maximal capacity are very adequately described by the model of Billet [1987] (section 3.4.3) for packed columns.

ad 3. Behaviour of reentrained droplets

Reentrainment will only take place at the high velocities that will occur in operation with shielded liquid drainage. The behaviour of these reentrained droplets can be characterized when the following properties are known:

- droplet size;
- initial droplet velocity;
- reentrainment rate.

If droplets are reentrained by the first mechanism, mentioned under ad 2, their droplet size can be determined according to equation 7.25.

It can be expected according to the same model, depicted in figure 7.27 that the droplet velocity can not be larger than the maximally occurring film velocity, v_{lmax} .

$$v_{lmax} \sim 2 * \bar{v}_1 \text{ (Re}_1 < 1000)$$

\bar{v}_1 is determined according to equation 7.25

The reentrainment rate depends on the surface roughness: specifically on the number of irregularities that penetrate through the boundary layer of the film. In case the film is so unstable that reentrainment can take place by roll wave crest shear off, it is referred to the corresponding original relations in either section 5.5 or the modified relations for centrifugal fields in AC-MOD2.

7.6.3 Block V-MOD3

Objectives: Formulation of practical relations that describe the operating characteristics of a vane separator.

Summary : Because V-EXP3 has not yet been started, no reliable means of validation for the models of this block was available. Therefore, only qualitative conclusions can be drawn. It is expected that Verlaan will pay extensive attention to this subject in his thesis.

In this section attention will be paid to the following operating characteristics:

1. primary efficiency (minimal capacity);
2. maximal capacity.

The pressure drop is reproduced reliably by V-MOD1. In the following it is assumed that the presence of liquid will have a negligible effect on the gas flow field as most vane blades consist of smooth stainless steel (see RFC-MOD4).

ad 1. Primary separation efficiency

In first instance the same three assumptions of particle trajectories as those in AC-MOD3 are taken to be valid with respect to the determination:

1. The gas flow field is not affected by the presence of liquid phase;
2. Turbulence has a negligible effect on particle trajectories;
3. Stokes' law is applicable.

The minimum gas flow velocity necessary to achieve practical separation efficiencies has been estimated for vane type separator C in figure 6.29. Values of $v_{g \min}$ between 2-4 m/s depending on droplet size distribution, were found, which corresponded to experimentally determined values on test-rig 3. However, because of still unquantified upscaling effects that might have influenced these results, these experiments are not suitable for validation purposes (Pouwels [1987]).

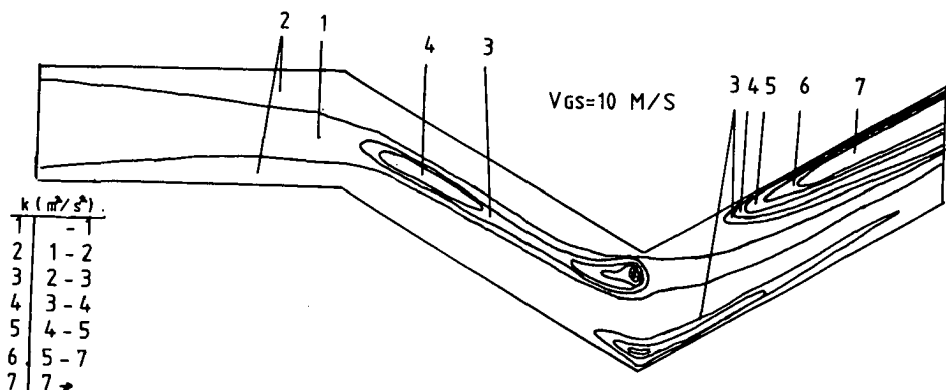


Figure 7.29 Simulated kinetic turbulent energy between vane blades

From simulations of gas flow fields at higher gas velocities it appears that the intensity of turbulence increases rapidly after each bend (figure 7.29). Because the turbulence intensity is high in the regions that the droplets have to traverse, it is questionable if the second assumption will prove to be valid. The basic cause of the increase of turbulence behind the bends is the occurrence of the vortices which are described in V-MOD1.

ad 2. Maximal capacity

From V-MOD2 two mechanisms are indicated that can limit the operation by causing reentrainment of separated liquid. Which one will occur depends on geometrical effects (surface roughness) and flow field characteristics (local tangential accelerations).

The effect of reentrainment will largely depend on the location of the drainage slits, and thus on the location of the wetted areas. Reentrained droplets can penetrate to the gas core if no sufficient centrifugal acceleration is available and/or when the gas flow has become too turbulent. All these effects, but the last can in principle be simulated with the combination of the model blocks presented in the two previous sections.

When adequate experimental results have been generated to verify the reliability of this model cluster, a powerful tool has been obtained to predict the operating characteristics of vane type separators that feature shielded liquid drainage.

7.6.4 Block V-MOD4

Objective: To quantify the effects of upscaling with respect to the operating conditions of a vane separator.

Summary : Of two effects, that have earlier been identified as possible contributors to reduction in separation efficiency, one has been investigated by means of simulation, although no experimental results were yet available to verify the simulation model.

In section 3.4.3 two detrimental effects were mentioned that play a role when the length/width ratio of the inflow area of a vane type separator, flowed through from the direction of its length (see figure 7.30A), is extreme:

1. gas will be maldistributed across the frontal inflow area causing local overloading;
2. (in case of horizontally flowed through vanes:) the capacity of the liquid drainage slots might be too low in the underside of the vane pack, causing liquid to flow out of the slots.

The second effect will not very likely occur in usual operation as the cross section of the slots in most geometries is large in relation to practical liquid loadings. Moreover, if it occurs, carry-over will be quite fast accommodated in following slots.

The first mechanisms might result in more serious effects, because too high superficial gas velocities will always lead to a decrease in efficiency.

For this reason a qualitative simulation based on the Phoenix code has been set up to assess the amount of maldistribution as a function of operating pressure, W/L ratio and pressure drop coefficient of the vane. The simulated situation is depicted in figure 7.30B.

An indicative example of the simulation results is depicted in figure 7.30B. The preliminary conclusion of this exercise is that the effects of maldistribution are much stronger than generally considered.

However, more effort must yet be put in these investigations to quantify the observed effects.

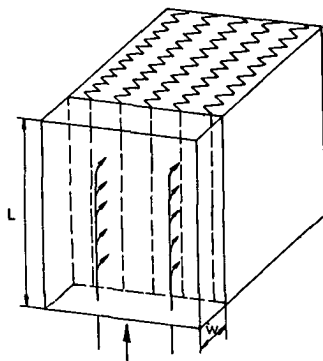
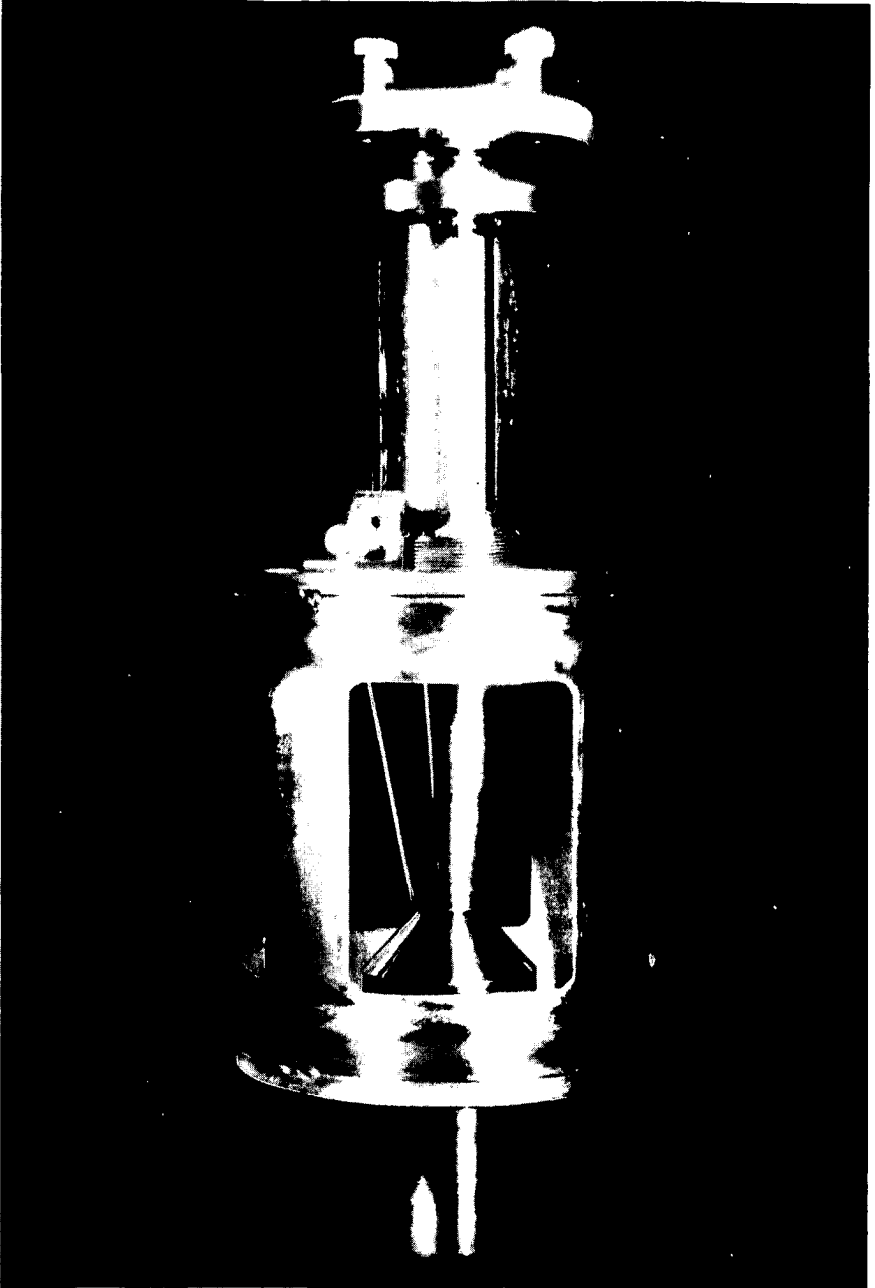


Figure 7.30A Configuration used for modelling



8. CONCLUSIONS: IMPROVED DESIGNS AND DESIGN PROCEDURES

8.1 Introduction

In chapter 8 the models that have been formulated in this thesis are applied to develop new separator designs and improved separator design procedures. In section 8.2 for each separator type the effects are summarized that have been found to limit the operation. Improvements are proposed to minimize or prevent the effects of these limitations. Along this line a dedicated axial and novel vane design cyclone are optimized and tested.

Although a conceptual design for an improved reverse flow cyclone is proposed as well, this separator type has not been developed further as the characteristics of the new axial cyclone proved to be superior in advance. In section 8.3 design procedures are distilled from the models that have been described in chapter 7.

In some cases it proves to be possible to extract simple and reliable relations from these models that have a practical value. In most cases, however, is referred to the complete model for exact predictions. Rules of thumb are given with which the influences of most important operating conditions can be quantified. The newly developed relations are compared to the traditional design rules and conclusions are drawn with respect to the consequences of discrepancies.

8.2 Improved designs

8.2.1 Axial cyclones

Prime limitations

It has been proven in section 7.4 that the maximal capacity is reached in axial cyclones because of a malfunctioning secondary separation zone and not because of reentrainment of the liquid film inside the settling zone (see for example figure 7.21).

Especially in case of radially purging (slit-) cyclones the detrimental effect of increasing gas density on the effectiveness of the secondary

separation zone is very strong (equation 7.24). In axial cyclones with efficient swirl elements a large part of the pressure drop across the cyclone is caused by the constriction of the vortex finder. The pressure drop across the vortex finder serves as the driving power of the secondary separation, but does not contribute to the primary separation (see for instance figures 6.10A and B).

Proposal for a compact axial cyclone dedicated to high pressure applications

In figures 3.29 and 3.30 it is shown for reverse flow cyclones how to reprocess fouled purge gas with the main gas stream. If this idea is applied to axial cyclones the secondary separation zone is not longer necessary.

Two different configurations (see figure 8.1) have been considered to reprocess the purge gas. The purge gas can either be fed back to the unprocessed main stream through the underpressure created by a venturi upstream of the cyclone, or use can be made of the available underpressure in the centre of the cyclone to create a driving force for the purge gas. Apart from eliminating the present limitation to the maximal throughput of traditional axial cyclones, the need for a narrow vortex finder (driving force behind secondary separation) has now been eliminated as well. This can result in a much lower pressure drop across the cyclone. For each of these two alternatives a design optimization has been carried out with the simulation models described in section 7.4.

In the following the optimization procedures and the final results are described for each of the two alternatives.

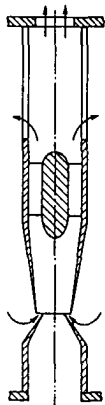


Figure 8.1A Venturi recycle axial
cyclone

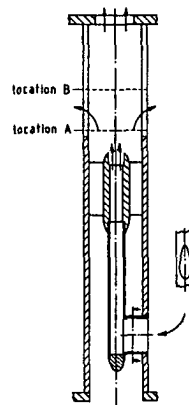


Figure 8.1B Internal recycle axial
cyclone

Design optimization procedures

Venturi-recycle type cyclone

Starting with some fixed geometrical values and ratios the primary separation zone was first optimally designed so that some stringent demands to the operating characteristics could be met. The geometrical starting conditions concerned especially the diameter of the cyclone (ϕ 50 mm) and the ranges of allowable variation of the other geometrical ratios so that the resulting design could still be accommodated in the test-rig. In the optimization procedure it has never been necessary to impose these constraints on the simulation results. The requirements with respect to operating characteristics concerned:

- the separation efficiency ($d_{50} < 5 \mu\text{m}$);
- pressure drop ($\xi < 10$, $\Delta p = \xi \frac{1}{2} \rho_g u_s^2$, of which $\xi_{sw} < 3$);
- turn down ratio ($Tr < 1/5$ at $\rho_g = 40 \text{ kg/m}^3$).

The pressure drop coefficient across the swirler (ξ_{sw}) had to meet stringent requirements as its value determines the necessary underpressure of the venturi (and thus the pressure drop across the venturi itself).

The simulation results specified the following properties of the cyclone geometry (see AC-MOD3):

- purge rate, $p\%$
- separation chamber length, L/D
- diameter of vortex finder, D_e/D
- minimal required swirl number, S_m .

With S_m the geometry of a low pressure drop swirl element can be derived from the information given in sections 5.5 and 6.3.1 AC-EXP1.

A swirl element was constructed (see figure 8.2) that met the criteria ($\xi = 2.7$ and S_m , the minimal required swirl number that was specified by the simulation).

From experiments appeared that the previously theoretically determined venturi geometry that should compensate for the pressure drop across the swirl element was not adequate. The purge rate was too low, and low efficiencies were measured.

The venturi diameter that did induce the specified purge rate was found experimentally.

The predicted efficiencies now coincided largely with the experimental values (see figure 8.3) which meant that no other limiting phenomena occurred that had not been anticipated.

The momentary decrease of measured separation efficiency at $\rho_g = 14 \text{ kg/m}^3$ was structural and is probably caused by film creep. Strangely enough this effect disappears at higher pressures. The target pressure drop coefficient of $\xi = 10$ could not be reached because of a disappointingly high pressure drop across the venturi (accounting for 55% of the total pressure drop).

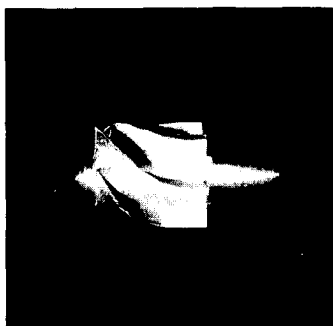


Figure 8.2 Optimized swirl element

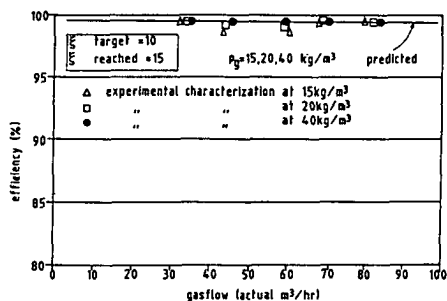


Figure 8.3 Characteristics of venturi recycle type cyclone

Internal recycle type cyclone

The optimization of the design of the primary separation zone was carried out similarly to the previous cyclone with an important extra assumption. The purge gas that entered the separation zone through the swirl element was considered to be assimilated by the swirling gas flow field. It is assumed that thereby it lowers the effective swirl number of the total flow proportionally. The justification of this assumption is shown in figure 8.4, in which the measured axial development of this swirling flow is depicted. At location A (corresponding to figure 6.10B) there is still a distinct plug flow in the centre, which has disappeared at location B. This means that the models formulated in AC-MOD3 can be applied. It should, however, be realized that a swirl element is necessary that invokes a swirl number that is p% higher than the swirl number with which the simulation has been carried out (if p% is the purge rate). With respect to the axial gas flow field the same assumptions are made as listed in AC-MOD1.

The simulations again specified the necessary geometrical parameters. Figure 8.5 gives the predictions necessary for the determination of the grade efficiency curve of the final geometry.

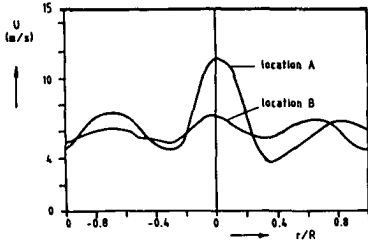


Figure 8.4A Axial flow field

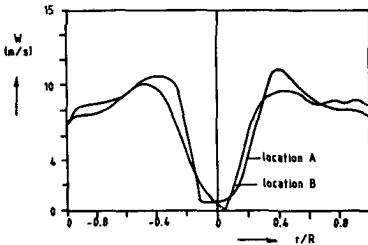


Figure 8.4B Tangential flow field

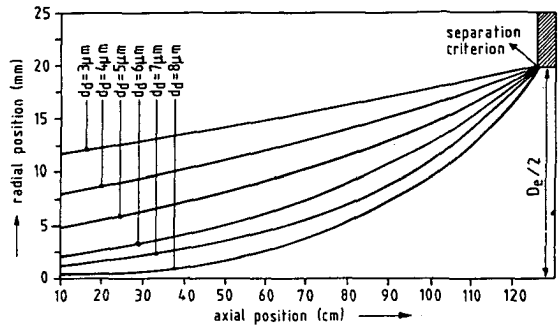


Figure 8.5 Simulated particle trajectories

The following special properties were required of the swirl element;

1. it should induce the specified minimal swirl intensity (S_m);
2. it should create a differential radial pressure drop large enough to induce the required purge rate;
3. it should withstand fouling operation.

With respect to the last demand the passage through the swirl element may not be narrower than 12 mm.

Experiments were carried out to verify the predictions. This time a very large discrepancy was encountered between predicted and measured separation efficiency and apparently a secondary limiting mechanism occurred in the separation process that had not yet been identified.

Internal investigations on test-rig 1 showed that very heavy film creep occurred across the top of the swirl element towards the centre of the cyclone. This liquid film was dispersed by the purge gas (see figure 8.6A) that entered the cyclone through the swirl element. This way very unfortunate conditions were created. An anticreep device was mounted on top of the swirl element (see figure 8.6B) which provided an adequate solution.

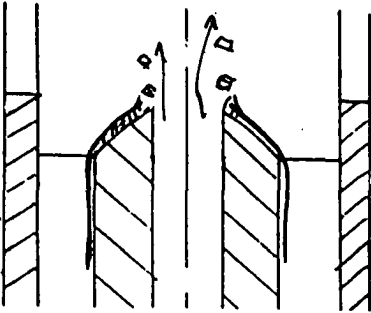


Figure 8.6A Dispersion of creep



Figure 8.6B Modified swirl element

The experimental characterization was now again conform to the predicted behaviour (see figure 8.7A). The pressure drop coefficient that was expected for this geometry amounted to $\xi = 7$; the effective pressure drop coefficient that was determined experimentally amounted to $\xi = 6$.

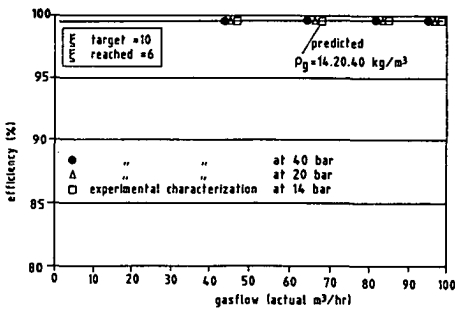


Figure 8.7A Characteristics of internal recycle type cyclone

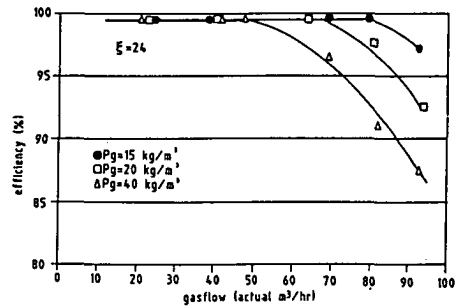


Figure 8.7B Characteristics of corresponding conventional cyclone

In figure 8.7B the same axial cyclone has been tested in the traditional form (see figure 6.10A). A secondary separation zone replaced the recycle provision. The diameter of the vortex finder had been chosen as such that an equal purge rate was developed. The effect of the difference in purge gas cleaning shows that the traditional solution is not at all suited for high pressure applications. More specific information with respect to the geometrical properties of these cyclones is confidential. It is in the possession of the sponsors of this project.

This design optimization has lead to a cyclone of which the measured maximal value of λ (related to the diameter of the cyclone) amounted to $\lambda = 2.5$ (!) (at $\rho_g = 40 \text{ kg/m}^3$ and $110 \text{ m}^3/\text{hr}$). This figure was at least 2.5 times higher than the measured maximal value of λ for the conventional cyclone. Meanwhile, the pressure drop across the new cyclone was four times lower.

8.2.2 Reverse flow cyclones

Prime limitations

It has been shown in section 7.5 that one of the probable bottle-necks with respect to gas throughput in gas/liquid reverse flow cyclones is formed by reentrainment of the separated liquid film and the high radial gas influx at the height of the vortex finder.

Proposal for a design dedicated for high pressure gas/liquid separation

A simple geometrical solution that reduces the local radial influx and at the same time takes the liquid away from the dangerous zone, is expansion of the separation zone at the height of the vortex finder (see figure 8.8). Although the same separation efficiency and turn down ratio could be reached, a reverse flow cyclone will probably always have a higher pressure drop and a larger size. Because no possible advantages are gained with respect to the designs that have been developed in the previous section, no further effort has been put in optimization of this design principle.

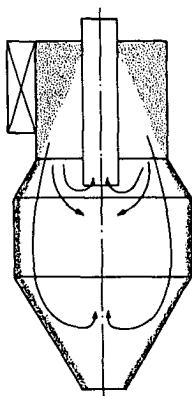


Figure 8.8 Adapted reverse flow cyclone for high pressure gas/liquid separation

8.2.3 Vanes

Prime limitations

In section 7.6 has been shown that, due to the poor aerodynamic properties of the flow path between the vane blades, the turbulence intensity will increase steadily from in- to outlet. The effect of the increased turbulence is threefold:

1. It has been shown that usually only the first two or three bends will contribute to an effective separation. From these bends onwards the movement of small mist particles becomes so erratic that only some turbulent deposition will take place.
2. Because of the turbulent fluctuations of the gas flow the maximal capacity (onset of reentrainment) is reached earlier than expected.
3. The pressure drop across the vane pack is higher than necessary.

The reentrainment mechanisms that can be encountered inside vane packs are also described in section 7.6 and are identified as:

- a. roll-wave crest shear off in case of low centrifugal stabilization of the film (poorly located discharge slits, outside the zones in which a centrifugal field exists);
- b. film shear off because of irregularities on the vane surface.

The most important reason for the downstream increase of turbulence between vane blades is caused by the radial pressure gradient that is invoked in the bends. The zone of low pressure at the innerside of the bend causes behind the bend an axial gradient that is directed against the general direction of flow. This effect gives rise to a vortex that forms an uncontrollable fluctuating 'obstacle' in the flow path (see figure 7.24 and V-MOD1).

Proposal for vane type separator design that is dedicated to high pressure gas/liquid separation

From personal communication with Nieuwstadt [1987] it appeared that a very elegant way of abolishing the vortices would consist of creating a low pressure zone behind the bends to compensate the radial pressure gradient in the bend. This low pressure zone should be created by reducing the width between the vane blades directly after the bend.

By choosing a careful increase in width, pressure could be regained and the level of turbulence could be kept to a minimum.

The maximal allowable width of the vane channel behind the bend in order to prevent the formation of a vortex can be quantified in a simplified way: if solid body rotation is assumed to take place in the bend, the radial pressure difference across the channel in the bend will be:

$$\Delta P_b = \int_{r_{in}}^{r_{out}} \rho_g \omega^2 r \, dr = \frac{1}{2} \rho_g \omega^2 r^2 \Big|_{r=r_{in}}^{r=r_{out}} \quad (8.1)$$

in which: r_{in} = the inner radius of the bend

r_{out} = the outer radius of the bend

ω = the angular velocity in the bend ($\sim u_b/r$)

u_b = the superficial velocity between the plates in the bend.

With the knowledge of the radial pressure gradient the necessary reduction in pressure behind the bend can be calculated; from this information the reduction in channel width can easily be estimated with Bernouilli's law:

$$\Delta P_r = \frac{1}{2} \rho_g (u_b - u_r)^2$$

in which: ΔP_r = the pressure reduction after the bend

u_r = the superficial velocity between the plates after the bend

The vortex behind the bend will not form if $\Delta P_r > \frac{1}{2} \Delta P_b$.

With the quantification described above a preliminary one-bend profile was set up and simulations with the earlier described V-MOD1 model were carried out to establish the sensitivity of the design. Two examples of the simulation results are shown in figures 8.9 and 8.10. As can be seen, the vortex behind the bend is in effect no longer present and the amount of turbulence is drastically reduced with respect to figure 7.29.

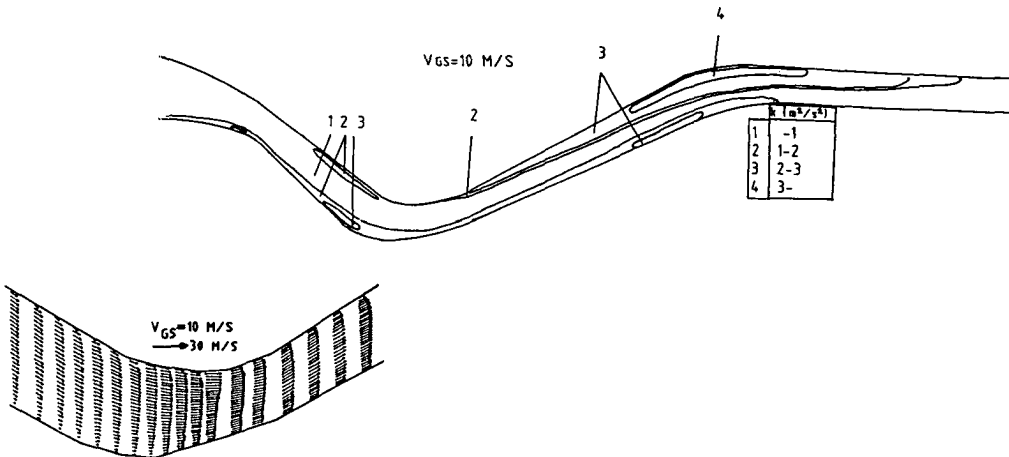


Fig. 8.9 Simulated flow field Fig. 8.10 Simulated turbulent kinetic energy

After the theoretical justification of the new design philosophy for the gas flow path a prototype vane separator was conceived that consisted of only one bend. Care was taken to optimally locate the drainage slots (according to the findings in section 7.6) and to provide the drainage slots with gradually curved smooth upstream lips (see figure 8.11) to ensure cohesion of the film to the metal surface and to prevent the second reentrainment mechanism mentioned.

This prototype featured a vertical shielded liquid drainage (see figure 3.12) to ensure a design as compact as possible which would be suited for fouling operation.

The experimental characterization showed in effect a drastically reduced pressure drop (it amounted to 20% of conventional vane packs with vertical shielded liquid drainage). The maximal capacity and separation efficiency proved to be comparable to conventional vane separators.

It was expected that the maximal capacity was limited by reentrained droplets from the still thick film flowing into the first drainage slot. After the first bend these droplets were hardly given a second chance to be separated. Therefore, a second prototype was designed that exchanged part of the large reduction in pressure drop of the first prototype for an extension of the turn down ratio. Instead of one bend, three bends were designed.

Figure 8.11 shows an indicative example of the vane geometry. The results of the experimental characterization are shown in figure 8.12. In this figure the characteristics are compared to those of a conventional vane type separator.

The prototype is presently being patented. For more specific information is referred to the sponsors. Vertical liquid drainage has been patented by Burgess Manning GmbH, which company has put this idea at the disposal of this project under certain conditions.

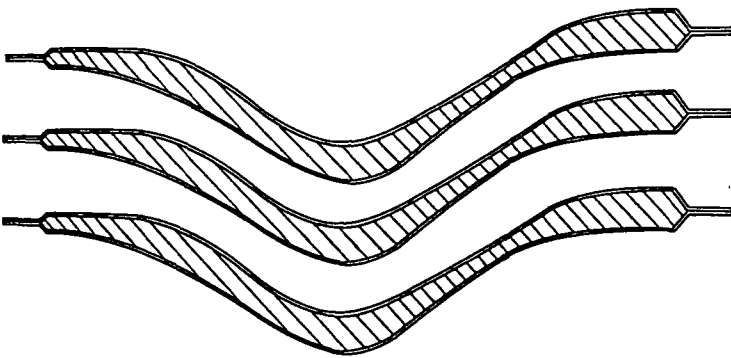


Figure 8.11 Geometry of first prototype for new vane (indicative)

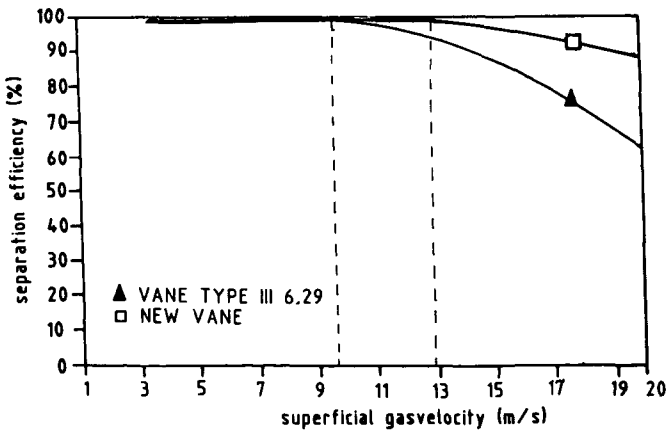


Figure 8.12 Extrapolated characteristics of second prototype

8.3 Improved design equations

8.3.1 Introductory remarks

In the next three subsections design equations are derived from the models of chapter 7 for axial cyclones, reverse flow cyclones and vane type separators.

Attention is paid to the same design equations as in chapter 3:

1. Maximal capacity as a function of gas density, liquid properties and separator geometry;
2. Minimal capacity (primary separation efficiency) as a function of the same variables;
3. Pressure drop as a function of the same variables and gas flow.

Except for axial cyclones, the models of chapter 7 are nearly always too complex to derive simplified, general relations from that fully account for geometrical variations. Therefore, the practical design equations that are derived from these models are in most cases given in a general form from which the influence of changes in operating conditions can be quantified in a relative way. For instance, in case of reverse flow cyclones, the mechanism that limits the throughput has been identified. With this information changes in operating conditions can be predicted qualitatively. For each separator type each of the new equations are compared to the traditional equations and the effect of the discrepancies is described shortly.

8.3.2 Traditional axial cyclones

Maximal capacity

In case of radially purging cyclones the most important limiting mechanism is the failure of the secondary separation zone to separate the discharged liquids from the purge gas. The criterion for reentrainment is described as follows (see equation 7.23):

$$\phi_{g \max} \geq \sqrt[3]{\frac{(\rho_l - \rho_g)}{\rho_g^2 \mu}} \cdot \sqrt[3]{S_A^2 \left(\frac{v\% D}{p\%^3}\right)} \cdot C \quad (8.2)$$

in which: ϕ_g = gas throughput
 D = cyclone diameter
 S_A = slit surface
 $p\%$ = percentage of purge gas
 $v\%$ = volume percentage of liquid in gas
 C = numerical constant

In case of coaxially purging cyclones the same mechanism may take place, but in this case $\phi_{g \max}$ is better described by (see equations 7.20 and 7.21):

$$\phi_{g \max} \geq \sqrt[3]{\frac{(\rho_l - \rho_g)}{\rho_g \cdot \rho_l}} \cdot \sqrt[3]{\frac{D^3}{p\% \cdot \tan^2 \alpha}} \cdot C \quad (8.3)$$

in which α = the swirl angle of the exit plane and determines the ratio between tangential and axial velocity components. It can be quantified exactly from relations in section 5.5 or from AC-MOD1 but as a simplification α can be taken equal to the swirler angle.

An other limitation of the capacity of this cyclone type may be formed by the reentrainment mechanism depicted in figure 6.11. In this case it is more difficult to derive general relations from AC-MOD3, as there is much larger influence of the cyclone geometry.

The magnitude of the radial velocities at the exit plane depends on, for instance, the swirl number. Generally, it can be expected that at swirl numbers lower than 0.8, high local radial inflow velocities are created.

If the simulated gas velocities in figure 7.14C are observed it is noted that for swirl numbers of $S = 0.55$ inward directed radial velocities up to 5 m/s occur. Generalizing it can therefore be said that if the vane angle is lower than 50-60° one should seriously account for this limitation mechanism.

To quantify $v_{g \max}$ in this case, the absolute values of the velocity components of the gas flow field should be derived from simulations. Qualitatively, the maximal capacity will depend on ρ_g , μ_l and σ as described by the equilibrium specified by equations 7.16, 7.17 and 7.19:

$$v_{gmax} = C_1 \cdot \frac{\rho_g^x \sigma}{\mu_1} \quad (8.4)$$

in which: $x = -0.5 < x < -0.1$, depending on swirl number;

if $S = 1.2$ $x \sim -0.15$

if $S = 0.55$ $x \sim -0.35$

C_1 = numerical constant depending on gas flow field

Minimal capacity

The minimally allowable gas throughput strongly depends on the specific form of the gas flow field, which necessitates gas flow field simulations for quantitative predictions. Qualitatively, the minimal capacity will depend on ρ_1 , ρ_g and d_d as specified by equations 7.12-7.15 (assuming that the centrifugal stabilization justifies $C_D = \frac{24}{Re}$).

$$v_{gmin} = \frac{C_2}{(\rho_1 - \rho_g) d_d^2} \quad (8.5)$$

in which: C_2 = numerical constant depending on gas flow field.

If the influence of operating pressure on the turn-down ratio (T_r) is determined from the above two characteristics it appears that:

$$T_r \sim \frac{(\rho_1 - \rho_g)}{\rho_g^{0.7}} \text{ in case of maximal capacity that is limited by a failing secondary separation zone and:} \quad (8.6)$$

$$T_r \sim \frac{(\rho_1 - \rho_g)}{\rho_g^{0.3}} \text{ in case of maximal capacity that is limited by reentrainment.} \quad (8.7)$$

Pressure drop

The pressure drop across an axial cyclone consists mainly of the pressure drop across the swirl element and the vortex finder. The pressure drop coefficient of the first can be approximately determined from table 6.I, while the determination of the second is straightforward.

If simulation modelling is not used the pressure drop can be manually determined by assuming that no other influences play a role (see section 7.4 for justification of this assumption) and that:

$$\Delta p = \xi_{ac} \frac{1}{2} \rho_g v_g^2 \quad (8.8)$$

in which: $\xi_{ac} = \xi_{sw} + \xi_{vf}$

ξ_{sw} = pressure drop coefficient of swirl element and

ξ_{vf} = pressure drop coefficient of vortex finder.

Evaluation of practical design equations for axial cyclones

Maximal capacity

One of the few references to the design of axial cyclones for higher operating pressures is:

$$\lambda = 0.3$$

$$\text{in which } \lambda = v_{gs} \sqrt{\frac{\rho_g}{\rho_l - \rho_g}} \text{ (the load factor);} \quad (8.9)$$

v_{gs} is the superficial axial velocity in the cyclone.

The cyclone in question is of the radial discharge type and has been tested in AC-EXP3 (table 6.IV, cyclone type II). The test results show a much larger dependency on ρ_g than predicted by equation 8.9 (see figure 6.12).

In figure 8.13 the actual influence and the influence predicted by equation 8.9 are compared.

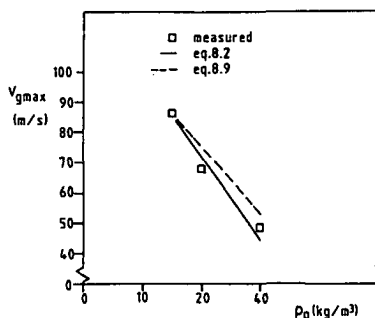


Figure 8.13 Comparison of traditional with improved design equation

The origin of the load factor (see appendix A 3.4.2) is not suited for the determination of the capacity of cyclones at all (see appendix A 3.4.2). This is reflected by the large discrepancy that appears when trying to describe the influence of ρ_g in experimental results with this equation. Relying on this equation might lead to gross underdesign of axial cyclones under high operating pressures.

An example may illustrate this: suppose that a certain axial cyclone separator for application at 100 bar operating pressure is designed by upscaling from atmospheric test data. With equation 8.9 a vessel will be designed in which the maximum allowable superficial gas velocity as specified by equation 8.2 is exceeded by a factor 2.5. The diameter of the vessel is chosen at least 1.5 times too small.

8.3.3 Reverse flow cyclones

Maximal capacity

The limiting mechanism can be compared to the second mechanism described for coaxially purging axial cyclones (see section 7.5.3). The same remarks apply with respect to the necessity of knowledge of the gas flow field. The gas flow field, especially in this case, is very difficult to characterize in a simple way. It is recommended to rely on the full simulation model (when completed) for quantification of the local gas velocities.

Because of the similarity of mechanism of limitation with coaxially purging axial cyclones the dependency of v_{gmax} on the operating conditions is also described by equations 7.16-1.19:

$$v_{gmax} = C_3 \cdot \frac{\rho_g^x \sigma}{\mu_1} \quad (8.10)$$

in which: $x = -0.5 < x < -0.1$, depending on swirl number;

if $S = 1.2$ $x \sim -0.15$

if $S = 0.55$ $x \sim -0.35$

C_3 = numerical constant depending on gas flow field

Minimal capacity

The exact determination needs to be carried out by simulations; dependency of v_{gmin} on operating conditions can be summarized as follows (see equations 7.12-7.15):

$$v_{gmin} = \frac{C_4}{(\rho_1 - \rho_g) d_d^2} \quad (8.11)$$

in which: C_4 = numerical constant depending on gas flow field.

The turn down ratio relates to the operating pressure as:

$$T_r \sim \frac{(\rho_1 - \rho_g)}{\rho_g^{0.3}} \quad (8.12)$$

Pressure drop

The pressure drop is well described by the relations in appendix A 3.4.4.4.

Evaluation of practical design equations for reverse flow cyclones

Maximal capacity

The design equations of which an inventory is made in appendix A 3.4.4 and that recognized reentrainment as limiting mechanism with respect to capacity, did not take the stabilizing effect into account of the centrifugal field. Hence, they describe too strong a dependency of v_{gmax} on ρ_g ($v_{gmax} \sim \rho_g^{-0.5}$). These criteria lead to oversized separators.

Most design equations that are used in the oil field practice either use again a load factor or a pressure drop criterion.

Minimal capacity

Usual a minimal capacity is assumed that is independent of operating conditions. This is not justifiable for smaller $(\rho_l - \rho_g)$ values.

8.3.4 Vanes

Maximal capacity

Two limiting mechanisms have been identified and described.

Both are treated in section 7.6. In case of shearing-off of the film from irregularities in front of the drainage slits it is difficult to give a simplified relation of significant reliability. It is recommended to use the complete model described in V-MOD3 to calculate the balance of reentrainment and redeposition.

In case of smooth vane surfaces the maximal capacity is limited by reentrainment by roll-wave crest shear off (section 7.3.3). The local status of the gas flow field determines the amount of centrifugal stabilization of the liquid film. In case of well located drainage slits the maximal velocity depends again on the operating conditions in the earlier described manner:

$$v_{gmax} = C_5 \cdot \frac{\rho_g^x \sigma}{\mu_l} \quad (8.13)$$

in which: $-0.5 < x < -0.3$, depending on locations of wetted areas and vane geometry: if wetted areas are located outside centrifugal field $x \sim -0.5$. Otherwise x may be larger, depending on gas flow field.

C_5 is a numerical constant.

Minimal capacity (primary efficiency)

The flow field between vane blades is too complex to be generalized by simple relations. For the exact determination of the primary efficiency is referred to the models formulated in V-MOD3.

Generally (see section 7.2) the dependency on ρ_g will be larger than predicted for cyclone separators. The centrifugal stabilization will probably not be strong enough to extend the range of Stokes' Law.

In case of smooth vane blades and for a given geometry and two-phase system the turndown ratio will be linearly dependent on:

$$T_r \sim \frac{\rho_l - \rho_g}{\rho_g^x} \quad 0.3 < x < 0.9 \text{ depending on locations of wetted areas and vane geometry} \quad (8.14)$$

Pressure drop

As the pressure drops strongly depends on the generated gas flow field (vortices!) between the vane blades it is difficult to formulate simplified relations that describe the influence exerted on this parameter by geometrical variations. Therefore, it is recommended to use the gas flow field simulation model to determine pressure drops.

Evaluation of practical design equations for vanes

Maximal capacity

Two different criteria are encountered in practice (see appendix C) to determine the maximal capacity in vanes with shielded liquid drainage:

$$1. \text{ a load factor } (v_{g \max} \sqrt{\frac{\rho_l - \rho_g}{\rho_l}}) \text{ limit varying between } 0.1 - 0.3, \text{ depending on several parameters} \quad (8.15)$$

$$2. \text{ a reentrainment criterion, } \frac{1}{2} \rho \frac{v_{g \max}^2}{\sigma} < C \text{ [m}^{-1}\text{]} \quad (8.16)$$

In the latter case is not accounted for the centrifugal film stabilization. In the first case there is no connection between the liquid properties and the limitation of mechanism. In both cases the effect of ρ_g on $v_{g \max}$ is assumed too strong if vanes are described in which the wetted areas are carefully chosen. This might lead to oversized separators at higher operating pressures, which can cause too low operating velocities, because T_r reduces strongly with increasing pressures (equation 8.14).

Again an example may illustrate this case: suppose that a certain vane type separator for application at 100 bar operating pressure is designed by upscaling from atmospheric test data with equation 8.15. If the exponent x in equation 8.13 amounts to $x = -0.3$, then a vane type separator is designed in which the maximum allowable superficial gas velocity is not reached by a factor 2.5.

Apart from the fact that an unnecessary large vessel is constructed (diameter 1.5 times larger than necessary) it is probable that in this case the separator will sometimes not function properly because of too low throughputs.

Minimal capacity

As appears from chapter 3 usually no consistent criteria if any are encountered with respect to this parameter.

LIST OF SYMBOLS

Note: Separator internal geometries are characterized separately in:
 figures 3.36, 5.17 and 6.10 (Axial cyclones)
 figure A.9 (Reverse flow cyclones)
 figures A.4 and A.5 (Vanes)

| | | |
|------------|--|---------------------------------------|
| b | film thickness | (m) |
| d | diameter of dispersed particle | (m) |
| d_D | droplet diameter | (m) |
| d_{eq} | diameter of spherical particle with equal frontal area | (m) |
| dsd | droplet size distribution | (-) |
| C_A | surface area of cyclone tube | (m ²) |
| D | diameter of flow duct | (m) |
| D_h | hydraulic diameter of flow duct | (m) |
| f | friction factor | (-) |
| g | gravitational acceleration | (m s ⁻²) |
| k | wave number | (m ⁻¹) |
| | turbulent kinetic energy | (m ² s ⁻²) |
| | height of film instabilities | (m) |
| K | Stokes Cunningham Correction | (-) |
| L | separator length | (m) |
| M_θ | flux of angular momentum | (kg m ² s ⁻²) |
| M_z | flux of axial momentum | (kg m s ⁻²) |
| N_μ | viscosity number | (-) |
| P | operating pressure | (kg m ⁻¹ s ⁻²) |
| r | radius | (m) |
| R_E | reentrainment rate | (kg m ⁻² s ⁻¹) |
| S | swirl number | (-) |
| t | time | (s) |
| T_A | modular surface area of axial cyclone | (m ²) |
| T_r | turndown ratio | (-) |
| u, U | axial velocity | (m s ⁻¹) |
| v | velocity | (m s ⁻¹) |
| V | radial velocity | (m s ⁻¹) |

| | | |
|----------|---|----------------------|
| v%, vol% | liquid volume percentage ($= \phi_1 / (\phi_1 + \phi_g)$) | (-) |
| w, W | tangential velocity | (m s ⁻¹) |

Greek

| | | |
|----------------|--|---------------------------------------|
| α | volume fraction | (-) |
| ϵ | dissipated energy | (kg m ² s ⁻²) |
| η_s, η | separation efficiency | (-) |
| θ | angle of rotation | (-) |
| λ | load factor = $v_{g \max} \sqrt{\frac{\rho_g}{(\rho_l - \rho_g)}}$ | (m s ⁻¹) |
| μ | viscosity | (kg m ⁻¹ s ⁻¹) |
| ν | kinematic viscosity | (m ² s) |
| ρ | density | (kg m ⁻³) |
| σ | surface tension | (kg s ⁻²) |
| τ | shear stress | (kg m ⁻¹ s ⁻²) |
| Φ | volume throughput | (m ³ s ⁻¹) |
| ϕ | swirl angle of flow field | (-) |
| ϕ_o | vane angle of swirler | (-) |
| ψ | Stokes' parameter | (-) |
| ω | angular velocity | (s ⁻¹) |

Indices

| | |
|----|----------------------------------|
| ac | axial cyclone |
| g | gas |
| gp | purge gas |
| g2 | gas in secondary separation zone |
| i | interface |
| l | liquid, film |
| p | particle |
| sw | swirler |

REFERENCES

- Alexander, R., "Fundamentals of cyclone design and operation", Proc. Aus. I.M.M. pp. 203-228 [1949].
- Andreussi, P., "The onset of droplet entrainment in annular downward flows", Can. J. Chem. Eng., Vol. 58 [1980].
- Andreussi, P., J.C. Asali and T.J. Hanratty, "Initiation of roll waves in gas-liquid flows", AIChE J., Vol. 31, no. 1, pp. 119-126 [1985].
- Andreussi, P. and B.J. Azzopardi, "Droplet deposition and interchange in annular two-phase flow", Int. J. Multiphase Flow, Vol. 9, no. 6, pp. 681-695 [1983].
- Arnold, K. et al., "Designing oil and gas production systems", World Oil, pp.73-98 [1984].
- Baker, O., "Simultaneous flow of oil and gas", Oil Gas J., 53, pp. 185 [1954].
- Bankoff, S.G., "Minimum thickness of a draining liquid film", Int. J. Heat Mass Transfer, 14, pp. 2143 [1971].
- Barth, W., "Berechnung und Auslegung von Zyklonabscheidern auf Grund neuerer Untersuchungen", Brennstoff-Wärme-Kraft, Vol.8, pp. 1-9 [1956].
- Beer, J.M. and N.A. Chigier, "Combustion Aerodynamics", Applied Science Publishers Ltd., Essex, England [1972].
- Bell, K.J., J. Taborek and F. Fenoglio, "Interpretation of horizontal in-tube condensation heat transfer correlations with a two-phase flow regime map", Chem. Eng. Proc. Symp. Ser., 66, p. 150-163 [1969].
- Besemer, F.G., "Testen en karakteriseren van multicyclonen", Delft University of Technology, Lab. for Process Equipment, June [1988].
- Bharatan, D., Electric Power Research Institute Report, EPR1 NP-786 [1978].
- Billet, R. and M. Schultes, "Capacity studies of two-phase countercurrent-flow columns", Symp. Distillation and Absorption, Brighton, 7-9 Sept. [1987].
- Bloor, M.I.G. and D.B. Ingham, "Turbulent spin in a cyclone", Trans. Instn. Chem. Engrs., Vol. 53 [1975a].
- Bloor, M.I.G. and D.B. Ingham, "The leakage effect in the industrial cyclone", Trans. Instn. Chem. Engrs., Vol. 53 [1975b].
- Bloor, M.I.G. and D.B. Ingham, "A theoretical investigation of the fluid mechanics of the hydrocyclone", Filtration & Separation, p. 266-269 [1984].

- Boussinesq, J., "Theorie de l'ecoulement tourbillant", Mem. Acad. Sci., 23, 46 [1877].
- Boysan, F., W.H. Ayers and J. Switherbank, "A fundamental mathematical modelling approach to cyclone design", Trans IChemE, Vol. 60 [1982].
- Boysan, F., et al., "Experimental and theoretical studies of cyclone separator aerodynamics, Inst. Chem. Eng. Symp. Ser., Vol. 69, p. 305-319, [1983].
- Boysan F., W.H. Ayers, J. Swithenbank and B.C.R. Ewan, "Theoretical modelling of cyclone performance", Filtration & Separation, p. 39-43, [1985].
- Bradie, J.K., "Entrainment Studies", Ph.D.-Thesis, Heriot-Watt University, Edinburgh [1969].
- Buckley, P.L., R.R. Craig, D.L. Davis and K.G. Schwatzkopf, AIAA paper nr. 80-1119, Hartford, Connecticut, 30, June/July [1980].
- Bürkholz, A., "Approximation formulae for particle separation in cyclones", Ger. Chem. Eng. 8, p. 351-358 [1985].
- Bürkholz, A. and E. Muschelknautz, "Tropfenabscheider. Übersicht zum Stande des Wissens", Chemie Ing. Techn., 44, nr. 8 [1972].
- Calvert, S., I.L. Jashnani, S. Yung and S. Stalberg, "Entrainment separators for scrubbers - initial report", NTIS, PB-241 189, EPA-650/2-74-119a [1974].
- Calvert, S., "Guidelines for selecting mist eliminators", Chem. Engrg., Vol. 85, no. 5, pp. 109-112 [1978].
- CHAM TR/125, "Special Ground & Satlit subroutines in use in the PHOENICS input library", H.I. Rosten and J.P. Edwards, [1986].
- CHAM TR/121, "Lecture Panels for PHOENICS Instruction courses", D.B. Spalding, [1986].
- CHAM TR/100 en TR/101, "PHOENICS Beginners's guide and user manual", H.I. Rosten and D.B. Spalding, [1986].
- CHAM TR/71, "GRAFFIC, the graffical representation and analysis of fluid flow by interactive computation", User manual, G.M. Mallison and K.A. Pericleous, [1981].
- Cheremisinoff, P.N. and N.P., "Cyclone dust collectors", Plant Engineering, p. 75-76 [1974].
- Chien, S.F. and W. Ibele, "Pressure drop and liquid film thickness of two-phase annular and annular-mist flows", ASM paper 62-WA-170 [1960].
- Colenbrander, G.W., "Turbulentiemodellen: Wonder- of lapmiddel?" for publication in I² [1988].

- Cooper, E.R. and D.F. Jankowski, "Experiments of the onset of instability of unsteady circular couette flow", J. Fluid Mech., Vol. 161, pp. 97-113 [1985].
- Crowe, C.T. and D.T. Pratt, "Analysis of the flow field in cyclone separators", Computers and Fluids, Vol. 2, p. 249-260, Pergamon Press [1974].
- Dallman, J.C. and T.J. Hanratty, "Two-phase momentum", Heat and Mass Transfer, Vol. 2, pp. 681, Hemisphere, New York [1979].
- Daniels, T.C., "Investigation of a vortex air cleaner", The Engineer, pp. 358-362, March [1957].
- Davies, E.E. and P. Watson, "Miniaturized separators proved high performance", World Oil, April [1980].
- Dietz, P.W., "Collection efficiency of cyclone separators", AIChE J. 68, 196 [1972].
- Dirgo, J. and D. Leith, "Cyclone collection efficiency", Aerosol Science and Technology [1985a].
- Dirgo, J. and D. Leith, "Performance of theoretically optimized cyclones", Filtration & Separation, p. 119-125, [1985b].
- Dobbins, R.A., K.A. Conti and D. Yeo, "Performance analysis of axial flow dust separators", Proc. 2nd World Filtration Congress, pp. 145-150 [1979].
- Doesschate, M.J. ten, "Opbouw en afregeling van de grote meetopstelling van het gas/vloeistofscheidingsonderzoek", Delft University of Technology, Lab. for Process Equipment [1986].
- Donaldson, C. du P., "A computer study of an analytical model of boundary layer transition, AIAA paper 68-83 [1968].
- Felton et al., "Direct measurement of concentration and size for particles of different shapes using laser light diffraction", Chem. Eng. Res. Des., Vol. 63, March [1985].
- Fletcher, R.S. (course organizer), "Gasturbine combustion", Short course at Cranfield Inst. of Techn., Bedford, England, May 14-18 [1973].
- Forde, M. and H. Norstrud, "Brief communication on fictional pressure gradient in annular flow", Int. J. Multiphase flow, Vol. 10, no. 1, pp. 115-119 [1984].
- Friedlander, S.K., Ind. Engng. Chem. 50, pp. 1161 [1958].
- Fuchs, N.A., "The mechanics of aerosols", MacMillan Co., New York [1964].
- Gardner, G.C., "HTFS design report no. 46, "Separation of liquids from gases or vapours", AERE Harwell and National Engineering Laboratory, AERE R.8917, HL 77/2844, [1977].

- Gardner, G.C., "Talk on natural separation and separation by impaction", Congress Norway [1984].
- Gibson, M.M. and B.E. Launder, ASME J. Heat Transfer, 98, 80 [1976].
- Graauw, J. de, "Olie- en gasbehandeling", Leidraad bij de cursus olie- en gasbehandeling binnen- en buitengaats, pp. II/1-67, Delft University of Technology, Lab. for Process Equipment [1984].
- Gupta, A.K., D.G. Lilley and N. Syred, "Swirl flows", Energy and Engineering Science Series, Abacus Press [1984].
- Hartley, D.E. and W. Murgatroid, Int. J. Heat Mass Transfer, Vol. 7, pp. 1003-1015 [1964].
- Helmholtz, H., "Über discontinuirliche Flüssigkeitsbewegungen", Monatsber. Dtsch. Akad. Wiss., Berlin, pp. 215-228 [1868].
- Helwig, E.B.M., "Fundamentele beschouwing van het stromingsgedrag in een axiale cycloon", TU Delft, Lab. for Process Equipment, [1986].
- Hershman, A. and T.J. Hanratty, "Initiation of roll waves", AIChE J., 7, pp. 488 [1961].
- Herwijnen, W.E.R. van, "Ontwikkeling meetprocedure voor de grote opstelling", Delft University of Technology, Lab. for Process Equipment, [1986].
- Hetsroni, G., "Handbook of multiphase systems", Hemisphere, Washington [1982].
- Hewitt, G.W. and Hall-Tayler, "Annular two-phase flow", Oxford, Pergamon Press [1970].
- Hiller, R. and F. Löffler, Staub-Reinhalt. Luft, 40, pp. 404-411 [1980].
- Hinze, J.O., "Turbulence", McGraw-Hill [1975].
- Hinze, J.O., "Fundamentals of the hydrodynamic mechanism of splitting in dispersion processes", AIChE J., Vol. 1, No. 3, pp. 289-295 [1955].
- Hughmark, G.A., "Film thickness, entrainment and pressure drop in upward annular and dispersed flow", AIChE J., 19, pp. 1062 [1973].
- Hulst, J.B., "Ontwerp en optimalisatie van de API-supervortex axiaal cycloon", Delft University of Technology, Lab. for Process Equipment, August [1988].
- Ishii, M. and M.A. Grolmes, "Inception criteria for droplet entrainment in two-phase concurrent flow", AIChE J., Vol. 21, p. 308-318 [1975].
- Ishii, M. and I. Kataoka, "Interfacial transfer in annular dispersed flow", Symposium, pp. 93-117 [1983].

- Ishii, M. and K. Mishima, "Liquid transfer and entrainment correlation for annular flow", paper TF20, 7th Int. Heat Trans. Conf., Munchen [1981].
- Jackson, R., "Mechanical equipment for removing grit and dust from gases", The British Coal Utilisation Research Association", [1963].
- James, P.W., G.F. Hewitt and P.B. Whalley, "Droplet motion in two-phase flow", UKAEA report, AERE-R9711 [1980].
- Joseph, A.F., "Fibre bed mist eliminators: latest developments", Filtration and separation, pp. 40-42, Jan./Feb. [1984].
- Kamp, C.M.B., "Het karakteriseren van de gasstroom in axiaal cyclonen", Delft University of Technology, Lab. for Process Equipment, August [1988].
- Karvinen, R. and H. Ahlstedt, "Use of Phoenixics with modifications in some process problems", First International PHOENICS Users Conference, Datford, [1985].
- Karvinen, R. et al., "Modelling of swirling flows and heavy fuel combustion", Proc. 2nd Int. Phoenixics User Conf., London [1987].
- Kecke, J., "Beitrag zur Klärung des Strömungsvorganges und der Staubbewegung im Zyklon", Thesis, TH Magdeburg [1967].
- Kelvin, W., "hydrokinetic solutions and observations", Phil. Mag., Vol. 4, pp. 374 [1871].
- Kerns, G.C., "New charts speed drum sizing", Petr. Refining, Vol. 39, no. 7, pp. 168 [1960].
- Kerstjens, J.M., "Numerieke simulatie van roterende gasstromen in axiaal cyclonen", Delft Univ. of Technology, Lab. for Process Equipment [1988].
- Koffman, J.L., Gas and Oil Power, 48, pp. 89-94 [1953].
- Kolmogoroff, A.N., Doklady Akad. Nauk. SSSR, 66, no. 5, pp. 825-828 [1949].
- Kort, G.C.I. de, "Stromingsonderzoek tussen vane platen", Delft Univ. of Technology, Lab. for Process Equipment [1987].
- Koster, R.J., "Modelvorming 'axial-flow' cyclonen", Delft Univ. of Technology, Lab. for Process Equipment [1987].
- Kropp, L.I. and O.P. Potapov, "Taking into account the battery effect in development of mechanical ash removal plant for thermal power stations", Therm. Eng., Vol. 28, p. 384-387 [1981].
- Kutateladze, S.S., "Elements of hydrodynamics of gas-liquid systems", Fluid Mechanics, Soviet Res., 29 [1972].
- Lapple, C.E., "Processes use many collector types", Chem. Engng., Vol. 58, no. 5, pp. 144-151 [1951].

- Lamb, H., "Hydrodynamics", Dover, New York (originally published in 1879) [1945].
- Leith, D. and W. Licht, "The collection efficiency of cyclone type particle collectors", AIChE Symp. Series no. 26, Vol. 68, pp. 196-206 [1972].
- Leith, D. and D. Metha, "Cyclone performance and design", Atmospheric Environment, Vol. 7, pp. 527-549 [1976].
- Leuckel, W., "Swirl intensities, swirl types and energy losses of different swirl generating devices", Doc. Nr. G02/a/16, International Flame Research Foundation [1968].
- Leijdens, H., "Stroming en warmteoverdracht II", Delft University of Technology [1984].
- Lilley, D.G., "Nonisotropic turbulence in swirling flows", Acta Astronautica, Vol. 3, p. 919-933 [1976].
- Lilley, D.G. and N.A. Chigier, "Nonisotropic turbulent stress distribution in swirling flows from mean value distributions", Heat and Mass Transfer, 14, p. 573-585 [1971].
- Lilley, D.G., "Prediction of inert turbulent swirl flows", AIAA Journal, 11, 7 [1973].
- Linden, A.J. ter, "Investigations into cyclone dust collectors", Inst. of Mech. Eng. Proc., Vol. 160, pp. 233-245 [1949].
- Linden, A.J. ter, "Der Zyklon als Tropfenabscheider", Chem. Ing. Techn., pp. 328-330, nr. 6 [1953a].
- Linden, A.J. ter, "Cyclone dust collectors for boilers", Trans. ASME, Vol. 75, p. 433-440 [1953b].
- Lodder, R.M., "Afregeling meetopstelling en eerste resultaten van de 'reverse flow' cyclonen", Delft University of Technology, Lab. for Process Equipment, March [1988].
- Löffler, F., "Partikelabscheidung an Tropfen und Fasern", Chem. Ing. Techn., 55, Nr. 3, pp. 171-178 [1983].
- Loxham, M., "The flow pattern in the exit pipe of a cyclone", Thesis, Delft University of Technology [1976].
- Lubin, B.T. and G.S. Springer, "The formation of a dip on the surface of a liquid draining from a tank", J. Fluid Mech., Vol. 29, pp. 385 [1967].
- Malin, M.R., "Axisymmetric, Two-phase flow in a gas-oil cyclone separator", PDR/CHAM UK/7, [1982].
- Mandhane, J.M., G.A. Gregory and K.A. Aziz, "A flow pattern map for gas-liquid flow in horizontal pipes", Int. J. Multiphase Flow, 1, pp. 537-553 [1974].

- Marr, R. and F. Moser, "Die Auslegung von stehenden Gas-Flüssig-Abscheidern - Schwerkraft- und Gestrickabscheider", Verfahrenstechnik 9, nr. 8, pp. 379 [1975].
- Mather, M.L. and N.R.L., "Swirling jets issuing from vane swirlers", J. Int. Fluel, 40, nr. 316, pp. 214-225 [1967].
- Moody, L.F., Trans. A.S.M., 66, p. 671 [1944].
- Morsi, S.A. and A.J. Alexander, "Particle trajectories in two-phase flow systems, J. Fluid Mech., 55, pp. 193-208 [1972].
- Mothes, H., "Bewegung und Abscheidung der Partikeln im Zyklon", Thesis, November, 1982.
- Mothes, H. and F. Löffler, "Zur Berechnung der Partikelabscheidung in Zyklonen", Chem. Eng. Process., 18, pp. 323-331 [1984a].
- Mothes, H., and F. Löffler, "Der Einfluß der Gutbeladung auf die Strömung im Gaszyklon", PARTEC: European Symposium on particle classification in gases and liquids, Nürnberg [1984b].
- Muschelknautz, E., Vt-Hochschulkurs LL: Mechanische Verfahrenstechnik, Krausskopf-Verlag, Mainz [1972].
- Muschelknautz, E. and W. Krambrock, "Aerodynamische Beiwerte des Zyklonabscheidern aufgrund neuer und verbesserte Messungen", Chem. Ing. Techn., Vol. 42, no. 5, pp. 247-255 [1970].
- Niemeyer, R.E., "Check these points when designing knockout drums", Hydrocarbon Processing and Petroleum Refiner, Vol. 40, pp. 155 [1961].
- Nieuwenhuis, W.J., "Het karakteriseren van multicyclonen in de grote opstelling", Delft University of Technology, Lab. for Process Equipment [1987].
- Nieuwstadt, F.T.M., Personal communications at the Delft University of Technology [1987].
- Overgaag, S.P.J., "Karakteriseren van verticaal doorstroomde gas-vloeistof scheidern", Delft University of Technology, Lab. for Process Equipment, March [1988].
- Paleev, I.I. and B.S. Filipovich, "Phenomena of liquid transfer in two-phase dispersed annular flow", Ing. J. Mass and Heat Transfer, Vol. 9, pp. 1089 [1966].
- Parida, A. and P. Chand, "Turbulent swirl with gas-solid flow in cyclone", Chem. Eng. Sci., Vol. 35, p. 949-954 [1979].
- Patankar, S.V., "Numerical heat transfer and fluid flow", McGraw-Hill [1980].
- Pelsma, M.H., "Modelvorming 'reverse flow' cyclonen", TU Delft, Laboratory for Process Equipment [1987].

- Pericleous, K.A. and N. Rhodes, "A hydrocyclone classifier - A numerical approach", Int. J. of Min. Proc., 17, 22-43 [1986].
- Pericleous, K.A., N. Rhodes and G.W. Cutting, "A mathematical model for predicting flow field in a hydrocyclone classifier", Int. Conf. on Hydrocyclones, Bath, England, September [1984].
- Plekhov, M. et al., "Investigation of a direct-flow centrifugal separator", Translation from Khim. Neft. Mash., No. 8, pp. 15-16, Aug. 1971 [1972].
- Pollak, A. and L.T. Work, "The separation of liquid from vapour, using cyclones", Trans. A.S.M.E., Vol. 63, pp. 31-41 [1942].
- Polyakov, L.E., "Cyclone separators for gas-liquid mixtures", Khimicheskoe i Neftyanoe Mashinostroenie, New Machinery and Equipment, No. 6, p. 6-8 [1986].
- Popov, N.K. and U.S. Rohatgi, "Effect of interfacial shear and entrainment models on flooding predictions", AIChE J., Vol. 32, no. 6, pp. 1027-1035 [1986].
- Potapov, O.P., "The influence of the installation of the cyclone elements on the efficiency of the battery cyclones", Soviet power engineering, no. 7 [1976].
- Pouwels, A.C., "Modellering van de stroming van gas/vloeistof mengsels in vane afscheiders", Delft University of Technology, Lab. for Process Equipment [1987].
- Prandtl, L., Z. angew. Math. u. Mech., 5, 136 [1925].
- Ranz, W.E., "Wall flows in a cyclone separator: A description of internal phenomena", Aerosol Science and Technology, 4, pp. 417-432 [1985].
- Reydon, R.F. and W.H. Gauvin, "Theoretical and experimental studies of confined vortex flow", Can. J. Chem. Eng., 59, pp. 14-23 [1981].
- Reynolds, O., Manch. Mem. vi., Scientific Papers, Cambridge, 1900, i. 231 [1877].
- Reznik, V.A. and V.V. Matsnev, "Comparing the characteristics of the elements in batteries of cyclones", Teploenergetika, Vol. 18 (12), p. 23-26 [1971]. Therm. Eng., Vol. 18, p. 324-329 [1971].
- Rodi, W., "Turbulence models and their application in hydraulics - a state of the art review", Int. Ass. for Hydraulic Research, Delft, 2nd rev. ed., February [1984].
- Rosin, P., E. Rammler and W. Intelmann, "Grundlagen und Grenzen der Zyklonentstaubung", Zeit. Ver. Deut. Ing., Vol. 76, pp. 433 [1932].
- Rossum, J.J. van, "Experimental investigation of horizontal liquid films", Chem. Eng. Sci., 11:35-32.

- Rumpf, "Optimale Dimensionierung von Zyklonen mit Hilfe vereinfachender Modellrechnung", Chem. Ing. Techn., 40, 21/22, pp. 1072-1082 [1968].
- Saemundson, H.B., "Abscheidung von Öltropfen aus stromender Luft mit Draht-gestrickpaketen", Verfahrenstechnik 2, 11 [1968].
- Sakaguchi, T., "Flow regime maps for developing steady air/water two-phase flow in horizontal tubes", Mem. Fac. Eng., Kobe Univ., p. 191-202 [1979].
- Schetz, J.A., "Injection and mixing in turbulent flow", Vol. 68, Progress in Astronautics and Aeronautics, Martin Summerfield [1980].
- Scheiman, A.D., "Horizontal vapour-liquid separators", Hydrocarbon processing and Petr. Refiner, Vol. 43, nr. 5, pp. 155 [1964].
- Schicht, H.H., "Flow patterns for adiabatic two-phase flow of water and air within a horizontal tube", Verfahrenstechnik, 3, pp. 153-161 [1969].
- Shearer, C.J. and R.M. Nedderman, "Pressure gradient and liquid film thickness in cocurrent upwards flow of gas-liquid mixtures", Chem. Eng. Sci. 20, p. 671 [1965].
- Shepherd, C.B. and C.E. Lapple, "Flow pattern and pressure drop in cyclone dust collectors; cyclone without inlet vane", Ind. Engng. Chem., Vol. 32, pp. 1246-1248 [1940].
- Sherwood, T.K., G.H. Shipley and F.A.L. Holloway, "Flooding velocities in packed columns", Ind. Engng. Chem., Vol. 30, pp. 765 [1938].
- Sleicher, C.A. jr., "Maximum stable drop size in turbulent flow", AIChE J. 8, pp. 471-477 [1962].
- Smellie, J., Iron and Coal Tr. Rev., 144, pp. 169 [1942].
- Smith, J.L., "An experimental study of the vortex in the cyclone separator", Trans. ASME, pp. 602-608 [1962].
- Smith, J.M., E. Stammers and L.P.B.M. Janssen, "Fysische transportverschijnselen I", Delftse Uitgevers Maatschappij [1984].
- Solbach, W., "Untersuchungen über den Abscheidvorgang in einem Axial Zyklon", Thesis, Technischen Hochschule Aachen [1958].
- Sorokin, Yu.L., et al., "The principles of drop separation from vapour or gas stream", Chem. and Petr. Engng., no. 8, pp. 664 [1968].
- Spalding, D.B., Lecture panels for Phoenix-84 instruction course, CHAM TR/121, December [1985].
- Stairmand, C.J., "The design and performance of cyclone separators", Trans. Inst. Chem. Engrs., Vol. 29, pp. 356-383 [1951].
- Stearman, F. and G.J. Williamson, "Spray elimination in processes for air pollution control", Nonhebel, 2nd ed., CRC Press, Cleveland [1972].

- Stenhouse, J.I.T., et al., "The behaviour of uniflow cyclones", Proceedings of 2nd World Filtration Congress, pp. 151-156 [1979].
- Stenhouse, J.I.T. and M. Trow, "Particle separation in uniflow cyclones", I. European Symp. on Particle Classification in Gases and Liquids", Nürnberg, 9-11 May [1984].
- Storch, O. et al., "Industrial separators for gas cleaning", Chemical Engineering Monographs, 6 [1979].
- Strauß, W., "Industrial gas cleaning", Pergamon Press [1966].
- Suneja, S.K. and C.H. Lee, Atmos. Environ. 8 [1974].
- Taitel, Y. and A.E. Dukler, "A model for predicting flow regime transitions in horizontal and near horizontal gas-liquid flow", AIChE J., 22, pp. 47-55 [1976].
- Tatterson, D.F., AIChE J., Vol. 23, 67 [1977].
- Umney, L.E.R., "Theory and design of an improved centrifugal air cleaner", National Gas Turbine Establishment, report no. R33 [1948].
- Ushiki, K. et al., "Performance of a droplet separator with multistage rows of flat blades", J. Chem. Engng. of Japan. Vol. 15, no. 4, [1982].
- Vemer, T.J.H., "Het karakteriseren van horizontaal doorstroomde vane platen pakketten", Delft University of Technology, Lab. for Process Equipment [1987].
- Verlaan, C.C.J., Thesis, Delft University of Technology, planned to be published in [1990]
- Wallis, G.B., "One-dimensional two-phase flow", McGraw-Hill, New York, pp. 345-531 [1969].
- Wallis, G.B. and D.A. Steen, "The transition from annular to annular-mist cocurrent downflow", AEC report NYO-3114-2 [1964].
- Waterreus, F.P.M., "Numerieke stromingssimulaties in cyclonen en vaneplaatpakketten", Delft University of Technology, Lab. for Process Equipment, May [1988].
- Whalley, P.B., G.F. Hewitt and P. Hutchinson, "Transient flow redistribution in annular two-phase flow", Paper at Symposium multi-phase flow systems, I. Chem. E. Symp. Ser. no. 38, Vol. 1 [1974].
- Wicks, M. and A.E. Dukler, "Entrainment and pressure drop in concurrent gas-liquid flow: air-water in horizontal flow", AIChE J., Vol. 6, [1960].
- Younger, A.H., "How to size future process vessels", Chem. Engng., Vol. 62, no. pp. 201 [1955].
- Zhivaikin, L.Ya., "Liquid film thickness in film-type units", Intern. Chem. Eng., 2(3), 337 [1962].

APPENDIX A

3.3.2 Knock-out vessels

2.A Operating characteristics (literature investigation)Vertical configuration

When considering the vertical knock-out vessel of figure 3.6, it can easily be seen that the droplet will not be separated when the drag force of the upflowing gas stream is larger than the gravity force.

A critical situation is reached when the terminal velocity of a certain droplet size equals the gas velocity.

Following from the equilibrium of gravity and drag forces:

$$v_{g \max} = \left[\frac{4}{3} \frac{g d_p}{C_D} \right]^{1/2} \cdot \left[\frac{\rho_l - \rho_g}{\rho_g} \right]^{1/2} \quad (\text{A.1})$$

As $v_{g \max}$ depends on the minimum value of d_p it is usually attempted to generalize equation A.1 by assuming a relation between v_g and d_p that predicts the largest droplet size at a certain maximal gas velocity upstream of the separation section (thus where the largest shear forces are exerted on the droplet phase).

$$We_{cr} = \frac{\rho_g v_{gpm}^2 d_p}{\sigma} \quad (\text{A.2})$$

in which: We_{cr} = critical Weber number for droplet break-up = 15

v_{gpm} = maximal gas velocity upstream of the separation section;

usually the ratio of v_{gpm} and v_g is taken as $\frac{v_{gpm}}{v_g} \sim 10$

σ = surface tension

If the load factor λ is defined as $\lambda = v_{gmax} \sqrt{\frac{\rho_g}{\rho_l - \rho_g}}$, substitution of equation A.2 results in:

$$\lambda = \left(\frac{v_{gpm}}{v_g} \right)^{1/2} \sqrt{\frac{4}{3} \frac{We_{cr} g}{C_D}} \sqrt{\frac{\sigma}{\rho_g}} \quad (\text{A.3})$$

λ depends only little on the physical properties and amounts in most practical circumstances to $\lambda \sim 0.1$ (A.4)

Although some very crude assumptions have been made (uniform gas flow) the dependency of $v_{g \max}$ on ρ_l and ρ_g is clear. For this reason this equation is usually applied in practice as a base for design procedures.

Horizontal configuration

When considering the horizontal knock-out vessel of figure 3.5, it can be deduced that the droplet will be separated if

$$\frac{\phi_g}{DL} = \frac{\pi}{4} v_{\text{term}} \quad (\text{A.5})$$

This theoretical equation is seldom used when designing horizontal knock-out vessels, because many of the necessary assumptions (especially uniform gas flow) are far from realistic.

2B. Availability and reliability of design procedures (literature investigation)

The design equations and methods used to calculate the dimensions of these separators are straight forward and easy to understand. In the following some presently applied design rules are inventarised.

Vertical configuration

Vessel diameter D_v : D_v is determined as such that:

- a. upward gas velocity will permit the settling of droplets;
- b. downward liquid velocity will permit the escape of entrained gas bubbles.

$$\text{ad a. } v_g = \frac{\phi_g}{\frac{1}{4} \pi D_v^2} < 0.07 \left(\frac{\Delta \rho}{\rho_g} \right)^{1/2} \quad (\text{de Graauw [1984]})$$

$$v_g = \frac{\phi_g}{\frac{1}{4} \pi D_v^2} < 0.06 \left(\frac{\Delta \rho}{\rho_g} \right)^{1/2} \quad (\text{Younger [1955]})$$

$$v_g = \frac{\phi_g}{\frac{1}{4} \pi D_v^2} < 0.04 \left(\frac{\Delta \rho}{\rho_g} \right)^{1/2} \quad (\text{Kerns [1960]}) \quad (\text{A.5})$$

A.3

$$\text{ad b. } v_1 = \frac{2.18 \cdot 10^{-8}}{\mu L} (\Delta \rho) \quad (\text{de Graauw [1984]})$$

$$v_1 = \frac{\phi_1}{\frac{1}{4} \pi D_v^2} < 0.04 \text{ m/s} \quad (\text{Younger [1955]}) \quad (\text{A.6})$$

Vessel length L_v : L_v is the sum of the lengths required for the different compartments for:

- a. degassing the liquid hold-up L_{v1} ;
- b. inlet device (establishing a uniform gas flow) L_{v2} ;
- c. Settling chamber L_{v3} .

$$\text{ad a. } \bar{t} = \frac{\phi_1}{\frac{1}{4} \pi D_v^2 L_{v1}} = 2-5 \text{ min. } L_{v1} > 0.6 \text{ m} \quad (\text{Scheimann [1964]})$$

$$\bar{t} = \frac{\phi_1}{\frac{1}{4} \pi D_v^2 L_{v1}} = 5-10 \text{ min.} \quad (\text{Younger [1955]})$$

$$\left[\frac{\rho_1 \phi_1^2}{\Delta \rho g L_{v1}^5} \right]^{\frac{1}{2}} = 2.51 \quad (\text{Lubin and Springer [1967]}) \quad (\text{A.7})$$

$$\begin{aligned} \text{ad b. } L_{v2} &= \frac{1}{2} D_v \quad L_{v2} > 0.5 \text{ m} & (\text{de Graauw [1984]}) \\ L_{v2} &= 0.4 D_v \quad L_{v2} > 0.3 \text{ m} & (\text{Marr and Moser [1975]}) \\ L_{v2} &> 0.15 \text{ m} & (\text{Niemeyer [1961]}) \quad (\text{A.8}) \end{aligned}$$

$$\text{ad c. } L_{v3} = 0.75 D_v \quad L_{v3} > 1 \text{ m} \quad (\text{Marr and Moser [1975]}) \quad (\text{A.9})$$

It can be seen that the velocity in the liquid pool, (D_v^{-2}) , and the retention time of the liquid in the pool, $(L_{v1} * D_v^2)^{-1}$, are used in design procedures as degassing criterion. It seems that D_v is the most sensible. L_{v1} is also determined by the possible necessity to accommodate large slugs that can not be drained immediately.

Inlet nozzle diameter d_i : d_i is chosen as such that no large mechanical, droplet shattering forces can occur.

If v_{gi} is the average velocity through the inlet device:

$$\rho_g v_{gi}^2 \leq 1000 \text{ N/m}^2 \quad (\text{Marr and Moser [1975], de Graauw [1984]}) \quad (\text{A.10})$$

Outlet nozzle diameter d_{u1} : When v_{gu} is the average gas outlet velocity:

$$\begin{aligned} v_{gu} &= 20-30 \text{ m/s} & (\text{Marr and Moser [1975]}) \\ \rho_g v_{gu}^2 &\leq 3000 \text{ N/m}^2 & (\text{de Graauw [1984]}) \end{aligned} \quad (\text{A.11})$$

Liquid outlet nozzle diameter d_{u2} : To prevent plugging of nozzle d_{u2} should be chosen larger than $d_{u2} > 75 \text{ mm}$ and as such the $v_{u2} > 1 \text{ m}$

$$(\text{Marr and Moser [1975]}) \quad (\text{A.12})$$

It is recommended to install vortex breakers above the liquid to prevent vortex formation with possible consequences for carry-under.

Horizontal configuration

Vessel diameter D_v : D_v is determined as such that de-gassing of separated liquid can take place.

The same rules apply here as to a vertical separator and:

$$\begin{aligned} H_1 &= 0.2 D_v \quad H_1 > 0.3 \text{ m} & (\text{Scheimann [1964]}) \\ H_1 &= 0.5 D_v & (\text{de Graauw [1984]}) \\ H_1 &= \text{liquid depth} \end{aligned} \quad (\text{A.13})$$

Vessel length L_v : L_v is determined as such that with prevailing gas velocities entrainment can reach the liquid surface (see figure 3.5)

$$L_v = \frac{0.275 H_g \phi}{A_g R^2} \left(\frac{\rho_g}{d\rho} \right)^{\frac{1}{2}} \quad (\text{Scheimann [1964]})$$

$$H_g = D - H_1$$

$$A_g = \text{interfacial surface area}$$

$$\frac{\phi}{\frac{1}{8} \pi D_v^2} = v_g \leq 0.1 \left(\frac{\Delta\rho}{\rho_g} \right)^{\frac{1}{2}} \left(\frac{L}{6.1} \right)^{0.56} \quad (\text{de Graauw [1984]}) \quad (\text{A.14})$$

Furthermore the ratio of L_v and D_v is dictated by economic considerations as follows:

$$L_v/D_v = 3 \text{ for } P < 20 \text{ bar}$$

$$L_v/D_v = 4 \text{ for } 20 < P < 40$$

$$L_v/D_v = 5 \text{ for } 40 < P < 60$$

$$L_v/D_v = 6 \text{ for } P > 60$$

$$(\text{A.15})$$

Other criteria are analogous to those for the design of the vertical knock-out vessel. The relative advantages of a vertically or a horizontally positioned vessel are given in section 3.6 where other, not yet described, influencing factors are taken into account.

3.4.2 Mesh type separators

2.A Operating characteristics (literature investigation)

As, up to now, no analytical or numerical models exist that can more or less exactly describe any of the three characteristics separators are judged on in this work (figure 3.2). Phenomenological models have been formulated which describe some aspects of the behaviour of the mesh type separator with empirical constants under certain circumstances.

On the other hand empirical correlations exist but it is not easy to transfer them to other applications than those for which they were originally developed. As it appears to be difficult to set up a general valid model, these empirical correlations are still most popular for design purposes.

Collection efficiencies

It is assumed that the collection efficiency is built up of two parts:

1. impact efficiency; the efficiency with which particles hit the wires;
2. holding efficiency; the efficiency with which these particles are held by the liquid film around the wires upon impact.

ad 1. Impact efficiency

The most popular models assume impact efficiency that is reached stepwise. When the impact efficiency of a single wire is known, the collective impact efficiency of a wire mesh pad can be deduced according to Löffler [1983]

$$\eta(d_p) = 1 - e^{-f \phi(d_p)} \quad (\text{A.19})$$

in which:

$\eta(d_p)$ = the impact efficiency of the total mesh pad as a function of droplet size;

$$f = \text{a characterization of mesh properties } f = \frac{4}{\pi} \frac{1 - \epsilon}{\epsilon} \frac{z}{d_w} \quad (\text{A.20})$$

$\phi(d_p)$ = the impact efficiency for a single wire as a function of d_p ,
 physical properties of two phase mixture and geometrical aspects;
 d_w = the wire diameter;
 z = the thickness of the mesh pad.

Up to now, the determination of $\phi(d)$ has been the reason for inadequacies of the model. Many correlations exist for $\phi(d)$ which not always agree very well. In case of inertial transport mechanisms and $Re_g > 50$ the following equation should agree well with experimental results (Löffler [1983]):

$$\phi(d) = \frac{\psi^3}{\psi^3 + f_1(Re) \psi^2 + f_2(Re) \psi + f_3(Re)} + 3 \left(\frac{2 \rho_g \psi}{Re \rho_1} \right)^{1/2} \quad (\text{A.21})$$

with

$$\begin{aligned} f_1(Re) &= -0.0133 \ln Re + 0.931 \\ f_2(Re) &= 0.0353 \ln Re - 0.36 \\ f_3(Re) &= -0.0537 \ln Re + 0.398 \end{aligned}$$

and ψ being the inertial parameter

$$\psi = \frac{\rho_1 v_g d_p^2}{18 \mu d_w} \quad (\text{A.22})$$

Bürkholz [1972] finds a substantial disagreement between his experimental results and following quantification of $\phi(d)$:

$$\phi(d_p) = \frac{6 \left(\frac{kT}{3\pi\mu} \right)^{2/3}}{\left(\frac{\mu}{\rho} \right)^{1/6} \cdot d_w^{1/2} \cdot d_p^{2/3} \cdot v^{1/2}} + \frac{3 d_p^2 \cdot v^{1/2}}{\left(\frac{\mu}{\rho} \right)^{1/2} \cdot d_w^{3/2}} \quad (\text{A.23})$$

Obviously the first part of above approximation applies to diffusional and the second part to inertial transportation.

ad 2. Holding efficiency

When the cohesive force of the film on the impact of the droplet is larger than the kinetic energy involved the droplet will be hold by the film and its kinetic energy will be dissipated.

A.7

Analogous to Hiller [1980], who made this calculation for solid particles attracted by Van der Waals forces, the following applies when the surface tension reduction is in equilibrium with the transferred kinetic energy:

$$E_{\text{surf tens}} = E_{\text{kin}} \quad (\text{A.24})$$

$$A_p \sigma = \frac{1}{2} m_p v_d^2 \cdot k_{ii} \quad (\text{A.25})$$

A_p = surface area of particle

in which k_{ii} is a constant that determines which part of the kinetic energy is not lost by inelastic effects during the impact. Hiller [1980] quantified k_{ii} between $0.4 < k_{ii} < 0.9$ for solid particles. A conservative assumption for liquid particles is thought to be 0.6 when considering the fact that due to deformation inelastic effects will probably be much larger.

So interception will take place when:

$$v_d < \sqrt{\frac{\sigma \cdot 6}{\rho_l d}} \quad (\text{A.26})$$

This is a condition that sets conservative restrictions, because large droplets will disperse into smaller droplets on the first impact. These smaller droplets are subsequently more susceptible to successful collection deeper in the mesh pad.

Maximal capacity

As will also appear from the experimental results in this report, the liquid hold-up in the horizontal mesh pad increases with increasing gas flow and/or increasing liquid supply to the pad. This is caused by the fact that the draining of the separated liquid flow from the mesh is a function of both liquid hold-up (increased hold-up results in an increased drain flow) and gas velocity (increased gas velocity results in a decreased drain flow).

So, on increase of either gas velocity or liquid supply the hold-up in the mesh pad will increase until a new equilibrium between liquid supply and drainage has been reached. The meshpad can only contain a certain maximal hold up, with an accompanying maximal drainage flow. When the liquid supply surpasses this value the meshpad stops functioning and floods.

Several theoretical models exist that describe this phenomenon under the assumption of film flow of the liquid phase and are generally developed for the operation of packed columns.

The results of the derivation of Billet [1987] is taken as an example:

$$v_{g \max} = \sqrt{\frac{29}{\xi_{\max}}} \cdot (\epsilon - h_{1,f1}) \sqrt{\frac{h_{1,f1}}{a}} \cdot \sqrt{\frac{\rho_l}{\rho_g}} \quad (\text{A.27})$$

in which:

- the flow factor under flooding conditions:

$$\xi_{f1} = \frac{g}{c_{f1}^2 \left[\frac{q_1}{q_g} \sqrt{\frac{\rho_g}{\rho_l}} \cdot \left(\frac{\eta_1}{\eta_g} \right)^2 \eta_{f1} \right]} \quad (\text{A.28})$$

c_{f1} was experimentally found to vary between 1.5 and 3.0 for different packings for $5 < q_1 < 80 \text{ m}^3/\text{m}^2\text{hr}$.

η_{f1} was experimentally found to be invariably -0.194.

- the liquid hold-up under flooding conditions $h_{1,f1} = 0.3741 \epsilon \left(\frac{\eta_1}{\eta_g} \cdot \frac{\rho_g}{\rho_l} \right)^{0.05}$ (A.29)

for $0.1 < q_1 < 200 \text{ m}^3/\text{m}^2\text{hr}$ and $\eta_1 > 10^{-4} \text{ kg/ms}$

Another more empirically tinged but well-known relationship between the flooding point of a packed column and the gas/liquid loading offered to it is formulated by Sherwood [1938]. He defined two parameters of which he determined the influence on the flooding point. The gas load is represented by:

$$\pi_g = v_g \left(\frac{\rho_g}{\rho_l} \right)^{0.5} \left(\frac{a}{\epsilon^3} \right)^{0.5} \left(\frac{\eta_g}{\eta_l} \right)^{0.05} \quad (\text{A.30})$$

in which a = specific surface of packing

ϵ = porosity of packing

The gas/liquid ratio is determined by the flow parameter $\phi = \frac{q_1}{q_g} \left(\frac{\rho_l}{\rho_g} \right)^{1/2}$.

Figure A.1 gives the flooding correlation for three types of packing.

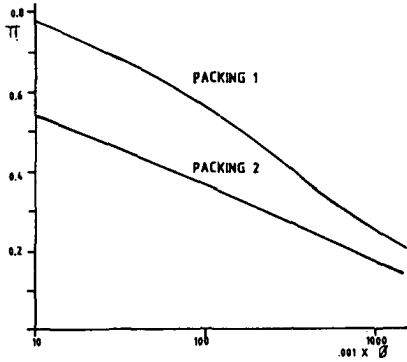


Figure A.1 Flooding correlation
of Sherwood

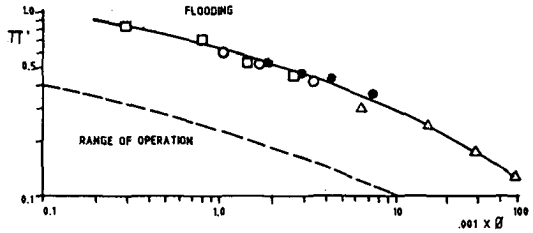


Figure A.2 Flooding correlation
of Burkholz

The correlation appears not to be completely geometry independent. It gives a good indication, though, of the influence of different physical properties. After a slight modification of π_g (the influence of η_1 was doubled and η_g omitted), Burkholz used these parameters to represent the results of his experiments with different meshpads under different circumstances and appears to have found good agreement (figure A.2).

Pressure drop

The pressure drop across the mesh pad ΔP_M will consist of two parts:

- pressure drop ΔP_{MD} across dry mesh;
- pressure drop ΔP_{ML} caused by liquid hold-up.

As the liquid hold-up of the mesh pad is a function of both liquid supply and gas velocity, ΔP_M may strongly increase when the gas flow increases. Many correlations exist for ΔP_{MD} . Saemundson [1968] has formulated a model in which all relevant geometrical mesh properties have been included.

$$\Delta P_{MD} = 2 \phi \frac{h}{D_v} \rho_g \frac{(1 - \epsilon)}{\epsilon^3} v_g^2 \quad (A.31)$$

in which: D_v = diameter of meshpad

h = height of meshpad

ϵ = porosity of meshpad

$$\phi = \frac{34}{Re_h} + \frac{1,4}{Re_h^{0,2}} \quad (\text{friction factor}) \quad (\text{A.32})$$

$$Re_h = \frac{\frac{d_w}{4(1-\epsilon)} v_g \rho_g}{\mu_g} = \frac{d_w v_g \rho_g}{4(1-\epsilon)\mu_g} \quad (\text{A.33})$$

Re_h refers to the hydraulic diameter of the pad.

d_w = diameter of wires

As the model set up by Billet [1987], summarized by equation A.27, gives an expression for the pressure drop at the flooding point ($\Delta P = \xi \frac{1}{2} \rho_g v_g^2$) a qualitative impression can be formed of the influence of the different two-phase properties. To this purpose figure A.3 gives an example of the influence of the liquid loading on pressure drop (Marr and Moser [1975]).

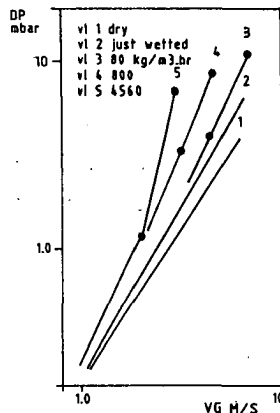


Figure A.3 Effect of liquid loading on maximal capacity

2.B Availability and reliability of design procedures (literature investigation)

In practice the design of the maximal gas velocity through a mesh-pad is carried out very empirically. More sophisticated methods (such as suggested by Billet) have not found wide-spread application.

This may be due partly to the uncertainty with which the operating conditions of a separator are formulated and partly to the very conservative nature of the oil industry.

The design equations most often applied have the form of:

$$v_{g \max} = \lambda \sqrt{\frac{\rho_1 - \rho_g}{\rho_g}} \quad (\text{A.34})$$

Obviously this equation has been 'borrowed' from the situation in which the gravity and drag forces determine whether a droplet is separated or not (equation 3.5). Usually λ is a function of liquid loading, liquid- and gas viscosity, surface tension and even ρ_1 and ρ_g . Nevertheless λ is assumed constant ($\lambda \sim 0,1$) in a broad range of applications. According to Sorokin [1968] λ should be quantified as

$$\lambda = \left(\frac{g^2 \sigma}{\rho_1 - \rho_g} \right)^{1/4} \phi \quad (\text{A.35})$$

in which ϕ is independent of the physical properties.

When substituting this in equation (A.34) it will appear that the original dependency of the v_g on $\sqrt{\frac{\rho_1 - \rho_g}{\rho_g}}$ is decreased.

These separators clearly bear much resemblance with the separators of section 3.3. The popular design procedures are also very analogous.

For the vertical separator two differences can be mentioned:

- D_v is chosen according to the maximum allowable velocity $v_{g \max}$ through the pad;

- $v_{g \max}$ is determined according to the procedure described above.

According to Marr and Moser velocity of the inlet device can be chosen so that $\rho_g v_{gi}^2 < 1500 \text{ N/m}^2$. (A.36)

For the horizontal meshpad separator the same design equations apply as given in section 3.3.2 for the horizontal knock-out vessel, but according to Marr and Moser the inlet velocity can be chosen higher (corresponding to equation A.36).

3.4.3 Vane type separators

2.A Operating characteristics (literature investigation)

In this subsection attention is paid to existing theories (according to figures 3.1 and 3.2) describing:

- a. collection efficiency
- b. maximal capacity
- c. pressure drop

Collection efficiency

A popular way of predicting the collection efficiency of a vane type separator is to approximate the efficiency of a single bend and consider the cumulative effect of all bends on the collective separation efficiency.

Many authors assume a regularly oscillatory motion of the gas flow between the parallel vane blades. The droplets are considered to be influenced by inertial and drag forces.

Ranz [1985], Calvert [1974], Bürkholz and Muschelknautz [1972], Ushiki [1982] amongst others approximated the gas flow motion as connected circle segments (figure A.4).

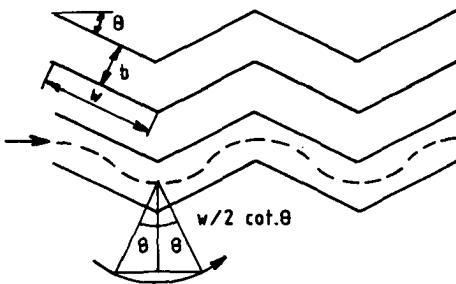


Figure A.4 Plate form assumed
in equation A.37

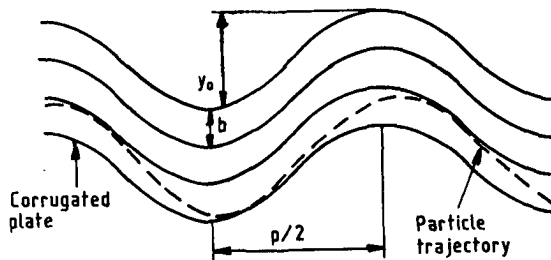


Figure A.5 Plate form assumed
in equation A.38

In this case the efficiency of a single bend can be written as:

$$\eta_B = \theta \psi_p = \theta \frac{\rho_p v_g d_p^2}{18 \mu S} \quad (\text{A.37})$$

in which: θ = bend angle

b = plate spacing perpendicular to gasflow

Gardner [1984] assumed the bends of the gas flow to be sinusoidal (figure A.5), but still considered centrifugal and drag forces the only influencing forces on the motion of the droplets. In this case the efficiency of a single bend can be written as:

$$\eta_B = 2 \frac{Y_O}{n} (1 + \psi_p^{-2})^{-1/2} \quad (\text{A.38})$$

in which: Y_O = the amplitude of the wave plate

ψ according to equation A.22

These two determinations of η_B apply only to horizontally flowed through vanes. For vertically flowed through vanes Gardner [1977] derived the following equation:

$$\eta_B = \frac{2 \left[1 + \frac{w^2}{(1-w)^4 \psi^2} \right]}{\frac{Y_O}{S} \left[\left(1 + \frac{1}{(1-w)^2 \psi^2} \right) \left(1 + \frac{w^2}{(1-w)^4 \psi^2} - \frac{2w}{(1-w)^4 \psi^2} \right) \right]^{1/2}} \quad (\text{A.39})$$

$$\text{in which } w = \frac{9P}{v_g^2}$$

P = the wave plate length

As potential flow is assumed in the derivations that lead to above expressions of η_B , no remixing of the two phases will take place after the bends. This would mean that after the very first bend no more liquid would be separated because the amplitude of the motion of the remaining droplets would not be large enough to reach the blades. As this is hardly a realistic

reproduction of the actual events, Bürkholz [1972], and Calvert [1974] assume complete mixing of both phases after each bend, and the restoring of potential flow before each next bend.

Under these assumptions they derive the following equation for η_{vt} , the total collection efficiency:

$$\eta_{vt} = 1 - (1 - \eta_B)^n \quad (A.40)$$

Gardner [1984] allows for incomplete mixing and states:

$$\eta_{vt} = 1 - (1 - \eta_B)^{\alpha n} \quad (A.41)$$

α is determined experimentally; Gardner reported values of α between 0.5 and 0.63, but recommends $\alpha = 1$ as he encountered unexpected additional separation mechanisms.

From above description it becomes clear that the existing models for predicting the collection efficiency are far from exact, unrealistic in their assumptions (for instance the assumption of potential flow will prove to be very much in contrast to real events) and obsolete in respect to the utilization of modern numerical simulation techniques.

The main shortcomings are:

1. quantification of the forces on the particle is not correct; the applied centrifugal force would only be justified if the particle would follow the gas stream lines.
2. the assumption of potential flow does not allow for remixing of droplets in gas, or taking into account effects caused by eddy currents, growing turbulence, etc.
3. no consideration is given to possible effects as reentrainment.
4. the geometry of the vane blades is of quite subordinate significance in the model.

Maximal capacity

The maximal gas velocity through a vane pack is usually determined by the onset of reentrainment of the film on the vane blades formed by separated droplets. One exception is formed by vertically flowed through vane packs

without shielded liquid drainage slots at higher liquid loading. Then, comparable to wire mesh packs, the maximal gas flow will be set by insufficient liquid drainage capability which will lead to flooding. Usually flooding will take place at considerable lower gas velocities than those at which the rate of reentrainment starts to play a significant role. Two other differences between flooding and reentrainment restricted separation, is that i) flooding leads to an immediate collapse of separation capability, while reentrainment only causes a gradual decline of efficiency with increasing gas velocity and ii) in case of flooding restricted separation, the maximal gas velocity strongly depends on the liquid loading of the gas, while in case of reentrainment this dependency will hardly be noticeable. Also in case of over-rectangular, horizontally flowed-through vane separators flooding can take place at high liquid loadings in the lower part of the vane-box when liquid drainage slots overflow.

Capacity limited by reentrainment

When reentrainment sets the limit Calvert [1974] assumes that for horizontally flowed-through vanes the maximal gas velocity is determined as follows:

$$v_{g \max} = \sqrt{\frac{\sigma \cos \theta}{\rho_g \delta}} \quad (\text{A.42})$$

in which $\frac{\delta}{\cos \theta}$ is the thickness of the liquid film, perpendicular to the gas flow (figure A.6) and reentrainment takes place at the end of the baffle.

In a later publication Calvert [1978] derives an expression for δ , under assumption of equal liquid distribution across the plates (no shielded drainage!). For a plate angle of 45° he finds the results given in figure A.7. Although this is the only example of this vane type, in which it is attempted to describe phenomenologically the physical events that set the limits for the gas capacity, the predictions unfortunately bear little resemblance to the experimental results described in later chapters.

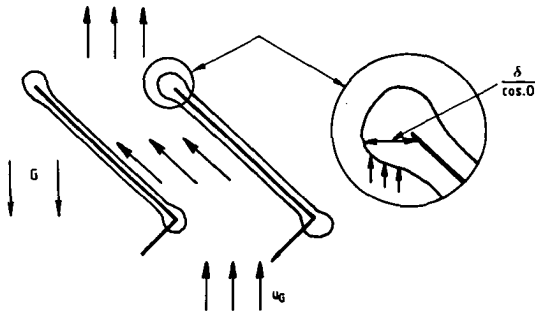


Figure A.6 Reentrainment on baffle edges

Calvert [1972] set up an elegant phenomenological model for predicting the maximal gas capacity for vertically flowed through vanes under the same assumptions as for his horizontal model. The predictions of this model relate much more to actual experimental results from capacity tests of vertically flowed-through vanes without shielded drainage. However, it is still questionable if this model will be suitable for 'universal' application, because the capacity limits for these vane packs are set by flooding and not by reentrainment. The predictions of the model are summarized in figure A.8.

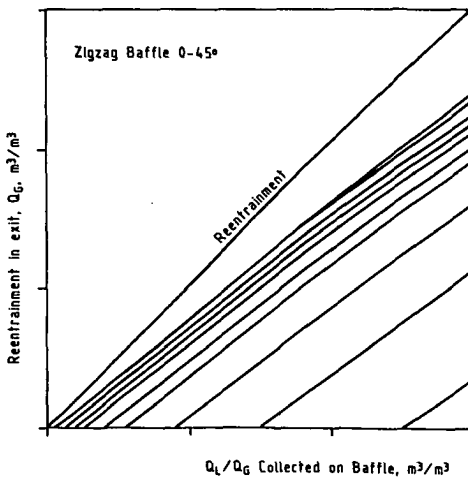


Figure A.7 Effect of liquid loading on reentrainment

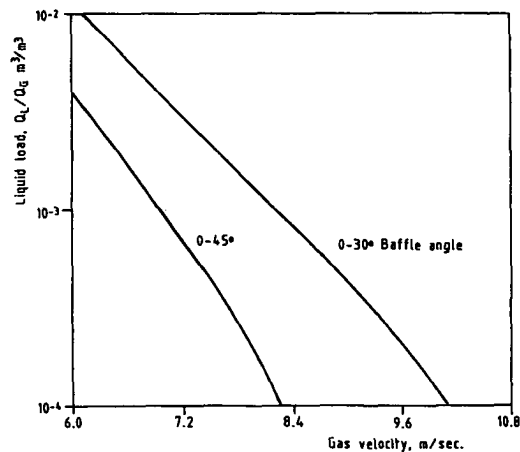


Figure A.8 Maximum liquid loading versus gas velocity in horizontal vanes

The reason for discrepancies lies mainly in the facts that:

- a. the reentrainment criterium is rudimental;
- b. the liquid film is assumed much thicker than in reality;
- c. geometry of the vane plates is of insubordinate significancies.

Capacity limited by flooding

If the maximal capacity is set by flooding in a vertically flowed through vane pack, the analogy to the generalizations made for the mesh pad in the previous chapter is clear. Gardner [1977] lists some authors who specifically tried to quantify the flooding behaviour of vane packs. Most of these authors generalize vertically flowed through separation devices as mesh pads, vane packs and dumped packings and suggest empirical flooding correlations set up for the latter to be applicable to the former two separator types as well (Bradie [1969]).

Mainly because of the fact that the behaviour of the gas flow between the vane blades has hardly been quantified, it appears that it is very difficult to derive exact models for predicting the maximal capacity through the vane under given circumstances. Although some phenomenological models have been set up, still most practical designing takes place with strictly empirical equations.

Pressure drop

The only reference in literature to the calculation of the pressure drop across a vane pack was found in Calvert [1974]:

$$\Delta P = n f_D \rho_g \frac{v_g^2}{2} \quad (A.43)$$

in which: n = the number of bends

f_D = the drag coefficient of a single plate held at a certain angle to the flow

As these are the only characteristics of the geometry of the vane pack, equation A.43 will probably not be very accurate. Especially not for vertically flowed through vane packs without liquid drainage, as no consideration is given to a possible liquid hold-up.

It appears very clearly that hardly any solid theory is available to describe efficiency, maximal capacities or pressure drop as a function of their influences. The design of vane type separators is a very good example of proprietary practice cloaked in secrecy, based on practical experience of the votaries of this art.

2.B Availability and reliability of design procedures (literature investigation)

In this section attention is only paid to the design of the actual vane pack itself, not to the total separator. Vane packs are usually applied in two stage separators of which the first stage is a knock-out vessel. This type of separator is described in section 3.6.

From personal communication the writer find out that in many cases the ubiquitous equation (A.44) is used in industrial practice. The expression for the load factor λ becomes very complicated now and depends nearly on all physical properties that are involved in the separation process.

Many manifestations of λ exist in different parts of the separation industry, which usually do not bear any resemblance, but which are regarded as a highly proprietary piece of information.

In SI quantities λ varies from 0.3 in atmospheric water/air systems down to 0.1 in high pressure applications with viscous liquids.

Maximal capacity

Horizontally flowed through vane packs

According to the earlier described empirical equations a maximal gas velocity is determined through the vanes as follows:

$$v_{gmax} = \lambda \sqrt{\frac{\rho_l - \rho_g}{\rho_g}} \quad (A.44)$$

$$\lambda \approx 0.1 - 0.3$$

This velocity sets the minimal inlet area of the vane. It is not recommended to rely on this procedure.

According to several sources the ratio between length and width of the inlet area should not exceed a value varying from 1.5 to 2.25 to prevent maldistribution and overflowing of the lower parts of the liquid slots at

higher liquid loadings. Sometimes when a more unfavourable ratio can not be avoided a perforated plate is mounted in front and at the back of the vanepack to induce a flow equalizing pressure drop. Often recommended perforated plates feature a free area of approximately 20% and are mounted 30-50 mm in front of the vane.

Other specific geometrical properties of the separator as diameters of the nozzles are usually calculated according to the appropriate equations given in the mesh pad section A 3.4.2 and knock-out vessel section A 3.3.2.

Vertically flowed through vane packs

When mounted in horizontal vessels the above applies equally to vertical flowed through vanes. When mounted in vertical vessels the diameter of the vessel is chosen as such that the maximal allowable velocity through the vanes is not exceeded.

The other geometrical parameters can be determined according to earlier described criteria (sections 3.3.2 and 3.4.2).

3.4.4.2 Reverse flow cyclones

2.A Operating characteristics (literature investigations)

In figure A.9 a standard nomenclature is given for the type of cyclone that is most often encountered in practice and for which most theoretical and experimental work has been performed.

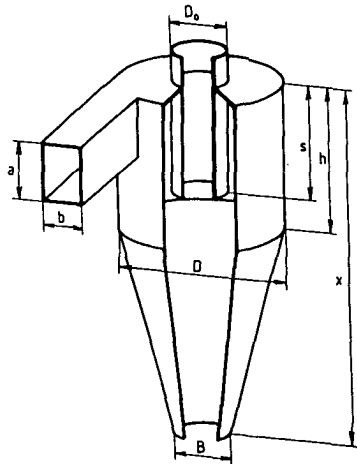


Figure A.9 Nomenclature for cyclone geometry

Collection efficiency

The published theories used for estimation of the collection efficiency of cyclones can usually be subdivided into three groups:

- a. models that determine a critical particle diameter. Particles of this size are assumed to be separated for 50% ("critical diameter models").
- b. models based on the assumption that the residence time of a particle is determining for collection ("residence time models").
- c. models that, with the help of powerful computational techniques, attempt to describe the complex flow inside the cyclone more accurately than is possible under the assumptions of above mentioned models referred to as "numerical models".

ad a. Critical diameter models

In these conceptually very simple models it is assumed that the highest tangential accelerations take place at the surface of an imaginary cylinder which extends downwards through the cyclone under the vortex finder.

Outside this cylinder the gas moves downward; inside this cylinder upward.

The downflowing gas is thought to reverse direction proportionally distributed across the surface of this cylinder.

Under these assumptions anywhere on the mentioned surface there will be a constant radially inward velocity, opposing the outward movement of the particles (figure A.10).

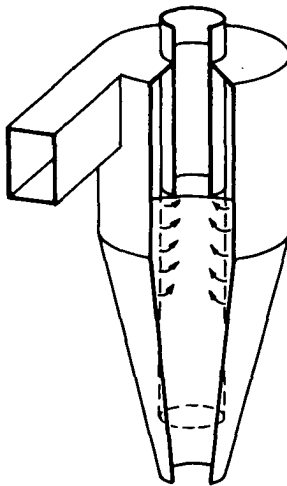


Figure A.10 Concept of critical diameter model

It is possible to calculate the critical diameter of particles that are in equilibrium at the surface of this cylinder. It is assumed that they will be separated with 50% efficiency.

The model predicts that particles smaller than this diameter will not be separated at all, while larger particles will be separated completely. This is clearly quite unrealistic and the gradual slope of the grade efficiency curve is brought into the model by empirical values.

These empirical values of the collection efficiency are plotted against the particle size, which is expressed as a ratio to the critical diameter. The merit of the model is thought to lie in the fact that once an experimental curve has been determined for a certain geometry, the curve can be transposed to other geometries through the theoretical description of the critical diameter. In practice turned out that these models are very fast and worthwhile methods to design cyclones with fixed geometrical ratios, but hardly applicable to design cyclones with a geometry type different from the original cyclone.

Lapple [1951] gives the following expression for d_{50} , which seems to have been derived from earlier work from Rosin et al. [1932] (see equation A.45).

$$d_{50} = 3 \left[\frac{\mu_g b}{2 \pi \Delta \rho v_g N} \right]^{1/2} \quad (\text{A.45})$$

in which N , the number of turns of the gas.

$$N = \frac{V}{\pi D a b}$$

in which V is the volume of the cylindrical body outside the vortex finder. (Actually, this model is not based on the assumptions mentioned before, but on those in the next subsection. The reason it is given here is that experimental values are necessary for the complete grade-efficiency curve).

Stairmand [1951] states:

$$d_{50} = \frac{3}{v_{gi} \phi} \left[\frac{\phi \mu_g \mu_g D_o}{2 \pi \Delta \rho (H - s) D} \right]^{1/2} \quad (\text{A.46})$$

in which:

$$\phi = - \left[\frac{\left(\frac{1}{X_1}\right)^{1/2} - \left[\frac{1}{X_1} + \frac{4 f X_2}{ab}\right]^{1/2}}{\frac{2 f X_2}{ab}} \right] \quad (\text{A.47})$$

in which:

$$X_1 = \frac{2 (D - a)}{D_0} \quad (\text{A.48})$$

and

$$X_2 = \frac{1}{4} \pi (D^2 - D_0^2) + \pi D h + \pi D_0 s + \frac{1}{2} \pi (D + a) [(H - h)^2 + \frac{1}{2}(D - a)^2]^{1/2} \quad (\text{A.49})$$

and the value of the friction factor, f , typically, 0.005.

Stairmand [1951] assumed that the maximum tangential velocity takes place at $r = \frac{1}{4} D_0$ (This was a quite progressive assumption that has been justified much later.)

Barth [1956] derived the following expression:

$$d_{50} = 3 \left[\frac{\mu_g \phi_g}{\pi \Delta \rho (H - S) v_{tr_0}^2} \right]^{1/2} \quad (\text{A.50})$$

in which v_{tr_0} is the tangential velocity at $\frac{1}{2} D_0$

$$v_{tr_0} \approx v_{gi} \cdot \frac{\frac{1}{4} \pi D^2}{ab + \frac{1}{2} (H - S) D \pi 4f} = v_{gi} \frac{D}{D_0 + \frac{2f H D v_{gi}}{v_t D_0}} \quad (\text{A.51})$$

$f = 0.02$

These values for f specifically apply to dust cyclones. In chapter 5 values for gas/liquid systems are given.

$$v_t = \frac{\phi g}{\frac{1}{4} \pi D_o^2} \quad (\text{A.52})$$

v_{tr_o} can also be estimated by taking $v_t r^x = \text{constant}$ in which $0.7 < x < 0.9$, see Muschelknautz [1972].

The equations of Barth have been confirmed by Muschelknautz [1970][1972].

With the above mentioned correlations an expression can be derived for the d_{50} of a typical cyclone geometry. The fractional efficiency curve is determined experimentally for one typical geometry.

Because different geometry types with an equal d_{50} have different grade efficiency curves, the weakness of this design method becomes very clear if a certain curve is taken as generally applicable.

In figure A.11 these curves have been drawn together with experimental values for three different cyclone geometries of which the particulars are given in the figure.

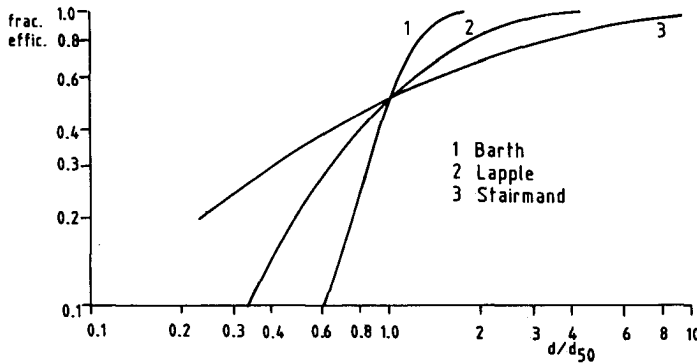


Figure A.11 Comparison of grade efficiency curves

Several authors have set up mathematical expressions to approximate the empirical curve that belongs to a certain geometry-family:

Rosin et al. [1932] assumed that $\frac{d_x}{d_{100}} = \left(\frac{x}{100}\right)^{1/2}$ (A.53)

This applies to the cyclone geometry suggested by Lapple [1951].

Dirgo and Leith [1985b] suggest the following expression for the experimental curve of Barth:

$$\eta = \frac{1}{1 + x^{-3.2}} \quad (\text{A.54})$$

in which x is the ratio of the settling velocity of a certain particle to the settling velocity of a particle of the critical diameter.

$$\text{According to the theory of Barth } x = \frac{\pi (H-S) v_{tr_o}^2 \Delta \rho d_p^2}{g \mu_g \phi_g} \quad (\text{A.55})$$

(If $x = 1$ the earlier given equation for d_{s_0} can be derived).

ad b. Residence time models

These models assume that a particle will only be separated on the wall of the cyclone. The time it needs to get there should not exceed the residence time of the particle.

In its simplest form a model like this consists of calculation of the different radial velocities of particles of different sizes (Stokes' law, gravity constant replaced by tangential acceleration). With these 'settling velocities' and under the assumption of uniformly mixed particles in the inlet duct the grade efficiency curve can be calculated for a certain average residence time. The residence time of the particles is assumed to be equal to that of the gas.

Leith en Licht [1972] recognized the importance of the profile of the tangential velocity in radial direction (also mentioned by Davies [1980], Stairmand [1951] and Strauß [1966]) and moreover, allowed for the turbulence induced backmixing of particles. According to their model the separation efficiency η can be expressed as:

$$\eta = 1 - e^{-2 C \psi \frac{1}{2n+2}} \quad (\text{A.56})$$

in which:

$$\psi = \frac{\Delta \rho d^2 v_{gi} (n+1)}{18 \mu_g D} \quad (\text{A.57})$$

$$n = 1 - [(1 - 0.67 D^{0.14}) \cdot (\frac{T}{283})^{0.3}] \quad (\text{A.58})$$

$$C = \frac{\pi D^2}{ab} [2(1 - \frac{D_e}{D})^2] (\frac{S}{D} - \frac{a}{2D}) + \frac{1}{3} (\frac{S+1-h}{D}) (1 - \frac{d}{D} + (\frac{d}{D})^2) + \frac{h}{D} - \frac{1}{D} (\frac{D_e}{D})^2 - \frac{S}{D} \quad (\text{A.59})$$

$$1 = 2 - 3 D_e [\frac{D_e^2}{ab}]^{1/3} \quad (\text{A.60})$$

$$d = D - (D - B) [\frac{S+1+h}{H-h}] \quad (\text{A.61})$$

In a later publication Dirgo and Leith [1985a] give a correction for C^x . In case $d < D_e$, C should be determined as follows:

$$C' = C + \frac{\pi D^2}{db} [\frac{S+1-h}{D-d} ((\frac{D_e}{D})^2 (\frac{D_e-d}{D}) + \frac{1}{3} (\frac{d^3}{D^3} - \frac{D_e^2}{D^3}))] \quad (\text{A.62})$$

In figures A.12, A.13, A.14 and A.15 the predictions of this model are plotted against experimental results obtained with three different cyclone geometries.

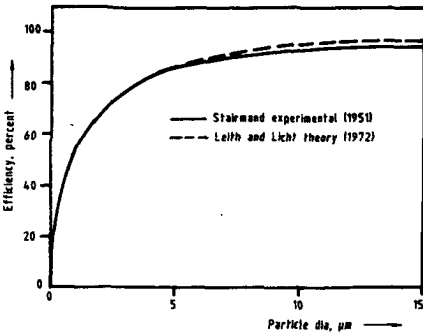


Figure A.12 Validation of model (1)

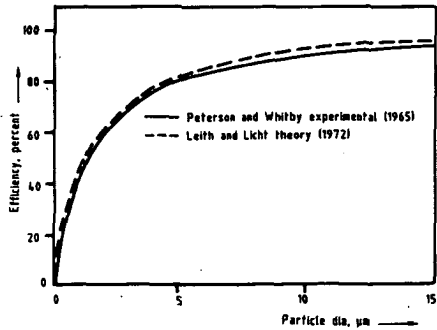


Figure A.13 Validation of model (2)

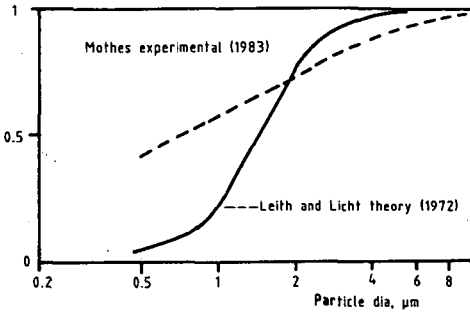


Figure A.14 Validation of model (3)

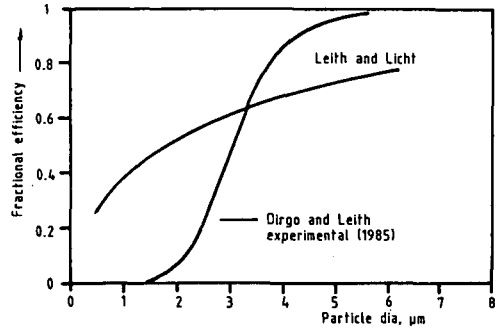


Figure A.15 Validation of model (4)

Dietz [1972] developed further refinements and proposed a model which does not assume a well mixed core and annular region and which allows for distribution of gas residence times and exchange of particles between the core and annulus.

The model exists of three interactive sub-models that describe the inlet region (between wall and vortex finder), the annulus region (in which the gas flow is directed downwards) and the core region (in which the gas is flowing upwards). According to Dirgo and Leith [1985a] Dietz derived the following expression for η :

$$\eta = 1 - [K_0 - (K_1^2 + K_2)^{1/2}] \exp \left[\frac{-\pi (2S-a) \rho_p d_p^2 v_{gi}}{18 \mu_{g,ab}} \right] \quad (A.63)$$

in which:

$$K_0 = \frac{1}{2} \left[1 + \left(\frac{D_e}{D} \right)^{2n} \left(1 + \frac{9 \mu_{g,ab}}{\pi \rho_p d_p^2 v_{gi}} \right) \right] \quad (A.64)$$

$$K_1 = \frac{1}{2} \left[1 - \left(\frac{D_e}{D} \right)^{2n} \left(1 + \frac{9 \mu_{g,ab}}{\pi \rho_p d_p^2 v_{gi}} \right) \right] \quad (A.65)$$

$$K_2 = \left(\frac{D_e}{D} \right)^{2n} \quad (A.66)$$

in which: l (free vortex length) = $2.3 D_e \left(\frac{D}{ab}\right)^{1/3}$

In figures A.16, A.17 and A.18 the predictions of this model are plotted against experimental results obtained on three different cyclone geometries.

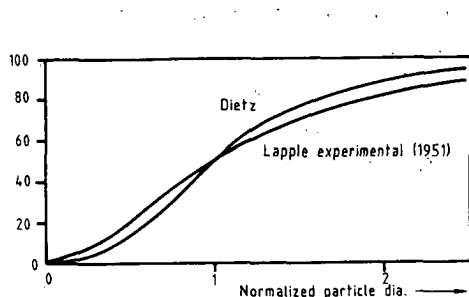


Figure A.16 Validation of model (5)

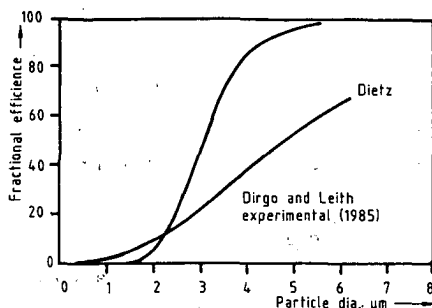


Figure A.17 Validation of model (6)

Mothes [1984a] suggested further refinements to the model of Dietz and extended the three region model to a four region model of which the fourth region symbolized the dust container underneath the vortex. From this region an exchange of particles to the active part of the cyclone is possible. This way it becomes possible to allow for reentrainment. Apart from this asset his model takes also into account a concentration gradient of the particles in the annular region, which depends on particle size.

This is in accordance to earlier work of Mothes [1982], and has hitherto not been considered by the models of Leith and Licht and Dietz, that employed uniform concentration. The predictions of this model are plotted against experimental results obtained on the listed cyclone geometry in figure A.19.

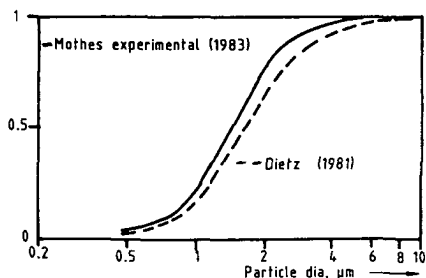


Figure A.18 Validation of model (7)

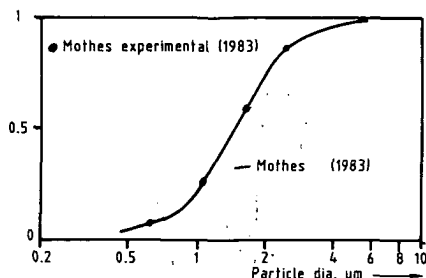


Figure A.19 Validation of model (8)

As appears from these figures there is no theory that closely follows all experimental results. Very disencouragingly, relatively simple models set up for a specific geometry type, are just as useful as complicated universal models. Some theoretically tinged models give very good results with their belonging geometry families (Mothes and Dietz with Barth cyclones). The discrepancies of the models can largely be explained by a too simplistic representation of the complex flow field inside the cyclone. Too little attention is paid to effects induced by turbulence. Realistic flow field modelling would result in a much more complex model with completely other computational requirements than the models described before.

ad c. Numerical models

Because the flow field in a cyclone is governed by physical laws that are not very easily modelled through an analytical approach, some efforts have been undertaken in the past few years to model the behaviour numerically.

The finite element or finite difference methods used for these numerical simulations tend to require considerable software development efforts and hardware investments. However, the popularity of these methods is strongly increasing with the introduction of configurable software packages and the possibility of implementing those on smaller computers with growing computing power for money ratios.

One of the first references in literature to an apparently very satisfactorily functioning numerical simulation of the behaviour of a dust cyclone is the work of Boysan and Swithenbank et al. [1982]. An example of the predicting possibilities of their model is given in figure A.20.

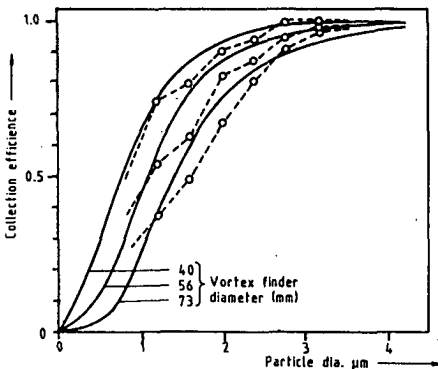


Figure A.20 Validation of numerical simulation

Karvinen [1985] presented also a good cyclone simulation. Of both models, though, no extensive proof was given of geometrical independence. Pericleous [1984] gives an example of a useful hydrocyclone model. As later in this report the numerical approach will be extensively covered, specific details are not given here. It must be remarked, though, that numerical simulation is a very powerful technique that has proven to have the possibilities to predict the behaviour of a cyclone more or less independent of geometry type. This way it will become possible for the first time to perform cyclone design optimization for a specific application.

Correlations and models for predicting the pressure drop across a dust cyclone

As in the design of dust separators the pressure drop across the cyclone is considered as a measure for the maximal capacity of the cyclone, many models and correlations exist for predicting the pressure drop.

It appears to be possible to predict this operating property accurately much easier than the collection efficiency.

Leith and Metha [1976] give an excellent review of pressure drop correlations up to 1976 and recommend the correlations of Barth [1956], Stairmand [1951, Shepherd and Lapple [1940] in this order after testing 12 different geometries.

All correlations are given as a factor of the entry velocity head:

$$\Delta P = \xi \frac{\rho v_i^2}{z}, \text{ in which according to:} \quad (\text{A.67})$$

$$(1) \text{ Shepherd \& Lapple [1940] } \xi = K \frac{ab}{d_e^2} \quad (\text{A.68})$$

in which:

$K = 16$ for a cyclone with a standard tangential inlet

$K = 7.5$ for a cyclone with an inlet vane (the inner wall of the tangential entry extends past the cyclone interwall to a point halfway to the opposite wall)

$$(2) \text{ Stairmand [1951] } \xi = 1 + 2 \phi^2 \left(\frac{2(D-b)}{D_e} - 1 \right) + 2 \left(\frac{4ab}{\pi D_e^2} \right), \quad (\text{A.69})$$

in which:

$$\phi = - \frac{\left(\frac{D_e}{2(D-b)} \right)^{1/2} + \left(\frac{D_e}{2(D-b)} + \frac{4fA}{ab} \right)^{1/2}}{\frac{2fA}{ab}}$$

$$A = \frac{\pi}{4} (D^2 - D_e^2) + \pi Dh + \pi D_e S + \frac{\pi}{2} (D + B) \cdot \left[(H - h)^2 + \left(\frac{D - B}{2} \right)^2 \right]^{1/2}$$

$$f = \text{friction factor} = 0.005$$

Stairmand assumes in this correlation that the pressure drop consists of energy loss in the cyclone vortex and entrance and exit losses.

$$(3) \text{ Barth [1956] } \xi = \left(\frac{u_i}{v_i} \right)^2 \left(\frac{4ab}{\pi D_e^2} \right)^2 (\epsilon_e + \epsilon_i) \quad (\text{A.70})$$

in which:

$$\epsilon_e = \frac{D_e}{D} \left(\frac{1}{\left(1 - \left(\frac{u_i}{v_i} \right) (H - S) \left(\frac{D}{D_e} f \right) \right)^2} \right)$$

$$\epsilon_i = \frac{4.4}{\left(\frac{u_i}{v_i} \right)^{2/3}} + 1$$

$$\frac{u_i}{v_i} = \frac{\frac{1}{2} D_e (D - b) \pi}{2 ab \alpha + (H - S) (D - b) \pi f}; \quad \alpha \approx 1 - 1.2 \frac{b}{D};$$

$$f \text{ (friction factor)} \approx 0.02$$

Barth assumes in this correlation that the pressure drop is the sum of two correlations; ϵ_e represents the entrance losses and internal friction, ϵ_i the exit losses.

The determination method suggested by Barth has found wide application.

Muschelknautz and Krambrock [1970] and Muschelknautz [1972] suggested some further refinements that essentially affect the estimated values of the friction factor and the losses caused by different inlet geometries. In figures A.21 and A.22 the results of their detailed measurements of the friction factor are given.

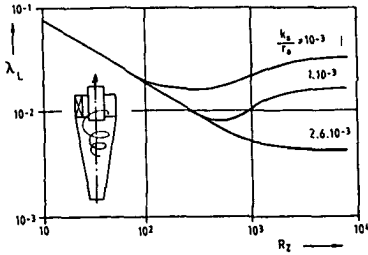


Fig. A.21 Wall friction factors (I)

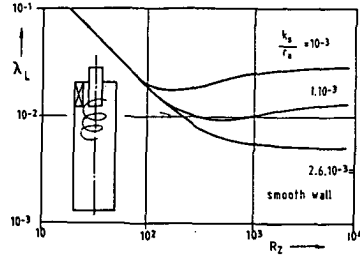


Fig. A.22 Wall friction factors (II)

Furthermore, Muschelknautz [1972] makes distinction between three kinds of swirl inducing geometries; the tangential inlet with guide vane, the tangential slit inlet and the axial inlet (figures A.23A, B and C).

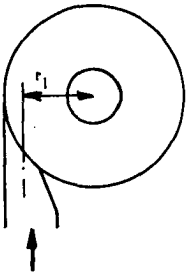


Fig. A.23A Inlet I

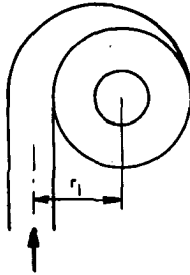


Fig. A.23B Inlet II

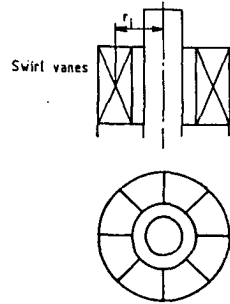


Fig. A.23C Inlet III

For determining the factor α which is of influence on the pressure drop calculation of the inlet section he states:

- vane type tangential inlet: $\alpha = 1 + \frac{\sqrt{3 \pi \lambda (D - \frac{1}{2} b)}}{\sqrt{ab}}$

- slit type tangential inlet: α according to figure A.24

- axial inlet

: $\alpha = 0.9-0.95$ for curved guide vanes

$\alpha = 0.85$ for simple straight guide values

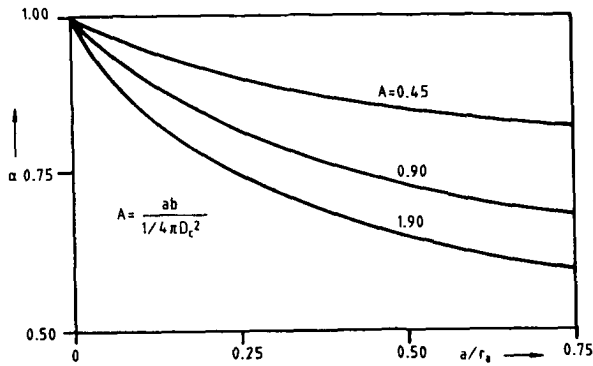


Figure A.24 Determination of α for slit entry cyclones

He recommends axial inlets for cyclones with: $\frac{D}{D_0} = 1.5 - 2$

(the slit would otherwise become too narrow) and for multicyclone batteries (for preventing maldistribution). The values of f mentioned in this section are typical for dust cyclones. In chapter 5 typical values for mist cyclones will be derived.

After these reasonably reliable correlations had been developed, little work was done on new correlations. Also numerical methods as discussed before appear to have little problems in predicting the pressure drop across a cyclone as can be seen in figure A.25 Boysan and Swithenbank [1982].

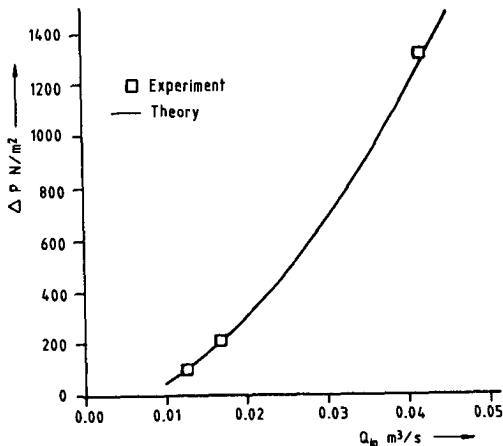


Figure A.25 Predicted pressure drop by numerical simulation

Models for predicting maximal capacity of dust cyclones

The maximal capacity through a certain dust cyclone is limited by two constraints:

1. a maximal pressure drop set by process conditions;
2. a maximal velocity inside the cyclone above which separated dust will be reentrained.

ad 1. With the given pressure drop correlations it will be straightforward to predict whether a cyclone can meet possible pressure drop requirements.

ad 2. No quantitative references have been found in literature to dust reentrainment criteria.

Other inlet geometries

Sofar mostly models and correlations have been discussed that concerned essentially only single dust cyclones, with one tangential inlet.

Except for a few examples (e.g. Muschelknautz [1972]) no information could be found with which the influence could be quantified of other inlet geometries as axial, double or tangential even quadruple tangential inlets, of which some are often applied in practice.

2.B Availability and reliability of design procedures (literature investigation)

Stairmand [1951] recommends two types of cyclones. One geometry for a high efficiency, the other for a high throughput cyclone. Both geometries and accompanying data are given in figures A.26 and A.27. Stairmand based his suggestions on extensive experimental results, of which most have been obtained under atmospheric conditions.

Barth [1956] recommends in the same line five types of geometries and uses the pressure drop across and required efficiency of the cyclone as two primary mutually dependent criteria for the design. As Muschelknautz [1972] later refines this method it will be superfluous to give more details here.

Rumpf [1968] suggests a method to optimize cyclone geometry to pressure drop and collection efficiency requirements. His optimization procedure starts with the two characteristic cyclone parameters that Barth and Leineweber described and that will be used again by Muschelknautz. Unfortunately Rumpf does not give any experimental verification of his predictions.

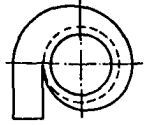
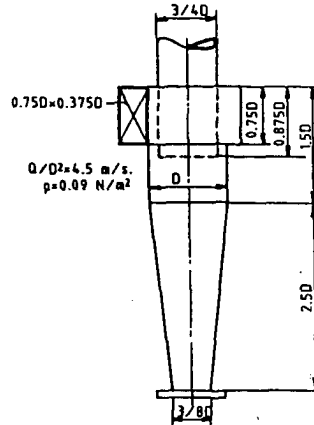
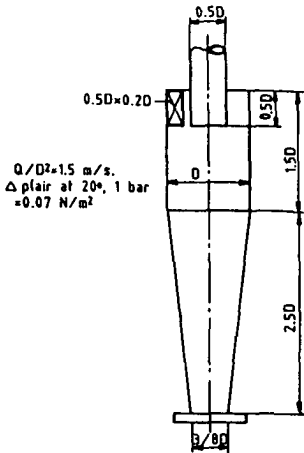


Figure A.26 Stairmand High Efficiency Figure A.27 Stairmand High Throughput

Muschelknautz [1970], [1972] starts from the same point and proposes a procedure with which the pressure drop across a cyclone can be minimized while maintaining constant collection efficiency and cyclone volume.

He theoretically described some experimentally developed optimal cyclone designs with standard expressions with respect to pressure drop and cyclone geometry (developed by Barth and Leineweber) and condensed these findings in the graphs of figure A.28.

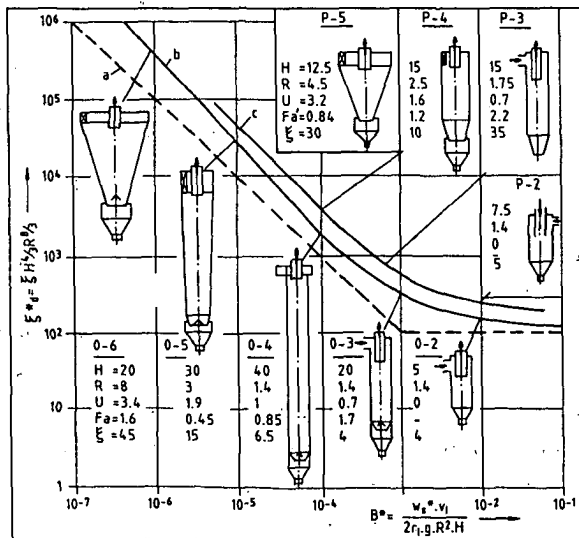


Figure A.28 Geometry optimization proposed by Muschelknautz

The characteristic numbers he proposes:

$$\xi_d^* = \frac{\Delta P}{\frac{1}{2} \rho_g v_a^{*2}} ; \text{ the resistance coefficient and}$$

$$B^* = \frac{w_s^* v_a^*}{g D} ; \text{ which characterizes cyclone size required collection efficiency.}$$

w_s^* represents the terminal settling velocity of particle under gravity

$$w_s^* = \frac{\Delta \rho g d_p^2}{18 \eta}$$

v_a^* represents a characteristic velocity inside the cyclone

$$v_a^* = \frac{q_g}{\left(\frac{1}{4} D^2 H\right)^{2/3} \cdot \frac{1}{4} \pi}$$

For a given geometry Δp can be calculated according to the method described by Barth and Muschelknautz given in the previous subsection. By an iterative trial and error method, D and H are varied for a given value of D_o as such that ξ_a^* is minimized. This is possible as Muschelknautz derived from his cyclone theory an unambiguous relation between the two mentioned parameters (line b). He succeeded to prove this kind of relationship with cyclones of varying geometries that had appeared to be practical in reality (line c). Muschelknautz suggests to use this curve under the following restraints:

$$\lambda \sim 0.01$$

$$\frac{D}{D_o} > 1.4$$

Still, very much care has to be taken not to take the geometries developed with this method for an absolute truth: a large part of this design procedure is still based on simplifications (for instance the assumed flow field).

Leith and Metha [1976] developed an algorithm that was based on the collection efficiency theory of Leith and Licht [1972]. Basically they rewrote the original theory as such that cyclone dimensions could easily be changed, under observation of theoretical consequences of these changes. As only one of all possible geometries has been tested to verify the results this method is not recommended for practical purposes.

In an overview article Leith and Dirgo [1985b] tested four designs they obtained with a geometrical optimization based on four different theories for predicting cyclone behaviour. They tested these new designs both theoretically (with the concerning theory used for optimization) and experimentally against the Stairmand high efficiency cyclone. Although the four new designs were predicted to be much more efficient, three had lower collection efficiencies and only one new design was about as efficient. This cyclone was developed by using the Barth pressure drop and a modification of his efficiency theories.

The theories for predicting collection efficiency used by Leith and Dirgo were those of Leith and Licht and a modification of the Barth theory.

Theories used for predicting pressure drop were of Barth and Stairmand.

The modification of the original Barth theory consists of an empirical alteration of the empirical curve suggested by Barth to fit other particle sizes than the critical diameter to obtain the fractional efficiency curve (see part 1 of this appendix).

As the above clearly illustrates, it is still more advisable to rely on empirical design information than to use blindly some of the theoretical design procedures described before. Especially for fields of applications of which relatively little information is available (as on earlier empirically developed optimal designs) there is quite an incentive to develop more powerful theories for predicting cyclone behaviour. Multiple experiments to achieve this can be quite expensive, in case of for instance high pressure applications. To this purpose extensive attention is paid to the development of a numerical approach to simulate the cyclone behaviour in chapter 7.

3.4.4.3 Mist cyclones

2.A Operating characteristics (literature investigation)

Collection efficiency and pressure drop

It is referred to the corresponding section of the dust cyclones; no specific theories have been published that take into account the differences in reentrainment behaviour between the two separated phases.

Maximal capacity

The maximal capacity through a certain cyclone is limited by two constraints

1. a maximal pressure drop set by process conditions;
2. a maximal gas velocity inside the cyclone above which reentrainment of the separated liquid will take place.

If the maximal pressure drop prescribed by the application leads to velocities lower than the reentrainment velocity, the correlations given in the previous chapter can be applied.

In the next chapter the physical phenomena that accompany reentrainment are extensively described. With this information the maximal allowable velocity can be determined.

Calvert [1974] cites Zhivaikin [1962] and recommends the following criteria for determining the onset of reentrainment in cyclones:

$$29.2 \frac{v_{g \max} \cdot \mu_1}{\sigma} = Re_1^{-\frac{3}{4}} \quad \text{for } Re_1 \leq \frac{0.085}{\frac{v_1^2}{2}} \quad (A.71)$$

$$100 \frac{v_{g \max} \cdot \mu_1}{\sigma} = Re_1^{-\frac{1}{4}} \quad \text{for } \frac{0.085}{\frac{v_1^2}{2}} \leq Re_1 \leq \frac{28.8}{\frac{v_1^2}{2}} \quad (A.72)$$

$$43.2 \frac{v_{g \max} \cdot \mu_1}{\sigma} = Re_1^{1.25} \quad \text{for } Re_1 \geq \frac{28.8}{\frac{v_1^2}{2}} \quad (A.74)$$

It will, however, be questionable if these correlations apply to the situation at hand as no consideration is given to increased gravity forces inside the tangential flow field.

Stairmand [1951] gives an even more general criterion and states that:

$$\rho_g v_{gi}^2 < 1800 \text{ kg/ms}^2 \text{ in case of gas/water separation and} \quad (\text{A.74})$$

$$\rho_g v_{gi}^2 < 3600 \text{ kg/ms}^2 \text{ in case of gas/oil separation.} \quad (\text{A.75})$$

Stearman and Williamson, quoted by Strauß [1966], have suggested values for above limits of 1330 and 2660 kg/ms² respectively.

With an atmospheric water and air system these correlations lead to the following maximal allowable gas velocities.

| | | |
|-------------------|--|--------|
| Zhivaikin/Calvert | : $v_{gi \text{ max}} = 10 - 50 \text{ m/s}$ | (A.76) |
|-------------------|--|--------|

| | | |
|-----------|---|--------|
| Stairmand | : $v_{gi \text{ max}} = 43 \text{ m/s}$ | (A.77) |
|-----------|---|--------|

| | | |
|---------------------|---|--------|
| Stearman/Williamson | : $v_{gi \text{ max}} = 33 \text{ m/s}$ | (A.78) |
|---------------------|---|--------|

It is expected that in reality this limit value will also depend strongly on other operating conditions and the cyclone geometry. The above mentioned figures should only be regarded as indicative.

2.B Availability and reliability of design procedures (literature investigation)

The basic form of a mist cyclone can be determined analogous to the procedures for dust cyclones. At the same time extra design features as skirts and straight discharges, described before, can be added. Meanwhile care should be taken that the maximal allowable inlet velocities, described in this appendix but refined in chapter 5, are not exceeded.

3.4.4.4 Multicyclones

2.A Operating characteristics (literature investigation)

The overall efficiency of a 'multicyclone' is not necessarily equal to the efficiency of a unit cyclone tested single. Kropp [1981] and Potapov [1976] found deteriorations of the overall efficiency from 1 up to 35% in respect to the efficiency of a single cyclone under comparable conditions.

They attributed this effect mainly to two reasons:

- a. constructional carelessness, like air leaks between bin and inlet section (0-11%);
- b. maldistribution of the gas/dust mixture to the different cyclones in the bundle (1-24%);

Although it is not very difficult to avoid the former defect, minimization of the latter is less trivial. Maldistribution of the gas/dust mixture effects the pressure of the cyclone dust (liquid) outlet which can cause dust laden gas to be transferred from one cyclone through an other to the clean gas outlet.

The gas phase can be maldistributed among the cyclones because of partial clogging of internal parts of the cyclones but also because of cyclones that are not properly positioned in respect to each other. When varying relative positions of cyclones in a multicyclone Kropp [1981] and Potapov [1976] found the overall separation efficiency to vary from 82% to 99%. They attribute this effect not only to maldistribution of the gas phase. They also found considerable variations in overall separation efficiency when varying the dust distribution among cyclones under otherwise comparable circumstances (from 91% to 99%). They explain this effect by stating that the relative dust content of a cyclone in operation is of considerable influence on its pressure drop. This is in accordance with experiments of Muschelknautz [1972], Mothes [1984b].

Jackson [1963] mentions the detrimental effect of unequal distribution of either phase to individual cyclones discharging in a common hopper as well. He describes an experiment performed by Smellie [1942] in which the carry-over of three identical cyclones related to each other as 2 : 1,5 : 1 because of non uniform dust distribution.

Koffman [1953] reports a reduction in efficiency from 96% to 92% when a 1.5 inch cyclone is grouped with 13 others to feed a common hopper.

The necessity to arrange the flow conditions of both gas and particulate phase to be similar for each individual cyclone in a multicyclone to ensure optimal operation has been stressed on many occasions.

None of the above mentioned authors, though, succeeded in formulating a generally applicable model or correlation. The nature of these gas/particulate phase distributions and pressure drop interactions is complicated to such an extent that only numerical simulations as described before could be of use when attempting to predict the multicyclone effect on the overall separation efficiency.

2.B Availability and reliability of design procedures (literature investigation)

The sizing of these multicyclones simplifies to choosing the number of cyclones and setting up a plan as how to distribute the cyclones over a certain minimal area.

The determination of the number of cyclones is very often done on the basis of a maximum pressure drop that can be allowed across the separator, at which the individual cyclone still functions well.

The importance of the distribution of both gas and particulate phase to the cyclones, however, seems hardly to be realised in this field of application and no standard design rules were found.

3.4.4.5 Straight-through cyclones

2.A Operating characteristics (literature investigations)

Again most models that are mentioned in literature concerned dust separating cyclones. Under the same preconditions as in the case of reverse flow cyclones, these models apply equally well to their mist separating counterparts.

Collection efficiency

As the flow field in the separation chamber of this type of cyclone is easier to predict than that of a reverse flow cyclone, different authors have succeeded in formulating residence time type models. Analogous to the reverse flow residence time models they achieved reasonably good agreement with experimental results for specific geometries, while the behaviour of other geometry types was less adequately predicted (although, generally, more satisfactorily than in the case of reverse flow cyclones). Good examples of these first models are those of Daniels [1957] and Solbach [1958].

Crowe and Pratt [1974] already succeeded in formulating a sophisticated numerical model based on a finite difference formulation of the Navier Stokes equations, based on earlier work of Spalding (see also []). Large computers were necessary at the time. Dobbins et al. [1979] suggested a very simplified way to represent the flow field. Nevertheless, the model seems to render some agreements that are fairly geometry independent.

Stenhouse and Trow [1979] succeeded in formulating a comparable kind of model in which they used experimental flow field measurements to carry out particle trajectory calculations. They validated it with extensive experimental results.

The collection efficiency models that have been formulated so far lack the reliability that is necessary for the exact information for designing purposes. This can, to a great extent, be explained by the simplifications of the flow field (except for the model of Crowe and Pratt) and by insufficiently accurate turbulence models that have been used.

Pressure drop

Plekhov [1972] summarized his pressure drop measurements across the cyclone depicted in figure A.29 with the following correlations:

$$\Delta p = \xi \frac{1}{2} \rho v_{gi}^2 \quad (A.80)$$

in which:

$$\xi = (5.2 m^{-1.4} + \xi_{2k}) \left(10 \frac{M_L}{M_G} + 1\right)^{0.08}$$

m = the ratio of the area of the tangential inlet slots to the cross sectional area of the tube $0.2 < m < 1.0$

ξ_k = hydraulic resistance coefficient of the internal ring at the outlet of the sleeve $0 < \xi_k < 3$

M_L = liquid feed in kg/s

M_G = gas feed in kg/s

$\frac{M_L}{M_G} 100 < 6\%$

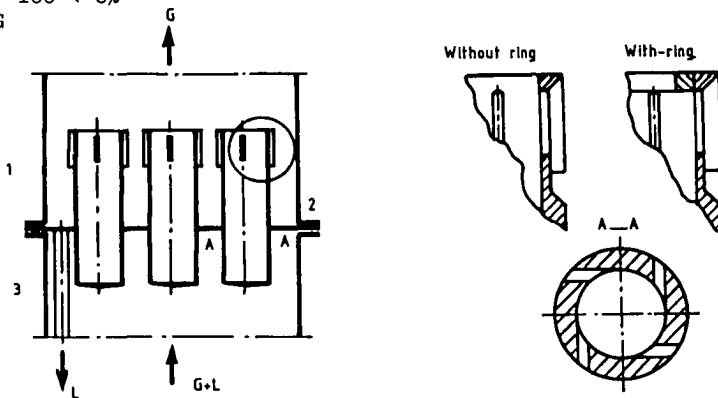


Figure A.29 Axial cyclone of Plekhov (1972)

Maximal capacity

As is the case for reverse flow cyclones the maximal capacity is either determined by the maximal allowable pressure drop or by the maximal allowable velocity inside the cyclone prior to the onset of reentrainment. Because no convincing pressure drop models could be cited, no explicit information is available for determining the former criterion.

As for the second criterion the same models can be used as given for the reverse flow cyclones. The maximum occurring velocity is difficult to predict inside a straight-through cyclone because of operation of the swirl element. A safe guess is that the maximal local velocities near the wall are 2-3 times the average axial velocity. In figures A.30 and A.31 the results of Plekhov [1972] are presented, obtained with experiments under different conditions with a cyclone of earlier described geometry.

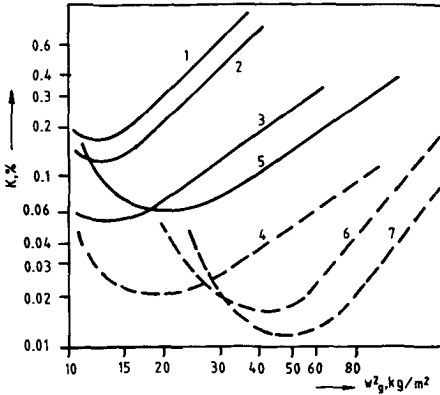


Figure A.30 Relations between reentrainment and geometry (I)

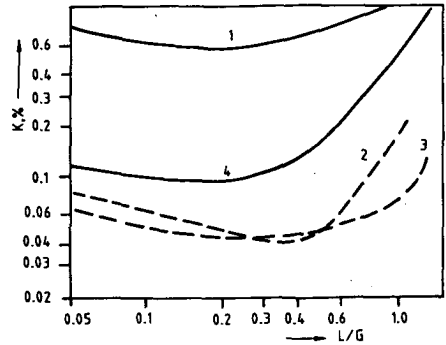


Figure A.31 Relations between reentrainment and geometry (II)

Designs and design procedures for axial cyclones

Sofar for axial cyclones no general design procedures exist. Therefore different designs will be described with specific information regarding the geometry given by the manufacturer that could be of importance to the operating characteristics of that design.

Length of separation chamber

Daniels [1957] found an optimal ratio between body length (L) and diameter (D) of 5:1. Stenhouse et al. [1982] an optimal ratio of 2.5:1. Most commercial units have values that lie in this range. However, both authors did not find a strong dependence of the separation efficiency on this design characteristic. Plekhov [1972] found a minimal pressure drop when $L/D \approx 1.0 - 1.3$.

Diameter of gas outlet, D_e (axial discharge)

Daniels [1957] and Stenhouse [1982] reported experiments in which D_e was varied between 0.8 and 0.96 D , respectively 0.25 and 0.5 D . Both found drastical improvements of efficiency with decreasing D_e at the cost of higher pressure drop (Stenhouse reported a 5.3 fold increase with a twofold decrease of D_e).

Area of gasoutlet (radial discharge)

No information has been found with respect to this subject.

Length of insertion of gas outlet L_e (axial discharge)

In most commercial designs $L_e/D < 0.3$. No experiments describing the influence of L_e/D are reported.

Inlet section

The specific advantages of both axial and tangential inlets have already been described in the main text. In most cases commercial designs make use of fairly simple fixed-angle swirl elements. To prevent a region of violent turbulence in the centre of the tube Umney [1948] suggests restrictions for the geometry of the swirler.

Smith [1962] concluded that a vane angle of 45° to the cyclone axis was optimal; a rapid rise in pressure loss was showed when vane angles were increased above 45° .

3.5 Diffusional separation

2.A Operating characteristics (literature investigation)

Collection efficiency

Theories describing the collection efficiency of a diffusional separator closely follow those set up for mesh type mist extractors. Analogous to equation (A.19) the total impaction efficiency can be represented by

$$\eta(D) = 1 - e^{-f \Phi(D)} \quad (\text{A.81})$$

in which the geometry constant f equals

$$f = \frac{4}{\pi} \frac{1 - \epsilon}{\epsilon} \frac{z}{d_w} \quad (\text{A.82})$$

$\Phi(D)$ in equation (A.81) represents the collection efficiency of a single fiber and is quantified as follows (according to an overview given by Löffler [1983]).

In case of diffusional separation ($v_g \sim 0.1$ m/s, $d_p < 0.5 \mu\text{m}$) $Re \ll 1$.

$$\eta = \frac{2.9}{k^{1/3} Pe^{2/3}} + \frac{0.624}{Pe} \quad (\text{Fuchs et al. [1964], Löffler [1983]}) \quad (\text{A.83})$$

$$K = -1/2 \ln(1 - \epsilon) - 0.5$$

$$Pe = \frac{v_g d_w}{D}; \quad D \text{ (diffusion coefficient)} = \frac{k^* T C_n}{3 \pi \mu x}$$

k^* = constant of Boltzmann; C_n = Cunningham correction

Inertial forces will prevail above these values mentioned of v_g and d_p

if $Re < 1$; ($v_g > 0.1$ m/s $d_p < 10 \mu\text{m}$)

$$\eta(D) = 1.03 + (0.6 Re - 1.5) 0.85^{(\psi + 0.5)} \quad (\text{Hiller [1980], Löffler [1983]}) \quad (\text{A.84})$$

if $0.5 < Re < 50$

$$\eta(D) = \left\{ \left(1 + \frac{(1.53 - 0.23 \ln Re + 0.0167 \ln^2 Re)}{2 \psi} \right)^{-2} + \left(\frac{2 \rho_g}{Re \rho_g \psi} \right)^{1/2} \right\} \cdot \left[1 + 3 \left(\frac{2 \rho_g \psi}{Re \rho_1} \right)^{1/2} \right] \quad (\text{A.85})$$

(Suneja [1974]).

As the kinetic energies of the droplets will be much smaller than those that will occur in mesh type separator operation, it can be assumed that a droplet will be held by the liquid film upon impaction. This means that the total collection efficiency of a fiber bed can be represented by equation A.81.

Maximal capacity

As the film of separated liquid moves in the same direction as the gas flow, the permitted maximal velocity through a fiber bed is very low (unless the fiber bed is operated as a coalescing element).

No specific correlations were found that gave indications how this maximal velocity is influenced by gas and liquid physical properties and by the geometry of specific designs. In most practical cases the fabricators provide the necessary information.

Pressure drop

The same as for mesh type separators applies here: adequate and well known general theories exist to calculate the pressure drop across porous media, but no effects of the liquid hold up in the fiber bed are taken into account in these calculations.

However, the most influencing factor on pressure drop is the rate of fouling of the fibre bed.

The maximal allowable pressure drop in this respect is the lifetime determining characteristic.

2.B Availability and reliability of design procedures (literature investigation)

As has become clear from the previous chapter, hardly any theoretical model can subsist a design procedure.

It can be expected that with increasing operating pressure forces on the liquid film that lead to reentrainment grow, and that the permitted maximal velocity of 0.15 m/sec in case of water and air operation will be substantially lower in case of high pressure oil field operation.

In practice values of $v_g = 0.05$ m/sec have been encountered in case of operating pressures of 70 bar.

Usually the required surface area is determined according to a maximally allowable pressure drop; a practical form of such a design correlation is for instance:

$$A_r = \frac{\phi_{gn}}{0,04 \sqrt{P}} \quad (A.86)$$

in which:

A_r = required surface area

P = operating pressure

ϕ_{gn} = gas flow in Nm^3/s (atmospheric conditions)

In case of coalescing operation it can be expected that a maximal velocity is prescribed for the outlet velocity. If the outlet velocity would be too high, redispersion of the coalesced droplets can be expected. In practice $v_{\text{out}} \leq 4 \text{ m/s}$. The above only applies to the situation in which the coalescer element is flowed through outside - inwards. The reverse would be more logical for coalescer operation if no fouling is expected.

APPENDIX B

REPRESENTATIVE EXAMPLES OF SWIRLING FLOW CHARACTERIZATIONS

B.1 Swirling flow in a smooth pipe

Loxham [1976] measured the evolution of a swirling flow in the vortex finder of a reverse flow cyclone. The vortex finder had a diameter of 50 mm. The measured axial and tangential velocity profiles are depicted in figures B.1 and B.2. The decay of the swirl number S is calculated from these data and depicted in figure B.3.

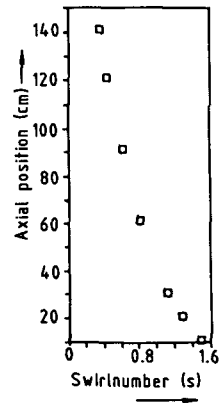
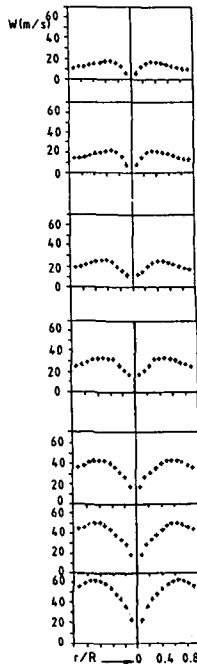
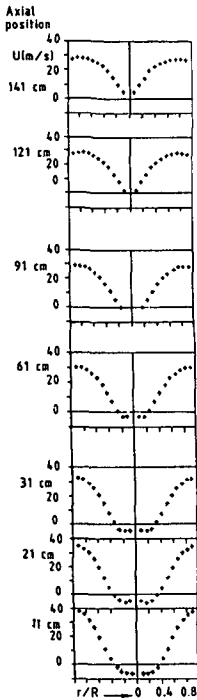


Fig. B.1 Axial profiles Fig. B.2 Tangential profiles Fig. B.3 Decay of S

Velocity measurements were carried out with a pitot tube of 3 mm ϕ .

B.2

B.2 Swirling flow in axial cyclones

Stenhouse [1979] carried out Laser Doppler Velocimetry measurements in axial cyclones.

The geometry is given in figure B.4. His results are depicted in figure B.5. The radial planes at which these measurements have been carried out are indicated in figure B.4.

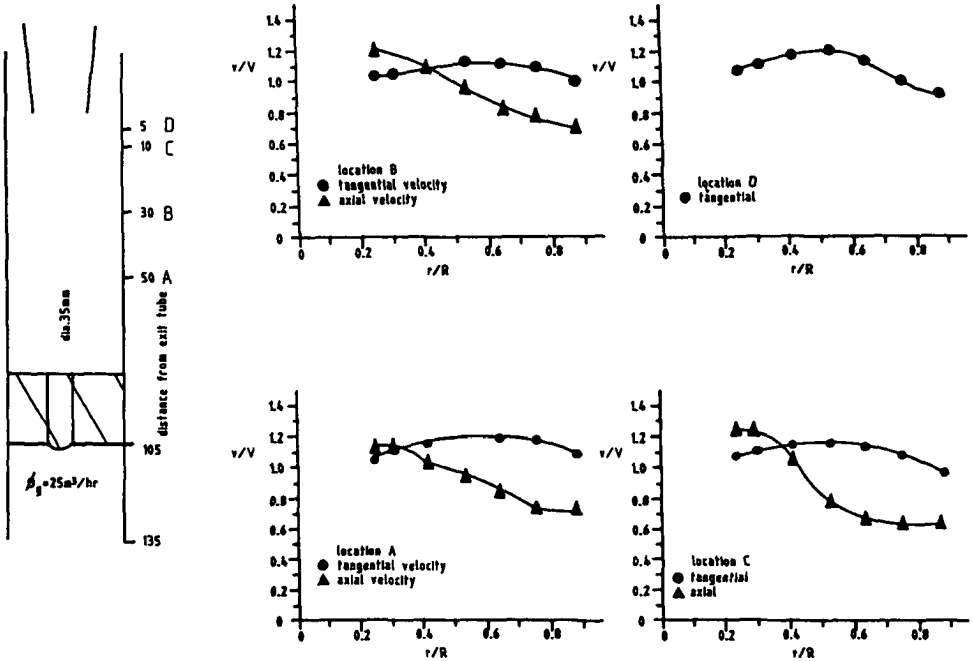


Fig. B.4 Geometry of Stenhouse Fig. B.5 Velocity measurements

B.3 Swirling flow in reverse flow cyclones

Mothes [1983] characterized with LDV techniques the cyclone of figure B.6. His results are given in figure B.7.

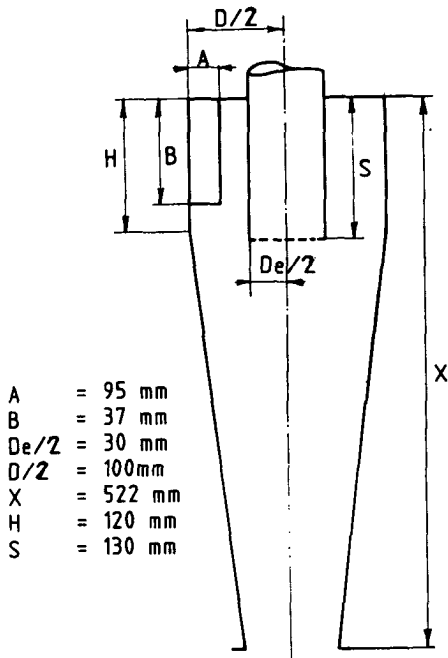


Figure B.6 Geometry of Mothes

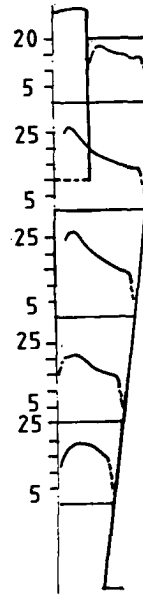


Figure B.7 Tangential profiles

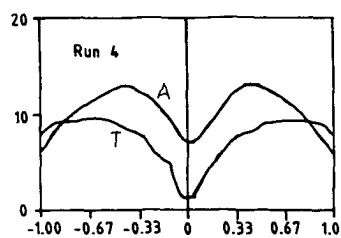
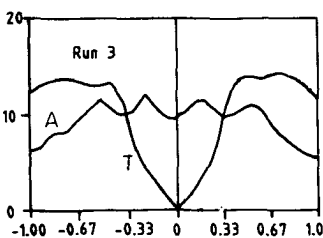
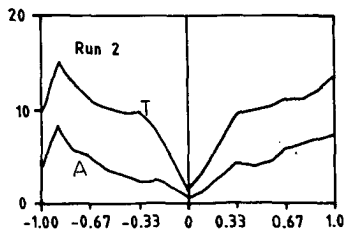
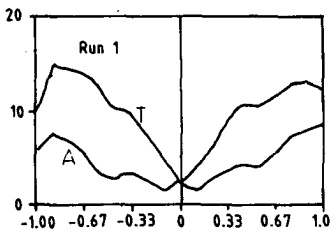
APPENDIX C

EXPERIMENTAL RESULTS

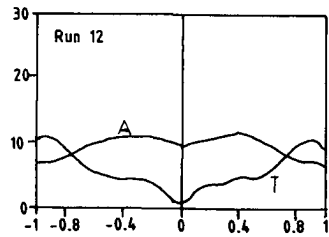
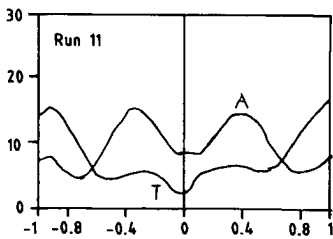
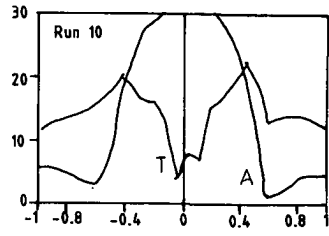
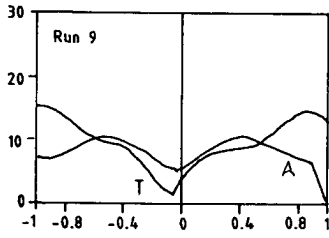
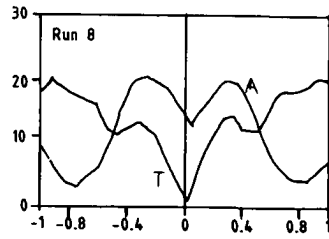
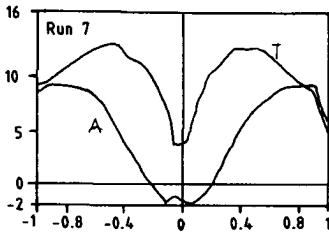
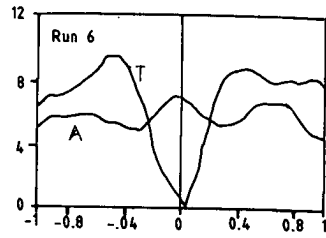
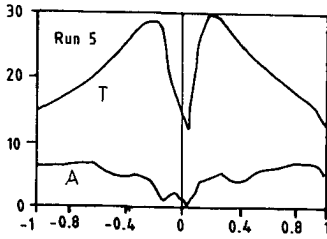
Physical properties of test fluids (20°C, 1 bar)

| | | |
|-----------------|------------------------------|-----------------|
| air | $\rho_g = 1.3$ | kg/m^3 |
| | $\mu_g = 1.9 \cdot 10^{-5}$ | Pa.s |
| SF ₆ | $\rho_g = 6.5$ | kg/m^3 |
| water | $\rho_l = 1000$ | kg/m^3 |
| | $\mu_l = 1.0 \cdot 10^{-3}$ | Pa.s |
| | $\sigma = 7.3 \cdot 10^{-2}$ | N/m |
| ethylene glycol | $\rho_l = 1113$ | kg/m^3 |
| | $\mu_l = 21 \cdot 10^{-3}$ | Pa.s |
| | $\sigma = 3.6 \cdot 10^{-2}$ | N/m |
| butanol | $\rho_l = 806$ | kg/m^3 |
| | $\mu_l = 2.9 \cdot 10^{-3}$ | Pa.s |
| | $\sigma = 2.5 \cdot 10^{-2}$ | N/m |

TABLE 6.II



C.2



C.3

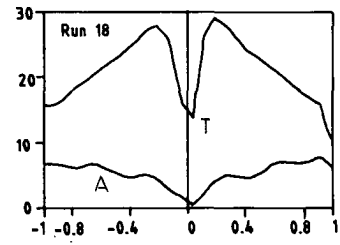
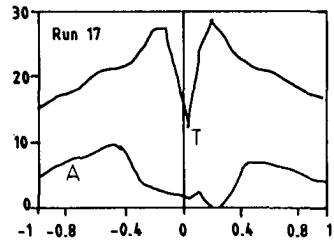
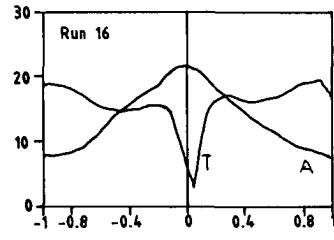
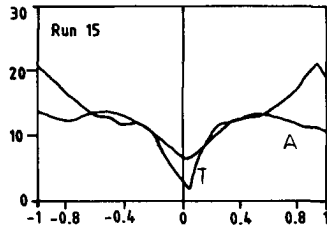
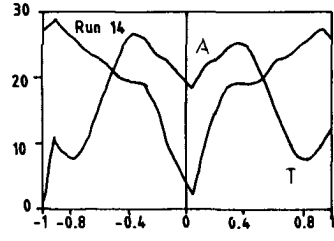
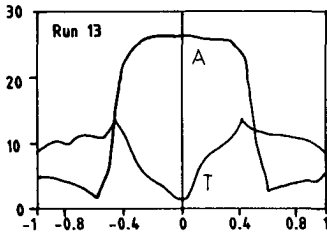


TABLE 6.IV

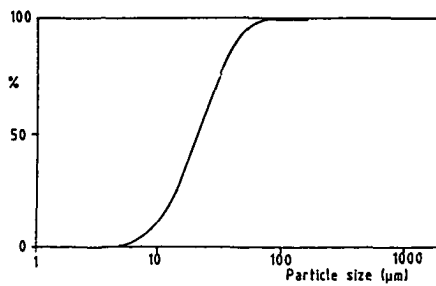
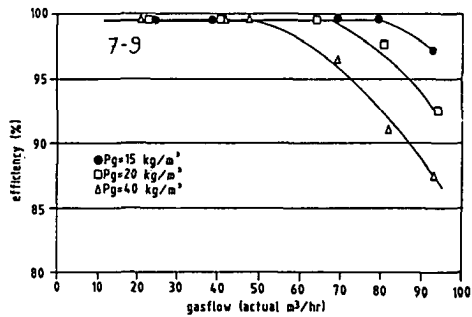
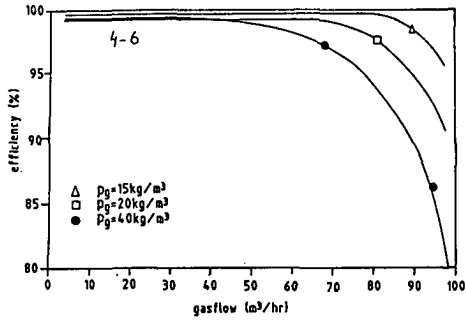
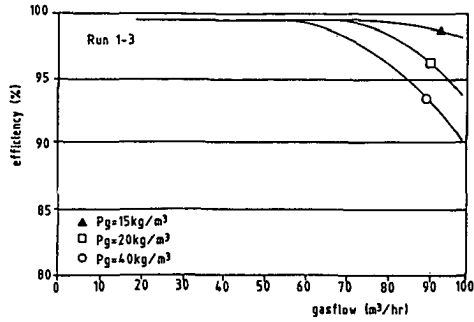


TABLE 6.V

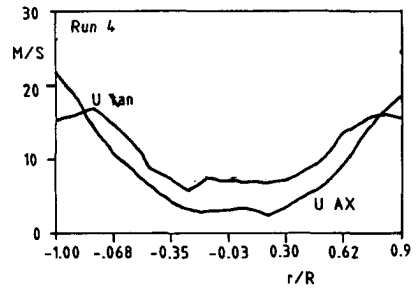
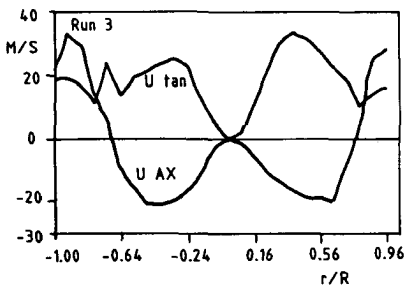
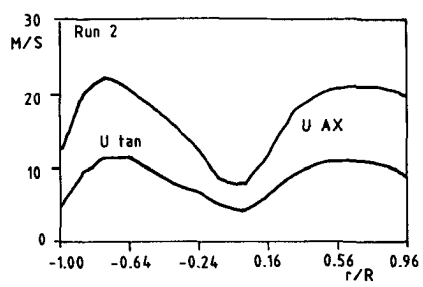
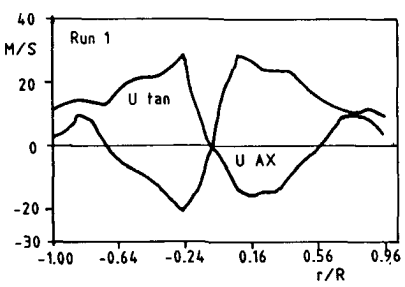


TABLE 6.VI

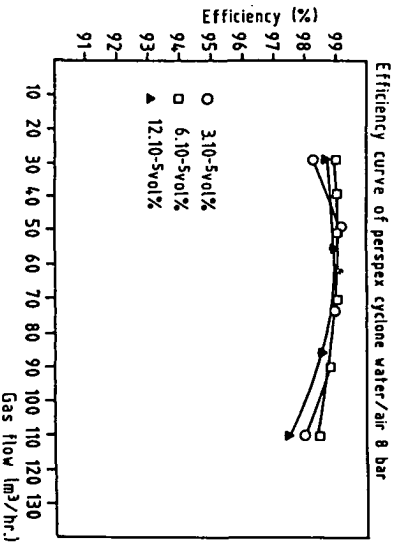
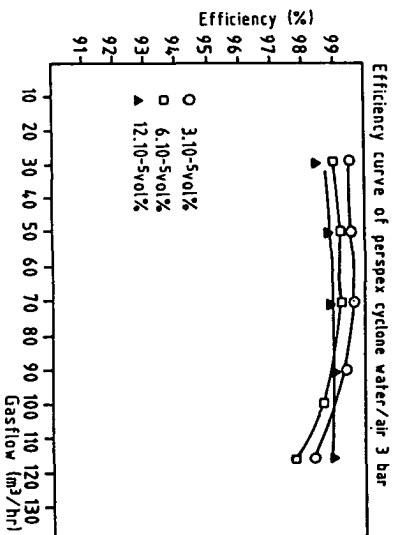
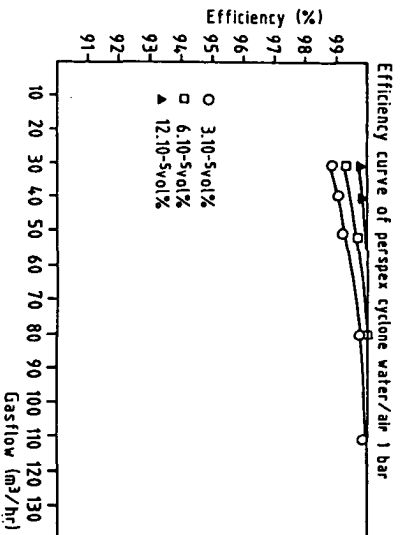
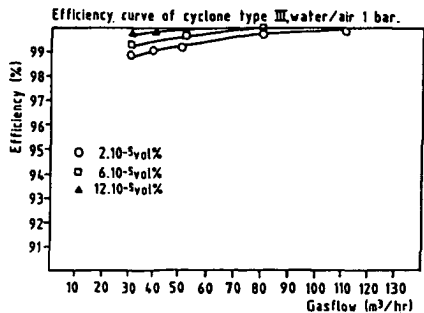
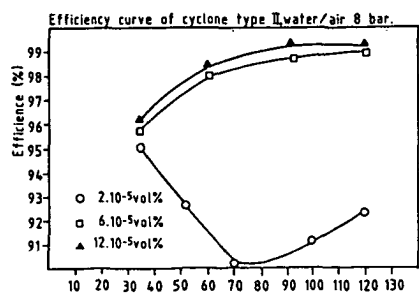
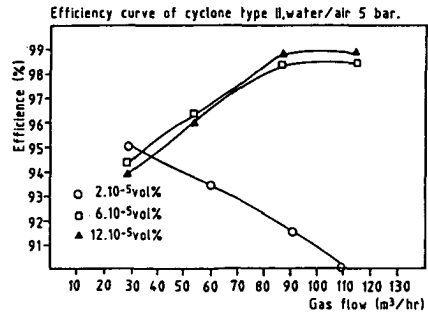
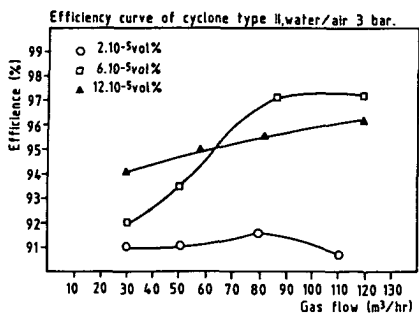
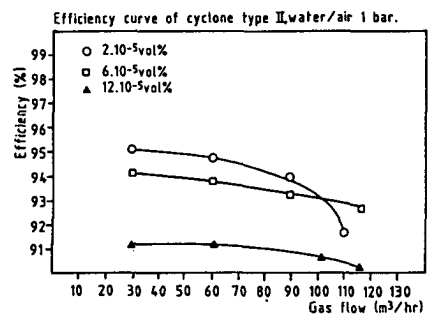
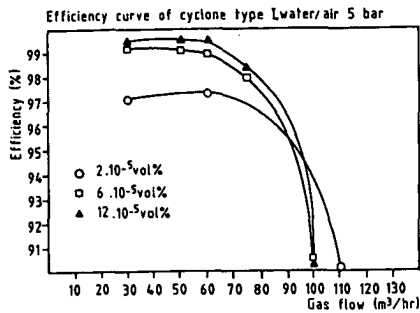
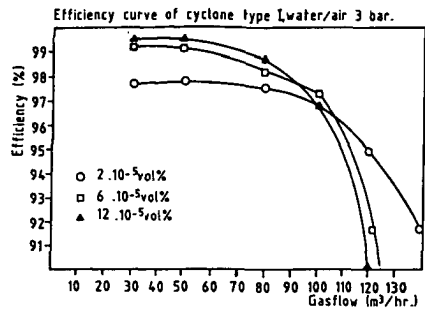
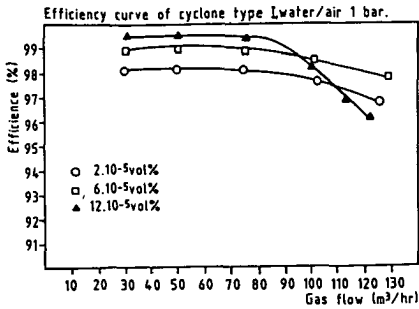
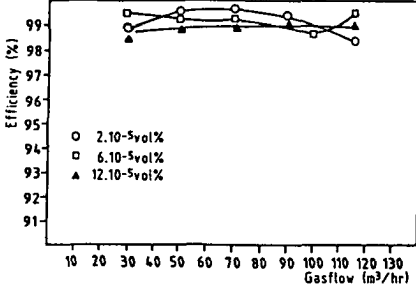


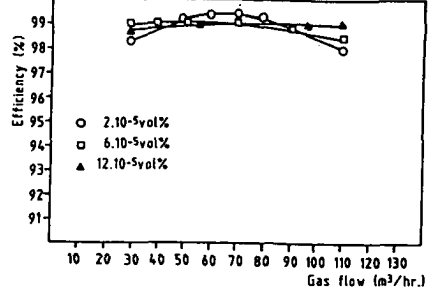
TABLE 6.VII



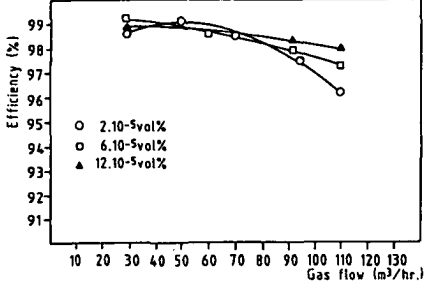
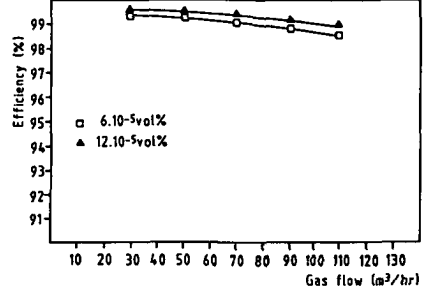
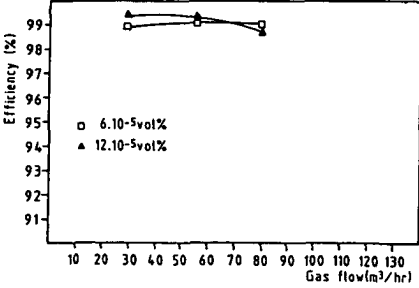
Efficiency curve of cyclone type III, water/air 3 bar.



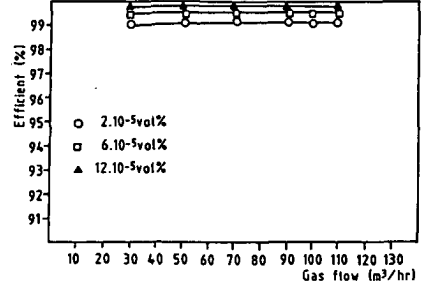
Efficiency curve of cyclone type III, water/air 5 bar.



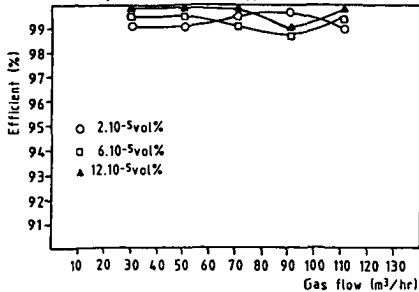
Efficiency curve of cyclone type III, water/air 8 bar.

Efficiency curve of cyclone type III, water/SF₆ 2 bar.Efficiency curve of cyclone type III, water/SF₆ 4 bar.

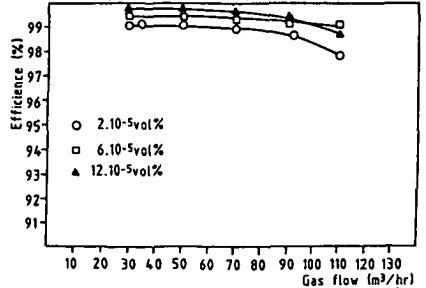
Efficiency curve of cyclone type III, butanol/air 1 bar.



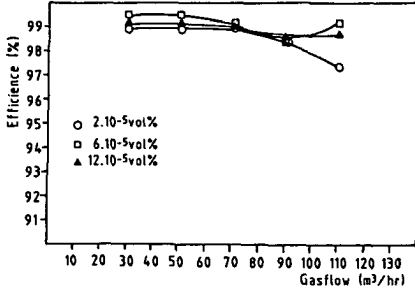
Efficiency curve of cyclone type III, butanol/air 3 bar.



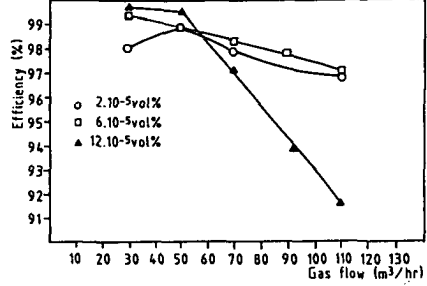
Efficiency curve of cyclone type III, butanol/air 5 bar.



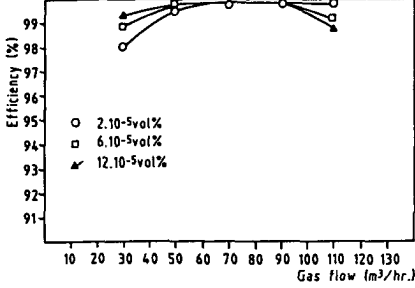
Efficiency curve of cyclone type III, butanol/air 8 bar.



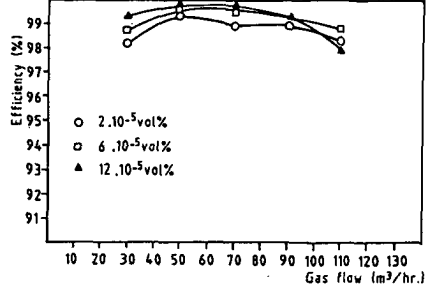
Efficiency curve of cyclone type III, glycol/air 5 bar.



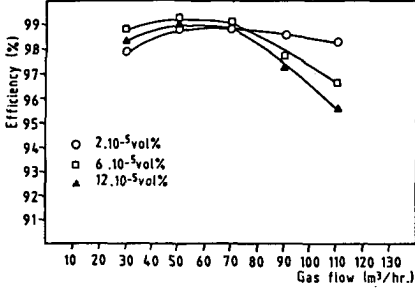
Efficiency curve of cyclone type IV, water/air 1 bar.



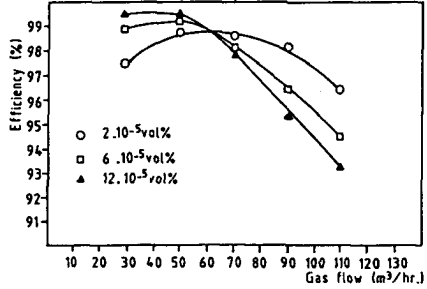
Efficiency curve of cyclone type IV, water/air 3 bar.



Efficiency curve of cyclone type IV, water/air 5 bar.



Efficiency curve of cyclone type IV, water/air 8 bar.



C.10

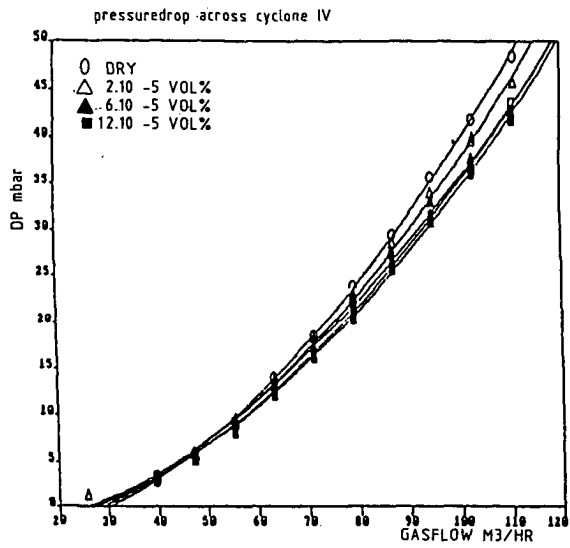
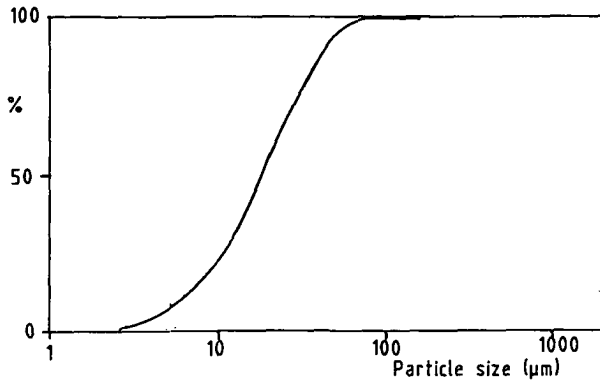
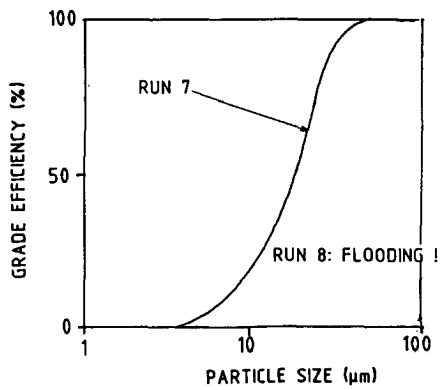
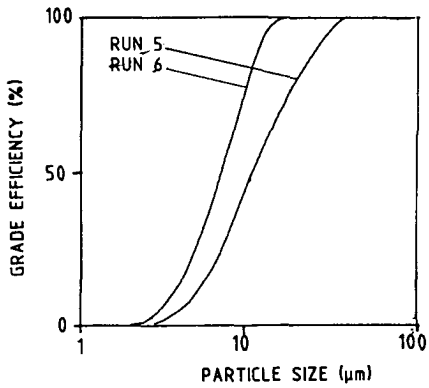
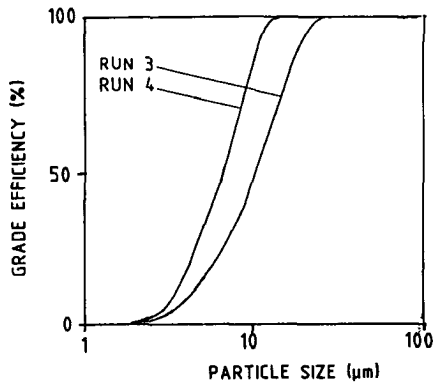
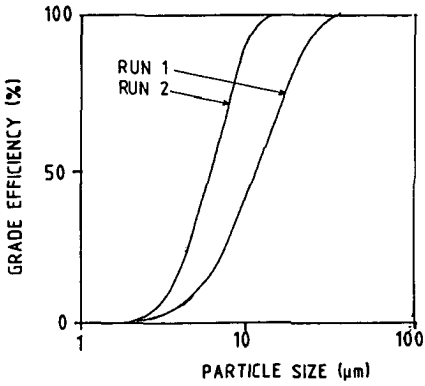


TABLE 6.X



APPENDIX D

TURBULENCE MODELS

It appeared from section 7.2 that assumptions have to be made with respect to the quantification of the turbulent shear stresses in order to be able to solve the Navier Stokes equations. These assumptions are usually referred to as turbulence models.

D.1 Turbulence models based on the concept of Boussinesq

D.1.1 Background of Boussinesq models

Already in 1877 Boussinesq assumed that, analogous to viscous stresses in laminar flows, turbulent stresses are proportional to the average velocity gradients.

$$-\langle u_i' u_j' \rangle = \frac{\tau_{ij}}{\rho} = \nu_t D_{ij} - \frac{2}{3} k \delta_{ij} \quad i, j = r, \phi, z \quad (D.1)$$

in which: δ_{ij} = the Kronecker delta; $\delta_{ij} = 0$ for $i \neq j$; $\delta_{ij} = 1$ for $i = j$
 ν_t = the turbulence viscosity ('eddy viscosity')
 D_{ij} = the deformation velocity tensor.

The different components of D_{ij} for cylindrical coordinates are:

$$\begin{aligned} D_{rr} &= 2 \frac{\delta v}{\delta r} & D_{r\phi} &= D_{\phi r} = \frac{\delta w}{\delta r} - \frac{w}{r} + \frac{\delta v}{r \delta \phi} \\ D_{\phi\phi} &= 2 \left(\frac{\delta w}{r \delta \phi} + \frac{v}{r} \right) & D_{\phi z} &= D_{z\phi} = \frac{\delta u}{r \delta \phi} + \frac{\delta w}{\delta z} \\ D_{zz} &= 2 \frac{\delta u}{\delta z} & D_{zr} &= D_{rz} = \frac{\delta v}{\delta z} + \frac{\delta u}{\delta r} \end{aligned} \quad (D.2)$$

The reason for the second term in equation D.1 is the fact that the sum of the $\langle u'^2 \rangle$, $\langle v'^2 \rangle$ and $\langle w'^2 \rangle$ (normal stresses) determined with only the deformation tensor will amount to zero. This assumption is not realistic as

D.2

the normal shear stresses, that act as a pressure, are always positive in turbulent flows. Therefore, each normal stress is assigned $\frac{2}{3}k$ resulting in $\langle u'^2 \rangle + \langle v'^2 \rangle + \langle w'^2 \rangle = 2k$, the original definition of k , representing the turbulent kinetic energy.

The determination of the six unknown stresses has been reduced to the determination of v_t . This turbulence viscosity is a scalar, which means that an isotropic gas flow field is assumed. The latter aspect is the largest disadvantage of this model concept when predicting anisotropic flow fields. The models to determine v_t are traditionally subdivided with respect to the number of partial differential equations (PDE) that has to be solved. In the following subsections turbulence models will be described that are based on the concept of Boussinesq, with 0, 1 and 2 PDE's.

D.1.2 Zero PDE models

A representative example of a zero PDE model is the Prandtl-mixing length model. Prandtl assumed that eddy currents in a fluid flow would behave corresponding to molecules in the kinetic gas theory. They collide and exchange impulse momentum. He assumed that the turbulence viscosity would be dependent of a turbulent velocity scale \hat{U} and a mixing length L_m . Analogous to the average velocities of gas molecules and their average free path they can traverse in the kinetic gas theory. The average velocity \hat{U} is defined as the mixing length multiplied by the gradient of the time averaged velocity (derived from the Reynolds decomposition).

$$v_t = L_m \cdot \hat{U}$$

$$\text{in which: } \hat{U} = L_m \left(\frac{\delta v}{\delta z} + \frac{\delta u}{\delta r} \right)$$

$$\text{so: } v_t = L_m^2 \left(\frac{\delta v}{\delta z} + \frac{\delta u}{\delta r} \right) \quad (D.3)$$

As appears from the notation used above, it is assumed that a main flow direction exists and that it is parallel to the z axis in the coordinate system. These two assumptions are not valid in cyclones with swirl intensities necessary for practical operation. L_m is usually determined by

empirical relations that will not be cited here, see for instance Pelsma [1987] or Rodi [1984].

D.1.3 One PDE models

In these models one extra partial differential equation is formulated that is solved iteratively. In the Prandtl Kolmogoroff relation this equation accounts for the transport of the turbulent kinetic energy (k). This quantity is used as a measure for the velocity scale \hat{U} of the eddy currents:

$$\begin{aligned} v_t &= L_m \cdot \hat{U} \\ \hat{U} &= c'_\mu k^{1/2} \\ v_t &= L_m c'_\mu k^{1/2} \end{aligned} \tag{D.4}$$

L_m and c'_μ are again determined empirically. k is determined with the transport equation for the turbulent kinetic energy that can be derived from the Navier-Stokes equations. This transport equation is described in the next subsection.

D.1.4 Two PDE models

These models accommodate a second partial differential equation with which the variation of L_m can be quantified.

In the well-known k - ϵ model a transport equation for ϵ is formulated. ϵ represents the dissipation of turbulent kinetic energy and relates to L_m in the following way:

$$\begin{aligned} L_m &= \frac{k^{3/2}}{\epsilon} \\ \text{when } \hat{U} &= c'_\mu k^{1/2} \text{ then:} \\ v_t &= c'_\mu \frac{k^2}{\epsilon} \end{aligned} \tag{D.5}$$

in which: $c'_\mu = 0,09$

The transport equations for k and ϵ are derived from the Navier Stokes equations and are represented as follows:

$$k: \quad u \frac{\delta k}{\delta z} + v \frac{\delta k}{\delta r} = \frac{\delta}{\delta z} \frac{v_t}{\sigma_\epsilon} \frac{\delta k}{\delta z} + \frac{1}{r} \frac{\delta}{\delta r} r \frac{v_t}{\sigma_\epsilon} \frac{\delta k}{\delta r} + P - \epsilon \quad (D.6)$$

|
|
|
|

convection
diffusion
produc-
dissi-

tion
pation

$$\epsilon: \quad u \frac{\delta \epsilon}{\delta z} + v \frac{\delta \epsilon}{\delta r} = \frac{\delta}{\delta z} \frac{v_t}{\sigma_\epsilon} \frac{\delta \epsilon}{\delta z} + \frac{1}{r} \frac{\delta}{\delta r} r \frac{v_t}{\sigma_\epsilon} \frac{\delta \epsilon}{\delta r} + c_{\epsilon 1} P \frac{\epsilon}{k} - c_{\epsilon 2} \frac{\epsilon^2}{k} \quad (D.7)$$

|
|
|
|

convection
diffusion
production
dissipation

σ_ϵ , $c_{\epsilon 1}$ and $c_{\epsilon 2}$ are determined experimentally. In both codes (Phoenix and Fluent) for simulation modelling they amounted to:

$$\begin{aligned} \sigma_\epsilon &= 1,3 \\ c_{\epsilon 1} &= 1,44 \\ c_{\epsilon 2} &= 1,92 \end{aligned}$$

This k - ϵ model is generally applied for fluid flows with a distinct main flow direction. It is not suited for the modelling of strongly rotating flows as has been demonstrated in chapter 7.

D.2 Direct modelling of turbulent shear stresses

In this section will be demonstrated how the equations for the individual turbulent shear stresses can be solved individually. The six partial differential equations can be solved directly, in which case the model is referred to as Reynolds stress model.

The six PDE's can also be simplified to algebraic equations, in which case the resulting model is the Algebraic Stress model. A short description of both models is given below.

Reynolds stress model

Starting from the full Navier Stokes equations the transport equations for the individual turbulent shear stresses can be derived. This will be done first for a Cartesian coordinate system, after which the expressions will be derived for cylindrical coordinates.

The general transport equation for the individual shear stress is represented by:

$$\begin{aligned}
 \frac{D \langle u'_i u'_j \rangle}{Dt} = & \underbrace{- \langle u'_j u'_k \rangle \frac{\delta u'_i}{\delta x_k} - \langle u'_i u'_k \rangle \frac{\delta u'_j}{\delta x_k}}_{\text{production} = p_{ij}} - 2 \nu \underbrace{\langle \frac{\delta u'_i}{\delta x_k} \frac{\delta u'_j}{\delta x_k} \rangle}_{\text{dissipation}} \\
 & + \underbrace{\frac{\delta}{\delta x_k} \left[\nu \frac{\delta \langle u'_i u'_j \rangle}{\delta x_k} - \langle u'_i u'_j u'_k \rangle - \left\langle \frac{p'}{\rho} (u'_i \delta_{jk} + u'_j \delta_{ik}) \right\rangle \right]}_{\text{diffusion}} \\
 & + \underbrace{\left\langle \frac{p'}{\rho} \left(\frac{\delta u'_i}{\delta x_j} + \frac{\delta u'_j}{\delta x_i} \right) \right\rangle}_{\substack{\text{pressure/stress} \\ \text{correlation}}}
 \end{aligned} \tag{D.8}$$

To express the dissipation, diffusion and pressure/stress correlation in quantifiable units some assumptions have to be used:

1. The dissipation is simplified by:

$$2 \nu \langle \frac{\delta u'_i}{\delta x_k} \frac{\delta u'_j}{\delta x_k} \rangle = \frac{2}{3} \epsilon \delta_{ij}$$

$$\text{in which: } \epsilon = \nu \langle \frac{\delta u'_i}{\delta x_k} \frac{\delta u'_i}{\delta x_k} \rangle$$

This only holds when the dissipation is equal in all directions, which is the case in areas where the local turbulent Reynolds numbers are large. Also in non-isotropic flows this assumption appears to be a simplification that does not influence the results strongly.

2. The turbulence diffusion is, according to Donaldson [1968], approximated by:

$$D_{ij} = \frac{\delta}{\delta x_k} v_t \frac{\delta \langle u'_i u'_j \rangle}{\delta x_k}$$

in which D_{ij} is the total diffusion and v_t the scalar turbulence viscosity, as follows from the k - ϵ model.

3. The pressure/stress correlation is, according to Gibson and Launder [1976], approximated by:

$$\left\langle \frac{p'}{\rho} \left(\frac{\delta u'_i}{\delta x_j} + \frac{\delta u'_j}{\delta x_i} \right) \right\rangle = -c_1 \frac{\epsilon}{k} \left(\langle u'_i u'_j \rangle - \frac{2}{3} k \delta_{ij} \right) - c_2 \left(P_{ij} - \frac{2}{3} P \delta_{ij} \right)$$

in which: c_1 and c_2 are constants

$$\begin{aligned} P &= \frac{1}{2} P_{ii} \\ P_{ij} &= - \langle u'_j u'_k \rangle \frac{\delta u'_i}{\delta x_k} - \langle u'_i u'_k \rangle \frac{\delta u'_j}{\delta x_k} \end{aligned}$$

Substitution of the three assumptions in equation D.8 gives:

$$\frac{D \langle u'_i u'_j \rangle}{Dt} = P_{ij} - \frac{2}{3} \epsilon \delta_{ij} + D_{ij} - c_1 \frac{\epsilon}{k} \left(\langle u'_i u'_j \rangle - \frac{2}{3} k \delta_{ij} \right) - c_2 \left(P_{ij} - \frac{2}{3} P \delta_{ij} \right) \quad (D.9)$$

This forms a set of six partial differential equations. With the three Navier Stokes equations and the transport equations for k and ϵ , 11 PDE's have to be solved for this Reynolds stress model.

Although it is possible to accommodate this model and its solution scheme in presently available hardware, it is sometimes preferable to simplify the first six PDE's mentioned above to an algebraic form.

Algebraic Stress model

To simplify the six PDE's represented by equation D.9 to an algebraic form, Rodi [1984] made an extra assumption: The transport of Reynold stresses is proportional to the transport of k .

This assumption is justified if the changes of the ratio between Reynolds stresses and K with respect to time and location are small in comparison to the change of the Reynold stresses themselves. If the convection and diffusion term are combined to a term T_{ij} , the assumption of Rodi is represented by:

$$T_{ij} = \frac{\langle u'_i u'_j \rangle}{k} (P - \epsilon) \quad (D.10)$$

Substitution in equation D.9 gives the general algebraic form of the Reynold stresses.

$$\begin{aligned} \langle u'_i u'_j \rangle = & \frac{2}{3} k \delta_{ij} \left[1 - \frac{(1 - c_2) \frac{P}{\epsilon}}{\frac{P}{\epsilon} - 1 + c_1} \right] + \frac{1 - c_2}{\frac{P}{\epsilon} - 1 + c_1} \frac{k}{\epsilon} (P_{ij} - \frac{2}{3} P \delta_{ij}) + \\ & + \frac{1}{\frac{P}{\epsilon} - 1 + c_1} \frac{k}{\epsilon} A_{ij} \end{aligned} \quad (D.11)$$

A_{ij} is the 'added convection' term, which is formed in the transformation from a cartesian to a cylindrical coordinate system.

In case of a rotating flow A_{ij} is of great importance. It consists of:

$$A_{ij} = \begin{vmatrix} 0 & \langle u'w' \rangle \frac{w}{r} & - \langle u'v' \rangle \frac{w}{r} \\ \langle u'w' \rangle \frac{w}{r} & 2 \langle v'w' \rangle \frac{w}{r} & - (\langle v'^2 \rangle - \langle w'^2 \rangle) \frac{w}{r} \\ - \langle u'v' \rangle \frac{w}{r} & - (\langle v'^2 \rangle - \langle w'^2 \rangle) \frac{w}{r} & -2 \langle v'w' \rangle \frac{w}{r} \end{vmatrix} \quad (D.12)$$

When equation 7.5 is substituted in equation 7.4 the algebraic form of the expressions for the individual Reynold stresses is obtained.

$$\langle u'^2 \rangle = \frac{1}{1 + 2 \alpha \frac{k}{\epsilon} \frac{\delta u}{\delta z}} \left[\frac{2}{3} k \left(1 - \alpha \frac{P}{\epsilon} \right) - 2 \alpha \frac{k}{\epsilon} \langle u'v' \rangle \frac{\delta u}{\delta r} \right] \quad (D.13)$$

$$\langle v'^2 \rangle = \frac{1}{1 + 2 \alpha \frac{k}{\epsilon} \frac{\delta v}{\delta r}} \left[\frac{2}{3} k \left(1 - \alpha \frac{P}{\epsilon} \right) - 2 \alpha \frac{k}{\epsilon} \langle u'v' \rangle \frac{\delta v}{\delta z} + 2(\alpha + \lambda) \frac{k}{\epsilon} \langle v'w' \rangle \frac{w}{r} \right] \quad (D.14)$$

$$\langle w'^2 \rangle = \frac{1}{1 + 2 \alpha \frac{k}{\epsilon} \frac{v}{r}} \left[\frac{2}{3} k \left(1 - \alpha \frac{P}{\epsilon} \right) - 2 \alpha \frac{k}{\epsilon} \langle u'w' \rangle \frac{\delta w}{\delta z} + 2 \frac{k}{\epsilon} \langle v'w' \rangle \left(\alpha \frac{\delta w}{\delta r} + \lambda \frac{w}{r} \right) \right] \quad (D.15)$$

$$\langle u'w' \rangle = - \alpha \frac{k^2}{\epsilon} \left[\frac{\langle u'^2 \rangle}{k} \frac{\delta w}{\delta z} - \frac{\langle v'w' \rangle}{k} \frac{\delta u}{\delta r} + \frac{\langle u'v' \rangle}{k} \left(\frac{\delta w}{\delta r} + \frac{\lambda}{\alpha} \frac{w}{r} \right) \right] / A_1 \quad (D.16)$$

$$\langle u'v' \rangle = - \alpha \frac{k^2}{\epsilon} \left[\frac{\langle v'^2 \rangle}{k} \frac{\delta u}{\delta r} + \frac{\langle u'^2 \rangle}{k} \frac{\delta v}{\delta z} + \frac{\langle u'w' \rangle}{k} \left(1 + \frac{\lambda}{\alpha} \right) \frac{w}{r} \right] / A_2 \quad (D.17)$$

$$\begin{aligned} \langle v'w' \rangle &= - \alpha \frac{k^2}{\epsilon} \left[\frac{\langle v'^2 \rangle}{k} \left(\frac{\delta w}{\delta r} - \frac{w}{r} \right) - \frac{\langle u'v' \rangle}{k} \frac{\delta w}{\delta z} + \frac{\langle u'w' \rangle}{k} \frac{\delta v}{\delta z} \right] / A_3 \\ &\quad - \alpha \frac{k^2}{\epsilon} \left[\frac{\langle v'^2 \rangle - \langle w'^2 \rangle}{k} \left(1 + \frac{\lambda}{\alpha} \right) \frac{w}{r} \right] / A_3 \end{aligned} \quad (D.18)$$

Version 2.9 of Fluent (that has been used in some of the models in chapter 7) accommodated the algebraic stress model described above.

In this version the used constants had the following values:

$$\begin{aligned} A_1 &= \left(1 - \alpha \frac{k}{\epsilon} \frac{\delta v}{\delta r} \right) = 1 \\ A_2 &= \left(1 - \alpha \frac{k}{\epsilon} \frac{v}{r} \right) = 1 \\ A_3 &= \left(1 - \alpha \frac{k}{\epsilon} \frac{\delta u}{\delta z} \right) = 1 \\ \alpha &= \frac{(1 - c_2)}{\left(\frac{P}{\epsilon} - 1 + c_1 \right)} \\ \lambda &= \frac{c_3}{\left(\frac{P}{\epsilon} - 1 + c_1 \right)} \end{aligned} \quad (D.19)$$

D.9

$$c_1 = 2,5 \quad c_2 = 0,55 \quad c_3 = 1$$

The production of turbulent kinetic energy, P, is given in cylindrical coordinates by:

$$P = - \langle u'z \rangle \frac{\delta u}{\delta z} - \langle v'z \rangle \frac{\delta v}{\delta r} - \langle w'z \rangle \frac{v}{r} - \langle u'w' \rangle \frac{\delta w}{\delta z} - \langle u'v' \rangle \left(\frac{\delta u}{\delta r} + \frac{\delta v}{\delta z} \right) - \langle v'w' \rangle \left(\frac{\delta w}{\delta r} - \frac{w}{r} \right) \quad (D.20)$$

CURRICULUM VITAE

Naam : Swanborn

Voornamen : Rombout Adriaan

Geboren : 15 augustus 1960 te Point Fortin, Trinidad

Adres : Oosterkade 69
3011 TV Rotterdam

Opleiding : Gymnasium β te Curaçao en Bussum, 1978
Mijnningenieur, Technische Hogeschool Delft, 1984
Afgestudeerd op de afregeling en optimalisatie van een
installatie om goud uit de tailings van een (goud)mijn
terug te winnen.

Werkgever : vanaf oktober 1987 werkzaam bij Unilever Engineering,
Vlaardingen

ACKNOWLEDGEMENTS

I like to thank Shell Internationale Petroleum Maatschappij B.V., The Ministry of Economic Affairs, Sombroek Zaandam B.V. and Stork Ketels B.V. for making this project possible.

I like to thank my promoters, prof.ir. E.J. de Jong and prof.dr.ir. J. de Graauw for initiating this project, for allowing me a great deal of freedom in the execution of it and for the many hours of fruitful discussions.

I like to thank all employees of the Laboratory for Process Equipment for their skilful assistance which proved to be very valuable for the progress of the project.

I like to thank all mechanical and chemical engineering students who participated in this project. Without their contributions it would never have been possible to cover the vast collection of subjects that have been investigated.

I like to thank the following persons or companies that have contributed to the progress of this research project:

- L.R. Hafkamp, H.E.A. van den Akker and G.W. Colenbrander of Koninklijke/Shell-Laboratorium, Amsterdam
- B. Jäger of Wolf Endoscopie GmbH
- G. Küpers of Neratoom B.V.
- F. Koene and R. Diekmann of Burgess Manning
- Euroform GmbH
- Paladon Engineering Ltd.

Finally, I like to thank my present employer, Unilever Engineering, for supporting this work.